



**HAL**  
open science

# Angular control of levitated magnetic particles for studies of gyromagnetism at the micro-scale

Maxime Perdriat

► **To cite this version:**

Maxime Perdriat. Angular control of levitated magnetic particles for studies of gyromagnetism at the micro-scale. Quantum Physics [quant-ph]. Université Paris Cité, 2023. English. NNT : 2023UNIP7050 . tel-04478554v2

**HAL Id: tel-04478554**

**<https://theses.hal.science/tel-04478554v2>**

Submitted on 27 Mar 2024

**HAL** is a multi-disciplinary open access archive for the deposit and dissemination of scientific research documents, whether they are published or not. The documents may come from teaching and research institutions in France or abroad, or from public or private research centers.

L'archive ouverte pluridisciplinaire **HAL**, est destinée au dépôt et à la diffusion de documents scientifiques de niveau recherche, publiés ou non, émanant des établissements d'enseignement et de recherche français ou étrangers, des laboratoires publics ou privés.

# Université Paris Cité

Ecole doctorale 564 : Physique en Île-de-France

Laboratoire de Physique de l'École Normale Supérieure UMR8023

Équipe Nano-Optique

## Angular control of levitated magnetic particles for studies of gyromagnetism at the micro-scale

par Maxime PERDRIAT

Thèse de doctorat de Physique

Dirigée par Gabriel HÉTET

Présentée et soutenue publiquement le 14 avril 2023

devant un jury composé de

Tracy E. NORTHUP	Professeure	Rapporteuse	Univ. Innsbruck
Olivier ARCIZET	Chargé de recherche (HDR)	Rapporteur	Institut Néel
Ivan FAVERO	Directeur de recherche (HDR)	Examinateur	Univ. Paris Cité
David GUÉRY-ODELIN	Professeur (HDR)	Examinateur	Univ. de Toulouse
Anaïs DRÉAU	Chargée de recherche	Examinatrice	Lab. Charles Coulomb
Derek F. KIMBALL	Professeur	Invité	Cal. State East Bay
Gabriel HÉTET	Maître de conférence (HDR)	Dir. de thèse	École Normale Sup.



**Titre : Contrôle angulaire de particules magnétiques en lévitation pour l'étude d'effets gyromagnétiques à l'échelle micrométrique.**

**Résumé :** Depuis l'avènement de la physique quantique il y a un siècle, de nombreuses interrogations demeurent sur la frontière entre le monde classique et le monde quantique. La génération d'états quantiques de systèmes de plus en plus massifs en opto-mécanique offre une opportunité pour explorer ces limites. Fort de cet élan, l'étude des régimes quantiques des modes mécaniques de particules micro/nanométriques en lévitation a connu un essor florissant au cours des dix dernières années. De par leur dynamique intrinsèquement non-linéaire, les degrés de liberté angulaires d'une particule en lévitation présentent une physique riche aussi bien sur le plan classique que quantique.

Dans cette thèse, nous nous intéressons à la physique du couplage entre les degrés de liberté angulaire et le magnétisme interne de cristaux en lévitation. La dualité entre le moment magnétique et le moment cinétique donne lieu à un couplage naturel entre la dynamique angulaire d'un cristal en lévitation et son magnétisme interne, plus connu sous le nom d'effets gyromagnétiques. Le but de ce travail est d'étudier la dynamique angulaire de particules magnétiques en lévitation à une échelle micrométrique où ces effets sont exacerbés. Nous considérons pour cela deux techniques de piégeages distincts: un piège magnétique pour la lévitation d'aimants ainsi qu'un piège électrique pour la lévitation de particules chargées.

Dans un premier temps, nous montrons que l'on peut faire léviter des aimants millimétriques dans un piège de Paul magnétique planaire macroscopique et nous proposons un design adapté à la lévitation d'aimants micro/nanométriques. Comparée à la lévitation supraconductrice, cette technique de piégeage offre de nombreux avantages de par la simplicité du dispositif expérimental et le degré de contrôle sur le potentiel de piégeage.

Il est aussi intéressant de pouvoir contrôler l'angle de particules magnétiques en lévitation de façon purement électrique. En particulier, nous montrons qu'une non-linéarité dans l'équation de la dynamique angulaire d'un piège électrique permet la rotation de particules piégées au kilohertz. Nous utilisons les centres NV dans un diamant piégé en rotation pour reconstituer la trajectoire angulaire de celui-ci et démontrer l'extrême stabilité de cette technique de rotation. Ces résultats ouvrent la voie à l'observation d'effets gyromagnétiques dans le référentiel tournant et pourraient avoir des applications en gyroscopie, spin-mécanique et magnétométrie.

Enfin, le couplage fort entre les spins et le degré de liberté angulaire a aussi été étudié avec des diamants en lévitation dans un piège électrique. Nous prouvons l'existence d'une nouvelle forme de magnétisme avec les centres NV, le spin-diamagnétisme, permettant d'orienter l'axe d'anisotropie d'un diamant micrométrique en lévitation avec l'axe du champ magnétique externe. Cette technique pourrait servir dans des protocoles d'hyperpolarisation avec des diamants en suspension dans des liquides.

**Mots clefs :** lévitation, centre NV, gyromagnétisme, piège de Paul, rotation.

**Title: Angular control of levitated magnetic particles for studies of gyromagnetism at the micro-scale.**

**Abstract:** Since the advent of quantum physics a century ago, many questions remain about the frontier between the classical and quantum worlds. The generation of quantum states of increasingly massive systems in opto-mechanics offers an opportunity to explore these boundaries. Taking advantage of this success, the study of quantum regimes of mechanical modes of levitating micro/nanometer particles has flourished over the past decade. Due to their intrinsically nonlinear dynamics, the angular degrees of freedom of a levitating particle present a rich physics both classically and quantumly, with no equivalent with the center-of-mass modes.

In this thesis, we are interested in the physics of the coupling between the angular degrees of freedom and the internal magnetism of levitating crystals. The duality between the magnetic moment and the angular momentum gives rise to a natural coupling between the angular dynamics of a levitating crystal and its internal magnetism, better known as gyromagnetic effects. The objective of this work is to study the angular dynamics of levitating magnetic particles at a micron level, where these effects are amplified. To achieve this, we are considering two different trapping methods: a magnetic trap for levitating magnets and an electric trap for levitating charged particles.

First, we show that millimeter magnets can be levitated in a macroscopic planar magnetic Paul trap and we propose a design suitable for levitating micro/nanometer magnets. Compared to superconducting levitation, this trapping technique offers many advantages due to the simplicity of the experimental setup and the degree of control over the trapping potential.

It is also interesting to be able to control the angle of levitating magnetic particles in a purely electrical way. In particular, we show that a nonlinearity in the angular dynamics equation of an electric trap allows the rotation of trapped particles at kilohertz. We use the NV centers in a rotating trapped diamond to reconstruct its angular trajectory and demonstrate the extreme stability of this rotation technique. These results open the way to the observation of gyromagnetic effects in the rotating reference frame and could have applications in gyroscopy, spin-mechanics and magnetometry.

Finally, the strong coupling between spins and angular degree of freedom has also been studied with diamonds levitated in an electric trap. We prove the existence of a new form of magnetism with NV centers, spin-diamagnetism, allowing to orient the anisotropy axis of a levitated micrometer diamond with the external magnetic field axis. This technique could be used in hyperpolarization protocols with diamonds suspended in liquids.

**Keywords:** levitation, NV center, gyromagnetism, Paul trap, rotation.

## **Titre : Contrôle angulaire de particules magnétiques en lévitation pour l'étude d'effets gyromagnétiques à l'échelle micrométrique.**

**Résumé long :** La physique quantique a conduit à de nombreuses avancées scientifiques remarquables, notamment le développement de l'imagerie par résonance magnétique (IRM) à des fins médicales, la découverte du transistor pour l'industrie électronique et l'émergence des lasers. Dans la seconde moitié du vingtième siècle, l'amélioration des techniques expérimentales a permis le contrôle des entités quantiques élémentaires telles que les atomes et les photons, permettant le développement de technologies quantiques. La plupart des efforts ont alors été dirigée vers la génération d'états quantiques avec un plus grand nombre de ces entités physiques, utilisant jusqu'à dix photons dans une cavité micro-ondes, des dizaines d'ions piégés refroidis par laser et des molécules constituées de centaines d'atomes. Au début de ce siècle, des avancées cruciales en nano-fabrication ont même permis de porter un résonateur mécanique nano/micrométrique composé de milliards d'atomes à l'état fondamental quantique.

Explorer les limites de la physique quantique à une échelle macroscopique reste l'une des principales motivations de la recherche expérimentale depuis la formulation de la célèbre expérience de pensée du chat de Schrödinger en 1935. Notamment, le couplage avec le champ électromagnétique médié par la pression de radiation en optomécanique a permis d'atteindre l'état fondamental quantique de résonateurs mécaniques en utilisant des techniques de bande latérale résolue et de refroidissement par rétroaction. Malgré la sensibilité extrême des états quantiques macroscopiques à l'environnement, atteindre l'état fondamental quantique pour de tels systèmes est maintenant couramment réalisé, et la génération d'états non classiques tels que les états comprimés ou les états intriqués est devenue l'objet d'attention. À la lumière de ces succès récents, répondre à des questions fondamentales sur l'unification des théories physiques, telles que la gravité quantique ou le problème de la mesure en physique quantique, ne semblent plus être des objectifs inaccessibles.

C'est dans ce contexte particulier que la communauté de la lévitation de particules micro/nanométriques a connu une croissance au cours des dix dernières années. L'avantage de l'utilisation des modes mécaniques des systèmes lévités par rapport aux systèmes fixés vient de la facilité avec laquelle on peut isoler la particule de l'environnement. Dans des conditions d'ultra-vide, des facteurs de qualité aussi forts que  $10^7$  peuvent être observés, même lorsque la température interne de la particule est de 300 K ou plus. Les sources restantes de décohérence sur les modes mécaniques proviennent de la fluctuation du champ électromagnétique du mécanisme de piégeage et du couplage à d'autres degrés de liberté externes et internes. Une étape importante pour la communauté a récemment été franchie avec le refroidissement du mode de centre de masse d'une sphère de silice à l'échelle nanométrique lévitant dans une pince optique jusqu'à l'état fondamental quantique à l'aide d'un refroidissement médié par une cavité optique et peu après avec le refroidissement par rétroaction active. Néanmoins, la génération d'états quantiques non gaussiens, tels que le premier état excité de l'oscillateur harmonique, nécessite l'introduction d'une non-linéarité dans le système, ce qui peut être fait, par exemple, en couplant l'oscillateur mécanique à un système à deux niveaux, un qubit. En ce sens, le centre NV (azote-lacune) négativement chargé dans le diamant est un candidat idéal en raison de la possibilité de

polariser optiquement et de lire son état de spin à température ambiante et en raison de sa longue durée de vie et de temps de cohérence de spin. Le couplage d'un oscillateur mécanique à un seul spin pour les systèmes fixés a permis la détection mécanique d'un seul spin et la lecture du mouvement d'un résonateur mécanique en utilisant un seul spin de centre NV. Récemment, le couplage fort d'un ensemble de centres NV au mode angulaire d'un micro-diamant en lévitation a été observé, permettant la lecture mécanique de la résonance de spin ainsi que le refroidissement du mode angulaire du diamant en utilisant les spins.

De manière plus générale, les matériaux magnétiques lévitant, qu'il s'agisse de diamants dopés au centre NV ou de matériaux ferromagnétiques, offrent aux physiciens un terrain de jeu plus large que la génération d'états quantiques intriqués. Voici une liste non exhaustive des différents domaines de recherche qui peuvent être explorés en utilisant des particules magnétiques en lévitation. Des propositions théoriques ont, par exemple, suggérées d'utiliser un mode mécanique d'une particule lévitant comme un bus quantique pour l'ensemble des spins internes. Cela pourrait permettre de réaliser des calculs quantiques ou d'étudier la physique à plusieurs corps comme dans la communauté des ions piégés. Cependant, la réalisation expérimentale de tels protocoles est actuellement loin d'être atteinte avec des systèmes lévitant. De plus, le couplage spin-mécanique entre les modes angulaires et les spins internes pourrait également servir de sonde du magnétisme interne de la particule en lévitation. En plus de cela, les particules ferromagnétiques en lévitation sont prédits pour être des magnétomètres très sensibles et pourraient dépasser la limite quantique standard (SQL) dans un régime où les spins internes corrélés et le ferromagnétique précèdent ensemble. Une autre particularité est que les spins à l'intérieur d'une particule en rotation accumulent une phase quantique. Cela a déjà été observé avec des centres NV dans des diamants en rotation mais pas avec des diamants lévitant en rotation. Enfin, l'étude des effets gyromagnétiques tels que l'effet Einstein-de Haas ou l'effet Barnett résultant de la correspondance entre le moment angulaire d'un spin et son moment magnétique est un domaine pour lequel les systèmes magnétiques micro/nanométriques lévitant semblent être des candidats idéaux.

Dans cette thèse, nous présentons des études sur la dynamique angulaire de cristaux magnétiques micrométriques lévités. Deux types de cristaux magnétiques sont considérés : des diamants fortement dopés avec des centres NV ainsi que des ferromagnétiques. L'objectif de cette thèse est de développer des outils théoriques et expérimentaux permettant l'étude de l'interaction entre la dynamique angulaire et le magnétisme dans les systèmes en lévitation. Voici un plan détaillé de la structure de ce manuscrit s'organisant en cinq chapitres distincts.

Dans le premier chapitre, nous passons en revue l'origine du paramagnétisme des impuretés présentes dans les cristaux isolants et semi-conducteurs tels que le diamant. Nous rappelons qu'il existe trois types de magnétisme pour ces impuretés : le diamagnétisme de Larmor, le paramagnétisme de Langevin ainsi que le paramagnétisme de Van Vleck. Nous appliquons ensuite cette théorie pour estimer la réponse magnétique d'un diamant enrichi en centres NV. Nous montrons ainsi qu'à l'équilibre thermique, les centres NV sont des défauts paramagnétiques dont les termes de Langevin et Van Vleck sont comparables. Nous montrons ensuite que la polarisation de l'état fondamental de spin du centre NV à l'aide d'un laser vert

donne lieu à une réponse paramagnétique exacerbée qui provient du terme paramagnétique de Van Vleck.

Dans le deuxième chapitre, nous nous concentrons sur l'aspect de lévitation de notre dispositif expérimental en rappelant le principe de fonctionnement des pièges de Paul. Nous discutons des types de cristaux qui peuvent être lévités dans notre piège. Nous détaillons ensuite les deux techniques qui nous permettent de détecter le mouvement angulaire du diamant. La première technique se base sur la collection de photons provenant de la lumière rétrodiffusée provenant des cristaux en lévitation, appelée tavelure. La deuxième méthode se base sur la collection de la lumière en transmission. Nous expliquons la différence de sensibilité de ces deux techniques de détection. Nous présentons ensuite le couplage spin-mécanique entre la magnétisation interne d'un cristal en lévitation avec les modes angulaires. Ce couplage, issu de l'anisotropie magnéto-cristalline, donne lieu à un couple sur la particule lévitée. Nous discutons des applications possibles en magnétométrie sur l'usage du couple magnétique exercé par un champ magnétique sur une particule magnétique en lévitation. La fin de ce chapitre est consacrée à l'explication des phénomènes gyromagnétiques qui pourraient être observés par des particules magnétiques micro/nanométriques lévitées. Ces phénomènes incluent d'une part l'effet Einstein-de Haas qui stipule que l'inversion de spins dans un cristal est responsable de la rotation du cristal par conservation du moment cinétique total du système. D'autre part, nous expliquons aussi les origines physiques de l'effet Barnett qui stipule que la rotation d'un matériau magnétique induit une magnétisation de celui-ci. L'étude de la dynamique de l'angle de particules magnétiques micrométriques en lévitation permet d'entrevoir l'observation de ces effets à une échelle jamais observée.

Dans le troisième chapitre, nous présentons une méthode de lévitation magnétique pour les ferromagnétiques durs : le piège magnétique de Paul. Dans un premier temps, nous passons en revue les différentes techniques de lévitation magnétiques d'aimants durs. Ensuite, nous rappelons les principes physiques de cette technique de lévitation, initialement développée dans les années 1980 pour le piégeage d'atomes neutres mais qui a été peu utilisée depuis cette période. Puis, nous proposons une nouvelle conception de piège magnétique de Paul microscopique basée sur les technologies de puce atomique développées dans la communauté des atomes froids. Ce type de piège micrométrique offre un grand degré de contrôle sur le piégeage des particules et semble idéal pour l'étude de la dynamique angulaire de matériaux magnétiques en lévitation. Nous construisons une version macroscopique de ce piège de Paul magnétique pour la lévitation d'aimants durs de quelques millimètres. Nous expliquons notamment le rôle des effets volumiques dans la lévitation de l'aimant. Enfin, nous expliquons pourquoi cette technique de lévitation semble prometteuse pour la réalisation de protocoles de spin-mécanique et pour l'étude du gyromagnétisme.

Dans le quatrième chapitre, nous étudions la dynamique angulaire des particules asymétriquement chargées dans un piège de Paul asymétrique. Nous montrons l'existence d'un régime de rotation complète de la particule dû à des non linéarités dans l'équation de la dynamique. Nous démontrons cet effet expérimentalement et le comparons avec les prévisions théoriques. Pour cela, nous obtenons un diagramme de stabilité expérimental des différents régimes de stabilité angulaire. Nous montrons que ce diagramme est en parfait accord avec les

prévisions théoriques. Nous démontrons également la capacité à manipuler de manière cohérente les centres NV à l'intérieur d'un diamant en rotation totale. Cela nous permet notamment de reconstruire précisément sa trajectoire angulaire prouvant l'extrême stabilité de cette méthode de rotation sur plusieurs heures. Cette rotation verrouillée offre des possibilités remarquables pour l'étude des effets gyromagnétiques, de la phase quantique géométrique et de la spin-mécanique dans le référentiel tournant pour les diamants et les aimants.

Dans le dernier chapitre, nous revenons sur le magnétisme des centres NV discuté dans le chapitre 1 et approfondissons le régime des champs magnétiques forts. Nous constatons que la réponse magnétique des centres NV passe d'une faible réponse paramagnétique à une forte réponse diamagnétique lorsque le dédoublement Zeeman dépasse l'énergie d'anisotropie. Cette transition est détectée mécaniquement en utilisant le couple magnétique exercé sur un diamant lévité. Nous démontrons que l'axe cristallin du diamant est aligné sur le champ magnétique externe sans avoir besoin de micro-ondes. Ce résultat ouvre la voie à un contrôle purement magnéto-optique de l'angle de diamants lévitant ou de diamants injectés dans des systèmes vivants de taille micrométrique.

Enfin, pour la clarté du message, les différents calculs nécessaires à la compréhension des résultats scientifiques présentés dans les différents chapitres sont exposés dans les annexes à la fin du manuscrit.





*Le savant n'étudie pas la nature parce que cela est utile ; il l'étudie parce qu'il y prend plaisir et il y prend plaisir parce qu'elle est belle.*

Henri Poincaré, *Science et Méthode*.



## Acknowledgments

C'est par l'écriture un peu fastidieuse de ce long document que se sont achevées mes trois années de doctorat au sein du laboratoire de physique de l'ENS. Je retiens de ces années qu'elles auront été très majoritairement heureuses, et cela notamment dû à mon épanouissement dans ma vie professionnelle, puisque c'est de cela dont il s'agit ici. La vie de jeune chercheur que j'ai vécu n'était au fond pas très loin de celle que j'avais pu imaginer et idéaliser avant de me lancer dans l'aventure : un condensé de calculs et d'équations rapidement menés au brouillon, de discussions scientifiques énergiques au tableau, d'idées sans lendemain, d'expériences tentées et puis surtout d'échecs, et puis encore d'autres échecs et parfois, quand tout se passe bien, des réussites, car il faut bien justifier sa paie à la fin du mois. Ces trois années de recherche auront aussi été marquées par de magnifiques voyages pour les conférences et collaborations, comme celui à Jérusalem, ainsi que par des événements hors du temps comme les mois de confinement pour cause de Covid, qui m'auront permis de mieux comprendre les équations de la spin-mécanique, et de pouvoir profiter d'un jardin en Vendée, ce qui n'était pas du luxe pendant cette période compliquée. Bref, j'ai adoré mes années de doctorats et il est désormais temps pour moi de remercier ceux qui y ont contribué.

L'achèvement de la thèse rime un peu avec la fin des études qui ont tout de même débuté il y a une vingtaine d'années sur les bancs du CP ! Dans ce contexte, il est difficile pour moi de ne pas avoir de pensée émue pour mes parents et mes frères qui m'ont accompagné pendant toutes ces années, et qui m'ont permis de m'épanouir pleinement dans mon parcours scientifique. A ma mère, qui a consenti à de nombreux efforts et de sacrifices pour mon éducation et pour me permettre d'en être là où j'en suis aujourd'hui. A mon père, qui m'a donné de nombreuses leçons particulières dès le plus jeune âge et qui m'a permis d'avoir ce gout prononcé pour les mathématiques, et un peu pour la physique. A mes frères avec qui nous avons partagé tant de bons moments et qui m'ont ouvert la voie de la vie, en même temps que celle des études supérieures. Merci beaucoup !

Je tiens aussi sincèrement à remercier mon directeur de thèse, Gabriel Hétet, avec qui j'ai passé trois années formidables. Il est difficile de faire une liste exhaustive de toutes les qualités humaines et scientifiques dont il a fait preuve durant ma thèse, mais en voici quand même quelques-unes qui m'ont particulièrement marqué. Tout d'abord, Gabriel est d'une immense disponibilité. Il m'est arrivé à de très nombreuses reprises de toquer à sa porte pour qu'il m'aide au labo ou bien pour lui faire part d'une idée qui me passait par la tête. J'ai toujours été accueilli avec écoute, intérêt et je n'ai jamais ressenti le fait de le déranger, quand bien même il avait probablement beaucoup mieux à faire. Je n'ai aussi jamais eu le sentiment d'avoir à me censurer dans nos interactions, de peur de dire des choses fausses, de poser des questions bêtes ou trop évidentes, ou bien tout simplement de révéler mes lacunes sur certains sujets. Cela a nettement contribué à créer un climat

---

de confiance, propice à la créativité et aux discussions stimulantes, sans avoir peur d'être jugé. Enfin, je dois reconnaître que Gabriel aura été d'une grande inspiration pour moi de par son approche de la physique expérimentale. Ma préférence pour la physique théorique par rapport à la physique expérimentale était un peu un secret de polichinelle en arrivant en thèse. Malgré tout, j'ai rapidement pris goût pour la recherche expérimentale grâce à la philosophie de Gabriel qui me convenait bien : ne pas être trop perfectionniste dans le montage d'un set-up expérimental, privilégier de tester des idées simples mais novatrices, être opportuniste au jour le jour et tenter des expériences farfelues car on ne peut jamais tout prédire à l'avance (c'est le propre de la physique expérimentale). Pour toutes ces raisons, je ne peux que chaleureusement te remercier Gabriel pour tout ton investissement tout au long de ces trois années.

Une autre personne qui aura joué un rôle majeur dans ma thèse est mon « co-thésard » Clément, avec qui j'ai partagé trois ans de vie commune dans le laboratoire de la L261. Je dois dire que cette « collocation professionnelle » s'est déroulée à merveille et j'ai particulièrement apprécié ces trois ans en ta compagnie. Tu as toujours été à l'écoute et disponible, notamment pour résoudre mes soucis expérimentaux, et il y en a eu, comme quand il fallait que je comprenne l'électronique de base (ca veut dire quoi une adaptation d'impédance ?) ou bien pour faire marcher tes programmes Python (qui après coup sont quand même plus simple à comprendre que Qudi). J'ai eu le sentiment que nos egos étaient rapidement mis de côté dans nos discussions, et tout cela dans l'intérêt commun de notre compréhension et de notre réussite en thèse. C'est donc un grand merci que je t'adresse aussi.

J'ai eu la chance d'avoir été accueilli et formé au tout début de ma thèse par deux jeunes et brillants chercheurs, Tom et Paul, que j'ai à cœur de remercier. Je dois dire qu'ils ont largement contribué d'une part à ma bonne intégration dans le groupe, et d'autre part à créer un climat de confiance au sein de l'équipe. Ils auront été tous les deux pour moi une grande source d'inspiration dans mon approche de la physique expérimentale.

La recherche étant un travail collectif, il me semble important de remercier nos collaborateurs sans qui ce travail de recherche n'aurait pas vu le jour. Tout d'abord, merci à Alrik pour cette année passée ensemble au laboratoire et à Julien à qui je souhaite bon courage pour ses trois années de thèse. J'aimerais beaucoup remercier nos collègues théoriciens Cosimo, Ben et Oriol qui ont toujours très disponible pour répondre à mes questions, parfois un peu longue et pointilleuse. Ce fut particulièrement précieux pour moi. Merci aussi à Jamal et Grégoire pour nous avoir accompagnés sur le projet de la lévitation du YIG. Malheureusement, on n'a pas eu les résultats escomptés mais je suis sûr qu'on arrivera à détecter cette fameuse résonance ferromagnétique dans un futur pas si lointain. Merci aussi à l'équipe du LSPM et de Chimie Paris, Midrel, Jocelyn, Alexandre, Philippe pour votre aide et la qualité de vos échantillons. Merci également aux membres du laboratoire Charles Coulomb à Montpellier, aux membres du laboratoire LuMin à Saclay et à toutes les autres personnes avec qui j'ai pu collaborer pendant ces trois ans.

J'aimerais également remercier tous les membres du groupe nano-optique, que ce soit les permanents, Christophe, Yannick, Carole, Emmanuel, Christos, et les thésards Théo, Romaric, Hadrien, Louis, Antoine, Raouf, Zakaria, Pierre-Louis, Federico, Marin, Marina (j'espère n'oublier personne...). Et même si les diamantaires ont un peu déserté la R18 pour le café, sachez que ce n'est pas contre vous, mais plutôt pour pouvoir profiter du jardin du LPENS.

Merci beaucoup à l'atelier mécanique, aux ingénieurs, tout particulièrement Pascal qui est d'une grande écoute et disponibilité, aux informaticiens et notamment Yann pour sa gentillesse et son efficacité. Un grand merci aussi aux personnels administratifs, et tout particulièrement à Christine dont l'énergie est communicative. Je souhaite également remercier la direction du LPENS et son directeur Jean-Marc Berroir de m'avoir permis de faire ma thèse dans leur laboratoire, dont le cadre est propice à l'épanouissement en tant que doctorant.

Il est temps de remercier les amis qui m'ont accompagné tout au long de mon parcours. Il y aura très probablement des oublis (désolé !) et des doublons (chanceux !). Tout d'abord les amis de longue date, et notamment Thomas, un des rares rescapés de mes amitiés du lycée à Angers, bon courage à toi pour la fin de thèse en droit ! Merci aux potes de MPSI, Keivan, Charles, Quentin, Clément, Simon, Simon, Robin, Nico, Justine, Eleanore, Sébastien et enfin Choundeh et Kevin. Merci à mes amis de l'X, et notamment la team hautement qualitative des interaillieurs, Théo, Renaud, Étienne, Amaury et Alex, les volleyeurs Martin, Etienne, Youssef, Clément, Maxence, Victor, Richard, Mehdi, aux Omar messengers Léo, Raphael et Omar. Merci au groupe des zinzins Ambre, Béa, Antonin, Jas, Louis, Laura, Alice etc, aux cueilleurs de champignons Rémi, Maximilien. Merci aux confinés Alice, Camille, Renaud, Martin et Samuel. Merci beaucoup aux amis volleyeurs de vacances Guillaume, Serge, Romain et Maxence. Merci aux copains du foot, Mathilde, Jerem et beaucoup de personnes précédemment citées. Et bien évidemment, un énorme merci à la lunch team dont les rendez vous quasi hebdomadaires auront ponctué ma thèse : à Flavien et son GUI que tout le monde connaît mais que personne n'a jamais vu, à Léa et ses problèmes amusants en physique qu'elle emmène dans ses bagages chaque matin au moment de la grande migration vers Saclay, à Renaud qui aura su transmettre avec force, vigueur et passion son amour des simulations numériques Monte Carlo diagrammatiques, à Victor l'américain qui nous aura ouvert avec beaucoup trop de sérénité la voie de la rédaction et de la soutenance orale et enfin à Théo, sacré Théo, j'ai toujours pas compris qu'est ce que tu faisais dans ce groupe de thésards.

Enfin, j'aimerais remercier les membres de mon jury de thèse Tracy Northup, Olivier Arcizet, Anaïs Dréau, Ivan Favero, Davi Guéry-Odelin et Derek Kimball pour avoir accepté d'évaluer mon travail de thèse. J'adresse un merci tout particulier à Tracy Northup et Olivier Arcizet pour la pertinence de leurs retours concernant le manuscrit.

Il est désormais pour moi plus que temps de souhaiter une bonne lecture aux quelques courageux ayant fait l'effort de rester jusqu'à la fin des remerciements !



# Contents

<b>Acknowledgments</b>	<b>3</b>
<b>Introduction</b>	<b>11</b>
<b>1 Chapter 1: Magnetism of doped insulating crystals</b>	<b>15</b>
1.1 Electronic structure of defects in insulating crystals . . . . .	15
1.1.1 Electronic band structure of insulating crystals . . . . .	16
1.1.2 Electronic structure of point defects in an insulator band gap . . . . .	17
1.1.3 The crystal field . . . . .	18
1.1.4 Spin-orbit and spin-spin interaction . . . . .	19
1.1.5 Color centers . . . . .	20
1.2 Magnetic response of defects in insulators crystals . . . . .	20
1.2.1 Basic definitions of magnetism . . . . .	20
1.2.2 Magnetism of uncorrelated defects in crystal . . . . .	23
1.3 Magnetism of a diamond embedded with $NV^-$ centers . . . . .	26
1.3.1 The $NV^-$ center defect in diamond . . . . .	26
1.3.2 Magnetism of $NV^-$ centers at thermal equilibrium . . . . .	31
1.3.3 Van Vleck paramagnetism of $NV^-$ centers with optical pumping . . . . .	33
1.3.4 Magnetism of $NV^-$ centers with a resonant microwave drive . . . . .	34
1.4 Conclusion . . . . .	36
<b>2 Chapter 2: Levitated magnetic particles: a promising system for torque magnetometry</b>	<b>37</b>
2.1 Levitation of magnetic particles: the experimental set-up . . . . .	37
2.1.1 Principle of the Paul trap . . . . .	37
2.1.2 Levitated magnetic particles . . . . .	42
2.1.3 Paul trap design . . . . .	43
2.1.4 Read-out of the mechanical motion . . . . .	46
2.2 Magnetic torques with anisotropic magnetic crystals . . . . .	48
2.2.1 System description and parametrization . . . . .	48
2.2.2 Magnetic torque . . . . .	49
2.3 Torque magnetometry with levitated magnetic particles . . . . .	52
2.3.1 Torque sensitivity with $15\ \mu\text{m}$ levitating particles at ambient pressure . . . . .	52
2.3.2 Torque detection of $NV^-$ centers magnetic resonance . . . . .	53
2.3.3 Torque magnetometry using levitating ferromagnets . . . . .	55
2.4 Gyromagnetic effects in levitating magnetic micro/nanoparticles . . . . .	56
2.4.1 Total angular momentum conservation: the Einstein-de Haas effect . . . . .	57

---

2.4.2	From the compass to the magnetic atom dynamics . . . . .	60
2.4.3	Pseudo magnetic field in rotating frame: the Barnett effect . . . . .	63
2.5	Conclusion . . . . .	64
<b>3</b>	<b>Chapter 3: Hard magnet levitation using a magnetic Paul trap</b>	<b>67</b>
3.1	Hard magnet levitation . . . . .	67
3.1.1	The magnetic Earnshaw's theorem . . . . .	67
3.1.2	Magnetic levitation of magnet . . . . .	68
3.2	Magnetic Paul trap . . . . .	69
3.2.1	Magnetic Paul trap theory . . . . .	69
3.2.2	Proposal for on-chip magnetic Paul trap . . . . .	74
3.2.3	Discussions and perspectives . . . . .	76
3.3	Experimental realization of a magnetic Paul trap . . . . .	76
3.3.1	The rotating saddle potential . . . . .	76
3.3.2	The rotating magnetic saddle . . . . .	79
3.3.3	Discussion . . . . .	83
3.4	Conclusion . . . . .	83
<b>4</b>	<b>Chapter 4: Fast electric rotation of trapped magnetic particles</b>	<b>85</b>
4.1	Angular stabilization in a Paul trap: the librating regime . . . . .	85
4.1.1	The Kapitza pendulum . . . . .	86
4.1.2	System description and parametrization . . . . .	86
4.1.3	The librating regime . . . . .	90
4.2	Full rotation in a Paul trap: the locking regime . . . . .	93
4.2.1	Origin of the locking regime . . . . .	93
4.2.2	Experimental observations . . . . .	98
4.2.3	Full angular stability in the rotating frame . . . . .	103
4.3	Magnetic particle rotation in the locking regime . . . . .	104
4.3.1	Angular motion read-out using $NV^-$ centers in a rotating diamond .	105
4.3.2	Rotation of ferromagnetic particles . . . . .	109
4.3.3	Discussion and perspectives . . . . .	110
4.4	Conclusion . . . . .	112
<b>5</b>	<b>Chapter 5: Mechanical detection of the <math>NV^-</math> centers diamagnetism</b>	<b>113</b>
5.1	$NV^-$ center magnetic response to a strong magnetic field . . . . .	113
5.1.1	System description and parametrization . . . . .	113
5.1.2	Van Vleck para/diamagnetism of the $NV^-$ center . . . . .	115
5.2	Angle locking of a levitating diamond using $NV^-$ centers diamagnetism . .	122
5.2.1	Calculation of the $NV^-$ centers diamagnetic torque . . . . .	122
5.2.2	Orientation control of the diamond using $NV^-$ centers diamagnetism	125
5.2.3	Librational frequency in the diamagnetic regime . . . . .	128
5.3	Librational magnetic energy . . . . .	131
5.3.1	Theoretical calculation of the librational magnetic energy . . . . .	132
5.3.2	Numerical simulation of the librational magnetic energy . . . . .	132
5.4	Conclusion . . . . .	133

---

<b>A</b>	<b>Appendix</b>	<b>137</b>
A.1	Magnetism in statistical and quantum physics . . . . .	137
A.2	Langevin paramagnetism . . . . .	137
A.3	Van Vleck paramagnetism . . . . .	138
A.4	Magnetization of $NV^-$ center under microwave excitation . . . . .	138
<b>B</b>	<b>Appendix</b>	<b>141</b>
B.1	Spin-mechanical dynamics equations . . . . .	141
B.1.1	Calculation of $[\hat{\mathbf{L}}, \hat{\mathcal{H}}_{s.m.}]$ . . . . .	141
B.1.2	Calculation of $[\hat{\mathbf{S}}, \hat{\mathcal{H}}_{s.m.}]$ . . . . .	143
B.2	Precessing magnet . . . . .	144
<b>C</b>	<b>Appendix</b>	<b>147</b>
C.1	Magnetic energy of a magnet in a magnetic Paul trap . . . . .	147
C.2	Stability condition taking into account gravity and a compensating mag- netic field gradient . . . . .	148
C.3	Eddy currents . . . . .	150
C.3.1	Eddy currents in the loops . . . . .	151
C.3.2	Induction current in the levitated magnet . . . . .	151
C.4	Rotating saddle . . . . .	152
C.4.1	Stability criterion . . . . .	152
C.4.2	Resulting motion . . . . .	152
<b>D</b>	<b>Appendix</b>	<b>155</b>
D.1	Angular electric energy in the small angle limit . . . . .	155
D.2	Non linear angular electric energy . . . . .	156
D.3	Angular potential in the rotating frame . . . . .	157
D.3.1	Angular electric energy . . . . .	157
D.3.2	Gyroscopic potential . . . . .	158
D.3.3	Total angular potential . . . . .	159
<b>E</b>	<b>Appendix</b>	<b>161</b>
E.1	Rotational invariance of the magnetic susceptibility tensor around the $NV^-$ center axis . . . . .	161
	<b>Bibliography</b>	<b>163</b>



## Introduction

Quantum physics has led to many remarkable scientific advances, including the development of Magnetic Resonance Imaging (MRI) for medical purposes (1; 2), the discovery of the transistor for the electronics industry (3) and the emergence of lasers (4). In the second part of the 20th century, the improvement of the experimental techniques enabled the control of elementary quantum entities such as atoms and photons (5; 6), allowing the development of quantum technologies (7; 8; 9). Most efforts were then directed towards generating quantum states with a larger number of these physical entities, using up to ten photons in a microwave cavity (10), tens of laser-cooled trapped ions (11), and  $C_{60}$  molecules (12). At the beginning of this century, crucial advances in nano-fabrication have even allowed bringing a micro/nano-scale mechanical resonator composed of billions of atoms into the quantum ground state (13).

Exploring the limits of quantum physics at a macroscopic scale remains one of the major motivations of experimental research since the formulation of the famous Schrödinger's cat thought experiment in 1935 (14). Notably, the coupling with the electromagnetic field mediated by radiation pressure in optomechanics (13) has enabled reaching the quantum ground state of mechanical resonators using resolved sideband (15; 16) and feedback cooling techniques (17). Despite the extreme sensitivity of macroscopic quantum states to the environment, reaching the quantum ground state for such systems is now routinely done, and the generation of non-classical states such as squeezed states (18) or entangled states (19; 20) has become the current focus of attention (21). In light of these recent successes, answering fundamental questions about the unification of physical theories, such as quantum gravity (22) or the measurement problem in quantum physics (23), no longer seem to be unattainable goals.

It is in this particular context that the micro/nanometer particle levitation community has grown over the past ten years (24). The advantage of using mechanical modes of levitated systems compared to tethered systems comes from the ease with which one can isolate the particle from the environment. Under ultra-high vacuum conditions, quality factors as strong as  $10^7$  can be observed, even when the internal temperature of the particle is at 300 K or more (25). The remaining sources of decoherence on the mechanical modes originate from the electromagnetic field fluctuation of the trapping mechanism and from the coupling to other external and internal degrees of freedom (24). A milestone for the community was recently achieved with the cooling of the center of mass mode of a nanoscale silica sphere levitated in an optical tweezer into the quantum ground state using cooling mediated by an optical cavity (26) and shortly after with feedback cooling (27; 28). Nevertheless, the generation of non-Gaussian quantum states, such as the first excited state of the harmonic oscillator, requires the introduction of a non-linearity in the

---

system, which can be done, for example, by coupling the mechanical oscillator to a two-level system, a qubit (29; 30). In this sense, the negatively charged Nitrogen-Vacancy (NV) center in diamond is an ideal candidate because of the possibility to optically polarize and read-out its spin state at room temperature (31) and because of its long spin life time and coherence time (32). The coupling of a mechanical oscillator to a single spin for tethered systems has allowed for the mechanical detection of a single spin (33) and for the read-out of the motion of a mechanical resonator using a single NV center spin (34; 35). Recently the strong coupling of an ensemble of NV centers to the angular mode of a levitating micro-diamond has been observed, allowing mechanical read-out of the spin resonance as well as the cooling of the diamond angular mode, the so-called spin-cooling (36).

More generally, levitated magnetic materials, whether they are diamonds doped with NV centers or ferromagnetic materials, offer physicists a wider playground than the generation of quantum entangled states. We have listed in Fig. 1 the research fields that can be explored using levitated magnetic particles. Theoretical proposals have, for instance, suggested using a mechanical mode of a levitating particle as a quantum bus for the internal spin ensemble (37; 38; 39). It could allow for performing quantum computation (40) or studying many-body physics as done in the trapped ion community (41; 42). However, the experimental realization of such protocols is currently far from being achieved with levitated systems (24; 43). In addition, the spin-mechanical coupling between the angular modes and the internal spins (44; 36) could also serve as a probe of the internal magnetism of the levitated particle. Furthermore, levitated ferromagnets are predicted to be highly-sensitive magnetometers and could surpass the Standard Quantum Limit (SQL) in a regime where the correlated internal spins and the ferromagnet precess together (45). Moreover, the magnetic spins inside a rotating particle accumulate a quantum phase. This has already been observed with NV centers in rotating tethered diamonds but not with rotating levitated diamonds (46). Finally, the study of gyromagnetic effects such as the Einstein-de Haas effect (47) or the Barnett effect (48) arising from the correspondence between the angular momentum of a spin and its magnetic moment is a field for which levitated micro/nanometer magnetic systems seem ideal candidates.

In this thesis, we present studies on the angular dynamics of levitated micrometric magnetic crystals. Two types of magnetic crystals are considered: diamonds that are highly doped with NV centers as well as ferromagnets. The aim of this thesis is to develop both theoretical and experimental tools allowing the study of the interplay between angular dynamics and magnetism in levitated systems.

In the first chapter, we review the origin of the paramagnetism of impurities present in insulating and semiconducting crystals such as diamond. Then we estimate the magnetic response of diamond enriched in  $NV^-$  centers. We show that laser polarization of the  $NV^-$  center spin ground state gives rise to a magnetic response that is larger than that of the diamond diamagnetism.

In the second chapter, we focus on the levitation aspect of our experimental device by recalling the principle of operation of Paul traps. We discuss the types of crystals that can be levitated in our trap and we detail the method for detecting the motion. We then present the spin-mechanical coupling of the internal magnetization to the angular modes. This coupling, originating from the magneto-crystalline anisotropy, gives rise to a torque on

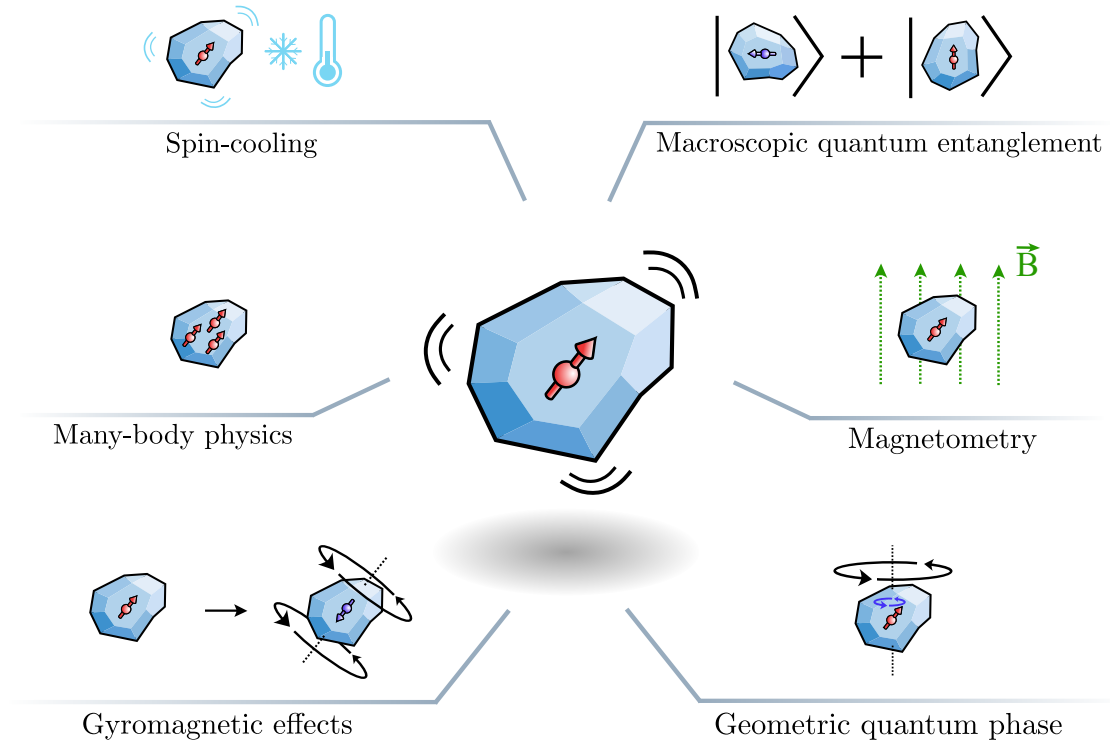


Figure 1: Different areas involving the coupling between the internal magnetism of a crystal and the angular degree of freedom.

the levitated particle. An application to magnetometry using the spin-mechanical coupling with levitating particles is given. The end of this chapter is devoted to the explanation of gyromagnetic phenomena that could be observed by levitating micro/nanometric magnetic particles.

In the third chapter, we present a magnetic levitation method for hard ferromagnets: the magnetic Paul trap. We first recall the physical principles of this levitation technique originally developed in the 1980s for the trapping of neutral atoms. Then, we propose a new microscopic magnetic Paul trap design based on the atom chip technologies developed in the cold atom community. We build a testbed macroscopic version for millimeter-size levitation of hard magnets. Finally, we explain why this levitation technique seems promising for the realization of spin-mechanics protocols and for studies of gyromagnetism. The results of this chapter have been published in (49).

In the fourth chapter, we study the angular dynamics of asymmetrically charged particles in an asymmetric Paul trap. We show the existence of a regime of full rotation of the particle. We demonstrate this effect experimentally and compare it with the theoretical predictions. We also demonstrate the ability to coherently manipulate the NV centers inside a fully rotated diamond, allowing to precisely reconstruct its angular trajectory. This locked rotation offers remarkable opportunities for the study of gyromagnetic effects, geometric quantum phase and spin-mechanics in the rotating frame for diamonds and magnets. The results of this chapter will be published soon.

In the final chapter, we return to the magnetism of the NV centers discussed in Chapter 1 and delve deeper into the regime of strong magnetic fields. We find that the magnetic

response of NV centers transitions from a weak paramagnetic response to a strong diamagnetic response when the Zeeman splitting exceeds the anisotropy energy. This transition is detected mechanically by using the magnetic torque exerted on a levitated diamond. We demonstrate that the diamond crystalline axis is aligned with the external magnetic field without the need for microwaves. This result opens the door to purely magneto-optical control of the angle of micrometric levitating diamonds or diamonds injected in living systems. The results of this chapter have been published in (50).

## Chapter 1: Magnetism of doped insulating crystals

---

During the 19th century, the work of many physicists such as Oersted and Ampère established the close link between electricity and magnetism. Following this, classical electromagnetism was developed and theorised, leading to Maxwell's equations governing the evolution of electric and magnetic fields (51). The first so-called classical approach to magnetism makes use of the previous classical electromagnetism formalism combined with the statistical physics developed by Boltzmann and the old quantum mechanics theory. It allowed Langevin to explain the paramagnetism and diamagnetism of atoms in the early years of the 20th century (52). However, in his doctoral manuscript in 1911, Niels Bohr pointed out that the paramagnetic and diamagnetic terms calculated by Langevin must in fact perfectly compensate each other (53). It was not until the 1920s and the remarkable advances in the new theory of quantum physics, such as the discovery of the electron spin (54) or the development of matrix quantum mechanics (55), that magnetic phenomena could be properly explained. To date, the application of the laws of quantum physics explain very well the magnetism of atoms, molecules and most solids.

In this chapter, we will take up the quantum magnetism approach developed by Van Vleck (Nobel 1977) in the 1930s to explain the magnetism of insulators containing crystalline defects and particularly the magnetism of diamond embedded with NV centers (56; 57). First, we will describe the electronic band structure of crystals and intra-band energy levels allowed by certain crystal defects in insulators. Then, we will discuss the different types of magnetism of isolated ions, which will allow us to understand the magnetism of defects in insulating crystals. Finally, we will close this chapter with the study of the system of interest for the rest of the dissertation, the magnetism of the diamond embedded with NV centers. This last part will allow the reader to understand the result presented in Chapter 5 on spin-diamagnetism.

### 1.1. Electronic structure of defects in insulating crystals

Crystalline defects in insulating materials have a discrete electronic structure similar to that of single free ions. These systems are therefore particularly attractive and have clear advantages over cold atoms and trapped ions because they are naturally trapped at room temperature. However, the spin lifetime of these defects is significantly reduced by their coupling to the phonon bath of the crystal lattice.

The aim of this section is to understand why the electronic structure of point defects in insulating crystals approximates that of an isolated ion. To this end, we give a brief reminder of the origin of the electronic band structure of insulators and semiconductors. Secondly, we show how point ions present in the crystal lattice of these materials allow the appearance of discrete energy levels in the band gap. Finally, we discuss the origin of the coupling of these defects with the crystal lattice that explains the poor spin relaxation time of these discrete levels compared to single trapped ions.

### 1.1.1 Electronic band structure of insulating crystals

A crystal is a solid material composed of atoms, ions or molecules arranged in a highly ordered manner (58), such as the sodium chloride (NaCl) shown in Fig. 1.1 (a) and (b). This is a complex system consisting of a large number of nuclei and electrons (about  $10^{23}$ ), which makes an analytical and numerical calculation of the energy levels of this system impossible. Fortunately, several approximations, which can be justified *a posteriori*, allow a drastic simplification of the problem. First, the atomic nuclei are  $10^4$  to  $10^5$  times heavier than the electrons, so we can consider their coordinates to be fixed compared to the coordinates of the electrons, which are dynamical. This is called the Born-Oppenheimer approximation (59). Second, the potential perceived by an electron is assumed not to depend on the instantaneous position of the other electrons. The dynamics of the individual electrons can thus be decoupled and the Hamiltonian of an electron in a crystal simply reduces to (60):

$$\hat{\mathcal{H}}_e = \frac{\hat{\mathbf{p}}^2}{2m_e} + \sum_{i=1}^{N_n} V_{\text{at}}(\hat{\mathbf{r}} - \hat{\mathbf{R}}_i), \quad (1.1)$$

where  $\hat{\mathbf{p}}$  is the kinetic momenta operator,  $m_e$  is the electronic mass,  $V_{\text{at}}$  is the periodic atomic potential,  $\hat{\mathbf{r}}$  is the electron position operator and  $\hat{\mathbf{R}}_i$  is the nucleus position operator.

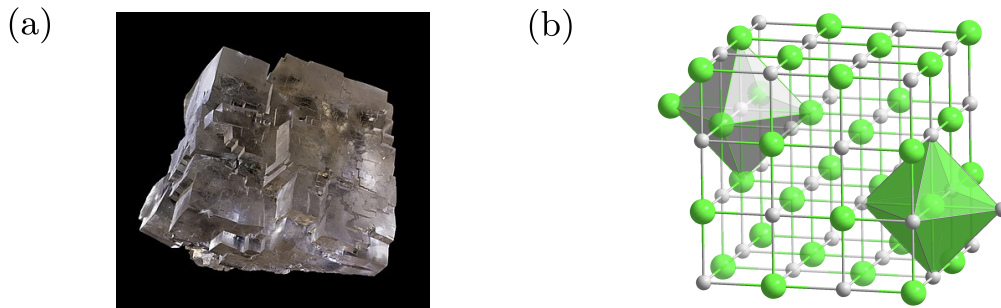


Figure 1.1: (a) Macroscopic crystal of sodium chloride. Taken from Wikimedia (Didier Descouens, GNU Free Documentation License). (b) Crystalline structure of a sodium chloride crystal. The green atoms correspond to the chlorine and the grey atoms to the sodium. Taken from Wikimedia (free License).

From now on, we consider only the case of a strong periodic atomic potential to explain the origin of the insulating behaviour of certain materials. In this case, the electrons of each atom are strongly bound to their nuclei and therefore remain localised near them. A treatment based on the Linear Combination of Atomic Orbitals method (LCAO)(60), which we will not discuss here, makes it possible to obtain a band structure for the electronic structure of a crystal that lifts the degeneracy between the same electronic levels of the different atoms. In Fig. 1.2 (a), the electronic energy levels of the first atomic orbitals for a hypothetical sodium crystal are plotted as a function of the spatial distance  $r$  of the different atoms. For very distant atoms, the electrons of the individual atoms are not affected by their atomic neighbours, resulting in the usual quantization of the electronic energy levels. For closer atoms, the electronic structure of the electrons of the individual atoms is directly influenced by the neighbouring atoms, resulting in a band structure of the energy levels.

Insulating and semiconducting materials are materials whose atomic potential is high enough to have a band structure that does not completely overlap and allow band gaps. Looking at the band structure of the crystal shown in Fig. 1.2 (a), the electrons should occupy the electronic energy level from the lower to the higher energy state following a Fermi-Dirac distribution. In Fig. 1.2 (b), we show the three main possible band configurations for the electrons with higher energies. On the left panel, an electronic band is partially filled leading to a metallic behaviour. On the central panel, the electrons almost completely occupy the lower band (the valence band), but the band gap energy is comparable to the thermal energy  $k_B T$  and then it allows the occupation of some electronic states of the upper band (the conduction band). These materials are called the semiconductors. On the right panel, the band gap is much larger than the thermal energy leading to a complete occupation of the valence band, leaving the conduction band empty. In the latter two cases, absorption of low frequency electromagnetic waves is almost impossible due to the band gap and the distribution of the electron population. These materials are therefore poor electronic conductors.

In the following, we study the electronic structure of defects in semiconductors and insulating crystals. In particular, we show that the presence of defects in the crystal lattice, such as single atoms, ions, or molecules, gives access to electronic energy levels in the band gap that have an orbital structure close to that of single atoms.

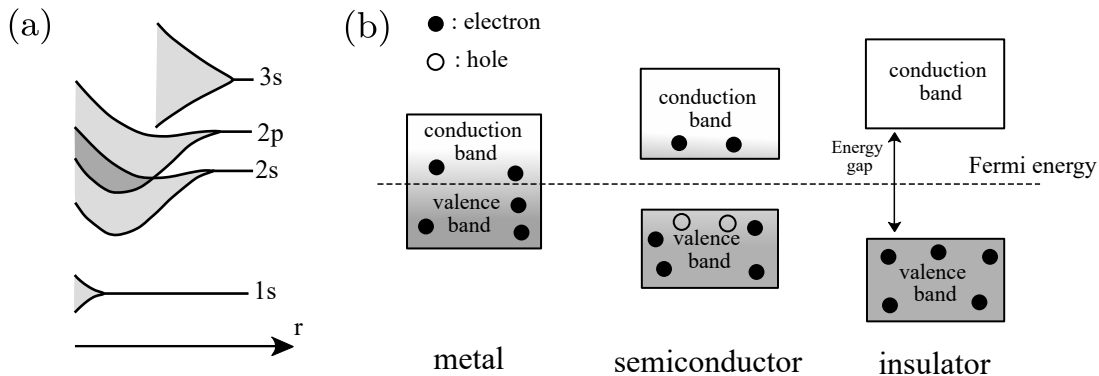


Figure 1.2: (a) Band structure of the atomic levels 1s, 2s, 2p and 3s of a sodium crystal as a function of the inter-atomic distance  $r$ . (b) Band structure for three different materials: a metal, a semiconductor and an insulator.

### 1.1.2 Electronic structure of point defects in an insulator band gap

A point defect in a crystal is a local anomaly in the crystallographic structure in which a vacancy, a single atom, an ion, or even a molecule replaces or supplements the original atoms of the crystal. In Fig. 1.3 (a), various examples of point defects in a crystal are shown. These point defects break the translational symmetry and thus slightly change the band structure of a crystal by adding discrete energy levels in the band gap.

In this part, we specifically study the case of isolated single ions replacing an original ion in the crystal lattice. In Fig. 1.3 (b), we show an example with the ionic impurity of chromium  $\text{Cr}^{3+}$  replacing an aluminium ion  $\text{Al}^{3+}$  in the sapphire crystal lattice  $\text{Al}_2\text{O}_3$ . This crystal with chromium impurities is a ruby and chromium impurities are responsible for the red colour of the crystal, as shown in Fig. 1.3 (b). There are many other impurities,

such as for instance the NV, SiV, GeV centers of diamond, transition ions such as  $\text{Fe}^{3+}$  and  $\text{Mn}^{2+}$  or lanthanides.

### 1.1.3 The crystal field

A single ion defect trapped in a crystal lattice is subject to an electric potential generated by the surrounding crystal ligands. This field is referred to as the crystal field. The Hamiltonian of an isolated ion defect in a crystal can be written:

$$\hat{\mathcal{H}} = \hat{\mathcal{H}}_0 + \hat{\mathcal{H}}_{\text{CF}}, \quad (1.2)$$

where  $\hat{\mathcal{H}}_0$  is the free ion Hamiltonian and  $\hat{\mathcal{H}}_{\text{CF}} = q\phi(\hat{\mathbf{r}})$  is the crystal field Hamiltonian. This concept of the crystalline field was first introduced by Bethe and Kramers in 1929 (61). The energies involved in the crystalline field are of the order of  $10^{-4}$  eV ( $\approx 10$  GHz) which is much lower than the typical energies involved in the Hamiltonian of the free ion. Therefore, this field can be treated as a perturbation. Moreover, the crystal field has the same symmetries as the crystal lattice. The presence of the crystal field reduces the symmetry group of the free ion and thus lifts some degeneracies for electrons of same energies.

In Fig. 1.3 (c), the energy levels of the  $\text{Cr}^{3+}$  ion impurity in the  $\text{Al}_2\text{O}_3$  crystal are shown. This impurity causes discrete energy levels to appear as for an isolated atom in the bandgap of  $\text{Al}_2\text{O}_3$ , which is a broadband semiconductor with a gap of 7 eV.

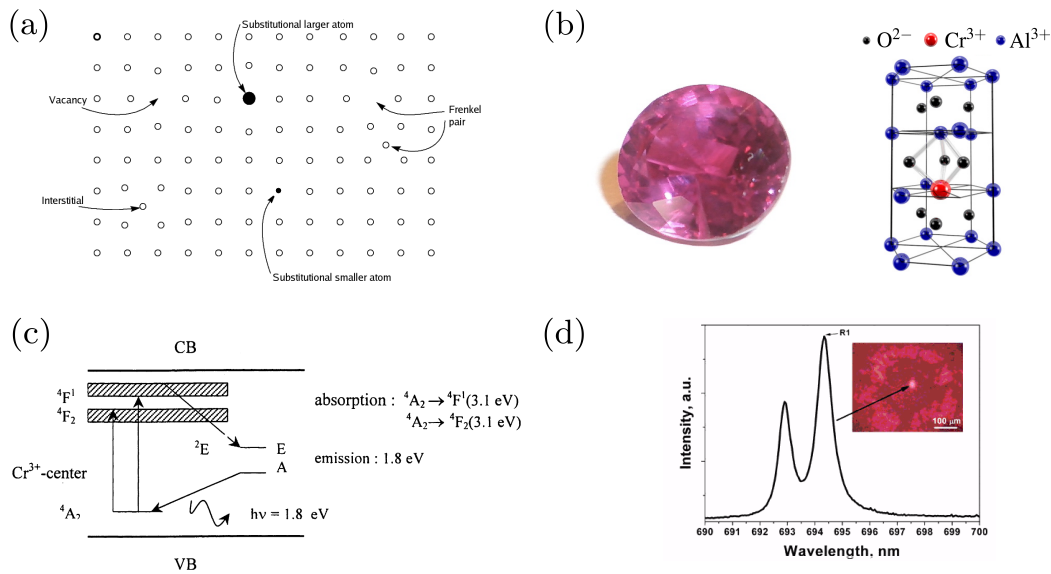


Figure 1.3: (a) Different types of point defects in a crystal. Taken from Wikimedia (free License). (b) Macroscopic ruby with its crystalline structure of  $\text{Al}_2\text{O}_3$  with a  $\text{Cr}^{3+}$  color center. Taken from Wikimedia (free License) and (62) (License number: RNP/24/FEB/075323). (c) Schematic energy level diagrams for absorption and emission of the  $\text{Cr}^{3+}$  color center in  $\text{Al}_2\text{O}_3$ . VB: valence band, CB: conduction band. Taken from (63) (License number: 5734870712400). (d) Emittance spectra of a ruby crystal (Reprinted with permission from (65). Copyright 2007 American Chemical Society.

### 1.1.4 Spin-orbit and spin-spin interaction

Spin-orbit coupling plays a fundamental role in the physics of defects in a crystal. This coupling of relativistic origin arises from the interaction between the spin of an electron and its orbital motion in an electric potential. The magnetic field perceived in the reference frame of the electron is written:

$$\mathbf{B} = -\frac{\mathbf{v} \times \mathbf{E}}{c^2}, \quad (1.3)$$

where  $\mathbf{v}$  is the electron velocity,  $\mathbf{E}$  is the electric field and  $c$  is the light velocity. This formula can be rewritten by introducing the orbital angular momentum  $\mathbf{L}$  of the electron and we obtain that the magnetic field  $\mathbf{B}$  is linearly related to  $\mathbf{L}$  via the equality:

$$\mathbf{B} = \frac{1}{m_e c^2} \frac{1}{r} |\nabla V| \mathbf{L}, \quad (1.4)$$

where  $V$  is the electric potential. This magnetic field is responsible for a change in the energy levels of the ion trapped in the crystal lattice due to the Zeeman effect, which gives rise to an additional term  $\hat{\mathcal{H}}_{\text{SO}}$  in the initial Hamiltonian of value:

$$\hat{\mathcal{H}}_{\text{SO}} = \hbar \lambda \mathbf{L} \cdot \mathbf{S}, \quad \text{with} \quad \lambda = -\hbar \frac{\gamma_e}{m_e c^2} \frac{1}{r} |\nabla V|, \quad (1.5)$$

with  $\gamma_e = -g_s e / 2m_e < 0$  the gyromagnetic constant of an electron spin with  $g_s \approx 2.0$  and  $\hat{\mathbf{S}}$  the Pauli observable of the electron spin<sup>1</sup>.

This notion plays a crucial role in the physics of point defects. First, the angular momentum observable  $\hat{L}_z$  no longer commutes with the total Hamiltonian of the system because  $[\hat{\mathbf{L}}, \hat{L}_z] \neq 0$ . The complete set of commuting observables relevant to this system now includes the total angular momentum of the system  $\hat{\mathbf{J}} = \hat{\mathbf{L}} + \hbar \hat{\mathbf{S}}$  commuting with the spin-orbit Hamiltonian  $\hat{\mathcal{H}}_{\text{SO}}$ . The relevant quantum number is thus the sum of the orbital momentum and spin quantum numbers  $m_j = m_l + m_s$ . This coupling thus causes a lift of degeneracies depending on the total quantum number  $m_j$  of the different electronic states, defining a fine structure.

Moreover, the spin-orbit coupling plays a crucial role for the spin relaxation time. Indeed, the electronic orbital of the defect is coupled to the phonon of the crystal via the crystal field. This same orbital is coupled to the spin via the spin-orbit coupling. Thus, the spins are indirectly coupled to the phonon bath of the crystal which reduces their lifetime. This is a notable difference from isolated atoms whose lifetime is simply limited by the coupling to the electromagnetic modes of the vacuum. The spin lifetime of an ion trapped in a crystal is therefore much shorter than for cold trapped atoms.

The spin-spin interaction between electrons describes the magnetic dipolar coupling between the spin of electrons. The spin-spin Hamiltonian can be written as:

$$\hat{\mathcal{H}}_{\text{s.s.}} = -\frac{\mu_0 g^2 \beta}{4\pi r^3} \left( 3(\hat{\mathbf{S}}^{(1)} \cdot \hat{\mathbf{r}})(\hat{\mathbf{S}}^{(2)} \cdot \hat{\mathbf{r}}) - \hat{\mathbf{S}}^{(1)} \cdot \hat{\mathbf{S}}^{(2)} \right), \quad (1.6)$$

<sup>1</sup>At this point, it should be noted that we adopt the convention of a negative gyromagnetic ratio for the rest of the manuscript. This convention differs from the usual convention for NV centers, which will result in a sign change in the usual NV Hamiltonian. Moreover, the observable  $\hat{\mathbf{S}}$  is considered to be a measure of the spin quantum number and thus  $\hbar \hat{\mathbf{S}}$  is homogeneous to angular momentum. This unusual convention has been chosen to be consistent with the NV center conventions.

where  $\hat{\mathbf{S}}^{(i)}$  is the spin operator of the  $i$ th electron,  $\beta$  is the Bohr magneton,  $g$  is the Landé factor,  $\mu_0$  the magnetic permeability of free space and  $\hat{\mathbf{r}}$  the position operator. Since the orbits of the electrons are directly impacted by the crystal field and are coupled to the electron spin due to the spin-orbit interaction, the symmetries of the crystal are reflected in the resulting Hamiltonian of the spin-spin interaction. This is notably the case for the  $\text{NV}^-$  center, as we will see later.

### 1.1.5 Color centers

Color centers are a special class of defects in crystals that have the property of showing absorption or/and emission features in the visible range. In Fig. 1.3 (d), the emission lines of  $\text{Cr}^{3+}$  color centers of  $\text{Al}_2\text{O}_3$  are shown. An electron in the ground state of the chromium ion can be excited with a blue or green laser. The de-excitation from the electronic excited state to the ground state leads to photons emission at 1.8 eV which corresponds to red photons of 690 nm. It is this de-excitation process in the visible region that gives the ruby crystal its red color.

These color centers therefore have the advantage that they can be excited by a laser in the visible region and emit in the visible region. Moreover, the spin lifetime and coherence time of color centers can be very long (about the millisecond-second), as is the case for nuclear spins in rare-earth ions in the crystal, making them promising candidates for the fabrication of quantum memories (66). In this manuscript, we will focus on the  $\text{NV}^-$  color center of diamond, which exhibits exceptional physical properties at room temperature.

## 1.2. Magnetic response of defects in insulators crystals

So far, the electronic structure of insulating crystals with point defects in the crystal lattice has been the focus of attention. We now seek to understand the origin of the magnetism of insulating materials doped with color centers. We neglect here the magnetism of the crystal host and consider only the magnetic response of the crystalline defects.

To this end, we first recall the elementary definitions of magnetism of sets of uncorrelated ions. Then, we will use the historical approach of Van Vleck to explain the magnetic response of an ensemble of uncorrelated ions, which is sufficient to understand the magnetic response of insulating crystals and their impurities (56).

### 1.2.1 Basic definitions of magnetism

In this section, we introduce the concepts of magnetism relevant to understanding the magnetism coming from the embedded spin impurities of an insulating crystal.

#### The magnetic moment

We consider the classical physics experiment where an ion consisting of  $N_e$  electrons of position  $\mathbf{r}_i$  and velocity  $\mathbf{v}_i$  is brought into a magnetic field  $\mathbf{B}$ . Due to the rotation of charges in an increasing magnetic field, the ion will acquire magnetic energy that equals:

$$W = -\mathbf{m} \cdot \mathbf{B}, \quad \text{with} \quad \mathbf{m} = -\sum_{i=1}^{N_e} \frac{e}{2m_e} \mathbf{L}_i, \quad (1.7)$$

where  $\mathbf{L}_i = m_e \mathbf{r}_i \times \mathbf{v}_i$ . The vector  $\mathbf{m}$  is called the orbital magnetic moment of the ion. The magnetic moment is directly related to the angular momentum of the electrons via the

gyromagnetic ratio. The intrinsic link between angular momentum and magnetic moment is already apparent. A part of Chapter 2 is devoted to the theoretical study of magnetic particles whose angular momentum carried by the electrons is not negligible compared to the macroscopic angular momentum of the particle leading to mechanical gyromagnetic effects.

The definition of the magnetic moment given in formula Eq. (1.7) corresponds to a particular case where an ion is brought into a magnetic field. One can also define the magnetic moment in a more general way as (67):

$$\mathbf{m} = -\frac{\partial E}{\partial \mathbf{B}}, \quad (1.8)$$

where  $E$  is the total energy of the system considered. As explained in the introduction of this chapter, classical physics cannot explain the origin of magnetism (53). It is therefore necessary to treat the magnetic moment from a quantum point of view.

The magnetic moment observable in quantum physics is therefore defined for a system with a Hamiltonian  $\hat{\mathcal{H}}$  by the relation:

$$\hat{\mathbf{m}} = -\frac{\partial \hat{\mathcal{H}}}{\partial \mathbf{B}}. \quad (1.9)$$

By considering the system to be in an eigenstate  $|\phi\rangle$  of the Hamiltonian  $\hat{\mathcal{H}}$ , a brief calculation demonstrates that  $\langle \hat{\mathbf{m}} \rangle = \langle \phi | \hat{\mathbf{m}} | \phi \rangle = -\partial E / \partial \mathbf{B}$  where  $E$  is the energy of the eigenstate. The classical and quantum definition of magnetic moment are thus consistent.

In the following, we will consider a large ensemble of identical defects in a crystal. One of the tools for dealing with a statistical set of identical but independent quantum systems is the density matrix  $\hat{\rho}$ . This formalism will be used to calculate the magnetic response of an ensemble of NV centers in the diamonds. Thus, we will use the following relation to calculate the mean value of the magnetic moment observable:

$$\mathbf{m} = \text{Tr}(\hat{\rho} \hat{\mathbf{m}}) = -\text{Tr}\left(\hat{\rho} \frac{\partial \hat{\mathcal{H}}}{\partial \mathbf{B}}\right). \quad (1.10)$$

### The magnetization

For a volume  $V$  of a material, the magnetization is defined as the average value of the magnetic moment  $\mathbf{m}_i$  of the  $N_{\text{at}}$  atoms in a volume  $V$ :

$$\mathbf{M} = d \langle \mathbf{m} \rangle, \quad \text{with} \quad d = \frac{N_{\text{at}}}{V} \quad \text{and} \quad \langle \mathbf{m} \rangle = \frac{1}{N_{\text{at}}} \sum_{i=1}^{N_{\text{at}}} \mathbf{m}_i = \text{Tr}(\hat{\rho} \hat{\mathbf{m}}), \quad (1.11)$$

where  $d$  is the volume density of ions. For a system of  $N_{\text{at}}$  identical non-interacting ions coupled to a thermal bath, an alternative expression for the magnetization can be given. The discrete energy levels of an ion are denoted  $\epsilon_k$  and the population  $p_k$  in each energy level is assumed to be given by a Boltzmann law satisfying  $p_k = \exp(-\beta \epsilon_k) / \sum_{k'=1}^N \exp(-\beta \epsilon_{k'})$  with  $\beta = 1/k_{\text{B}}T$  and  $N$  the number of eigenstates. Using the quantum definition of the magnetic moment given in Eq. (1.10), it is shown in Appendix A.1 that the magnetization

is:

$$\mathbf{M} = -d \sum_{k=1}^N \frac{\partial \epsilon_k}{\partial \mathbf{B}} p_k. \quad (1.12)$$

The formula Eq. (1.12), which is an alternative definition of the magnetization, is perfectly valid in a system subjected to a thermal bath which destroys the quantum coherences between states. However, in certain cases such as for the NV center, optical pumping and mechanisms related to the quantum phase no longer allow the system to be considered in thermal equilibrium with the external bath. In this case, one should consider the quantum definition of the magnetization of Eq. (1.11).

The total magnetic moment  $\boldsymbol{\mu}$  of the system is also simply defined as the product of the magnetization  $\mathbf{M}$  and the volume  $V$  such that  $\boldsymbol{\mu} = V\mathbf{M}$ . In the following, we should therefore try not to confuse the magnetic moment carried by an ion or a physical species  $\mathbf{m}$  with the total magnetic moment carried by a solid  $\boldsymbol{\mu}$ .

### The magnetic susceptibility tensor

To study the magnetic response of a system, it is natural to estimate the evolution of the magnetization under a small magnetic perturbation. Therefore, we define the magnetic susceptibility tensor  $\underline{\chi}/\mu_0$  as the differential of the magnetization  $\mathbf{M}$  with respect to the magnetic field  $\mathbf{B}$ . We thus have the equality:

$$\mathbf{M}(\mathbf{B}_0 + \boldsymbol{\delta B}) = \mathbf{M}(\mathbf{B}_0) + \frac{\underline{\chi}}{\mu_0} \cdot \boldsymbol{\delta B} + o(\boldsymbol{\delta B}) \quad \text{with} \quad \underline{\chi} = \mu_0 \frac{\partial \mathbf{M}}{\partial \mathbf{B}}(\mathbf{B}_0), \quad (1.13)$$

where  $\mathbf{B}_0$  is a permanent magnetic field,  $\mathbf{M}(\mathbf{B}_0 + \boldsymbol{\delta B})$  is the magnetization of the system under the magnetic field  $\mathbf{B}_0 + \boldsymbol{\delta B}$ ,  $\mathbf{M}(\mathbf{B}_0)$  is the magnetization of the system under the magnetic field  $\mathbf{B}_0$ , and  $\boldsymbol{\delta B}$  is a magnetic field perturbation.

In the case of the magnetic response of crystalline defects, the magnetic response of the ions considered is not necessarily isotropic because of the crystal field. The magnetic susceptibility tensor takes into account the anisotropy in the magnetic response of crystalline defects.

The magnetic susceptibility tensor is usually defined as the derivative of the magnetization as a function of the magnetic field in vacuum. In the cases treated in this manuscript, the materials have a weak magnetic response so that we can always consider  $\mathbf{B} = \mu_0 \mathbf{H}$ .

Considering the statistical physics definition of the magnetization given by Eq. (1.12), one can obtain an explicit expression for the magnetic susceptibility tensor:

$$\chi_{ij} = -d\mu_0 \sum_{k=1}^N \frac{\partial \epsilon_k}{\partial B_i} \frac{\partial p_k}{\partial B_j} - d\mu_0 \sum_{k=1}^N \frac{\partial^2 \epsilon_k}{\partial B_i \partial B_j} p_k. \quad (1.14)$$

The matrix elements of the magnetic susceptibility tensor are a sum of two contributions, one of which depends on the first derivative of the energies of the eigenstates and one on the second derivative. Since the magnetic susceptibility tensor is not a scalar, it is not relevant to refer to paramagnetic (resp. diamagnetic) materials as the ones with a positive (resp. negative) magnetic susceptibility. In the following, a material whose diagonal elements of the magnetic susceptibility tensor are positive (resp. negative) will be called paramagnetic (resp. diamagnetic).

### 1.2.2 Magnetism of uncorrelated defects in crystal

Now that we have established the relevant concepts of magnetism, we can turn our attention to the study of the magnetic response of an ensemble of defects in crystals<sup>2</sup>.

#### Hamiltonian derivation

We will take up the historical theoretical approach used by Van Vleck (56; 57; 58). In the presence of an external magnetic field  $\mathbf{B}$ , the Hamiltonian of an ion will undergo two notable modifications. The first change concerns the momentum of each electron  $\hat{\mathbf{p}}_i$ , which is modified by the quantity:

$$\hat{\mathbf{p}}_i \rightarrow \hat{\mathbf{p}}_i + e\mathbf{A}(\hat{\mathbf{r}}_i), \quad (1.15)$$

where  $\mathbf{A}$  is the potential vector. We consider that  $\mathbf{A}$  verifies the Lorenz gauge.

The second change concerns the addition of the interaction Hamiltonian of the electron spin with the external magnetic field  $\mathbf{B}$ , which is written:

$$\hat{\mathcal{H}}_B = -\hbar\gamma_e\mathbf{B} \cdot \hat{\mathbf{S}}. \quad (1.16)$$

Finally, if we develop the electron Hamiltonian of an ion and take into account the commutation laws between the conjugate quantities  $\hat{\mathbf{r}}_i$  and  $\hat{\mathbf{p}}_i$ , we obtain that the Hamiltonian of an ion in the presence of a magnetic field is modified by the quantity

$$\Delta\hat{\mathcal{H}} = \frac{\mu_B}{\hbar}(\hat{\mathbf{L}} + g_s\hbar\hat{\mathbf{S}}) \cdot \mathbf{B} + \frac{e^2}{8m_e} \sum_{i=1}^{N_e} (\mathbf{B} \times \hat{\mathbf{r}}_i)^2. \quad (1.17)$$

#### Perturbative treatment

The energy variation induced in the presence of a magnetic field given by Eq. (1.17) will generally remains very low compared to the energies of atomic excitations. Indeed, for a magnetic field as strong as 1 T, the energy variation due to the perturbation does not exceed 1 meV. Considering that the unperturbed Hamiltonian gives rise to energy levels  $\epsilon_k$  for the eigenstates  $|k\rangle$ , the variation of these energy levels to second order in the magnetic field  $\mathbf{B}$  treated as a perturbation equals

$$\Delta\epsilon_k = \langle k | \Delta\hat{\mathcal{H}} | k \rangle + \sum_{k' \neq k} \frac{|\langle k | \Delta\hat{\mathcal{H}} | k' \rangle|^2}{\epsilon_k - \epsilon_{k'}}. \quad (1.18)$$

By inserting Eq. (1.17) into Eq. (1.18), one finally obtains a dependence of the variation of the ion energy as a function of the magnetic field to second order:

$$\begin{aligned} \Delta\epsilon_k = & \frac{\mu_B}{\hbar} \mathbf{B} \cdot \langle k | \hat{\mathbf{L}} + g_s\hbar\hat{\mathbf{S}} | k \rangle + \sum_{k' \neq k} \frac{|\langle k | \frac{\mu_B}{\hbar} (\hat{\mathbf{L}} + g_s\hbar\hat{\mathbf{S}}) \cdot \mathbf{B} | k' \rangle|^2}{\epsilon_k - \epsilon_{k'}} \\ & + \frac{e^2}{8m_e} \langle k | \sum_{i=1}^{N_e} (\mathbf{B} \times \hat{\mathbf{r}}_i)^2 | k \rangle, \end{aligned} \quad (1.19)$$

This perturbative treatment gives rise to three different contributions to the energy varia-

<sup>2</sup>The following theory also applied to gases consisting of independent ions or atoms such NO or N<sub>2</sub>.

tion of the ion that leads to the three following magnetisms: the Langevin paramagnetism, the Van Vleck paramagnetism and the Larmor diamagnetism. For the remainder of this section, we consider a thermal filling of the energy levels of uncorrelated ions.

### The Langevin paramagnetism

The first term of Eq. (1.19) corresponds to a change in first order energies in the magnetic field  $\mathbf{B}$  and gives rise to Langevin paramagnetism:

$$\Delta\epsilon_k^{(\text{Lan})} = \frac{\mu_B}{\hbar} \mathbf{B} \cdot \langle k | \hat{\mathbf{L}} + g_s \hbar \hat{\mathbf{S}} | k \rangle. \quad (1.20)$$

This term is almost always dominant with respect to the other two contributions when it is not zero, i.e. when the states are magnetic ( $\langle k | \hat{\mathbf{L}} + g_s \hbar \hat{\mathbf{S}} | k \rangle \neq 0$ ). It gives rise to a necessarily positive magnetic susceptibility for a thermal filling of the states (the proof is presented in Appendix A.2) and thus to a paramagnetic behaviour. The diagonal terms of this magnetic susceptibility equal

$$\chi_{\text{Lan},ii} = -d\mu_0 \sum_{k=1}^N \frac{\partial \Delta\epsilon_k^{(\text{Lan})}}{\partial B_i} \frac{\partial p_k}{\partial B_i} > 0. \quad (1.21)$$

In Fig. 1.4 (a), we have represented the physical origin of the Langevin paramagnetism for a spin one-half ensemble satisfying  $m_s = \pm 1/2$  with no orbital momenta i.e.  $\mathbf{L} = 0$ . The presence of a magnetic field perturbation  $\mathbf{B}$  splits the two degenerate energy levels of the spin  $|\pm 1/2\rangle$ . The energy of the state  $|-1/2\rangle$  decreases while the opposite behaviour appears for the state  $|+1/2\rangle$ . Due to the thermal distribution of the population, the state with lower energy becomes more populated, leading to a magnetization of the system that is positive, i.e., a paramagnetic behaviour.

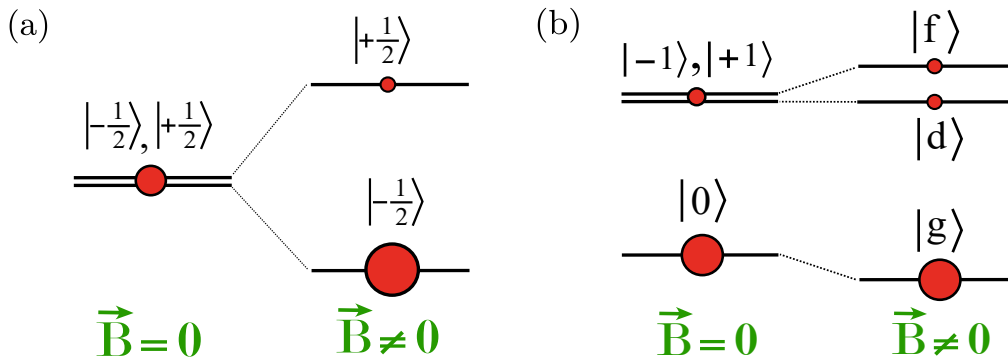


Figure 1.4: (a) Langevin paramagnetism: energy and population evolution of a spin 1/2 system under an external magnetic field. (b) Van Vleck paramagnetism: energy and population evolution of a spin 1 system under an external transverse magnetic field.

### The Van Vleck paramagnetism

The Van Vleck paramagnetism arises from the change of the ion's energy to second order in the magnetic field and equals

$$\Delta\epsilon_k^{(V.V.)} = \sum_{k' \neq k} \frac{|\langle k | \frac{\mu_B}{\hbar} (\hat{\mathbf{L}} + g_s \hbar \hat{\mathbf{S}}) \cdot \mathbf{B} | k' \rangle|^2}{\epsilon_k - \epsilon_{k'}}. \quad (1.22)$$

This term is often negligible compared to the Langevin term and arises due to mixing between the eigenstates. Here again, it can be proven that the diagonal terms of the magnetic susceptibility tensor corresponding to this term are always positive at thermal equilibrium (calculation in Appendix A.3) and is given by:

$$\chi_{V.V.,ii} = -d\mu_0 \sum_{k=1}^N \frac{\partial^2 \Delta\epsilon_k^{(V.V.)}}{\partial B_i^2} p_k. \quad (1.23)$$

In Fig. 1.4 (b), we show the energy evolution and population distribution of a spin 1 triplet with a lifting of degeneracy between  $|0\rangle$  and  $|\pm 1\rangle$  states, which could be caused by a crystalline anisotropy, such as in the case of the  $NV^-$  center in diamond. We consider a magnetic perturbation perpendicular to the anisotropy axis, resulting in no first-order energy evolution and therefore no Langevin paramagnetism. The eigenstates mix, causing their energy levels to repel. The energy of the unperturbed ground state decreases, while the energy of the state with the highest energy increases. Since the ground state  $|0\rangle$  was initially more populated, this leads to a decrease in magnetic energy, resulting in Van Vleck paramagnetism. This contribution to paramagnetism was first discovered by Van Vleck (68; 57) and was confirmed by experimental results on the magnetism of NO gas and lanthanides (69; 70). Van Vleck found that for certain gases, Curie's law did not match the experimental observation, and that the computation of the magnetic susceptibility had to take into account the contribution from second-order perturbation theory to be accurate.

### The Larmor diamagnetism

The third energy contribution to Eq. (1.19) gives rise to a second order magnetic energy increase in the magnetic field  $\mathbf{B}$  which purely depends on the square position of the electrons but not on the orbital and spin momenta and reads:

$$\Delta\epsilon_k^{(Lar)} = \frac{e^2}{8m_e} \langle k | \sum_{i=1}^{N_e} (\mathbf{B} \times \hat{\mathbf{r}}_i)^2 | k \rangle. \quad (1.24)$$

This positive variation in energy gives rise to a diamagnetic response. The Larmor diamagnetism gives a magnetic susceptibility with diagonal terms equal to:

$$\chi_{Lar,ii} = -d\mu_0 \sum_{k=1}^N \frac{\partial^2 \Delta\epsilon_k^{(Lar)}}{\partial B_i^2} p_k. \quad (1.25)$$

Considering Eq. (1.24) and Eq. (1.25), one can be convinced that the Larmor magnetic susceptibility is negative. This formula of diamagnetic susceptibility explains particularly well the magnetism of noble gases for which there is no Langevin and Van Vleck paramagnetism because  $\mathbf{J} = 0$  and  $\mathbf{S} = 0$  in the ground electronic state (valence band completely

filled). This also explains very well the magnetism of the alkali halides, for which the electronic orbital structure of the ions is only slightly modified by the crystal environment.

Understanding the magnetism of a set of uncorrelated ions has thus allowed us to understand the magnetism of ionic impurities in insulating crystals. For the following, we will keep in mind the origin of the three different magnetic contributions that are the Larmor diamagnetism, the Langevin paramagnetism and the Van Vleck paramagnetism.

### 1.3. Magnetism of a diamond embedded with $NV^-$ centers

Diamond is a diamagnetic material with a magnetic susceptibility at 300 K that is equal to (71; 72; 73):

$$\chi_{ii}^{\text{Diam}} = -2.2 \times 10^{-5}. \quad (1.26)$$

Furthermore, diamond is a large gap semi-conductor with a bandgap that equals 5.49 eV (74), which allows for the presence of numerous color centers and notably paramagnetic impurities such as the Nitrogen-Vacancy center (NV). In the following, we study the magnetic response of a diamond embedded with  $NV^-$  centers. Our goal is to show that the magnetic susceptibility of the  $NV^-$  centers can be stronger than the diamond diamagnetism.

To do so, we first examine the electronic structure and exceptional physical properties of  $NV^-$  centers, including optical pumping at room temperature, photoluminescence readout of its spin state, and weak coupling to diamond phonons. Secondly, we estimate the magnetic response of the  $NV^-$  center for different scenarios: thermal distribution of states, optical pumping in the spin ground state or microwave resonant excitation with a magnetic transition.

#### 1.3.1 The $NV^-$ center defect in diamond

Diamond is a large gap semiconductor which makes it a particularly good host for optically active defects. In diamond, more than 500 defects have been identified (74), some of which are responsible for the different colors of diamonds. One of its impurities, the  $NV^-$  center, is the subject of intense research for its unique properties at room temperature, which make it a major candidate for quantum technologies like quantum communication (75), quantum sensing (9) and quantum computation (? ).

##### $NV^-$ electronic structure

The NV center in diamond is a defect that replaces two carbon atoms by a nitrogen atom and a vacancy. In Fig. 1.5 (a), a NV center surrounded by carbon atoms is shown. The crystal field felt by the NV center has a  $C_{3v}$  symmetry. The direction formed by the NV center, denoted by the vector  $\mathbf{e}_3$  in Fig. 1.5 (a), is called the anisotropy axis of the NV center. This direction is fixed in the diamond frame but not necessarily in the laboratory frame. This is why we employ the notation  $\mathbf{e}_3$  to designate the NV axis and not the usual  $\mathbf{e}_z$  convention. For instance, in a rotating diamond or a levitating angularly stable diamond subjected to gas collisions, the anisotropy direction is not fixed in the laboratory frame. We will see in the following section that the anisotropy of the NV center is a key ingredient leading to torque magnetometry using the NV centers.

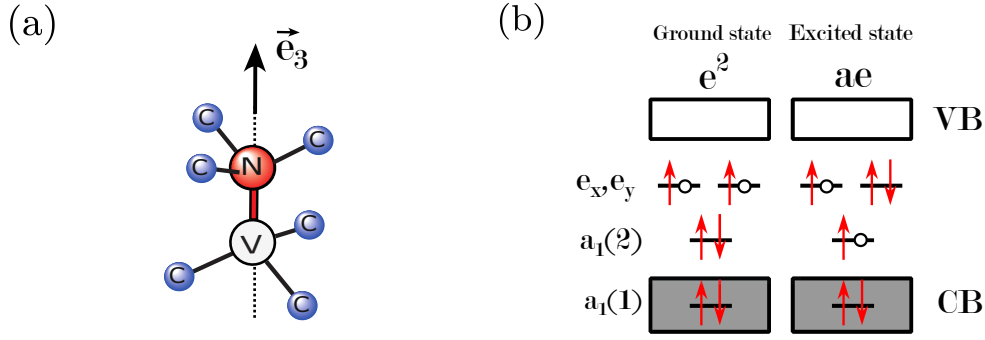


Figure 1.5: (a) NV center in a diamond oriented along a crystalline anisotropy axis referred to as  $\mathbf{e}_3$ . N: Nitrogen, V: vacancy, C: Carbon. (b) Electronic distributions of the ground and excited states  $e^2$  and  $ae$  of the  $NV^-$  center. VB: Valence Band, CB: Conduction Band. Taken from (76) (Licence ouverte/Open license).

The NV center has two main charged state configurations: the  $NV^0$ , which is electrically neutral, and the  $NV^-$ , which has captured an electron. We are only investigating the  $NV^-$  electrical configuration. Fig. 1.5 (b) shows the energy levels of the  $NV^-$  center eigenstates that can be obtained using the symmetry rules of the  $C_{3v}$  group. The  $NV^-$  center is composed of six electrons: two electrons are shared from the nitrogen atom, three neighboring carbon atoms share each one electron and the last electron has been captured. Fig. 1.5 (b) shows the six electrons filling the electronic energy level structure leading to two unoccupied states for the electronic ground and excited states of the  $NV^-$  center. According to Fig. 1.5 (b), there are three combinations in the electrons's distribution. Either two  $e$  states are vacant, leading to the  $e^2$  subspace, or one  $e$  state and one  $a$  state are vacant, leading to the  $ae$  subspace, or two  $a$  states are vacant leading to the  $a^2$  terminology (not shown in Fig. 1.5 (b)). The  $a^2$  space is not contributing to the  $NV^-$  center's physical properties that we are interested in so we do not consider this state in the following. The  $e^2$  state is called the  $NV^-$  center ground state, and the  $ae$  state is called the excited state. There are two holes in the electronic configuration, which means that the system is a spin 1 system, leading to a spin singlet where  $\mathbf{S} = 0$ , and a spin triplet, where  $\mathbf{S} = 1$ .

At thermal equilibrium, only the spin triplet with the same orbital configuration that does not carry orbital momenta,  $\mathbf{L} = 0$ , is occupied. Using the spin 1 operators  $(\hat{S}, \hat{S}_1, \hat{S}_2, \hat{S}_3)$ , where  $\mathbf{e}_1, \mathbf{e}_2$  designate directions perpendicular to the anisotropy direction  $\mathbf{e}_3$ , the electronic Hamiltonian in the ground state is given by:

$$\hat{H} = \hbar D \hat{S}_3^2 + \hbar E (\hat{S}_1^2 - \hat{S}_2^2) - \hbar \gamma_e \mathbf{B} \cdot \hat{\mathbf{S}}, \quad (1.27)$$

where  $D = 2\pi \times 2.87$  GHz is the anisotropy energy due to spin-spin interaction (77) and  $E$  is an energy that comes from local mechanical strain or residual electrical fields, which vary from  $2\pi \times 100$  kHz to  $2\pi \times 5$  MHz depending on the diamond fabrication techniques. We have included the Zeeman Hamiltonian in the presence of an external magnetic field  $\mathbf{B}$ . The gyromagnetic ratio of the  $NV^-$  center equals  $\gamma_e = -2\pi \times 28.0$  GHz/T and is

negative<sup>3</sup>. In the rest of the manuscript, we neglect the term  $\hbar E(\hat{S}_1^2 - \hat{S}_2^2)$  since it does not play any role when a sufficiently strong magnetic field ( $B > 0.1$  mT) is applied. In the following, we designate by  $(|m_s = 0\rangle, |m_s = -1\rangle, |m_s = +1\rangle)$  the eigenstates of the anisotropy term  $\hbar D\hat{S}_3^2$ . These states will also be denoted  $(|0\rangle, |-1\rangle, |+1\rangle)$ . In Fig. 1.6 (a), we have represented the energy of the spin triplet of the ground state. The red circles designate the populations in each state, which are almost the same at room temperature because  $\hbar D \ll k_B T$ . The energy of  $|m_s = 0\rangle$  equals zero while the energies of the states  $|m_s = -1\rangle$  and  $|m_s = +1\rangle$  are equal to  $\hbar D$ .

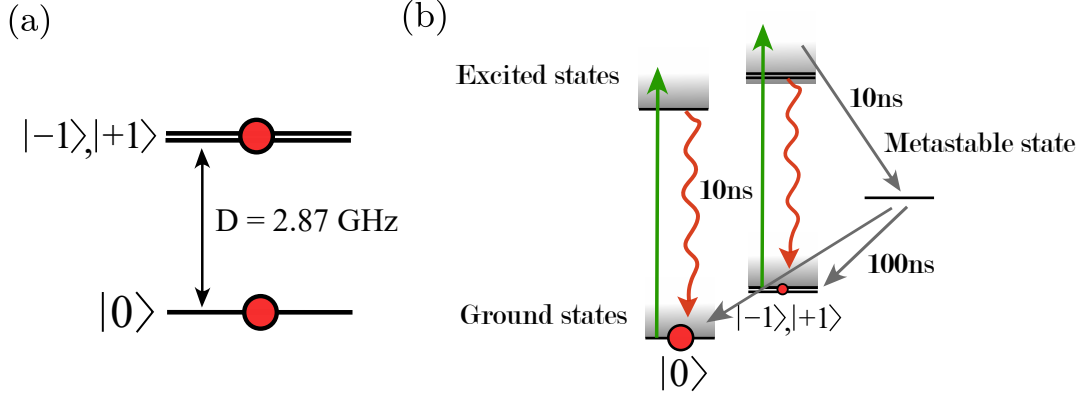


Figure 1.6: (a) Energy structure of the  $\text{NV}^-$  center ground state. The  $|m_s = 0\rangle$  state and the  $|m_s = \pm 1\rangle$  states are separated by  $D = 2\pi \times 2.87$  GHz. (b) Optical pumping mechanism that leads to the filling of the  $|m_s = 0\rangle$  state. The green arrow designates the green laser excitation into the optically excited states. Direct radiative decay may occur, generating red photons, and conserving the initial spin state. An indirect path including a spin singlet metastable state allows the  $|m_s = \pm 1\rangle$  excited state to decay into the  $|m_s = 0\rangle$  or the  $|m_s = \pm 1\rangle$  states.

### Room temperature optical pumping

The property that makes the  $\text{NV}^-$  center a widely studied defect is the possibility to perform optical pumping at room temperature with a green laser that populates the  $|m_s = 0\rangle$  state at 80% (78; 79). The optical pumping process involves asymmetry in the decay process from the excited-state spin triplet to the ground-state spin triplet. In Fig. 1.6 (b), we have represented the optical pumping process of the  $\text{NV}^-$  center. The green laser allows population transfer from the ground states to the excited states. The  $|m_s = 0\rangle$  state of the excited state can only decay to the  $|m_s = 0\rangle$  state of the ground state, with a characteristic time of 10 ns. This is not the case for the  $|m_s = \pm 1\rangle$  optical excited states, which have two paths that allow decay to the  $|m_s = 0\rangle$  ground state. The first path is the same as for  $|m_s = 0\rangle$  with the same time constant, and the second path involves decay to a metastable state that can decay either to the  $|m_s = 0\rangle$  or the  $|m_s = \pm 1\rangle$  states. This asymmetry in the decay processes is at the origin of the optical pumping in the  $|m_s = 0\rangle$  state.

<sup>3</sup>This is not the usual convention for the  $\text{NV}^-$  center. The use of this convention is motivated by the consideration of gyromagnetic effects in the following chapter, where the gyromagnetic ratio sign is important.

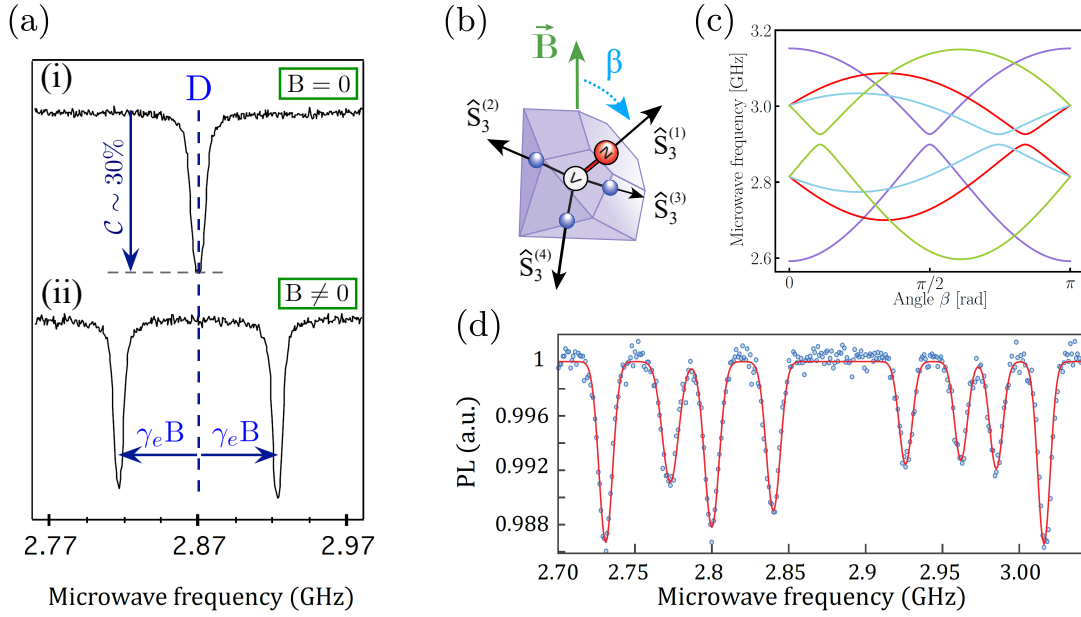


Figure 1.7: (a) ODMR spectra of a single  $\text{NV}^-$  center as a function of the microwave frequency without (i) and with (ii) an external magnetic field. Taken from (76)(Licence ouverte/Open license). (b) Schematic of a diamond containing the four classes of  $\text{NV}^-$  centers with the four spin operators given by the anisotropy direction. (c) Transition energies between the  $|m_s = 0\rangle \rightarrow |m_s = -1\rangle$  and the  $|m_s = 0\rangle \rightarrow |m_s = +1\rangle$  states for the four  $\text{NV}^-$  center classes as a function of the angle  $\beta$ . (d) ODMR spectrum for a diamond containing  $\text{NV}^-$  centers of the four classes.

### Spin state optical read-out

During the relaxation process from the excited state to the ground state after optical excitation from the green laser, the  $\text{NV}^-$  center can photoluminesce and emit red photons. The photoluminescence depends strongly on the initial spin state of the  $\text{NV}^-$  center, which allows a destructive optical readout of the initial spin state by collecting the photoluminescence. Indeed, when the  $\text{NV}^-$  center is initially in the  $|m_s = 0\rangle$  spin state and is optically excited with the green laser, the de-excitation process that returns it to the  $|m_s = 0\rangle$  spin state leads to the emission of a red photon, as shown in Fig. 1.6 (b). When the  $\text{NV}^-$  center is initially in an excited  $|m_s = \pm 1\rangle$  spin state, the de-excitation from the excited state can pass through the metastable state shown in Fig. 1.6 (b) which does not lead to emission of a red photon. This asymmetry allows optical readout of the spin state. The  $|m_s = 0\rangle$  state is therefore called a bright state, and the  $|m_s = \pm 1\rangle$  states are called dark states.

### Optically Detected Magnetic Resonance (ODMR)

This remarkable property permits us to perform Optical Detection of the Magnetic Resonance (ODMR) at room temperature. In Fig. 1.7 (a), we present two ODMR spectra of a single  $\text{NV}^-$  center while pumping to the  $|m_s = 0\rangle$  state with the green laser (76). The microwave frequency is scanned while measuring the emitted photons. When one of the resonance conditions  $|m_s = 0\rangle \rightarrow |m_s = \pm 1\rangle$  is met, there is a population transfer between the  $|m_s = 0\rangle$  and  $|m_s = \pm 1\rangle$  states, leading to a decrease of the photoluminescence.

The ODMR spectrum in Fig. 1.7 (a)-(i) has been performed without external magnetic field, meaning that the  $|m_s = \pm 1\rangle$  states are degenerate. In Fig. 1.7 (a)-(ii), an external magnetic field lifts the degeneracy between the two states  $|m_s = \pm 1\rangle$ , leading to two resonances.

A crucial point is that the diamond has four possible directions of anisotropy due to the tetrahedral diamond crystalline structure. There are consequently four possible directions for the  $NV^-$  axis, which are referred to as the four  $NV^-$  center classes. In Fig. 1.7 (b), we represent a diamond and the four spin operators  $\hat{S}_3^{(i)}$  that correspond to the four  $NV^-$  center classes. For a given direction of the magnetic field  $\mathbf{B}$ , the projection of the magnetic field on each class is different. Consequently, the transition frequencies between the  $|m_s = 0\rangle \rightarrow |m_s = \pm 1\rangle$  states are not necessarily the same. In Fig. 1.7 (c), we have plotted the energy of the four classes as a function of the angle  $\beta$  for a magnetic field strength of 5 mT. In Fig. 1.7 (d), we have plotted an experimental ODMR spectra where eight resonances clearly appear (80). This is due to the four  $NV^-$  center classes and the two possible resonances for each class, which leads to eight resonances.

An important point is that knowing the direction of the diamond crystalline structure thus allows us to determine the strength as well as the direction of an external magnetic field. More interestingly, by reversing the point of view, knowing the direction of the magnetic field allows us to fully determine the anisotropy direction of each of the four  $NV^-$  classes up to one rotation around the magnetic field axis. Using a second magnetic field with a different orientation allows us to fully determine the anisotropy direction of each of the four  $NV^-$  classes. As the anisotropy axes are fixed in the diamond crystal, it directly gives us the angular position of the diamond. By making use of this information, we are able to precisely read out the angular position of the diamond. This magnetometry technique will be used in Chapter 4 to read the angular motion of a rotating levitating diamond.

### Relaxation time $T_1$ and dephasing time $T_2^*$

The physical processes affecting the spin state of the  $NV^-$  center can be described with the two characteristic times used in NMR: the longitudinal relaxation time  $T_1$  (also called decay or life time) and the transverse spin relaxation time  $T_2^*$  (also called decoherence or dephasing time).

As previously explained, the coupling of the spin with the phonon bath of the crystal lattice mediated by the spin-orbit coupling is at the origin of the spin lifetime  $T_1$ . Cross-relaxation with other spin impurities also plays an important role in the spin lifetime. However, this phenomenon does not dominate the relaxation dynamics at room temperature but becomes dominant at cryogenic temperatures (81). The lifetime of the  $NV^-$  center is exceptionally long for an electron spin at room temperature and is on the order of  $100 \mu\text{s} - 1 \text{ ms}$  for our samples. This is due to the fact that the electronic ground state of the  $NV^-$  center is weakly coupled to the phonon bath of the crystal via the modulation of the spin-spin interaction.

The transverse relaxation time  $T_2^*$  of the spin is limited by the dipolar coupling of the  $NV^-$  center with paramagnetic impurities. In High Pressure High Temperature (HPHT) diamonds, such as those used in our levitation experiments, the diamonds are rich in crystal defects consisting of a single nitrogen atom called the  $P_1$  center. This spin bath fluctuates on characteristic time scales on the order of a hundred nanoseconds, which

gives its value to the  $T_2^*$  dephasing time of the NV<sup>-</sup> centers (80). We define the ODMR resonance linewidth as  $\Gamma_2^* = 2\pi/T_2^*$ , and it is typically on the order of  $2\pi \times 5 - 10$  MHz (80). As this typical timescale is stronger than all of the other timescales, including the mechanical timescale, that we consider in the following chapters (typically on the order of kilohertz), we treat the  $P_1$  bath as a Markovian bath in the following even if it is technically not the case.

### Density matrix formalism with NV<sup>-</sup> centers

The density matrix formalism  $\hat{\rho}$  will be used to describe the evolution of the electronic ground state spin triplet of the NV<sup>-</sup> center. The advantage of this formalism is that it allows us to take into account the coupling with external baths such as the ones responsible for the longitudinal and transverse spin dissipation phenomena previously mentioned. Moreover, the density matrix is particularly well suited to describe the evolution of a statistical ensemble of uncorrelated quantum objects, as is the case with ensembles of NV<sup>-</sup> centers in a diamond. We will not study dynamical effects that can arise from the coupling of the angular degrees of freedom of a levitating diamond and the NV<sup>-</sup> centers that has led to spin-cooling of the motion of a levitating diamond (36). For the rest of the manuscript, we therefore simply consider the stationary solutions of the NV<sup>-</sup> center master equation:

$$0 = \frac{\partial \hat{\rho}}{\partial t} = -\frac{i}{\hbar} [\hat{\mathcal{H}}, \hat{\rho}] + \mathcal{L}(\hat{\rho}), \quad (1.28)$$

with the Hamiltonian

$$\hat{\mathcal{H}} = \hbar D \hat{S}_3^2 - \hbar \gamma_e \mathbf{B} \cdot \hat{\mathbf{S}}, \quad (1.29)$$

and the Lindbladian  $\mathcal{L}(\hat{\rho})$  that takes into account the green laser optical pumping rate to the  $|m_s = 0\rangle$  state given by the constant  $\gamma_{\text{las}}$ , which can be as large as  $2\pi \times 100$  kHz in our experiment, the longitudinal decay rate  $\Gamma_1 = 2\pi/T_1$ . The Lindbladian operator is given by

$$\mathcal{L}(\hat{\rho}) = \sum_{i,j} \Gamma_{i,j} \left( \hat{\sigma}_{i,j} \hat{\rho} \hat{\sigma}_{j,i} - \frac{1}{2} \{ \hat{\sigma}_{j,i} \hat{\sigma}_{i,j}, \hat{\rho} \} \right). \quad (1.30)$$

with  $\hat{\sigma}_{i,j} = |i\rangle \langle j|$ . Under a magnetic field, the only non-zero decay rates  $\Gamma_{i,j}$  and pure-dephasing rates  $\Gamma_{i,i}$  are

$$\Gamma_{1,1} = \Gamma_{-1,-1} = 2\Gamma_2^*, \quad (1.31)$$

$$\Gamma_{1,0} = \Gamma_{-1,0} = \Gamma_1, \quad (1.32)$$

$$\Gamma_{0,1} = \Gamma_{0,-1} = \Gamma_1 + \gamma_{\text{las}}. \quad (1.33)$$

In the rest of this section, we study the magnetic response of the NV<sup>-</sup> center using the density matrix formalism and the magnetic concepts previously defined.

### 1.3.2 Magnetism of NV<sup>-</sup> centers at thermal equilibrium

The NV<sup>-</sup> centers' magnetism in diamond can completely be treated with the previously developed Van Vleck theory as the NV<sup>-</sup> centers constitute a set of uncorrelated spins. In

the following, we consider diamonds highly doped with NV centers, with a concentration of 3.5 ppm NV<sup>-</sup> centers. Taking into account the four different possible classes, the density of a single class of NV<sup>-</sup> centers is then equal to  $d = 1.6 \times 10^{23} \text{ m}^{-3}$ . At room temperature and without optical pumping with the green laser, only the electronic ground state of the NV<sup>-</sup> center is populated. We will calculate the different contributions to the magnetism under these assumptions.

The term giving rise to Larmor diamagnetism calculated in Eq. (1.25) is neglected in the theory leading to the electronic structure of the NV<sup>-</sup> center (77). A quick calculation of the susceptibility of this term using the formula Eq. (1.25) confirms that the contribution of this term is negligible:

$$\chi_{\text{Lar}}^{\text{th,NV}} = -d\mu_0 \frac{e^2}{6m_e} r_0^2 \approx -10^{-11}, \quad (1.34)$$

where  $r_0 \approx 5 \times 10^{-11} \text{ m}$  is the Bohr radius. The Larmor diamagnetism of the NV<sup>-</sup> centers is quite negligible and is 6 orders of magnitude below the diamond diamagnetism, which is consistent with the fact that there are  $10^6$  times fewer NV<sup>-</sup> centers than carbon atoms contributing to the diamond diamagnetism. Thus, only the paramagnetic contributions, i.e., the Langevin and the Van Vleck paramagnetism terms, contribute to the NV<sup>-</sup> centers' magnetism.

Due to the anisotropy of the NV<sup>-</sup> center, we expect the magnetic susceptibility to depend on the direction of the perturbing field  $\delta\mathbf{B}$ .

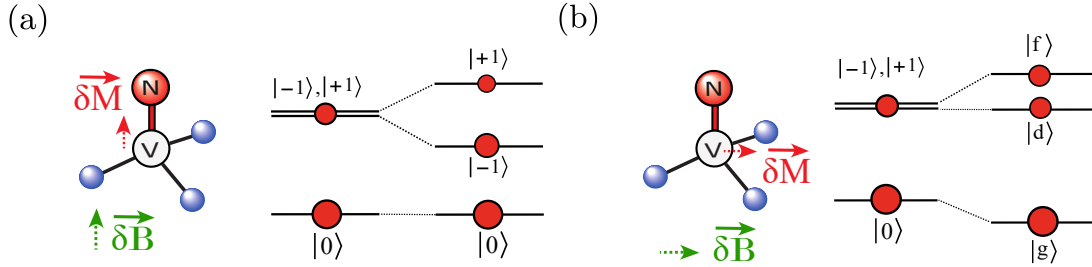


Figure 1.8: (a) Langevin paramagnetism of an NV<sup>-</sup> center for a magnetic field perturbation in the anisotropy axis direction at thermal equilibrium. (b) Van Vleck paramagnetism of an NV<sup>-</sup> center for a magnetic field perturbation perpendicular to the anisotropy axis direction at thermal equilibrium.

Fig. 1.8 (a) shows the magnetization of an NV<sup>-</sup> center in the case of a longitudinal perturbing field  $\delta\mathbf{B} = \delta B\mathbf{e}_3$  directed along the anisotropy axis of the NV<sup>-</sup> center as well as the energy evolution of the eigenstates. The perturbing field does not induce any mixing between the states because it commutes with the anisotropy term  $\hbar\hat{S}_3^2$ , so there is no Van Vleck paramagnetism. The energy of the state  $|m_s = -1\rangle$  decreases, leading to a stronger thermal occupation, while this is the opposite for the state  $|m_s = +1\rangle$ . It leads to a Langevin paramagnetism. Using the formula Eq. (1.21), we obtain:

$$\chi_{\text{Lan},\parallel}^{\text{th,NV}} = \frac{2}{3} d\hbar^2 \mu_0 \frac{\gamma_e^2}{k_B T}. \quad (1.35)$$

Fig. 1.8 (b) shows the magnetization of an NV<sup>-</sup> center in the case of a perturbing field  $\delta\mathbf{B} = \delta B \mathbf{e}_1$  perpendicular to the anisotropy axis of the NV<sup>-</sup> center as well as the energy evolution of the eigenstates. There is no Langevin paramagnetism in this case since the energy levels do not evolve to first order in the perturbation. However, the transverse magnetic field leads to a mixing between the eigenstates, which results in Van Vleck paramagnetism. Using the formula Eq. (1.23), we find

$$\chi_{V.V.,\perp}^{\text{th,NV}} = \frac{2}{3} d\hbar^2 \mu_0 \frac{\gamma_e^2}{k_B T}. \quad (1.36)$$

The diagonal terms of the magnetic susceptibility tensor of an NV<sup>-</sup> center are therefore identical (82). Moreover, the non-diagonal terms are in fact zero. Unexpectedly, the magnetic susceptibility tensor for a set of NV<sup>-</sup> centers thermalized at 300 K is diagonal and isotropic. For the considered density of NV<sup>-</sup> centers, we obtain

$$\chi^{\text{th,NV}} \approx 10^{-8} \ll |\chi_{\text{Diam}}|. \quad (1.37)$$

The paramagnetism of thermally populated NV<sup>-</sup> centers can thus be neglected at 300 K compared to the Larmor diamagnetism of the diamond.

### 1.3.3 Van Vleck paramagnetism of NV<sup>-</sup> centers with optical pumping

In this part, we consider the same configuration as in the previous section, but we add the green laser optical pumping on the NV<sup>-</sup> center that polarizes the NV<sup>-</sup> spin in the  $|m_s = 0\rangle$  state. We assume  $\gamma_{\text{las}} \gg \Gamma_1$  such that we can consider that the population is fully in the  $|m_s = 0\rangle$  state, i.e.,  $p_0 \approx 1 \gg p_{-1}, p_{+1}$ .

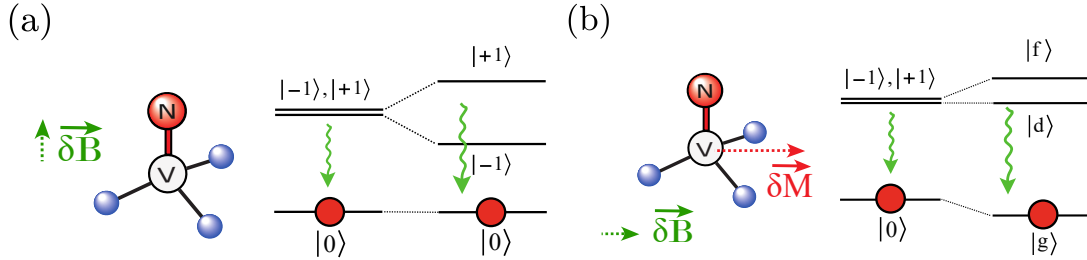


Figure 1.9: (a) Langevin paramagnetism of NV<sup>-</sup> centers for a magnetic field perturbation parallel to the NV<sup>-</sup> center anisotropy axis with a green laser optical pumping. (b) Van Vleck paramagnetism of NV<sup>-</sup> centers for a magnetic field perturbation perpendicular to the anisotropy axis with optical-pumping with a green laser.

Fig. 1.9 (a) shows the evolution of the energy levels and the populations in the case of a magnetic field perturbation aligned with the NV<sup>-</sup> center anisotropy axis. We remark that the energy of the fully populated state  $|m_s = 0\rangle$  does not evolve such that the NV<sup>-</sup> center's magnetic response in this case is equal to zero:

$$\chi_{\text{Lan},\parallel}^{\text{laser,NV}} = 0. \quad (1.38)$$

Fig. 1.9 (b) shows the evolution of the energy levels and the populations for a transverse

magnetic field. In this case, the mixing between the  $|m_s = 0\rangle$  state and the  $|m_s = \pm 1\rangle$  states leads to a repulsion of the energy states such that the energy of  $|m_s = 0\rangle$  decreases. Using the formula Eq. (1.14), we obtain

$$\chi_{V.V.,\perp}^{\text{laser,NV}} = 2d\hbar\mu_0 \frac{\gamma_e^2}{D}. \quad (1.39)$$

Inserting the numerical values for the highly doped diamond used in our experiment leads to

$$\chi_{V.V.,\perp}^{\text{laser,NV}} \approx 10^{-5}. \quad (1.40)$$

The  $NV^-$  centers thus exhibit Van Vleck paramagnetism in the presence of optical-pumping process with a green laser that is on the order of the Larmor diamagnetism of the diamond. This Van Vleck magnetism has been recently observed for a levitating diamond in (83).

### 1.3.4 Magnetism of $NV^-$ centers with a resonant microwave drive

Until now, we have studied the paramagnetic response of  $NV^-$  centers at zero magnetic fields for a thermally distributed population and for a population distribution given by the green laser optical pumping. In this part, we calculate the magnetization of the  $NV^-$  centers in the presence of optical pumping by a green laser and a microwave drive on the transitions  $|m_s = 0\rangle \rightarrow |m_s = \pm 1\rangle$ .

The two magnetic states  $|m_s = \pm 1\rangle$  are degenerate, so an external magnetic field  $\mathbf{B}_0$  is required to lift the degeneracy between the  $|m_s = \pm 1\rangle$  states, so that we can drive single transitions between the  $|m_s = 0\rangle \rightarrow |m_s = -1\rangle$  and  $|m_s = 0\rangle \rightarrow |m_s = +1\rangle$ . For the sake of simplicity, we consider an external magnetic field  $\mathbf{B}_0 = B_0\mathbf{e}_3$  directed along the anisotropy axis of the  $NV^-$  center and a microwave drive  $\mathbf{B}_{\mu w}(t) = \hbar\Omega_r \cos(\omega_{\mu w}t)\mathbf{e}_1$  perpendicular to the anisotropy direction. The frequency  $\Omega_r/2\pi$  is the Rabi frequency and  $\omega_{\mu w}/2\pi$  is the microwave frequency.

The Hamiltonian of the  $NV^-$  center is then given by

$$\hat{\mathcal{H}}_0 = \hbar D \hat{S}_3^2 + \hbar\omega_0 \hat{S}_3 + \hbar\Omega_r \cos(\omega_{\mu w}t) \hat{S}_1, \quad (1.41)$$

where  $-\gamma_e B_0 = \hbar\omega_0$ .

Moving into the microwave rotating frame by performing the unitary transformation  $\hat{U} = e^{i\omega_{\mu w}\hat{S}_3 t}$  and making the rotating wave approximation (neglecting the term rotating at  $2\omega_{\mu w}$ ), we obtain

$$\hat{\mathcal{H}}_1 = \hbar\omega_{+1,0} | +1\rangle \langle +1| + \hbar\omega_{-1,0} | -1\rangle \langle -1| \quad (1.42)$$

$$+ \hbar \frac{\Omega_r}{2\sqrt{2}} (| +1\rangle \langle 0| + | 0\rangle \langle +1| + | 0\rangle \langle -1| + | -1\rangle \langle 0|), \quad (1.43)$$

where  $\omega_{+1,0} = D + \omega_0 - \omega_{\mu w}$  and  $\omega_{-1,0} = D - \omega_0 - \omega_{\mu w}$ . The resonance condition for the  $|m_s = 0\rangle \rightarrow |m_s = \pm 1\rangle$  transition is thus achieved when  $\omega_{\mu w} = D \pm \omega_0$ .

Using the density matrix formalism and the master equation in the steady states  $0 = \frac{\partial \hat{\rho}}{\partial t} = -\frac{i}{\hbar} [\hat{\mathcal{H}}_1, \hat{\rho}] + \mathcal{L}(\hat{\rho})$ , we can express  $\mathbf{M}$  as a function of  $B_0$  and  $\omega_{\mu w}$ . The magnetization

can be calculated using the formula Eq.(1.11):

$$\mathbf{M} = d\hbar\gamma_e \text{Tr}(\hat{\rho}\hat{\mathbf{S}}), \quad (1.44)$$

which can be explicitly written using the density matrix coefficients:

$$M_1 = d\hbar\gamma_e \frac{\rho_{0-1} + \rho_{0-1}^* + \rho_{10} + \rho_{10}^*}{\sqrt{2}}, \quad (1.45)$$

$$M_2 = d\hbar\gamma_e \frac{i(\rho_{0-1} - \rho_{0-1}^* + \rho_{10} - \rho_{10}^*)}{\sqrt{2}}, \quad (1.46)$$

$$M_3 = d\hbar\gamma_e(\rho_{11} - \rho_{-1-1}). \quad (1.47)$$

The coherences are rotating at the frequency of the microwave. The NV<sup>-</sup> center has on average no transverse magnetization, such that  $M_1, M_2 = 0$ . The values of the populations  $\rho_{11}$  and  $\rho_{-1-1}$  are not affected by moving into the rotating frame because  $\hat{U}$  commutes with  $|+1\rangle\langle+1|$  and  $|-1\rangle\langle-1|$ . In the case of strong optical pumping, i.e.,  $\gamma_{\text{las}} \gg \Gamma_1$  presented in Appendix A.4, the magnetization along the NV<sup>-</sup> center anisotropy axis  $\mathbf{e}_3$  is:

$$M_3 = d\hbar\gamma_e \left( \frac{4\Gamma_1(\Gamma_2^{*2} + \omega_{+1,0}^2) + \Omega_r^2\Gamma_2^*}{4\gamma_{\text{las}}(\Gamma_2^{*2} + \omega_{+1,0}^2) + 2\Omega_r^2\Gamma_2^*} - \frac{4\Gamma_1(\Gamma_2^{*2} + \omega_{-1,0}^2) + \Omega_r^2\Gamma_2^*}{4\gamma_{\text{las}}(\Gamma_2^{*2} + \omega_{-1,0}^2) + 2\Omega_r^2\Gamma_2^*} \right). \quad (1.48)$$

Fig. 1.10 shows the magnetization of the NV<sup>-</sup> center in the direction  $\mathbf{e}_3$  as a function of the microwave power  $\omega_{\mu\text{w}}$  using formula Eq. (1.48). The parameters are  $d = 1.6 \times 10^{23} \text{ m}^{-3}$ ,  $\Omega_r/2\pi = 10 \text{ MHz}$ ,  $\Gamma_2^*/2\pi = 3 \text{ MHz}$ ,  $\gamma_{\text{las}}/2\pi = 100 \text{ kHz}$  and  $\Gamma_1/2\pi = 10 \text{ kHz}$ , as in the experiment of Chapter 5. The NV<sup>-</sup> transition is saturated at resonance. The magnetization is positive when the microwave field is on resonance with the  $|m_s = 0\rangle \rightarrow |m_s = -1\rangle$  transition while it is negative when it is resonant with the  $|m_s = 0\rangle \rightarrow |m_s = +1\rangle$  transition. The maximal absolute value that  $M_3$  can take is when the microwave saturates a transition, which gives an upper bound

$$|M_3| = \frac{d\hbar|\gamma_e|}{2} \approx 1 \text{ A/m}. \quad (1.49)$$

The maximum value of the magnetization is on the order 1 A/m, which is rather logical considering the density of NV<sup>-</sup> center spins<sup>4</sup>.

In this section, we were able to estimate the magnetization of the NV<sup>-</sup> centers in different cases relevant to our experiments: a thermal distribution of states, and a distribution of states due to the optical pumping of the green laser with or without resonant microwaves on a spin transition. These calculations will be particularly useful for estimating the value of the magnetic torque  $\boldsymbol{\tau}_{\text{mag}} = V\mathbf{M} \times \mathbf{B}$  due to the NV<sup>-</sup> centers in the next chapter.

<sup>4</sup>The magnetization of a hard ferromagnet at saturation is on the order of  $M_{\text{magnet}} = 10^6 \text{ A/m}$ , which is six orders of magnitude larger than a diamond with all the NV<sup>-</sup> centers magnetized. This is coherent with the fact that the density of NV<sup>-</sup> centers that we have considered for our simulations is on the order of 1 ppm.

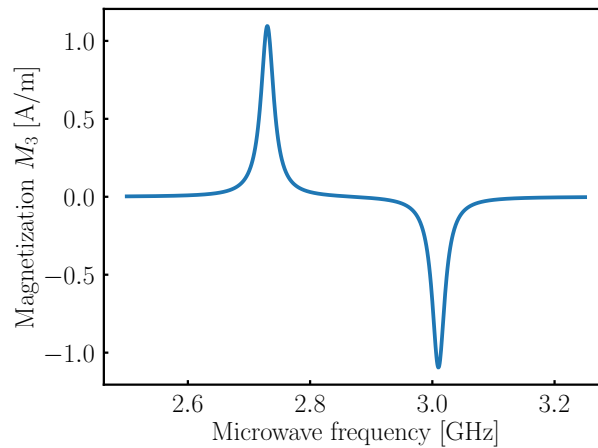


Figure 1.10: Magnetization  $M_3$  in the anisotropy direction  $\mathbf{e}_3$  of a highly doped diamond as a function of the microwave frequency drive, assuming a single  $\text{NV}^-$  class with the following parameters:  $d = 1.6 \times 10^{23} \text{ m}^{-3}$ ,  $\Omega_r/2\pi = 10 \text{ MHz}$ ,  $\Gamma_2^*/2\pi = 3 \text{ MHz}$ ,  $\gamma_{\text{las}}/2\pi = 100 \text{ kHz}$  and  $\Gamma_1/2\pi = 10 \text{ kHz}$ .

#### 1.4. Conclusion

In this chapter, we have estimated the magnetic response of a diamond doped with  $\text{NV}^-$  centers. To do this, it was first necessary to understand the electronic structure of crystals and in particular that of insulators and semiconductors. In addition, it has been shown that the presence of color centers in an insulator gives access to optically controllable electronic energy levels. The magnetic response of these defects was then studied using the Van Vleck formalism for a set of uncorrelated ions, and we proved the existence of three specific types of magnetism: Larmor diamagnetism, Langevin paramagnetism and Van Vleck paramagnetism. Finally, these previous results were applied to the special case of a diamond highly doped with  $\text{NV}^-$  centers to understand the magnetism of this material.

The concepts, formulae and numerical results obtained in the last part of this chapter will be of great help in understanding the origin of the magnetic torque for levitating microdiamonds doped with  $\text{NV}^-$  centers in Chapters 2 and 5. We will often refer to this chapter later on when we talk about the magnetism of  $\text{NV}^-$  centers.

## Chapter 2: Levitated magnetic particles: a promising system for torque magnetometry

---

The first traces of magnetism in materials date back to the Chinese and Greek civilizations, several hundred years before Christ, with the discovery of lodestones, which have the ability to attract iron particles. Centuries later, navigators used magnetic compasses to find their way at sea using the torque exerted by the Earth's magnetic field on the compass. The mechanical detection of the magnetic field with a magnetic particle is therefore an ancient but powerful method of magnetometry. In recent decades, the magnetic coupling between torsional and bending modes of thin wires with paramagnetic spins, such as electron spins in the diphenylpicrylhydrazyl salt (DPPH), has enabled the mechanical detection of magnetic spin resonances using the magnetic force (84) and the Einstein-de Haas torque (44; 85). This technique called Mechanical Detection of Magnetic Resonance (MDMR), has notably permitted the mechanical detection of a single spin in 2004 (33).

In this chapter, we extend these previous works by exploring the detection of magnetism in levitated magnetic particles by measuring the magnetic torque. We focus on two types of particles: diamonds highly doped in  $NV^-$  centers and ferromagnetic particles. In the first section, we review the experimental techniques developed in our team that allow the levitation and detection of the motion of these particles. Then, we explain and calculate the microscopic origin of the magnetic torque for the considered magnetic particles, which originates from crystalline anisotropy. We also discuss the measurement of magnetic fields using the torque exerted on these levitated particles. Finally, we discuss potential gyromagnetic phenomena that could be studied in the future thanks to the development of levitation techniques of micro/nanometric magnetic particles.

### 2.1. Levitation of magnetic particles: the experimental set-up

In this section, we recall the experimental techniques of levitation utilized in our team. We begin by highlighting the method of levitation employed, electric Paul traps which rely on alternating electric potentials. Then, we provide an in-depth explanation of the experimental setup used in our experiment, including the types of particles levitated, the geometry of the Paul trap and the optical detection methods used to observe the motion of the particles.

#### 2.1.1 Principle of the Paul trap

Particle levitation requires the application of a force that can confine the center of mass motion in all three dimensions of space. The two main forces that can lead to confinement are the electric and the magnetic forces. In this part, we will focus on the electric levitation of charged particles using Paul traps.

##### The electric Earnshaw's theorem

We begin by recalling a fundamental theorem that clearly constrains the possibility of levitating charged particles with electric fields: the electric Earnshaw's theorem. This

theorem states that the levitation of electrically charged particles with static fields is impossible. We explain in the following the origin of this theorem. In the case of an electrically charged particle of total charge  $q$  in a static electric potential  $U(\mathbf{r})$ , the energy of the system equals  $E_{\text{ele}}(\mathbf{r}) = qU(\mathbf{r})$ . According to Poisson's law, the sum of the curvatures of the electric potential must be equal to zero,  $\Delta U(\mathbf{r}) = 0$ , leading to

$$\Delta E_{\text{ele}}(\mathbf{r}) = 0 \quad \text{i.e.} \quad \frac{\partial^2 E_{\text{ele}}}{\partial x^2} + \frac{\partial^2 E_{\text{ele}}}{\partial y^2} + \frac{\partial^2 E_{\text{ele}}}{\partial z^2} = 0. \quad (2.1)$$

Thus, it is not possible to have confinement in the three directions of space, which would require the three components  $\partial^2 E_{\text{ele}}/\partial \nu^2$  to be positive for  $\nu = x, y, z$ . This condition is in clear contradiction with Poisson's law.

One way to circumvent Earnshaw's theorem for levitating electric particles is to use alternating potentials. This technique was originally developed by Wolfgang Paul (Nobel 1989) to trap ions (86; 87) but is now widely used in the micro/nanometer particle levitation community (24).

### Ponderomotive traps

In this part, we aim to provide a physical understanding to the reader on how ponderomotive traps that use oscillating harmonic potentials, such as Paul traps, can lead to stable trapping. We will be following the approach proposed in the paper (88).

In Fig. 2.1, we consider a physical system of a particle subjected to a mechanical potential that alternates between a positive curvature  $E_{\text{pot}}^+(x) = 1/2m\omega_x^2 x^2$  and a negative curvature  $E_{\text{pot}}^-(x) = -1/2m\omega_x^2 x^2$  each  $\Delta t = \pi/\Omega$ . The potential is equal to  $E_{\text{pot}}^+(x)$  when  $t \in [2n\pi/\Omega, (2n+1)\pi/\Omega]$  and equals  $E_{\text{pot}}^-$  when  $t \in [(2n+1)\pi/\Omega, (2n+2)\pi/\Omega]$ . The dynamics of this system can be easily solved since it only involves solving two ordinary differential equations. Given the normalized initial condition  $X_0 = (x(t=0), \dot{x}(t=0)/\omega_x)$ , we can calculate the value of  $X_{2n} = (x(t=2n\pi/\Omega), \dot{x}(t=2n\pi/\Omega)/\omega_x)$  using the expression:

$$X_{2n} = (AB)^n X_0 \quad (2.2)$$

with:

$$A = \begin{pmatrix} \cosh \alpha & \sinh \alpha \\ \sinh \alpha & \cosh \alpha \end{pmatrix} \quad \text{and} \quad B = \begin{pmatrix} \cos \alpha & -\sin \alpha \\ \sin \alpha & \cos \alpha \end{pmatrix} \quad \text{with} \quad \alpha = \pi \frac{\omega_x}{\Omega}. \quad (2.3)$$

A crucial point in ponderomotive traps is that, even if the potentials applied during the different time periods are simply opposite, the dynamics are quite different in each time step. Indeed, a confining potential gives rise to oscillating dynamics, represented by the cosine matrix  $B$ , whereas an anti-confining potential gives rise to an exponential fall, represented by the matrix  $A$ . The stability of such a system therefore results from a competition between these two different dynamics. The system is stable if and only if the norm of the eigenvalues of the matrix  $AB$  is less than or equal to 1. This condition can be written as the following inequality:

$$|\cos(\alpha) \cosh(\alpha)| < 1 \quad (2.4)$$

This inequality is always valid when  $\alpha < 1.88$ , which gives the condition

$$\Omega > 1.68 \omega_x. \quad (2.5)$$

Other solutions exist when  $\alpha$  is close to  $n\pi + \pi/2$ . We will not discuss these solutions in the following. When  $\Omega \gg \omega_x$ , the dynamics given by the cosine evolution dominate the exponential dynamics of the anti-confining potential, leading to a confining potential. When  $\Omega \ll \omega_x$ , the two potentials do not alternate quickly enough, and the particle accumulates too much kinetic energy during the anti-confining potential period, which cannot be compensated for the confining period. On long time scales, the exponential dynamics overpower the cosine dynamics of the confining potential, and the particle is not confined.

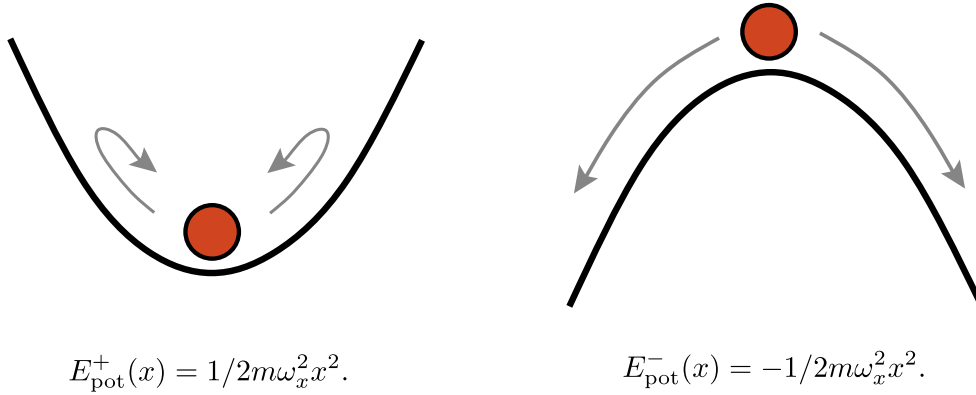


Figure 2.1: Left: positively curved potential energy of the particle when  $t \in [2n\pi/\Omega, (2n+1)\pi/\Omega]$ . Right: negatively curved potential energy of the particle when  $t \in [(2n+1)\pi/\Omega, (2n+2)\pi/\Omega]$ .

We can keep in mind this example for the following, which is closely related to the physics of the Paul trap.

### The electric Paul trap

As we have previously discussed, alternating potentials can lead to stable trapping. However, the evolution of the potential used in the previous example is discontinuous and therefore difficult to generate using physical systems. In this part, we will consider an oscillating electric potential that smoothly transitions from a confining potential to an anti-confining potential. We consider the electric potential created by a ring shaped trap in which the sum of a constant voltage and an oscillating voltage is applied. The electric potential generated at the center of the ring is, to second order in position

$$U(\mathbf{r}, t) = (U_{\text{DC}} + U_{\text{AC}} \cos(\Omega t)) \frac{z^2 - \frac{1}{2}(y^2 + x^2)}{z_0^2}, \quad (2.6)$$

where  $U_{\text{DC}}$  is the bias voltage,  $U_{\text{AC}}$  is the amplitude of the oscillating voltage and  $z_0$  is a characteristic dimension of the electrode.

For the same reasons as in the previous section, oscillating potentials can stably trap charged particles at sufficiently high values of the Paul trap driving frequency  $\Omega/2\pi$ . The

equations of motion for a particle of total charge  $Q$  are

$$\ddot{x} - \frac{Q}{mz_0^2} (U_{\text{DC}} + U_{\text{AC}} \cos(\Omega t)) x = 0, \quad (2.7)$$

$$\ddot{y} - \frac{Q}{mz_0^2} (U_{\text{DC}} + U_{\text{AC}} \cos(\Omega t)) y = 0, \quad (2.8)$$

$$\ddot{z} + 2\frac{Q}{mz_0^2} (U_{\text{DC}} + U_{\text{AC}} \cos(\Omega t)) z = 0. \quad (2.9)$$

The stable levitation of a charged particle requires that the particle is confined in the three directions of space. To study the stability of the three previous dynamic equations, we introduce the dimensionless parameters  $a_\nu$  and  $q_\nu$ , defined as

$$a_x = a_y = -\frac{a_z}{2} = \frac{-4QU_{\text{DC}}}{mz_0^2\Omega^2}, \quad (2.10)$$

$$q_x = q_y = -\frac{q_z}{2} = \frac{-2QU_{\text{AC}}}{mz_0^2\Omega^2}, \quad (2.11)$$

which leads to a Mathieu equation (89):

$$\nu'' + (a_\nu - 2q_\nu \cos(2\tau))\nu = 0, \quad (2.12)$$

where  $\tau = \Omega/2t$ ,  $\nu = x, y, z$  and  $\nu''$  designates the second derivative of  $\nu$  as a function of the variable  $\tau$ . The stability of this equation depends on the two parameters  $a_\nu$  and  $q_\nu$  and can be studied analytically. In Fig. 2.2, we present a stability diagram as a function of  $a_z$  and  $q_z$ . The blue area designates the stability region for the  $x$  and  $y$  components while the red area designates the stability region in the  $z$  direction. The particle can be fully confined in the overlap of the red and the blue regions.

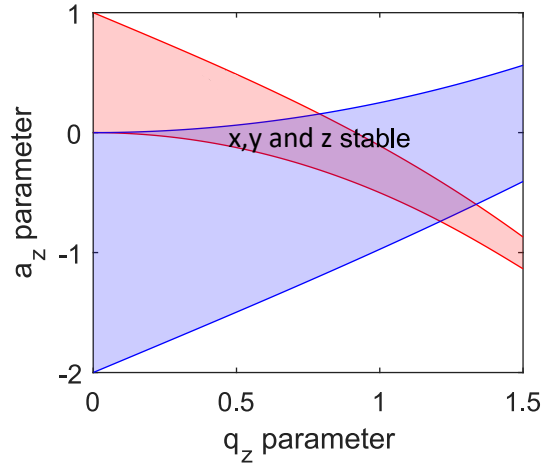


Figure 2.2: Stability diagram of a levitated particle in a Paul trap as a function of  $a_z$  and  $q_z$ . Modified from (90)(Licence ouverte/Open license).

Within the stability domain, the motion of each center of mass mode can be decomposed into two motions of different frequency. The first motion is a fast oscillation at the frequency  $\Omega/2\pi$  called the micromotion and is a direct consequence of the oscillating

potential at  $\Omega/2\pi$ . The second motion is a slow motion at a frequency  $\tilde{\omega}_\nu/2\pi$  that is the trapping frequency of the particle. This motion is called the macromotion. Under the condition  $q_\nu < 0.4$ , the trapping potential resulting from the ponderomotive confinement can be modeled as a harmonic potential that equals

$$U_{\text{sec}} = \frac{1}{2}m \sum_\nu \tilde{\omega}_\nu^2 \nu^2, \quad \text{with} \quad \tilde{\omega}_\nu = \frac{\Omega}{2} \sqrt{a_\nu + \frac{q_\nu^2}{2}}. \quad (2.13)$$

We have represented in Fig. 2.3 the motion in the  $x$  direction of the particle subject to an oscillating harmonic potential at the frequency  $\Omega/2\pi$  for different values of  $q_\nu$ , keeping  $a_\nu = 0$ . In Fig. 2.3 (a) and (b),  $q_\nu < 0.9$  and the particle is stably trapped. In Fig. 2.3 (a),  $q_\nu = 0.4$  and the ponderomotive potential resulting in macromotion cannot be modeled by a harmonic potential. In Fig. 2.3 (b),  $q_\nu = 0.1 < 0.4$  and the ponderomotive potential resulting in macromotion can be modeled by a harmonic potential at a frequency  $\tilde{\omega}_\nu/2\pi$  using the formula Eq. (2.13).

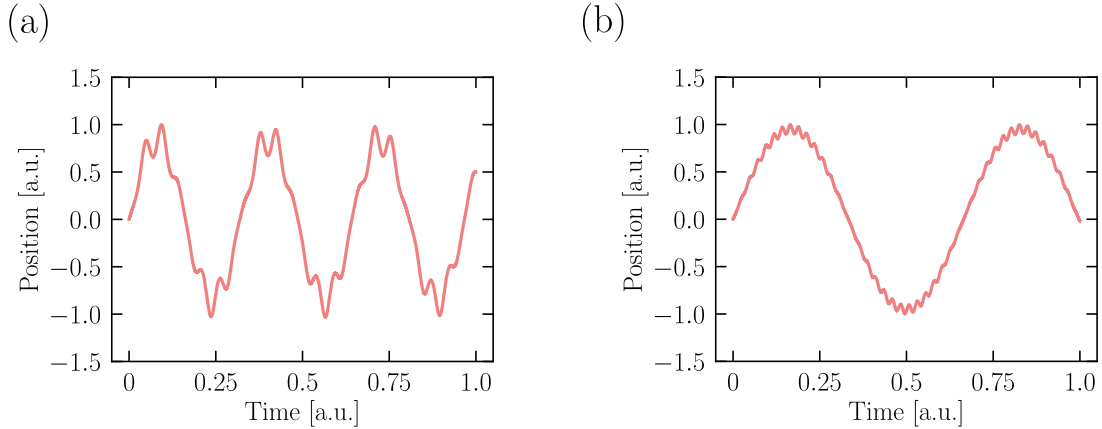


Figure 2.3: (a) Numerical simulation of the position of the particle as a function of time for  $q = 0.4$ . (b) Numerical simulation of the position of the particle as a function of time for  $q = 0.1$ .

In our experiment, the typical parameters used to levitate the charged particles are  $V_{\text{AC}} = 2000$  V and  $\Omega/2\pi = 1 - 10$  kHz. We do not use a DC voltage.

### Angular confinement

In the previous part, we saw how a charged particle could levitate using alternating harmonic potentials. For an asymmetrically charged particle levitating in an asymmetric Paul trap, we can convince ourselves that the angular degrees of freedom are also subject to an alternating angular potential which can lead to angular ponderomotive confinement, as demonstrated in (29; 80; 36). The physics of the angular dynamics of charged particles in Paul traps will be developed in detail in Chapter 4.

For the rest of this chapter, we consider that the charged particles levitating in our Paul traps are angularly stable.

### 2.1.2 Levitated magnetic particles

Electrical levitation of magnetic particles has the advantage of not depending on the magnetic state of these particles, which is convenient for studying their magnetic properties. Additionally, most particles between 1 and 20 microns are electrically charged on the surface and can therefore be levitated in electric Paul traps. We provide a non-exhaustive list of particles that can be levitated in our Paul trap.

#### Diamond samples

The first type of particles that can levitate in these traps is monocrystalline diamond. The quality of the diamond plays a crucial role in determining the spin properties of the  $NV^-$  centers inside. The four types of diamond samples that can be levitated in our traps were all fabricated by the method of High Pressure High Temperature (HPHT). This method is efficient for producing a large quantity of diamonds in powder, but it also introduces a lot of crystalline defects that can decrease the coherence time of the diamond  $NV^-$  centers. Another method, Chemical Vapor Deposition (CVD) (91), allows for better control of the impurities present in the diamond crystal lattice. However, CVD-grown diamond powders are not readily available in large quantities and must be produced in collaboration with specialized teams at Chimie Paristech and Université de Villetaneuse (92). It is problematic because our method of injecting diamonds into Paul traps is statistical and relies on having a large number of diamonds available.

The first diamond sample is synthetic MSY monocrystalline diamonds from the company Pureon, ranging in size from 8 to 20 microns. Fig. 2.4 (a) shows a microscopic image of a diamond of about 10 microns in size. The apparent color of these diamonds is grayish, probably due to graphitization of the diamond surface. The number of  $NV^-$  centers in these diamonds can vary from one diamond to another and is estimated at 1 ppb. The coherence rate  $\Gamma_2^*$  is of the order of 8 MHz (80; 90).

The second diamond sample is natural monocrystalline diamonds from the Pureon company, ranging in size from 8 to 20 microns. Fig. 2.4 (b) shows a microscopic image of it. The apparent color of these diamonds is white. The number of  $NV^-$  centers inside has not been precisely estimated but is less than for MSY diamonds.

The third diamond sample is the MDNV15umHi50mg monocrystalline diamonds from the Adamas Nanotechnologies company. These diamonds are 15  $\mu\text{m}$  in size. We frequently use these diamonds in our experiment because they have a high density of  $NV^-$  centers, around 3.5 ppm, resulting in a strong magnetic torque, as we will see later. Fig. 2.4 (c) shows a microscopic image of an Adamas diamond. The red color is typical for a diamond that is highly doped with  $NV^-$  centers. The powder of these diamonds is shown in Fig. 2.4 (c). The coherence time is also better than for the previous diamonds, and the decoherence rate is  $\Gamma_2^* = 3$  MHz.

Finally, the fourth and last diamonds are irradiated MSY diamonds from Pureon company between 10 and 20 microns by the group of A. Tallaire at Chimie ParisTech. Fig. 2.4 (d) shows a microscopic image of these diamonds. The density of  $NV^-$  centers has not been precisely estimated but is between 1 ppb and 1 ppm. The  $NV^-$  concentration is high enough to observe a magnetic torque coming from these impurities.

In the remainder of this thesis, the diamonds used are the highly doped  $NV^-$  center diamonds from the Adamas company.

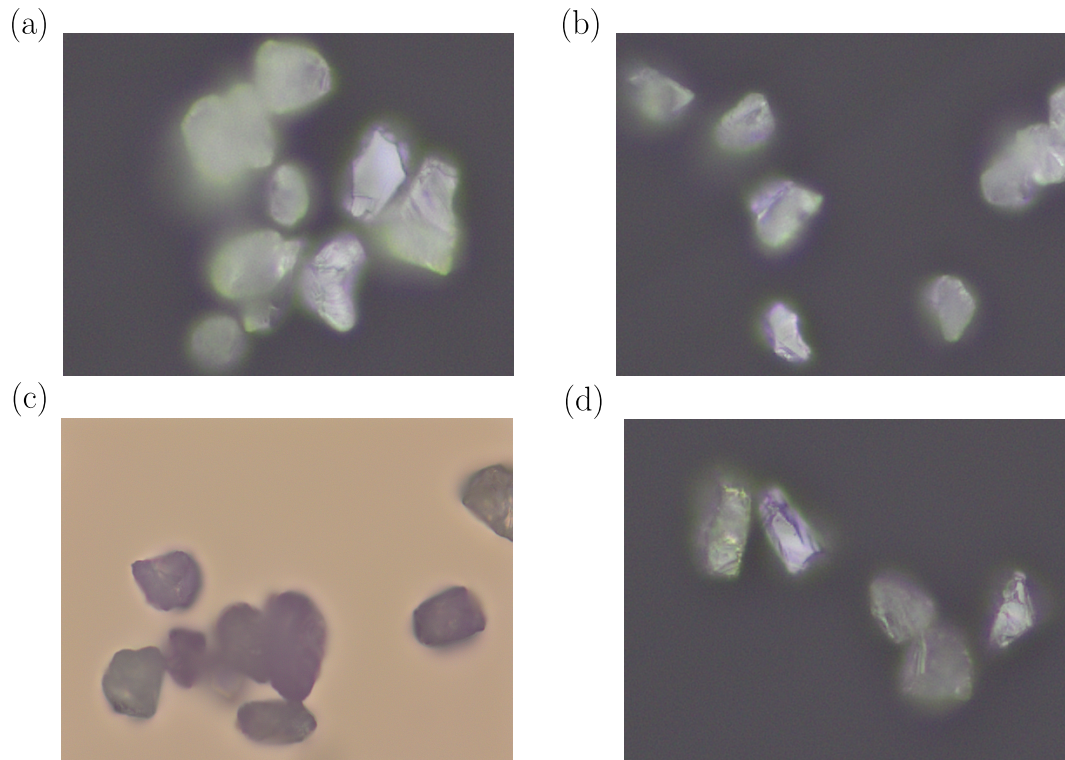


Figure 2.4: Microscopic images of different particles: (a) 10 – 20  $\mu\text{m}$  MSY diamonds from Pureon company. (b) 10 – 16  $\mu\text{m}$  natural diamonds from Pureon company. (c) 15 – 20  $\mu\text{m}$  diamonds from Adamas Nanotechnologies company. (d) Irradiated MSY diamonds from Pureon company.

### Ferromagnetic samples

Other magnetic particles that are studied are soft ferromagnetic particles such as soft iron as well as hard ferromagnetic levitated particles. For example, a 1 micron spherical iron particle from GoodFellow FE006045 is shown in Fig. 2.5 (a) and can be levitated electrically (93). We can also levitate a ferrimagnetic material, the yttrium iron garnet (YIG) manufactured at the Lab-STICC laboratory by J. Ben Youssef. This material is initially in the form of a macroscopic crystal which is then ground to obtain a powder of about ten microns in size as shown in Fig. 2.5 (b). The advantage of this material is that it has the best ferromagnetic resonance (FMR) quality factor of the ferromagnetic particles. Moreover, coupling effects between mechanics and magnetism have already been observed with mechanical resonators made of YIG (94). Finally, we are able to inject hard ferromagnetic materials like neodymium magnet powder. To obtain a powder of this compound, a macroscopic hard magnet is ground with sandpaper and the magnetic powder thus created is recovered.

Other types of particles containing paramagnetic impurities could be injected in this trap such as DPPH, rare earth ion doped crystals or ruby.

### 2.1.3 Paul trap design

This section is devoted to explaining the design and construction of the Paul traps used, as well as the method for injecting particles into the trap.

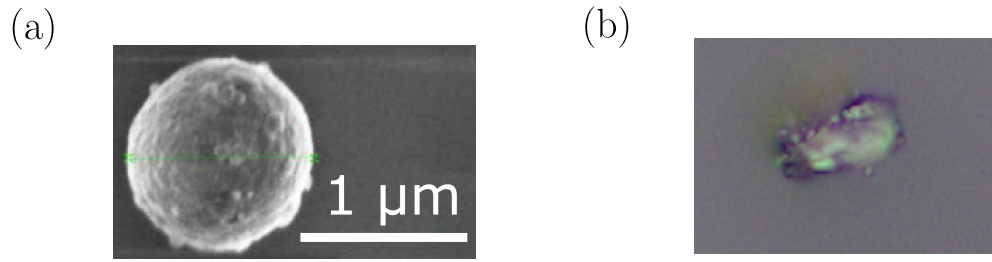


Figure 2.5: (a) Scanning electron microscopy image of an iron particle. (b) Microscopic image of a  $10 \mu\text{m}$  YIG particle.

### Micro ring trap

The Paul traps used to levitate these particles are handmade micro ring Paul traps in open configuration, meaning that the ring does not loop back on itself. Fig. 2.6 (a) shows a microscope image of one of these traps. The wire used to form the trap is either a  $25 \mu\text{m}$  diameter tungsten wire or a  $15 \mu\text{m}$  diameter tungsten wire with a gold coating. The advantage of micro traps is that the harmonic potential is stiffer than for millimetric traps due to the proximity between the electrodes. This allows for ponderomotive confinement both for the center of mass and for the angular modes with the same drive frequency of the Paul trap (the dynamics of the angle in Paul traps will be discussed in more detail in Chapter 4). Fig. 2.6 (b) shows a schematic of the Paul trap used. Particles can be trapped in two distinct areas where the electric potential is harmonic due to symmetry considerations: the center of the ring and the bottleneck. The particles levitating in the bottleneck are particularly stable because the electrodes formed by the two wires with opposite curvatures are very close. Additionally, the loop configuration of the trap allows a microwave current to be passed inside to excite the  $\text{NV}^-$  centers in the levitating diamonds. This is accomplished by using a bias tee upstream of the circuit to sum the low frequencies of the Paul trap (kHz) with the high frequencies of the microwave (GHz). Fig. 2.6 (c) shows a diamond of size between  $10 - 20 \mu\text{m}$  levitating in the bottleneck of the Paul trap, the wire of which is  $15 \mu\text{m}$  in diameter. The diamond is angularly stable on the image. The proximity of the diamond to the wire constituting the electrode also allows for high microwave powers when polarizing the  $\text{NV}^-$  centers in a levitated diamond. The maximum Rabi frequency that can be reached is about 10 MHz.

### Trap fabrication

The advantage of these micro traps is that they allow confinement of both the center of mass and the angle of the levitated particles, and that we can have efficient microwave driving power. However, one of the negative aspects of these traps is that they are very fragile due to the small diameter of the wires, and they are difficult to manufacture. Figure 2.7 (a) shows a picture of the setup used to design them. Figure 2.7 (b) shows an explanatory diagram of how to make these traps. The first step (i) is to wrap the  $15 \mu\text{m}$  wire making up the trap around a  $200 \mu\text{m}$  diameter wire and pull the two ends of the  $15 \mu\text{m}$  wire hard enough to form the ring shape of the trap. The second step (ii) is to bring two razor blades precisely aligned at the crossing of the gold wire to pinch the wire. Then, in a third step (iii), the wire is pulled to give the trap a bottleneck shape. Finally, the razor blades are moved away and the  $200 \mu\text{m}$  diameter wire is cut to remove

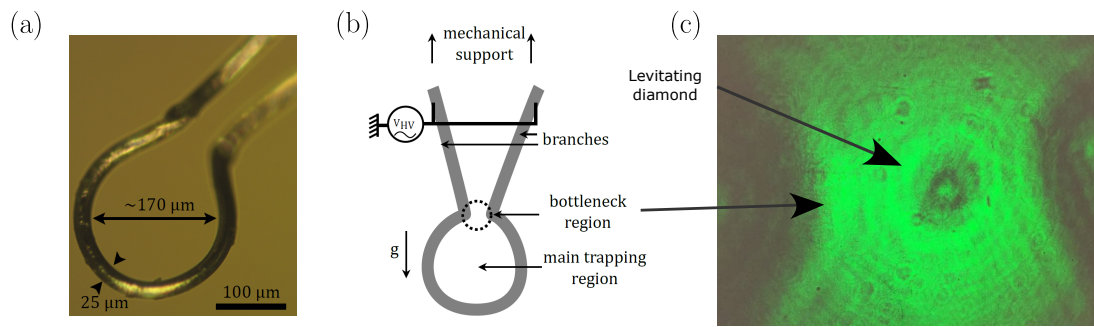


Figure 2.6: (a) Microscope photo of a home-made micro ring Paul trap. (b) Schematics of a Paul trap. Taken from (90)(Licence ouverte/Open license). (c) Confocal imaging of a stable diamond levitating in the bottleneck of a home-made Paul trap.

the manufactured micro-trap as shown in (iv). The crucial step is not to break the  $15\ \mu\text{m}$  wire when pulling on it to give its neck shape with the razor blade.

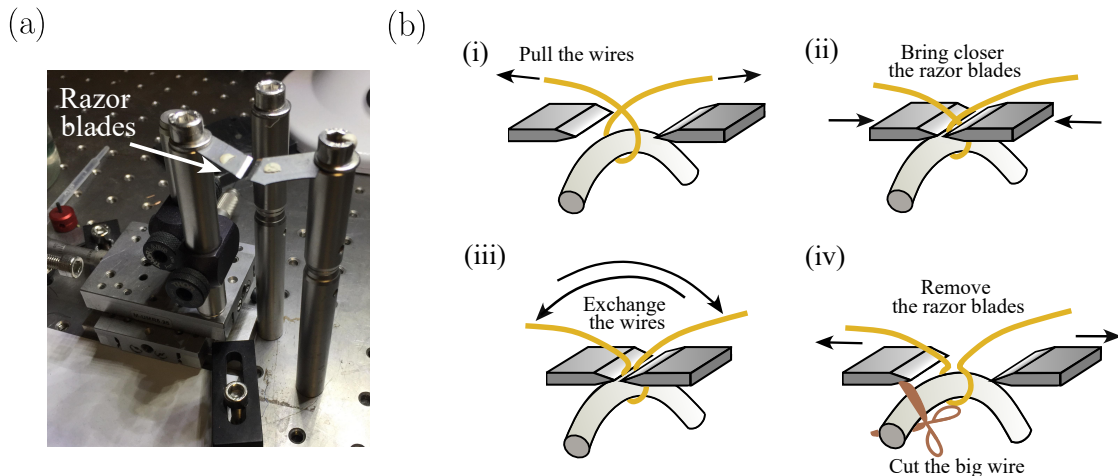


Figure 2.7: (a) Photo of the device used to make hand-made Paul traps. (b) Schematics of the manufacturing process of a hand-made Paul trap in four steps. (i) First step: the wire of the Paul trap is pulled on both ends to form a loop. (ii) Two razor blades are brought together to pinch the wire of the Paul trap at the wire crossing. (iii) The ends of the wires of the Paul trap are exchanged to form the bottleneck. (iv) The razor blades are removed, and the big wire giving the ring shape is cut to extract the final Paul trap.

### Particle injection

The injection of particles is a crucial step in the study of levitated particles. Although the fabrication of micro/nanometric particles with well-controlled shapes is well established, it can often be challenging to produce them in large quantities. For example, diamonds with excellent spin properties must be produced using the CVD method. Therefore, it would be ideal to inject particles in a deterministic way, i.e., to identify a specific particle that has been characterized beforehand and to inject it in the trap. However, in our experiments, we have samples of particles in powder in reasonable quantities and with homogeneous properties from one particle to another, which allows us to use a statistical

injection technique.

As shown in Fig. 2.8 (a), we use a metallic injection wire that is previously placed into the diamond samples, so that there are hundreds of diamonds that coat the tip of the injection wire. This wire is then brought close to the micro-trap. Due to the high voltage previously switched on, the charged particles on the injection wire are expelled, and some of them are injected into the trapping zone. Several particles can be trapped, as shown in Fig. 2.8 (b); it is then necessary to adjust the trap parameters to remove the particles that are less charged and isolate the desired one.

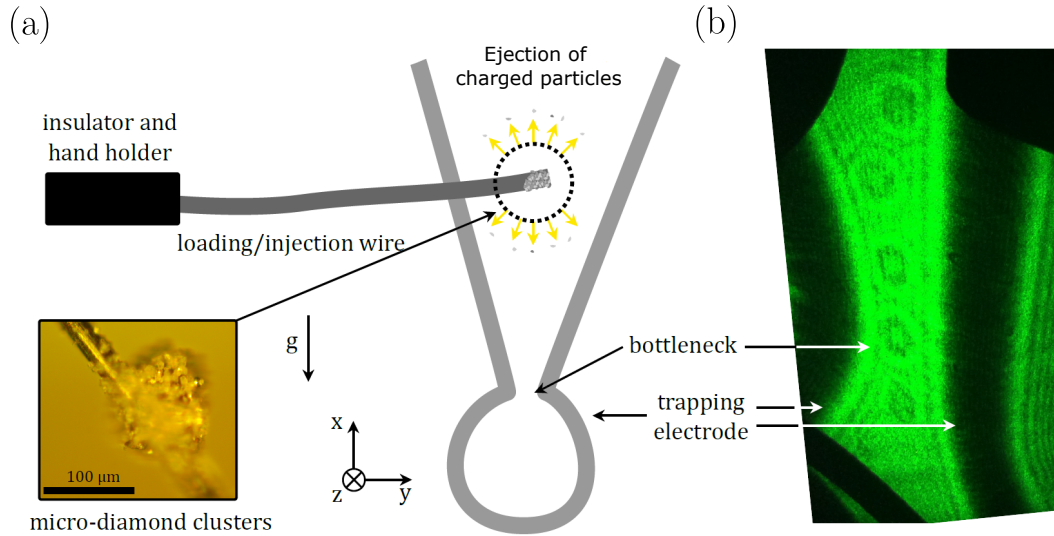


Figure 2.8: (a) Schematic of the injection of particles in the homemade Paul trap using an injection wire. (b) Transmission imaging of diamonds levitating in the bottleneck of the Paul trap. Taken from (90)(Licence ouverte/Open license).

### 2.1.4 Read-out of the mechanical motion

An efficient detection of the mechanical modes of the levitated magnetic particles is crucial for observing magnetic torque effects.

#### Optical set-up

In Fig. 2.9, the optical setup of the levitation experiment is depicted. The levitated particle is illuminated by a green laser with a wavelength of 532 nm and a power of 4 mW. The laser focus is positioned before the particle location in the  $z$  direction, allowing for observation of the transmitted image of the diamond on a screen, as shown in Fig. 2.6 (c) and Fig. 2.8 (b). The light passes through an Acousto-Optical Modulator (AOM) before reaching the lens, which allows for quick switching on and off of the laser. The intensity of the laser can also be tuned using a half-wave plate and a polarizing beam splitter.

It is worth noting that the green laser serves a dual purpose in these experiments; it polarizes the  $NV^-$  centers of the levitated diamonds, and it allows us to visualize and monitor the motion of the levitated particle. The Paul trap is placed in a vacuum chamber on a three-axis stage for adjusting its position relative to the lens. The chamber is equipped with a vacuum pump and pressure gauge for maintaining the desired level of vacuum and

pressure control. High voltage and microwave signals are fed into the chamber via vacuum feedthroughs.

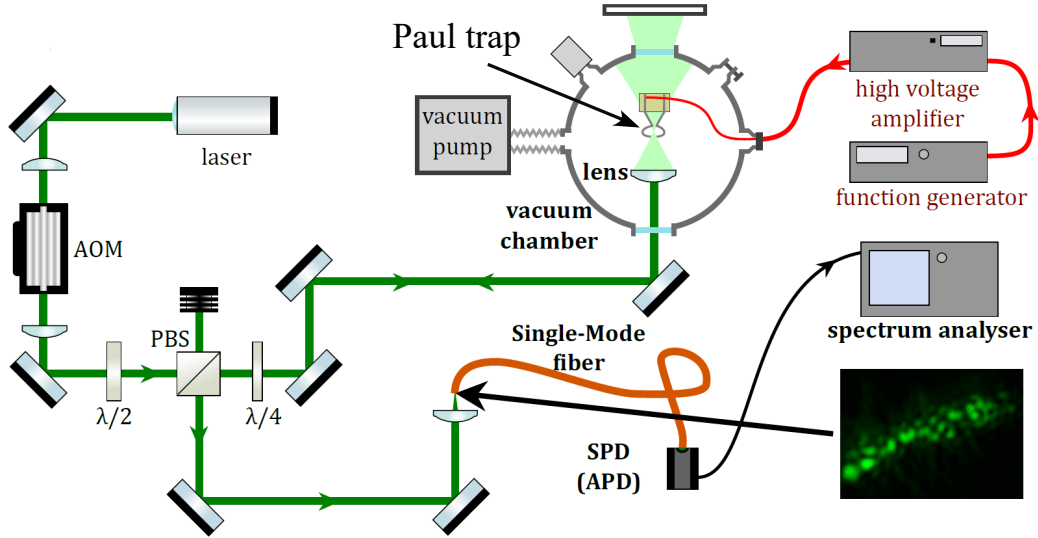


Figure 2.9: Optical set-up of the particle motion read-out using back-scattered light. Taken from (90)(Licence ouverte/Open license).

#### Detection using the back-scattered light

The first detection method uses backscattered light from the diamond to form an interference pattern in the image plane called the speckle pattern. A characteristic speckle pattern is shown in Fig. 2.9 for a particle of about  $10\ \mu\text{m}$ . The existence of this pattern is due to the fact that the laser wavelength is small compared to the size of the particle and also because diamonds are not spherical and have a rough surface. The advantage of using this interference pattern is that it is very sensitive to the angular displacement of the particle. A small area of this speckle is then injected into an optical fiber that is connected to an avalanche photodetector APD SPCM-ARQ-15 from Perkin-Elmer. We thus obtain a one-dimensional signal sensitive to the motion of the particle, particularly to the angular modes of the particle. We can then inject this signal into a spectrum analyzer to detect the different mechanical modes.

The sensitivity of this method is about  $100\ \mu\text{rad}/\sqrt{\text{Hz}}$  (36) and is shotnoise limited by the detection laser. Only few percents of the backscattered light are collected in the avalanche photodetector. One would notably increase the sensitivity value by making use of the information contained in the whole speckle pattern. However, this would require post-treatment and the sensitivity we currently have is sufficient enough for detecting mechanical displacements we are looking for.

#### Detection using the transmitted light

The second method of detection is based on the collection of the transmitted light by a photodetector from Thorlabs after it passes through the levitated particle in levitation. A D-shaped mirror can be used to differentiate between the left and right-side light signals of the particle, providing increased sensitivity to the center of mass motion along that

direction.

As shown in Fig. 2.10, we use an experimental setup to read out the motion of the particle collecting the transmitted light. The transmitted light is spatially filtered using a pinhole in order to collect only the light that passed through the levitated particle. The selected area is then collimated by a lens and directed onto a photodetector that delivers a current proportional to the intensity of the collected light.

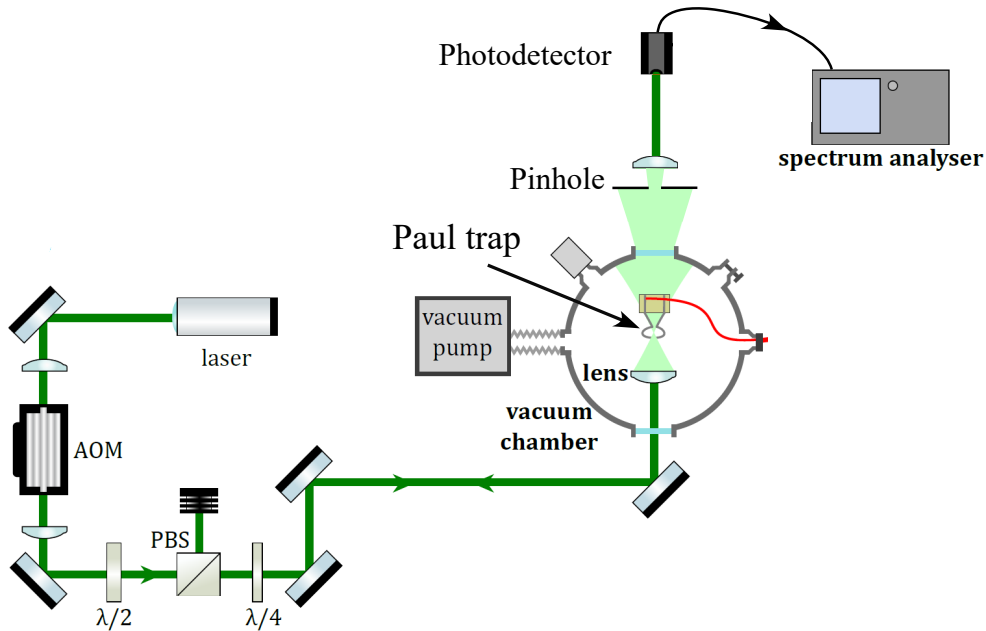


Figure 2.10: Optical set-up of the particle motion read-out using transmitted light.

This detection method is more sensitive to the center of mass motion and less sensitive to the angular motion. However, by using a pinhole to select small parts of the particle, we can adjust the sensitivity to different modes and increase the sensitivity to the angular motion.

## 2.2. Magnetic torques with anisotropic magnetic crystals

In order to estimate the sensitivity of torque magnetometry using magnetic levitating particles, we need to calculate the magnetic torque exerted on a levitating magnetic particles.

### 2.2.1 System description and parametrization

In this part, we introduce the relevant parameters to describe the motion of a levitating magnetic particle subject to a magnetic field. In Fig. 2.11, we illustrate the two different types of levitating magnetic particles that we study: a diamond embedded with  $NV^-$  centers and a hard ferromagnet. We assume that the trapping method fully stabilizes the center of mass motion as well as the angles. We neglect any possible coupling between the center of mass motion and the angular motion that could be induced by the trapping method. For simplicity, we assume that these two particles are spherical, that the inertia  $I$  is the same in all directions. We use the  $zyz$  convention of the Euler angle operators

$\hat{\Omega} = \{\hat{\alpha}, \hat{\beta}, \hat{\gamma}\}$  to parametrize the angular degree of freedom of the particles. We designate by  $O\mathbf{e}_1\mathbf{e}_2\mathbf{e}_3$  the body-fixed reference frame of the levitating particle and by  $O\mathbf{e}_x\mathbf{e}_y\mathbf{e}_z$  the laboratory frame. The direction  $\mathbf{e}_3$  is related to the crystalline anisotropy axis of both materials. For the diamond, the direction  $\mathbf{e}_3$  corresponds to the anisotropy direction of a  $\text{NV}^-$  center class. In the case of the magnet, it corresponds to the easy axis of magnetization, which is the direction determined by the total magnetic moment  $\boldsymbol{\mu} = \mu\mathbf{e}_3$ . The total magnetic moment vector  $\boldsymbol{\mu}$  is related to the magnetization of the system by the relation  $\boldsymbol{\mu} = V\mathbf{M}$ , where  $V$  is the volume of the particle.

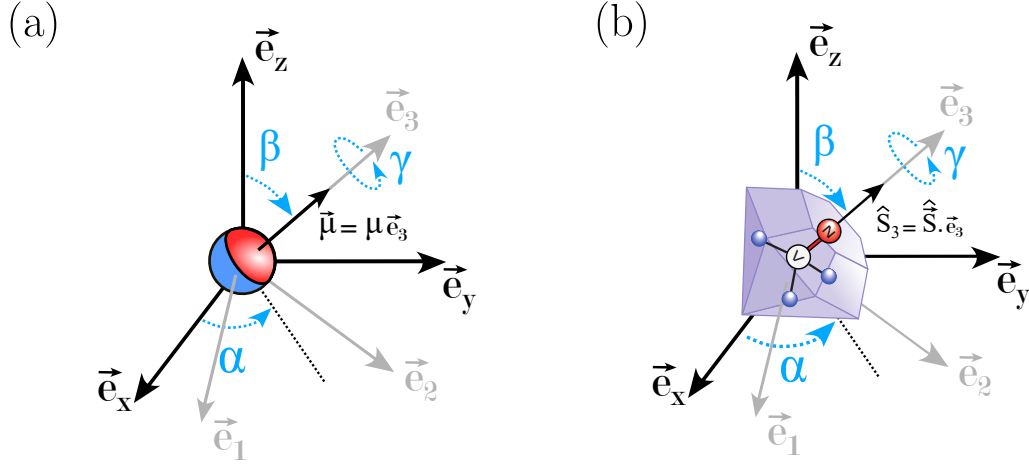


Figure 2.11: (a) Schematics showing a hard ferromagnet and its parametrization. The laboratory frame is parametrized by the basis  $(\mathbf{e}_x, \mathbf{e}_y, \mathbf{e}_z)$ . We use the  $zyz$  Euler angles convention to describe the angular motion of the magnet given by the angle  $\hat{\Omega} = \{\hat{\alpha}, \hat{\beta}, \hat{\gamma}\}$ . The magnetization direction is along the vector  $\mathbf{e}_3$  such that the magnetic moment equals  $\boldsymbol{\mu} = \mu\mathbf{e}_3$ . (b) The convention for the  $\text{NV}^-$  center in diamond is the same as that for the hard ferromagnet but the  $\mathbf{e}_3$  axis is given by the anisotropy axis of an  $\text{NV}^-$  center.

The body-fixed frame and the laboratory frame are related by the relation  ${}^t(\mathbf{e}_1, \mathbf{e}_2, \mathbf{e}_3) = {}^tR(\hat{\Omega}){}^t(\mathbf{e}_x, \mathbf{e}_y, \mathbf{e}_z)$  with:

$$R(\hat{\Omega}) = R_z(\hat{\alpha})R_y(\hat{\beta})R_z(\hat{\gamma}) = \begin{pmatrix} c_{\hat{\alpha}} & -s_{\hat{\alpha}} & 0 \\ s_{\hat{\alpha}} & c_{\hat{\alpha}} & 0 \\ 0 & 0 & 1 \end{pmatrix} \begin{pmatrix} c_{\hat{\beta}} & 0 & s_{\hat{\beta}} \\ 0 & 1 & 0 \\ -s_{\hat{\beta}} & 0 & c_{\hat{\beta}} \end{pmatrix} \begin{pmatrix} c_{\hat{\gamma}} & -s_{\hat{\gamma}} & 0 \\ s_{\hat{\gamma}} & c_{\hat{\gamma}} & 0 \\ 0 & 0 & 1 \end{pmatrix}. \quad (2.14)$$

where  $c_{\hat{\nu}} = \cos(\hat{\nu})$  and  $s_{\hat{\nu}} = \sin(\hat{\nu})$ .

The two vector bases  $(\mathbf{e}_1, \mathbf{e}_2, \mathbf{e}_3)$  and  $(\mathbf{e}_x, \mathbf{e}_y, \mathbf{e}_z)$  thus coincide when  $\hat{\Omega} = 0$ .

We make use of this parametrization to calculate the magnetic torque exerted on the magnetic particle.

### 2.2.2 Magnetic torque

In this part, we aim to calculate the magnetic torque exerted on a levitating diamond embedded with  $\text{NV}^-$  centers and on a hard ferromagnet with a total magnetic moment of  $\boldsymbol{\mu}$  in an external magnetic field  $\mathbf{B} = B_x\mathbf{e}_x + B_y\mathbf{e}_y + B_z\mathbf{e}_z$ . The goal is to demonstrate and

understand the magnetic torque formula:

$$\boldsymbol{\tau}_{\text{mag}} = \boldsymbol{\mu} \times \mathbf{B}. \quad (2.15)$$

Despite the apparent simplicity of this formula, it should be noted that it is not verified for all magnetic materials. For example, particles without magnetocrystalline anisotropy, such as crystals embedded with spin 1/2 impurities, do not experience a magnetic torque. The right-hand side of Eq. (2.15) typically represents the magnetic torque exerted on the spins of the material, but it does not necessarily correspond to the resulting torque applied to the material containing the spins. The crystalline anisotropy is the physical element that transfers the magnetic torque from the spins to the crystal lattice.

Figure 2.12 illustrates the origin of the magnetic torque for a levitating diamond embedded with  $\text{NV}^-$  centers. The three main ingredients to understand the origin of the magnetic torque are the magnetic field  $\mathbf{B}$  (represented by a green vector), the anisotropy axis  $\mathbf{e}_3$  (represented by a black vector) and the magnetization  $\mathbf{M}$  (represented by a blue vector). The magnetic torque's origin can be understood in four phases. In phase 1, the  $\text{NV}^-$  center spin states are polarized into the  $|m_s = 0\rangle$  state. In phase 2, microwave radiation is resonantly applied to a  $|m_s = 0\rangle \rightarrow |m_s = \pm 1\rangle$  transition to polarize a magnetic state. In phase 3, the magnetization  $\mathbf{M}$  of the diamond tends to align with the magnetic field due to the magnetic torque applied to the spins. Finally, in phase 4, the diamond's anisotropy axis  $\mathbf{e}_3$  follows the magnetization, resulting in the whole diamond's angular motion. The magnetization  $\mathbf{M}$  does not fully align with the magnetic field  $\mathbf{B}$  due to the restoring torque of the Paul trap.

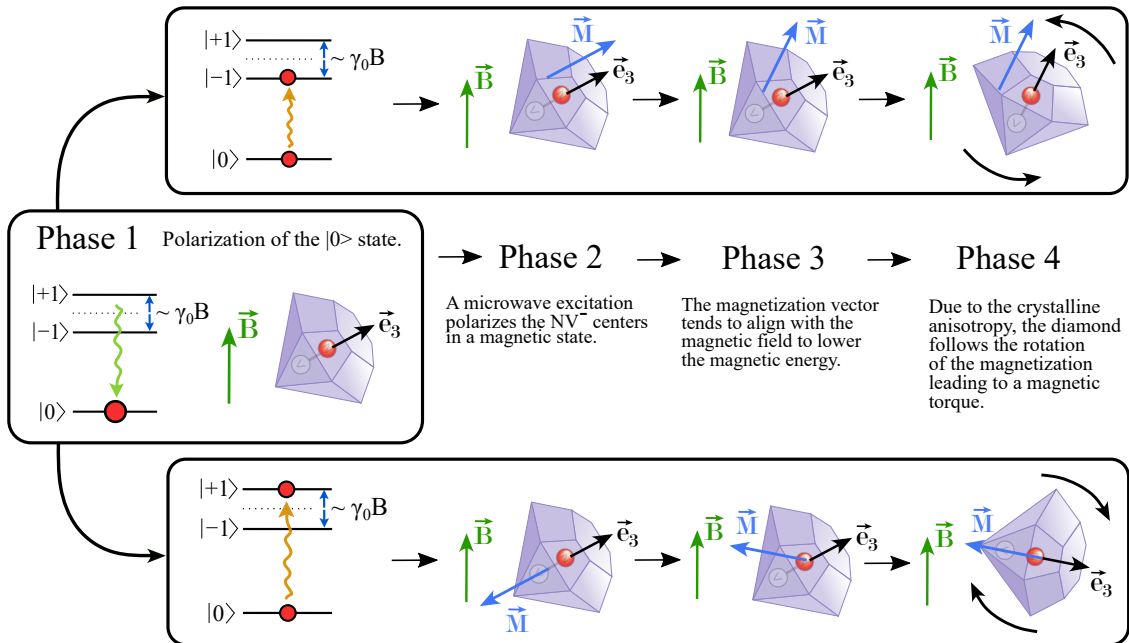


Figure 2.12: Diagram showing the origin of the magnetic torque in diamond doped with  $\text{NV}^-$  centers. Depending on the magnetic state, the  $\text{NV}^-$  spins tend to become aligned or misaligned with the magnetic field direction. The anisotropy term that induces a coupling between the spin state and the diamond orientation leads to a full rotation of the diamond explaining the origin of the magnetic torque.

In the following, we will calculate the magnetic torque exerted on the diamond. For simplicity, we will consider a single class of  $\text{NV}^-$  center in a levitating diamond. We will then treat the magnetic torque exerted on a hard ferromagnet, but the demonstration will rely on the same principles. The Hamiltonian of the Spin-Mechanical (S.M.) system for  $N$   $\text{NV}^-$  centers of a single class is as follows:

$$\hat{\mathcal{H}}_{\text{s.m.}} = \frac{\hat{\mathbf{L}}^2}{2I} + \hbar D \sum_{i=1}^N \left( \hat{S}_3^{(i)} \right)^2 - \hbar \gamma_e \mathbf{B} \cdot \left( \sum_{i=1}^N \hat{\mathbf{S}}^{(i)} \right) + U_{\text{trap}}(\hat{\alpha}, \hat{\beta}, \hat{\gamma}), \quad (2.16)$$

where  $\hat{\mathbf{L}}$  is the angular momentum operator of the diamond. The first term corresponds to the angular momentum energy. The second term corresponds to the crystalline anisotropic energy responsible for the coupling between the angular position of the diamonds and the  $\text{NV}^-$  center spin. The third term is the Zeeman splitting of the  $\text{NV}^-$  centers' spin. The last term corresponds to the restoring torque exerted by the trapping mechanism that confines the diamond.

Using the Ehrenfest theorem, the dynamic equation for the classical quantities  $\mathbf{L} = \langle \hat{\mathbf{L}} \rangle$  and  $\mathbf{S}^{(i)} = \langle \hat{\mathbf{S}}^{(i)} \rangle$  is given by

$$\frac{d\mathbf{L}}{dt} = \frac{1}{i\hbar} \left\langle \left[ \hat{\mathbf{L}}, \hat{\mathcal{H}}_{\text{s.m.}} \right] \right\rangle, \quad (2.17)$$

$$\forall i \in [1, N], \quad \frac{d\mathbf{S}^{(i)}}{dt} = \frac{1}{i\hbar} \left\langle \left[ \hat{\mathbf{S}}^{(i)}, \hat{\mathcal{H}}_{\text{s.m.}} \right] \right\rangle. \quad (2.18)$$

The calculation of the commutators is presented in Appendix B.1 and relies on the theoretical toolbox developed in (95). We obtain the following dynamic equations:

$$\frac{d\mathbf{L}}{dt} = \boldsymbol{\tau}_{\text{anis.}} + \boldsymbol{\tau}_{\text{trap}}, \quad (2.19)$$

$$\forall i \in [1, N], \quad \hbar \frac{d\mathbf{S}^{(i)}}{dt} = -\boldsymbol{\tau}_{\text{anis.}}^{(i)} + \boldsymbol{\tau}_{\text{mag}}^{(i)}, \quad (2.20)$$

where  $\boldsymbol{\tau}_{\text{anis.}} = \sum_{i=1}^N \boldsymbol{\tau}_{\text{anis.}}^{(i)}$  is the torque exerted by the  $\text{NV}^-$  centers' spins on the diamond due to the crystalline anisotropy,  $\boldsymbol{\tau}_{\text{trap}}$  is the trap restoring torque,  $-\boldsymbol{\tau}_{\text{anis.}}^{(i)}$  is the torque exerted by the diamond on the individual  $\text{NV}^-$  centers and  $\boldsymbol{\tau}_{\text{mag}}^{(i)}$  is the magnetic torque exerted on a single  $\text{NV}^-$  center. The expression of the anisotropy torque  $\boldsymbol{\tau}_{\text{anis.}}$  does not present any interest except that it is directly related to the anisotropy strength given by  $D = (2\pi) 2.87$  GHz, as expected. We give an expression for  $\boldsymbol{\tau}_{\text{anis.}}$  in Appendix B.1. The magnetic torque  $\boldsymbol{\tau}_{\text{mag}}^{(i)}$  exerted on a single  $\text{NV}^-$  center spin is as follows:

$$\boldsymbol{\tau}_{\text{mag}}^{(i)} = \hbar \gamma_e \mathbf{S}^{(i)} \times \mathbf{B}. \quad (2.21)$$

We define the total spin quantity  $\mathbf{S} = \sum_{i=1}^N \mathbf{S}^{(i)}$  and the total magnetic torque  $\boldsymbol{\tau}_{\text{mag}} = \sum_{i=1}^N \boldsymbol{\tau}_{\text{mag}}^{(i)}$ . The  $\text{NV}^-$  centers are not coupled, so we can perform a statistical averaging of the sum  $\mathbf{S} = \sum_{i=1}^N \mathbf{S}^{(i)} = N \text{Tr}(\hat{\rho}^{(i)} \hat{\mathbf{S}}^{(i)})$ . Finally, by considering a density  $d$  of  $\text{NV}^-$  centers in a volume  $V$ , we obtain  $\boldsymbol{\mu} = V\mathbf{M} = \hbar \gamma_e \mathbf{S}$ . Thus, we obtain the expected value of the magnetic torque presented in Eq. (2.15). By combining Eq. (2.19) and Eq. (2.20), we finally obtain the equation of motion for the total angular momentum of the

spin-mechanical system  $\mathbf{J} = \mathbf{L} + \hbar\mathbf{S}$ :

$$\frac{d\mathbf{J}}{dt} = \boldsymbol{\tau}_{\text{mag}} + \boldsymbol{\tau}_{\text{trap}}. \quad (2.22)$$

We now return to the case of a levitating hard magnet. The spins inside a hard ferromagnet are also subject to the same type of crystalline anisotropy as the  $\text{NV}^-$  centers' spin in diamond. Nevertheless, the spins inside a hard ferromagnet cannot be considered as independent, and they strongly interact each other. They are highly correlated and behave as a single macroscopic spin: this is the macrospin approximation. Under this approximation, the Hamiltonian of a levitating hard magnet can thus be written according to (95):

$$\hat{\mathcal{H}}_{\text{magnet}} = \frac{\hat{\mathbf{L}}^2}{2I} - \hbar D' \hat{S}'^2 + \hbar \gamma_0 \mathbf{B} \cdot \hat{\mathbf{S}}' + U_{\text{trap}}(\hat{\alpha}, \hat{\beta}, \hat{\gamma}), \quad (2.23)$$

where we designate by  $\hat{\mathbf{S}}'$  the macrospin of the magnet. The anisotropy coefficient  $D'$  for a hard magnet is extremely large and takes values that exceed  $k_{\text{B}}T$ . The hard magnet Hamiltonian is very similar to the  $\text{NV}^-$  center Hamiltonian. The calculations leading to the equations of motion are identical to the  $\text{NV}^-$  case, and the magnetic torque equals  $\boldsymbol{\mu} \times \mathbf{B}$ .

A notable difference between diamonds embedded with  $\text{NV}^-$  centers and ferromagnets comes from the contribution of the spin  $\hbar\mathbf{S}'$  in the total angular momentum  $\mathbf{J}$ . For a nanomagnet, the spin angular momentum  $\hbar\mathbf{S}'$  can even dominate the particle angular momentum, leading to interesting gyromagnetic effects. We later come back to these effects in part 2.4.

Now that we have been able to express the magnetic torque as a function of the magnetization and the external magnetic field, we can perform numerical calculations on the sensitivity of torque magnetometry.

### 2.3. Torque magnetometry with levitated magnetic particles

We now have all the necessary components to calculate the torque sensitivity to an external magnetic field for both diamonds embedded with  $\text{NV}^-$  centers and hard ferromagnets.

#### 2.3.1 Torque sensitivity with 15 $\mu\text{m}$ levitating particles at ambient pressure

The typical size of the levitating particles used in our experiment is between 5–20  $\mu\text{m}$ . For the sake of simplicity, we consider the average size of the diamonds, which is 15  $\mu\text{m}$ , and reduce the angular dynamics of the levitating particle to a one-dimensional problem, considering only the angle  $\beta$ . This approximation is well-justified since the three angular degrees of freedom are not coupled to first order, and the torque sensitivity is not affected by this simplification. We also assume that the evolution of the angular momentum  $\hbar\mathbf{S}$  carried by the spin is negligible compared to the evolution of the angular momentum of the particle  $\mathbf{L}$ , which is well-justified for particles of 15  $\mu\text{m}$ . Therefore, we consider  $\mathbf{J} \approx \mathbf{L}$  in the equation of motion. We assume that the main source of noise on the angular dynamics of a levitating magnetic particle comes from the random collisions with the gas background. For pressures greater than  $10^{-2}$  mbar, the noise due to collisions with the

gas during the angle measurement dominates the shot noise of the detection signal. At ambient pressure, the shot noise is thus negligible. Including the damping term  $\gamma_\beta$  and introducing the angular resonant frequency given by the trapping mechanism  $\omega_\beta/2\pi$ , we can write the Langevin equation:

$$I\ddot{\beta} + I\gamma_\beta\dot{\beta} + I\omega_\beta^2\beta = \tau_L(t) + \tau_{\text{meas}}(t) \quad (2.24)$$

with  $\tau_L(t)$  the Langevin torque that satisfies  $\langle \tau_L \rangle = 0$ ,  $\langle \tau_L(t)\tau_L(t') \rangle = 2\gamma_\beta I k_B T \delta(t-t')$  and  $\tau_{\text{meas}}(t) = \tau_{\text{meas}} \cos(\omega' t)$  the torque that one wishes to measure. We assume  $\tau_{\text{meas}}$  to oscillate at a frequency  $\omega'$  (the case of a constant torque is the limit  $\omega' \rightarrow 0$ ). Moving into Fourier space at a frequency  $\omega$ , we find the expression

$$\beta(\omega) = \chi(\omega)(\tau_L(\omega) + \tau_{\text{meas}}(\omega)), \quad (2.25)$$

where

$$\chi(\omega) = \frac{1}{I(\omega^2 - \omega_\beta^2 + i\gamma_\beta\omega)}. \quad (2.26)$$

The Power Spectral Density (PSD) of the angular mode  $\beta$  is equal to  $S_{\beta\beta}^{\text{total}}(\omega) = \langle |\beta(\omega)|^2 \rangle$ . Since the Langevin torque and the torque  $\tau_{\text{meas}}$  are not correlated, we can separate them as

$$S_{\beta\beta}^{\text{total}}(\omega) = |\chi(\omega)|^2 (S_{\beta\beta}^{\text{th}} + S_{\beta\beta}^{\text{meas}}) \quad (2.27)$$

The minimum torque that can be detected in a time  $t$  is given by the formula (96)

$$\tau_{\text{meas}}^{\text{min}} \sqrt{t} = \sqrt{4I\gamma_\beta k_B T} \quad (2.28)$$

Using this formula, we can estimate the torque sensitivity of our experiment. With a typical particle size of  $15 \mu\text{m}$ , the moment of inertia is on the order of  $I = 10^{-22} \text{ kg.m}^2$ . We consider that the particle is at thermal equilibrium with the ambient gas. The temperature of the angular mode is thus  $T = 300\text{K}$ . The damping coefficient  $\gamma_\beta$  can be calculated using (97) and also experimentally estimated. In our experiment, a typical damping value is  $\gamma_\beta \approx (2\pi) \times 1 \text{ kHz}$ . Substituting the numerical values gives the sensitivity of our experiment to an external torque:

$$\tau_{\text{meas}}^{\text{min}} \sqrt{t} = 10^{-19} \text{ N.m}/\sqrt{\text{Hz}} \quad (2.29)$$

We can now estimate the time required to measure the magnetic torque  $\tau_{\text{mag}}$  on levitating magnetic particles in our experiment.

### 2.3.2 Torque detection of $\text{NV}^-$ centers magnetic resonance

In order to determine the sensitivity of the torque magnetometry with levitating diamonds, we first need to estimate the value of the magnetic torque in our experiment. The magnetic torque is given by the formula  $\tau_{\text{mag}} = \boldsymbol{\mu} \times \mathbf{B}$ . It depends on the strength of the external magnetic field  $\mathbf{B}$  as well as the total magnetic moment  $\boldsymbol{\mu}$  of the particle. The optical pumping and read-out of the  $\text{NV}^-$  center spin state are decreased when the

external magnetic field has a transverse component to the anisotropy direction that is typically stronger than 10 mT. We thus assume that the magnetic field strength remains below 10 mT in the following of this part.

In a presence of a microwave field  $\mathbf{B}_{\mu w}(t)$  driving the  $NV^-$  resonances  $|m_s = 0\rangle \rightarrow |m_s = \pm 1\rangle$ , the magnetic momenta  $\boldsymbol{\mu}$  can be estimated using Eq. (1.48):

$$\boldsymbol{\mu} = VM_3(\omega_{\mu w})\mathbf{e}_3. \quad (2.30)$$

When  $\mathbf{B}$  is aligned with  $\mathbf{e}_3$ , there is no magnetic torque because the vector product between  $\boldsymbol{\mu}$  and  $\mathbf{B}$  equals zero. We thus assume that the magnetic field and the anisotropy axis are not aligned. We can estimate the magnetic torque:

$$\tau_{\text{mag}} \approx VM_3(\omega_{\mu w})B. \quad (2.31)$$

The magnetic torque is maximized when the microwave is resonant with a  $NV^-$  transition i.e. when  $\omega_{\mu w} = \omega_{NV}$ . For a 15  $\mu\text{m}$  diamond from the Adamas company with a concentration of  $NV^-$  centers around 3.5 ppm and for a magnetic field  $B \approx 10$  mT, we find that the magnetic torque equals:

$$\tau_{\text{mag}} \approx 10^{-17} \text{ N.m.} \quad (2.32)$$

According to the torque sensitivity given by the formula Eq. (2.29), the typical time required to detect the magnetic torque equals:

$$t_{\text{mag}}^{\text{meas}} = 100 \mu\text{s}. \quad (2.33)$$

This characteristic time value is rather low. It allows us to perform torque detected magnetic resonances of the  $NV^-$  center spins on small time scales.

In Fig. 2.13, we present four torque-detected magnetic resonance spectra for different levitating diamonds using the back-scattered light detection scheme described in part 2.1.4. In the following, we use the terminology MDMR for Mechanically Detected Magnetic Resonance to designate these spectra. When a  $NV^-$  center spin resonance is driven, the magnetic torque applied on the diamond leads to a new stable angular position, resulting in a signal modification in our measurement signal. Apart from the MDMR presented in Fig. 2.13 (b) where eight resonance peaks clearly detach from the background noise, it is quite common not to mechanically detect the eight  $NV^-$  resonances. Multiple reasons can be invoked. The detection may not be sensitive to angular displacement of the diamond along certain axes. It can also be due to the fact that a  $NV^-$  center class can be aligned with the magnetic field direction, which suppresses the magnetic torque.

As with the ODMR spectroscopy technique, MDMR allows us to determine the relative angle of the diamond with respect to the magnetic field direction as well as the magnetic field strength  $B$ . It is worth noting that it is not necessary to see all eight resonances of the four  $NV^-$  classes to obtain quantitative informations on the magnetic field. We use this highly sensitive technique in Chapter 4 to characterize the Van Vleck diamagnetism of the  $NV^-$  center by measuring the angle between a  $NV^-$  center class and the magnetic field direction.

Usual  $NV^-$  center magnetometry techniques make use of the sensitivity of the photo-

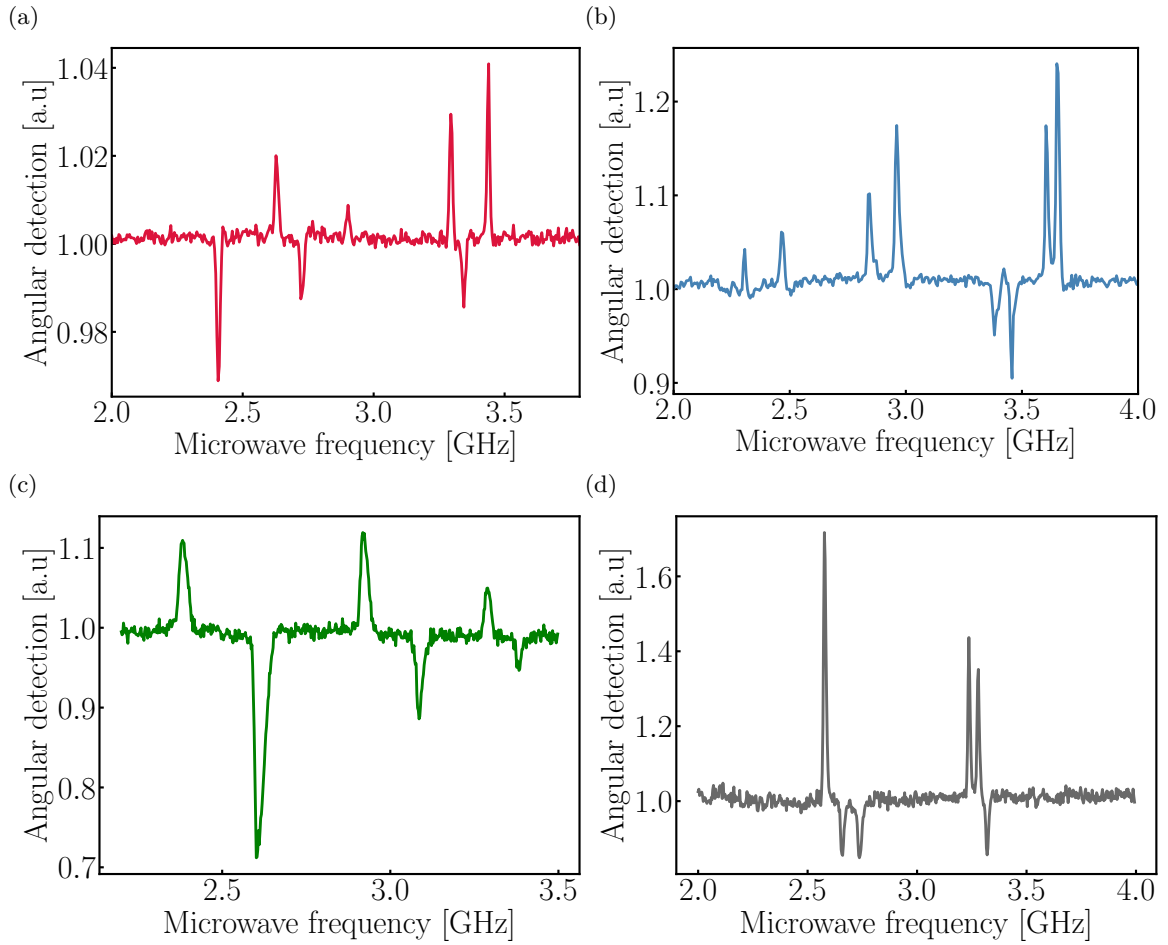


Figure 2.13: (a) (b) (c) (d) Angular displacement of a levitating diamond highly doped in  $\text{NV}^-$  centers as a function of the microwave frequency averaged for several seconds.

luminescence signal to an external magnetic field perturbation while a microwave is driven on the slope of a  $\text{NV}^-$  center magnetic resonance. The evolution of the photoluminescence signal enables to measure whether the magnetic field increases or decreases. As explained in Fig. 2.14 (a), if the magnetic field strength  $\delta B$  increases, then the resonance shifts on the left leading to an increase of the total  $\text{NV}^-$  photoluminescence. Conversely, a decrease in the magnetic field strength  $\delta B$  will shift the resonance to the right, leading to a decrease in the photoluminescence. The width of the magnetic resonance is limited by the  $T_2^*$  time. The steeper the slope, the better the magnetometer. Thus, the quality of the samples is crucial in  $\text{NV}^-$  center magnetometry.

In Fig. 2.14 (b), we plotted a MDMR signal for a single  $\text{NV}^-$  transition. The magnetometry protocols that makes use of the photoluminescence signal could also work using the mechanical detection signal. Further investigations will be conducted soon to estimate the sensitivity of this mechanical magnetometer.

### 2.3.3 Torque magnetometry using levitating ferromagnets

Compasses have been used for centuries to detect the direction of the Earth's magnetic field. A levitated ferromagnet can be thought of as a microscopic compass that levitates.

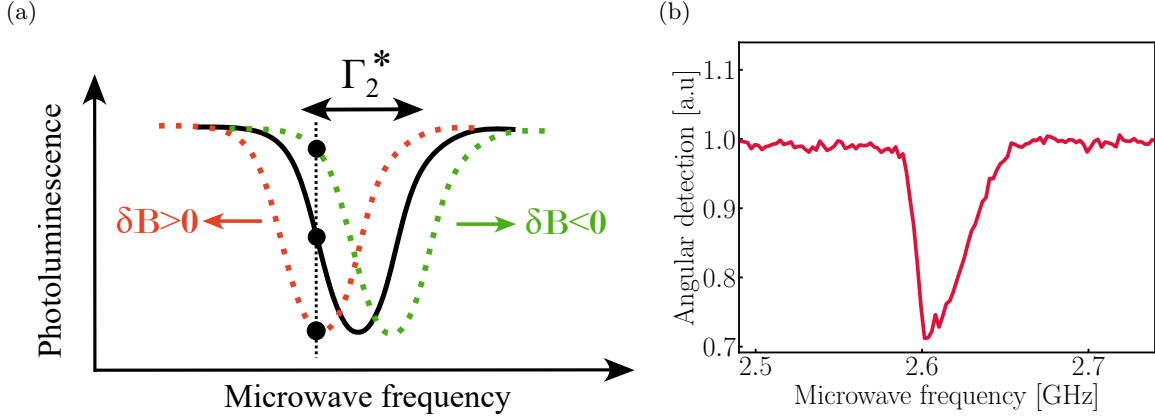


Figure 2.14: (a) Photoluminescence modification of the  $\text{NV}^-$  transition  $|m_s = 0\rangle \rightarrow |m_s = -1\rangle$  with an external magnetic field perturbation  $\delta B$ . (b) Asymmetrical MDMR of a single  $\text{NV}^-$  center spin transition.

By using the formula in Eq. (2.29), we can estimate the sensitivity to a small magnetic field  $\delta B$  of a hard magnet levitating at ambient pressure:

$$\delta B \sqrt{t} = \frac{\mu_0 \sqrt{4I\gamma\beta k_B T}}{B_{\text{sat}} V} \approx 100 \text{ pT}/\sqrt{\text{Hz}}, \quad (2.34)$$

where  $\mu = V \frac{B_{\text{sat}}}{\mu_0}$  with  $B_{\text{sat}}/\mu_0$  the magnetization at saturation on the order of 1 T.

A few remarks can be made about this formula. First, the sensitivity of this magnetometer is size-dependent. The ratio  $\sqrt{I}/V$  depends on the inverse of the square root of the radius. Reducing the size of the levitated magnet can increase the sensitivity of this magnetometer. Additionally, lowering the pressure in the vacuum chamber will also enhance the sensitivity of this magnetometer. For example, working at a pressure of  $10^{-3}$  mbar would already lead to a sensitivity below  $1 \text{ pT}/\sqrt{\text{Hz}}$ . However, working with levitated particles at lower pressures can be challenging because external heating sources, such as a laser light focused on the particle, are no longer dissipated through gas collisions. This often leads to the loss of the particle.

Levitated magnetic particles are thus a platform that could be further explored to perform highly sensitive magnetometry.

In the next section, we explore the intriguing physics of the gyromagnetic effects that have yet not been observed with levitating magnetic particles. These effects could lead to several applications and notably in magnetometry.

## 2.4. Gyromagnetic effects in levitating magnetic micro/nanoparticles

The dynamics of systems carrying magnetic moments differ greatly between the macroscopic and the microscopic world. In Fig. 2.15 (a), a compass subjected to an external magnetic field naturally librates (i.e. oscillates) around the equilibrium position given by the magnetic field direction. On the other hand, the magnetic moment of a trapped neutral atom represented in Fig. 2.15 (b) freely precesses around the magnetic field direction. Despite the apparent difference between these two systems, they both carry a mass

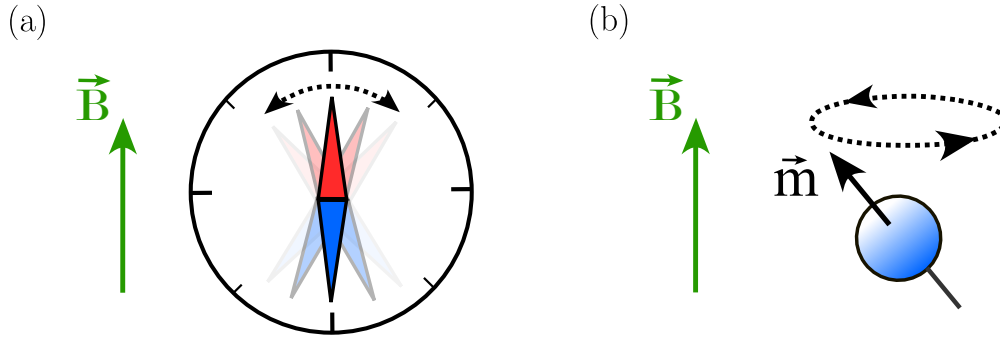


Figure 2.15: (a) A compass librates i.e. oscillates around the equilibrium position given by the magnetic field direction. (b) A magnetic atom precesses around the external magnetic field.

and a magnetic moment that scale the same way with respect to the size. In order to explain why the angular dynamics differs, we consider the total angular momenta  $\mathbf{J}$  of the system, which is the relevant quantity governing the system dynamics. As shown in the previous section,  $\mathbf{J}$  is the sum of the spin angular momentum  $\hbar\mathbf{S}$  and the particle angular momentum  $\mathbf{L}$ . The spin angular momentum scales with the third power of the system size while the particle angular momentum scales with the fifth power. The proportion of each contribution to the total angular momentum of the system thus depends on the size of the system. The dynamics of the angular momentum is therefore size-dependent, as we can see with the compass and the atom examples. The levitation of micro/nano magnetic particles allows for the study the angular dynamics at a mesoscopic scale where both librating and precessing dynamics occur.

In this section, we show how gyromagnetism affects the dynamics of a levitating magnetic particle, particularly at a scale where the spin angular momentum dominates the particle angular momentum. To do so, we introduce the law of conservation of angular momentum and provide a reminder on the historical Einstein-de Haas experiment (47) which proves that spins carry angular momentum. We then derive the dynamic equation of motion for a hard magnet in the presence of a magnetic field, showing the existence of two size-dependent dynamic angular regimes: the libration and the precession regimes. We also provide perspectives that motivate the experimental observation of the precession regime with a levitating magnet. Finally, we conclude this section by highlighting the ability to stably rotate levitating particles and giving two possible applications that have not been observed with levitating magnetic nanoparticles: the Levitron and the Barnett effect (48).

#### 2.4.1 Total angular momentum conservation: the Einstein-de Haas effect

The angular dynamics of a magnetic system can be strongly affected by the angular momentum carried by the spin. To properly understand the effect of gyromagnetism on levitating magnetic particle, we focus our attention on the law of conservation of total angular momentum. We illustrate this conservation law using the Einstein-de Haas experiment.

**The angular momentum conservation**

In section 2.2.2, we prove the conservation law of the total angular momentum  $\mathbf{J}$  for a freely floating magnetic particle i.e. a magnetic particle that is not subjected to external torque:

$$\frac{d\mathbf{J}}{dt} = 0. \tag{2.35}$$

The total angular momentum  $\mathbf{J}$  can be decomposed in two components. The first component is the rotational angular momentum  $\mathbf{L}$  of the rigid particle, which equals the product of the moment of inertia  $I$  and the instantaneous rotational vector  $\boldsymbol{\omega}$ . The second component is the angular momentum carried by the spins of the particle, which equals  $\hbar\mathbf{S} = \hbar \sum_{i=1}^N \mathbf{S}^{(i)}$  where  $\mathbf{S}^{(i)}$  are the spin value for each spin inside the magnetic particle. The total angular momentum conservation law can also be written:

$$\mathbf{L} + \hbar\mathbf{S} = \text{constant}. \tag{2.36}$$

The magnetic moment  $\boldsymbol{\mu}$  and the angular momentum of the spin are related by the gyromagnetic constant  $\boldsymbol{\mu} = V\mathbf{M} = \hbar\gamma_e\mathbf{S}$ . The total angular momentum conservation law can also be interpreted as a torque exerted on the particle that depends on the derivative of the magnetization  $\boldsymbol{\mu}$ . The dynamic equation of the particle's angular momentum then reads:

$$\frac{d\mathbf{L}}{dt} = \boldsymbol{\tau}_{\text{E.d.H.}} \quad \text{with} \quad \boldsymbol{\tau}_{\text{E.d.H.}} = -\frac{1}{\gamma_e} \frac{d\boldsymbol{\mu}}{dt}. \tag{2.37}$$

An experiment that allows to observe the angular momentum conservation consists in reversing the magnetic moment  $\boldsymbol{\mu}$  and observing a change in the particle angular momentum  $\mathbf{L}$ . One has to be extremely careful not to add any extra angular momentum to the system during the spin inversion. This experiment has been performed by Einstein and de Haas and is explained in the following part.

**The Einstein-de Haas experiment (1915)**

The transfer of angular momentum from the spin to the particle angular momentum was observed for the first time by Einstein and de Haas in 1915<sup>1</sup>. In Fig. 2.16, we show a simplified version of the experimental set-up used by Einstein and de Haas. The set-up consists of a soft ferromagnetic bar suspended on a thin string that is placed inside a cylindrical coil. The coil generates a uniform magnetic field that can be inverted by reversing the current in the coil. The magnetic field generated by the coil is always aligned with the easy axis of magnetization of the soft ferromagnetic bar. The magnetization of the bar is therefore always aligned with the magnetic field generated by the coil. There is thus no magnetic torque applied on the bar. The total angular momentum of the system is therefore conserved.

Figure 2.16 depicts the motion of the magnetic bar before and after reversing the magnetic field generated by the coil. The magnetization of the magnet is reversed, which results in a reversal of the angular momentum carried by the spin. As a result of the conservation of angular momentum, the magnet rotates at twice the Einstein-de Haas

---

<sup>1</sup>This experiment is remarkable since it is widely considered to be the only experiment performed by Einstein.

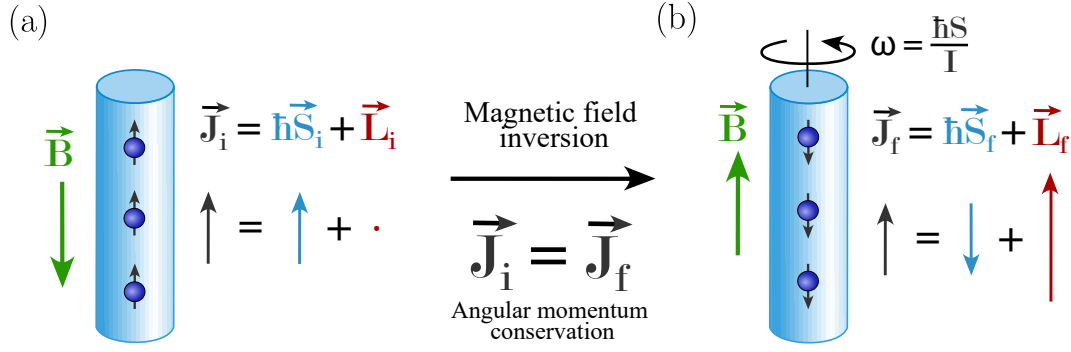


Figure 2.16: (a) Schematic picture of a freely floating soft magnet in a presence of a magnetic field  $\vec{B}$  generated by a coil oriented in the easy magnetization axis of the magnet. The magnet has no initial angular momentum  $\vec{L}_i = 0$  but carries an initial spin angular momentum  $\hbar\vec{S}_i \neq 0$  due to the presence of a magnetic field. (b) Schematic picture of a rotating soft magnet due to the angular momentum transfer from the spin to the particle.

(EdH) angular velocity  $\omega_I$ , which is given by:

$$\omega_I = \frac{\hbar N}{I} \quad (2.38)$$

where  $N$  is the number of inverted spins. The angular velocity  $\omega_I$  depends on the inverse of the square of the magnetic bar radius because of the ratio  $N/I$ . Considering a magnetic sphere of radius  $r$ , we can express the EdH angular velocity  $\omega_I$  as a function of the spin volumic density  $\rho_s$  and the density  $\rho_m$ . We obtain:

$$\omega_I = \frac{5}{2} \frac{\hbar \rho_s}{r^2 \rho_m}. \quad (2.39)$$

Considering a magnetic bar of length 10 cm, a magnetic field  $B \approx 1$  mT, a ferromagnetic susceptibility  $\chi = 10^2$ , the resulting angular velocity equals:

$$\omega_I = 10^{-6} \text{ rad.Hz}. \quad (2.40)$$

This value is relatively small, so experiments must be done carefully in order to effectively measure the motion induced by the conservation of angular momentum. In (98), it has been shown that the magnetic torque arising from the Earth's magnetic field can have a mechanical impact that is  $10^7$  times larger than the Einstein-de Haas effect. Magnetic shielding and compensation of ambient magnetic noise is thus a key requirement to perform this experiment. One can therefore question if the few videos on the internet claiming to reproduce the original Einstein-de Haas experiment are actually showing a rotation induced by the conservation of angular momentum rather than by residual magnetic torque.

The angular velocity  $\omega_I$  increases with decreasing size of the magnet due to the size scaling law. This makes the levitation of micro/nanomagnets an attractive option for performing the Einstein-de Haas experiment. For a soft magnet of 1  $\mu\text{m}$  diameter, the rotation induced by the angular momentum transfer is roughly 10 rad.kHz, which is a

measurable value. However, the magnetic torque also increases for smaller magnetic particles making it challenging to distinguish the Einstein-de Haas torque from the magnetic torque.

K. Mori et al. (2020) (94) successfully reproduced the Einstein-de Haas experiment using a ferrimagnetic microresonator made of Yttrium Iron Garnet (YIG). They were able to differentiate the Einstein-de Haas torque from the magnetic torque by using an oscillating magnetic field and analyzing the phase of the mechanical response.

### 2.4.2 From the compass to the magnetic atom dynamics

In the previous section, we have seen how a change of magnetization can induce rotation due to the angular momentum conservation law and how decreasing the size of the magnet increases the impact of the spin transfer into rotation. In this section, we return to the compass and atom example discussed in the introduction of this section and demonstrate the existence of two dynamic regimes, depending on the particle size: the librating regime and the precessing regime. In a second time, we present an analogy between the physics of a hard magnet precessing in a magnetic field and a spinning top in a gravitational field. Finally, we show potential applications of gyromagnetic effects, such as performing quantum levitation or making a magnetometer with sensitivity below the Standard Quantum Limit (SQL).

#### The librating and precessing regime in a presence of a magnetic field

In this part, we will examine the experiment depicted in Fig. 2.17 (a), which shows a hard ferromagnet subjected to an external magnetic field. We will calculate the angular dynamics of the magnet, taking into account the contribution of the internal spins to the total angular momentum. Our goal is to demonstrate that the system exhibits two dynamic regimes: the librating and the precessing regimes. We will assume that the center of mass is fixed and decoupled from the angular dynamics, and that the only external torque applied to the particle is the magnetic torque, given by  $\tau_{\text{mag}} = \hbar\gamma_e \mathbf{S} \times B\mathbf{e}_z$ .

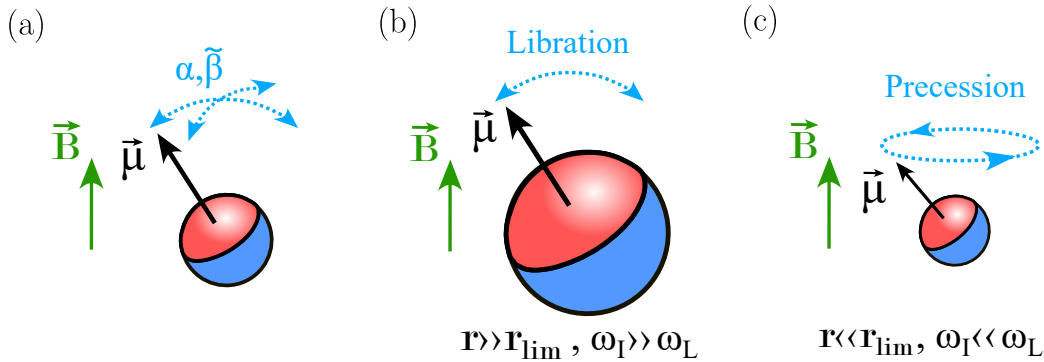


Figure 2.17: (a) Angular parametrization of a hard magnet. (b) Hard magnet in the librating regime. (c) Hard magnet in the precessing regime.

For a hard magnet, the direction of the magnetic moment  $\mu$  is fixed in the particle frame. Furthermore, the magnetic moment norm  $|\mu|$  is constant. Thus, the macrospin vector  $\mathbf{S}$  can simply be re-expressed as  $\mathbf{S} = -\hbar N \mathbf{e}_3$  where  $\mathbf{e}_3$  verifies the relation  $\dot{\mathbf{e}}_3 = \boldsymbol{\omega} \times \mathbf{e}_3$  with  $\boldsymbol{\omega} = \mathbf{L}/I$  the instantaneous rotation vector. We thus obtain a dynamic equation for the spin orientation  $\mathbf{S}$ . Adding the two dynamic equations of angular momentum, we

obtain the set of coupled equations:

$$\frac{d\mathbf{J}}{dt} = \omega_L \hbar \mathbf{S} \times \mathbf{e}_z, \quad (2.41)$$

$$\frac{d\hbar \mathbf{S}}{dt} = -\omega_I \mathbf{L} \times \mathbf{e}_3. \quad (2.42)$$

with  $\omega_L = -\gamma_e B$  the larmor pulsation and  $\omega_I = \hbar N/I$  the E.d.H. angular velocity. Using the angular convention defined in Fig. 2.17 (a), we can derive the dynamic angular equations in the regime of small angular displacement around the magnetic field axis (see Appendix B.2 for the calculation):

$$\ddot{\alpha} = -\omega_L \omega_I \alpha - \omega_I \dot{\beta}, \quad (2.43)$$

$$\ddot{\beta} = -\omega_L \omega_I \tilde{\beta} + \omega_I \dot{\alpha}. \quad (2.44)$$

The first term in the right-hand side of the first equation that depends on  $\omega_L \omega_I$  comes from the magnetic torque, and the second term in  $\omega_I$  is from the angular momentum nature of the spin. The coupled differential equations, Eq. (2.44) are stable if and only if:

$$\omega_L > -\frac{1}{4} \omega_I \quad (2.45)$$

We can distinguish two regimes of stability, which are presented in Fig. 2.17 (b) and (c). When  $\omega_L \gg \frac{1}{4} \omega_I$ , the angular dynamics due to the magnetic field torque dominates the dynamics arising from the angular momentum conservation. In this case, the magnet dynamics consists of strong libration motion at the pulsation  $\sqrt{\omega_L \omega_I}$  and a small precession motion at the frequency  $\omega_I$ : this is the libration regime. In the case where  $|\omega_L| \ll \omega_I$ , the angular motion of the magnet consists of two precession motions: a slow precession at  $\omega_L$  as for a magnetic atom and a small and quicker precession motion at  $\omega_I$ . This regime is called the precession regime. The comparison between  $\omega_L$  and  $\omega_I$  can be reformulated by introducing the magnet radius  $r$  and the limit radius  $r_{\text{lim}}$  that equals:

$$r_{\text{lim}} = \sqrt{\frac{\hbar \rho_s}{\rho_m \gamma_0 B}}. \quad (2.46)$$

When  $r \gg r_{\text{lim}}$ , the magnet exhibits a libration motion similar to that of a compass. When  $r \ll r_{\text{lim}}$ , the magnet exhibits a precession motion similar to that of an atomic magnetic moment.

Under the condition  $|\omega_L| \ll \omega_I$ , the magnet can be angularly stable even if the magnetic moment  $\boldsymbol{\mu}$  is opposed to the direction of the magnetic field  $\mathbf{B}$ . In this regime, the equations of motion of the magnet are similar to those of a spinning top. In Fig. 2.18 (a), a spinning top is spinning along the  $\mathbf{e}_3$  axis. Due to the laws of angular momentum and energy conservation, the top is angularly stable, even though it would be expected to tip due to the gravitational field. In Fig. 2.18 (b), the magnetic field tends to reverse the direction of the magnetic moment. However, the angular momentum carried by the spin acts as if the magnet was spinning on its own, and can stabilize the magnet in this angular position due to gyromagnetism. Due to the laws of angular momentum and energy conservation, the magnet stably precesses around the magnetic field.

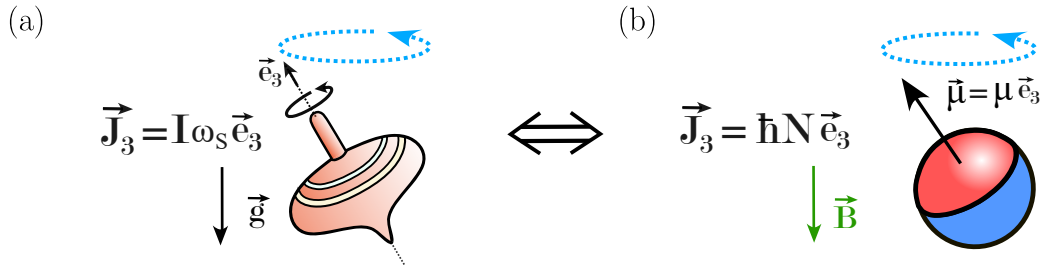


Figure 2.18: (a) Precession motion of a spinning top in a presence of the gravity field that tends to turn the spinning top. (b) Precession motion of a hard magnet in a presence of a magnetic field that tends to turn the hard magnet.

### Magnet in the precessing regime: perspectives

In the previous part, we demonstrated that a sufficiently small hard magnet has the same dynamic as a precessing atomic spin. Optical atomic magnetometers that make use of the precession motion of paramagnetic atoms are known to be the most precise magnetometers, reaching sensitivities close to  $\delta B \approx 10^{-12} \text{ G} \cdot \sqrt{\text{Hz}}$  (99; 100; 101). This value is only one order of magnitude beyond the Standard Quantum Limit (SQL) (102; 103; 104). The sensitivity of such a system is ultimately limited by the decoherence rate of each individual atom. For uncorrelated systems such as for a cloud of paramagnetic atoms, the phase measurement that is directly related to the magnetic field depends on the inverse of the square root of the number of atoms. However, highly correlated systems such as spins in a ferromagnetic material are protected from individual dephasing due to the strong coupling between the spins. The sensitivity of such system to magnetic fields is thus better than for uncorrelated systems such as paramagnetic atoms.

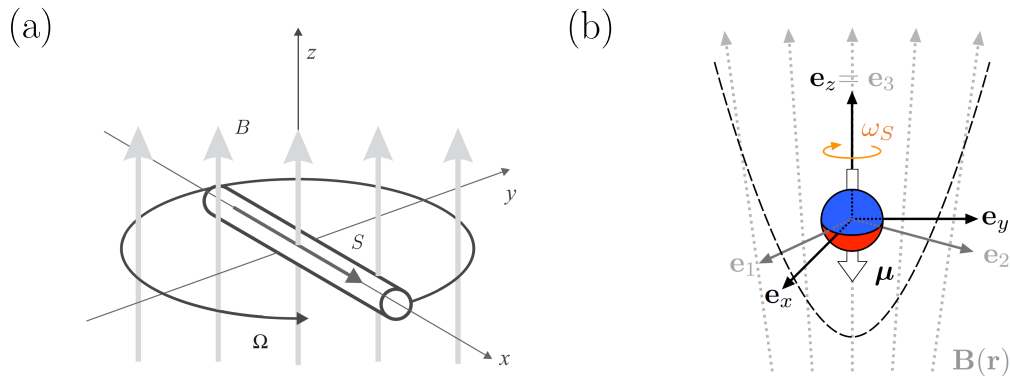


Figure 2.19: (a) Schematic picture of a precessing hard magnet that precesses due to an external magnetic field which makes it a highly sensitive magnetometer. Taken from (45) (License RNP/24/FEB/075324). (b) Schematic picture of the quantum levitation of a magnet in a Ioffe Pritchard trap. Taken from (95) (License RNP/24/FEB/075325).

A levitating precessing magnet such as the one depicted in Fig. 2.19 (a) is thus an ideal system to perform magnetometry since the spins inside the magnet are highly correlated. This idea was proposed by D.J. Kimball et al. in (45). By using a cryogenic environment and a  $10 \mu\text{m}$  long levitating cylindrical ferromagnet, the sensitivity of the system could

potentially reach as low as  $\Delta B_Q \approx 10^{-20} \text{ G}\cdot\text{Hz}^{\frac{3}{2}}$ , which is significantly below the Standard Quantum Limit (SQL). This highlights the potential of levitating micro/nano magnets for research in this field.

Another intriguing perspective is quantum levitation using a static magnetic field. The Earnshaw theorem forbids classical levitation of magnets using a static field. However, this theorem does not take into account the angular momentum carried by the spin. C.C. Rusconi et al. proposed in (95; 105; 106) to levitate a hard nanomagnet in a Ioffe Pritchard Trap (IOP). Figure 2.19 (b) shows a schematic picture of quantum stabilized magnetic levitation.

These two applications are interesting as they make use of the quantum nature of the spin, either to create an extremely sensitive magnetometer or to perform quantum levitation. Reaching the precessing regime is a key requirement for these two protocols, which motivates the experimental study of micro/nanomagnets levitation.

### 2.4.3 Pseudo magnetic field in rotating frame: the Barnett effect

One of the great interests of levitating micro/nano particles is the ability to rotate them at high speeds. Rotation of levitated particles can be achieved using circularly polarized lasers (107; 108; 109), rotating electric fields (110; 111; 112) or electric field vortices (113). The small moment of inertia of nano particles allow for rotation in the GHz frequency range (108; 109). This far exceeds the maximum rotation values in the tens of kHz for clamped systems, which are ultimately limited by mechanical and magnetic noises from the motor.

Previously, we discussed how a change in the magnetization of a magnetic particle induces mechanical rotation due to the conservation of angular momentum. The Einstein-de Haas effect has a reverse effect, known as the Barnett effect, which states that the rotation of a magnetic particle leads to magnetization of the particle. It is due to the appearance of a pseudomagnetic field in the rotating frame that directly depends on the rotation speed. In this part, we will explain the origin of the Barnett effect and demonstrate how the fast rotation of levitating magnetic particles, such as diamonds embedded with  $\text{NV}^-$  centers, are promising for observing the Barnett effect.

#### The Barnett effect

It is well known that the fundamental principles of dynamics are affected when moving into non-inertial frames. A rotating frame at a constant speed  $\omega_s$  is an example of non-inertial frame in which centrifugal and Coriolis forces occur. Similarly, electron spins are composed of an angular momentum that is also affected when moving into a non-inertial frame. In Fig. 2.20 (a), we consider a freely floating magnetic particle rotating at  $\omega_s = \omega_s \mathbf{e}_z$ , such as a diamond. Unlike a static magnetic particle, the direction of the spins rotates during the particle rotation. Due to the angular momentum conservation law in the laboratory frame, this change in direction of angular momentum must be compensated by a torque.

Considering the laboratory frame (R) where  $\mathbf{J}$  is conserved and the rotating frame (R'), we have:

$$0 = \left. \frac{d\mathbf{J}}{dt} \right|_{(R)} = \left. \frac{d\mathbf{J}}{dt} \right|_{(R')} + \boldsymbol{\omega}_s \times \mathbf{J} \quad (2.47)$$

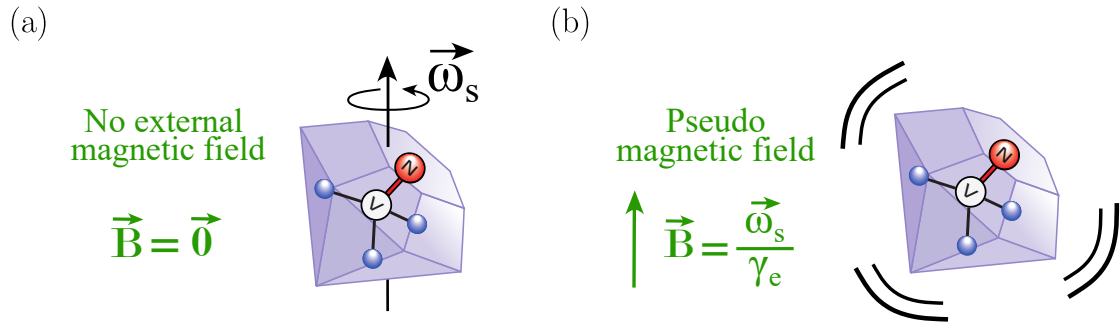


Figure 2.20: (a) Rotating diamond in the laboratory frame in the absence of external magnetic field. (b) Angularly stable diamond in the rotating frame feeling a pseudo magnetic field due to the Barnett effect.

By developing the right-hand side, we have the equality in the rotating frame:

$$\left. \frac{d\mathbf{J}}{dt} \right|_{(R')} = \boldsymbol{\tau}_{\text{classic}} + \boldsymbol{\tau}_{\text{Barnett}}, \quad (2.48)$$

where  $\boldsymbol{\tau}_{\text{classic}}$  is the classical torque in inertial frame and  $\boldsymbol{\tau}_{\text{Barnett}}$  is the torque due to the Barnett effect. These two torques equal:

$$\boldsymbol{\tau}_{\text{classic}} = -\boldsymbol{\omega}_s \times \mathbf{L}, \quad (2.49)$$

$$\boldsymbol{\tau}_{\text{Barnett}} = \boldsymbol{\mu} \times \mathbf{B}_s \quad \text{with} \quad \boldsymbol{\omega}_s = \gamma_e \mathbf{B}_s. \quad (2.50)$$

The classical torque  $\boldsymbol{\tau}_{\text{classic}}$  causes gyroscopic effects such as the gyroscopic confinement, while the Barnett torque is a result of the generation of a pseudo magnetic field  $\mathbf{B}_s$  in the rotating frame, as shown in Fig. 2.20. The induced Larmor frequency equal to the rotation speed  $\omega_s$ .

### Perspectives

The Barnett effect has already been observed with nuclear (114) and electron spins, such as  $\text{NV}^-$  centers (115), in clamped systems that rotate around 10 kHz. In these experiments, the generated pseudo magnetic fields did not exceed  $1 \mu\text{T}$ , but the extreme sensitivity of  $\text{NV}^-$  centers spin resonance to small magnetic field allows them to be detected. Another interesting effect that arises in a rotating frame is the accumulation of a quantum geometric phase, namely the Berry phase, which has been observed with rotating  $\text{NV}^-$  centers (46). The influence of the Barnett effect and the quantum geometric phase depends crucially on the rotation speed, but reaching rotation speed that exceeds 10 kHz is challenging for clamped systems. Rotation of levitated particles can overcome this issue.

## 2.5. Conclusion

In this chapter, we reviewed the experimental setup that we used to levitate magnetic microparticles. Specifically, we explained the principle of the Paul trap, how we load particles into the trap, and how we detect their motion. Next, we discussed the origin of the magnetic torque for anisotropic magnetic crystals and showed how torque detection using magnetic resonance can be used to measure magnetic fields. Lastly, we emphasized

the importance of levitating magnetic micro/nanoparticles by explaining the gyromagnetic effects that occur at this size scale.



## Chapter 3: Hard magnet levitation using a magnetic Paul trap

---

As discussed in the previous chapter, micro/nanoscale levitated ferromagnetic particles are ideal candidates for magnetometry with a precision below the Standard Quantum Limit (45) as well as for quantum levitation (116; 105). The development of new experimental techniques for magnetic levitation of micro/nano magnets is therefore particularly topical. In this chapter, we recall a magnetic levitation technique based on alternating magnetic fields, a magnetic Paul trap, and show that this technique has many advantages compared to the usual levitation techniques.

Firstly, the different magnetic levitation techniques are recalled, as well as their advantages and disadvantages. We then develop the theory of magnetic Paul traps and propose a robust and flexible on-chip trap design that is perfectly feasible with current technologies. Finally, we experimentally realize a test-bed version of a magnetic Paul trap. We notably uncover the role played by the particle size. This levitation technique seems promising to perform spin-mechanical experiments with micrometric magnets coupled to  $NV^-$  centers (93) or to observe gyromagnetic effects (45; 117).

### 3.1. Hard magnet levitation

In this section, a fundamental theorem, the Earnshaw's theorem, is invoked which prohibits the magnetic levitation of magnets under certain assumptions. We will introduce several commonly used magnetic levitation techniques that do not fulfill the conditions of Earnshaw's theorem.

#### 3.1.1 The magnetic Earnshaw's theorem

In this part, we discuss an important theoretical result that strongly constrains the levitation of hard magnets using magnetic fields: the Earnshaw's theorem. We remind that a hard magnet is a particle that carries a constant magnetic moment  $\mu$  that is fixed in the body frame. This theorem can be enonciated as follow (118):

*Earnshaw's Theorem:* a purely magnetic levitation of a hard magnet is not possible if the three following conditions are fulfilled:

- the trapping magnetic field is permanent (this excludes induced magnetic fields).
- the hard magnet is not rotating.
- the angular momentum carried by the spin can be neglected.

We do not demonstrate this theorem here but we give examples showing that levitation is possible if at least one of these assumptions is not verified.

The first assumption stipulates that the magnetic field of the trap is permanent. Magnets can indeed levitate in magnetic trap made of diamagnetic material such as superconducting material and also in dynamic trap such as the magnetic Paul trap.

The second assumption stipulates that the levitated magnet is not rotating. A rotating magnet can indeed levitate in a special configuration of the magnetic field: this is the Levitron.

The third assumption stipulates that the angular momentum of the spin can be neglected. It is indeed possible to use the angular momentum of the spins to levitate a hard magnet (116; 105). We have already discussed this quantum levitation technique in Chapter 2 and we do not come back on these theoretical proposals in this section.

In the following, the previously mentioned magnetic levitation techniques are briefly reviewed, explaining the advantages and disadvantages they may have.

### 3.1.2 Magnetic levitation of magnet

In this section, various techniques of magnetic levitation of permanent magnets are briefly recalled.

#### Diamagnetic levitation

One of the most common levitation techniques is levitation using materials that repel the magnetic field, i.e. diamagnetic materials. A diamagnetic material generates a magnetic field so that it opposes to the external magnetic field. If the external magnetic field is generated by a magnet, the diamagnetic material exerts therefore a repulsive force on the magnet. Thus, a magnet can levitate between diamagnetic materials on this principle (119).

The magnetic response of diamagnetic materials is often weak and the diamagnetic susceptibility of materials at room temperature is less than  $\chi = 10^{-4}$ . However, at low temperature, some materials have the exceptional property of becoming superconducting and have the particularity of completely repelling the magnetic field. The magnetic susceptibility of these materials equals  $\chi = -1$  (120; 121; 122; 123; 124).

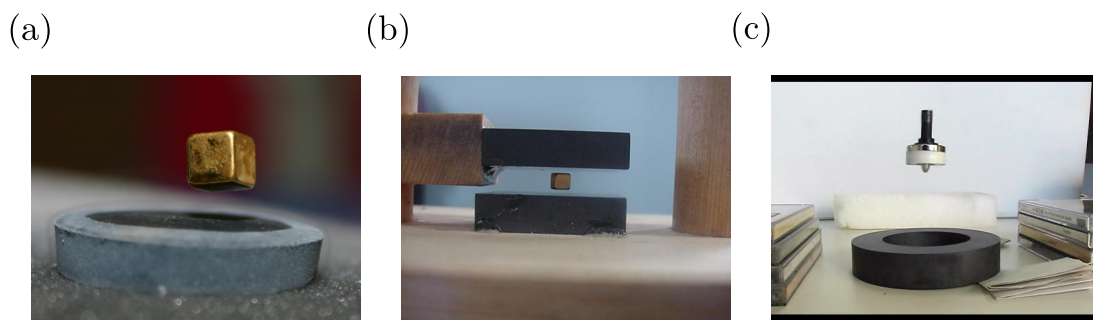


Figure 3.1: (a) Levitation of a magnet over a superconducting material. Taken from Wikiledia (free to share, Peter Nussbaumer). (b) Levitation of a magnet between two diamagnetic plates. Note that the magnetic field gradient applied to compensate for gravity is not shown in the picture. Taken from Instructables workshop website. (c) A Levitron toy: levitation of a rotating magnet above a magnet. Taken from Supermagnete website.

In Fig. 3.1 (a), a cubic Neodymium magnet is shown to be levitating above a superconducting material that has been previously cooled below the critical temperature  $T_c$ . The superconducting material generates electric currents on the surface which produces a

magnetic image of the magnet that repels it. Figure 3.1 (b) shows a Neodymium magnet levitating between two graphite plates which are among the best diamagnetic materials at room temperature. Due to the low intensity of the diamagnetism, a magnet located further above (not shown in the picture), is needed to compensate the gravitational field.

These two passive levitation techniques are very stable but do not allow to reach confining frequencies of mechanical modes beyond one kilohertz and are thus susceptible to low frequency noises. Furthermore, the superconductivity levitation method requires working in a cryogenic environment, which is experimentally constraining.

### Levitron

Another levitation technique based on a rotating magnet in a static magnetic field is the Levitron (125; 126; 127; 116). In Fig. 3.1 (c), a Levitron is shown to be levitating above a ring magnet. Here, the contribution of the macroscopic angular momentum adds gyroscopic confinement terms to the angular dynamics that can prevent the rotating magnet from switching to the other direction. We will not go too much in details in the physics of the Levitron but the speed of the magnet has to be carefully chosen to allow levitation.

## 3.2. Magnetic Paul trap

Following the same logic as for electric Paul trap for charged particles to bypass Earnshaw's theorem, the use of an oscillating magnetic field can provide harmonic confinement of a hard magnet. To avoid confusions, we will refer to magnetic (resp. electric) Paul traps as the levitation technique that uses oscillating magnetic field (resp. electric). We will use the acronym MPT to refer to the magnetic Paul trap. The MPT was used to trap neutral atoms in the early days of Bose-Einstein condensation (128; 129). This technique has also been used thirty years ago to trap a macroscopic bar magnet using a combination of permanent magnets and Helmholtz coils (130). The parametric excitation of a magnetic bearings has also permitted to trap magnets (131; 132; 133). Again, the magnetic Paul trap has not found much use so far. In view of the recent interest in micro-magnet levitation as well as the important progress on the miniaturisation of current carrying wire used in the cold atom community, this technology could be of great interest in a near future.

We first describe the physical origin of the MPT and we then propose an on-chip design that could allow to levitate nano/micromagnet using this technique.

### 3.2.1 Magnetic Paul trap theory

In this part, we develop the theory of the magnetic Paul trap levitation taking into consideration the angular and center of mass dynamics.

#### Magnetic field configuration

Contrary to the electric energy, the magnetic energy of a hard magnet depends on the direction of the magnet with respect to the magnetic field direction. It is therefore important to consider the angular dynamics of the levitating magnet.

In Fig. 3.2 (a), we represent a levitating magnet in a magnetic Paul trap. The homogeneous magnetic field  $\mathbf{B}_0$  represented in green orients the magnet in the magnetic field direction without interplaying with the center of mass motion. The oscillating harmonic magnetic field  $\mathbf{B}_1(\mathbf{r}, t)$  confines the magnet center of mass on the same principle than for electric Paul trap. The magnetic field lines of  $\mathbf{B}_1(\mathbf{r}, t)$  are represented in black in Fig. 3.2

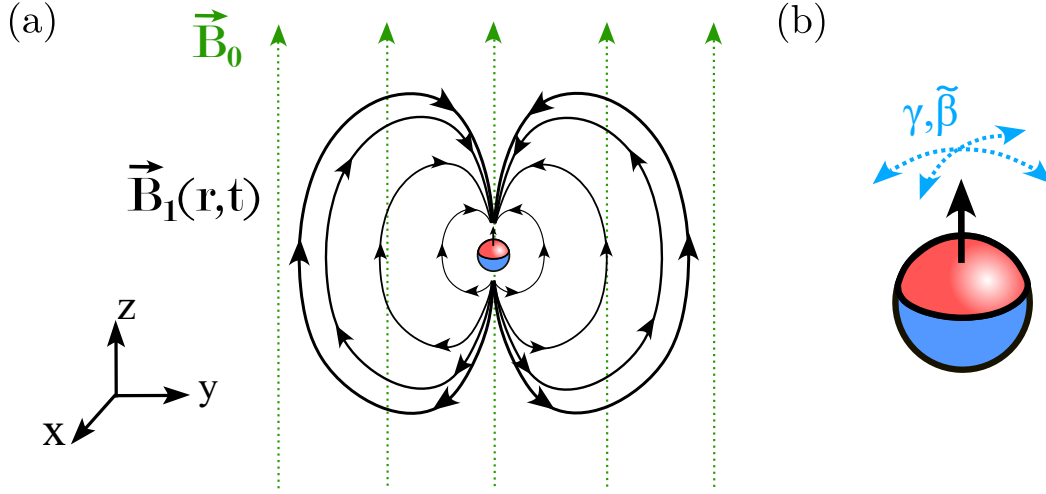


Figure 3.2: (a) Drawing of a levitated magnet subjected to the sum of the fields  $\mathbf{B}_0$  and  $\mathbf{B}_1(\mathbf{r}, t)$ . (b) Angular parametrization of the levitating magnet.

(a). To avoid any confusion, we precise that this field is not the dipolar magnetic field generated by the levitating magnet but this is a field created by an external magnetic system. In the basis of the laboratory frame ( $O\mathbf{e}_x\mathbf{e}_y\mathbf{e}_z$ ), the total magnetic field  $\mathbf{B}(\mathbf{r}, t)$  for a magnetic Paul trap reads:

$$\mathbf{B}_{\text{tot}}(\mathbf{r}, t) = \mathbf{B}_0 + \mathbf{B}_1(\mathbf{r}, t), \quad (3.1)$$

with:

$$\mathbf{B}_0 = B_0 \begin{pmatrix} 0 \\ 0 \\ 1 \end{pmatrix} \quad \text{and} \quad \mathbf{B}_1(\mathbf{r}, t) = \frac{B_1''}{2} \cos(\Omega t) \begin{pmatrix} -xz \\ -yz \\ z^2 - \frac{1}{2}x^2 - \frac{1}{2}y^2 \end{pmatrix}, \quad (3.2)$$

where  $B_0$  is the homogeneous magnetic field strength,  $B_1''$  is the time varying magnetic field curvature and  $\Omega/2\pi$  is the Paul trap driving frequency. The  $x$  and  $y$  components of  $\mathbf{B}_1(\mathbf{r}, t)$  do not play any role in the dynamics of the magnet since the magnet will preferentially orient its magnetic moment in the  $\mathbf{z}$  direction given by the homogeneous field  $\mathbf{B}_0$ . The presence of these components is however imposed by Maxwell's equations. We can now calculate the magnetic energy of the system.

### Magnetic energy

We use the  $zyz$  Euler angles convention to parametrize the angular motion of the magnet. We consider that the magnetic moment of the magnet  $\boldsymbol{\mu}$  is almost aligned with the  $\mathbf{z}$  direction. Using the two relevant angles  $\tilde{\beta}$  and  $\gamma$  defined in Fig. 3.2 (b), we have  $\tilde{\beta}, \gamma \ll 1$  and  $\boldsymbol{\mu}$  equals in the laboratory basis:

$$\boldsymbol{\mu} = \mu \begin{pmatrix} \tilde{\beta} \\ -\gamma \\ 1 - \frac{\tilde{\beta}^2}{2} - \frac{\gamma^2}{2} \end{pmatrix}. \quad (3.3)$$

The detailed development of the calculation is presented in appendix C.1. The magnetic energy can simply be calculated using the formula  $E_{\text{mag}} = -\boldsymbol{\mu} \cdot \mathbf{B}_{\text{tot}}(\mathbf{r}, t)$  up to second order around the position  $(\tilde{\beta}, \gamma, x, y, z) = 0$ :

$$E_{\text{mag}} = \mu B_0 \left( \frac{\gamma^2}{2} + \frac{\tilde{\beta}^2}{2} \right) - \frac{\mu B_1''}{2} \left( z^2 - \frac{1}{2}(x^2 + y^2) \right) \cos(\Omega t). \quad (3.4)$$

The magnetic energy of the angular and the center of mass modes are fully decoupled to second order. The angular confinement is directly given by the strength of the homogeneous field  $B_0$ . The center of mass confinement is a ponderomotive confinement that depends on the curvature of the magnetic field  $B_1''$  as well as on the driving frequency  $\Omega/2\pi$ . In the following, we calculate the confining frequency of these modes.

#### Angular and center of mass confinement

We can now estimate the value of the angular and center of mass resonance frequencies. We consider a levitating spherical neodymium magnet of radius  $a$  with a saturation magnetization that equals  $B_{\text{sat}} \approx 1.0$  T. The magnetic moment norm  $\mu$  equals  $\mu = B_{\text{sat}}V/\mu_0$ , where  $V = 4/3\pi a^3$  is the volume of the magnet. The magnet density constant is written as  $\rho_m$ . The angular frequency given by the magnetic confinement equals:

$$\omega_{\tilde{\beta}} = \omega_{\gamma} = \sqrt{\frac{5}{2} \frac{B_0 B_{\text{sat}}}{\mu_0 \rho_m a^2}}. \quad (3.5)$$

The angular frequency depends on the inverse of the magnet radius given by  $a$ . Considering a 1  $\mu\text{m}$  size magnet in the presence of an external magnetic field  $B_0 = 10$  mT, we obtain  $\omega_{\tilde{\beta}} = \omega_{\gamma} = (2\pi)300$  kHz. Compared to other levitation techniques for magnets (120; 121; 122; 123; 124), the angular frequencies in MPT are extremely high and could be further enhanced by increasing the magnetic field strength  $B_0$  or by lowering the magnet size  $a$ . The high value of the angular confinement in magnetic Paul traps could be used in spin-mechanical protocols with  $\text{NV}^-$  centers for example (93; 123).

The center of mass confinement can be calculated using the dimensionless parameters  $a_u$  and  $q_u$  introduced in Chapter 2. Here, we do not consider a constant harmonic magnetic field, so  $a_u = 0$ . Within the stability domain  $|q_u| < 0.9$ , the resulting center of mass frequencies equal:

$$\tilde{\omega}_z = 2\tilde{\omega}_x = 2\tilde{\omega}_y = \frac{\Omega}{2} \frac{|q_z|}{\sqrt{2}} \quad \text{with} \quad q_z = \frac{2B_1'' B_{\text{sat}}}{\mu_0 \rho_m \Omega^2}. \quad (3.6)$$

The  $q_u$  factors for the  $x$  and  $y$  modes are defined as  $q_z = -2q_x = -2q_y$ . Taking the experimentally accessible value  $B_1'' = 10^5$  T.m<sup>-2</sup> and a driving frequency  $\Omega/2\pi = 2.0$  kHz, we obtain  $q_z = 0.2$  and  $|q_x| = |q_y| = 0.1$ . these values are well below 0.9. The resulting frequencies equal  $\tilde{\omega}_z = 2\tilde{\omega}_x = 2\tilde{\omega}_y = (2\pi)100$  Hz. These values are comparable with the usual method for magnet levitation.

In Fig. 3.3, we show the results of numerical simulations where the position of a levitated magnet is plotted as a function of time. The parameters are  $B_0 = 10$  mT and  $B_1'' = 10^5$  T.m<sup>-2</sup>. The center of mass dynamics of the  $x$  mode (blue curve) and the  $z$  mode (red curve) are represented in Fig. 3.3 (a). As expected, the motion of both modes is composed of a fast micromotion at the Paul trap frequency  $\Omega/2\pi$  as well as a

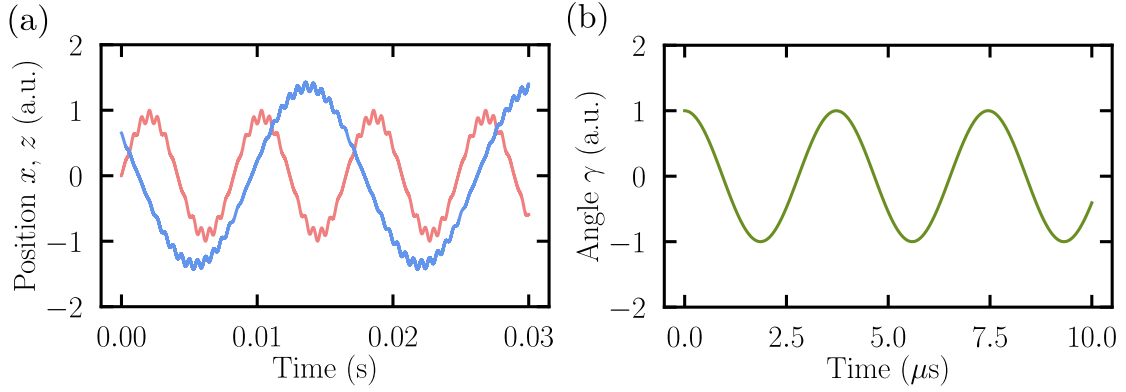


Figure 3.3: (a) Numerical simulations of the position  $x$  (blue curve) and  $z$  (red curve) as a function of time. (b) Numerical simulation of the angular position as a function of time.

slow oscillating macromotion at a frequency given by  $\tilde{\omega}_u$  with  $u = x, z$ . The confinement frequency of the  $z$  mode is twice as large as the confinement frequency of the  $x$  mode as predicted by the formula Eq. (3.6). The typical order of magnitude of the frequency  $\tilde{\omega}_u$  is about  $(2\pi)100$  Hz. We have also represented the angular dynamics in Fig. 3.3 (b) whose confinement does not originate from a ponderomotive torque but a static torque. Thus, there is no micromotion and the frequency of the angular mode is in the  $(2\pi)100$  kHz range as predicted by the analytical theory. In the following, we discuss the impact of gravity on the trapping stability.

#### Gravity compensation with a magnetic field gradient

So far, the impact of gravity on the motion of the levitating magnet has not been taken into account. Using the previously calculated confinement frequencies, we can calculate that the equilibrium position  $z_0$  of the magnet is shifted of  $z_0 = -g/\tilde{\omega}_z^2 \approx -20 \mu\text{m}$ . This is problematic for the following reasons: first, the capture volume of the trap must be at least a hundred microns to ensure that the magnet does not escape from the trap. Second, this will induce unwanted micromotion on the center of mass of the particle.

A magnetic field gradient  $\mathbf{B}_2(\mathbf{r})$  can be used to compensate for gravity. It will take the following form:

$$\mathbf{B}_2(\mathbf{r}) = B'_2 \begin{pmatrix} -x/2 \\ -y/2 \\ z. \end{pmatrix}. \quad (3.7)$$

The gravitational force and the magnetic force both depend on the magnet volume such that the compensation gradient is the same for all particle sizes. The required magnetic field gradient to compensate for gravity equals:

$$B'_2 = \frac{\mu_0 \rho_m g}{B_{\text{sat}}}. \quad (3.8)$$

Taking the following density value for a neodymium magnet  $\rho_m = 7.0 \times 10^3 \text{ kg.m}^{-3}$  and a saturation magnetization  $B_{\text{sat}} = 1.0 \text{ T}$ , we obtain:

$$B'_2 = 8.0 \times 10^{-2} \text{ T.m}^{-1}. \quad (3.9)$$

The value of the gravity compensating magnetic field gradient is straightforward to achieve experimentally.

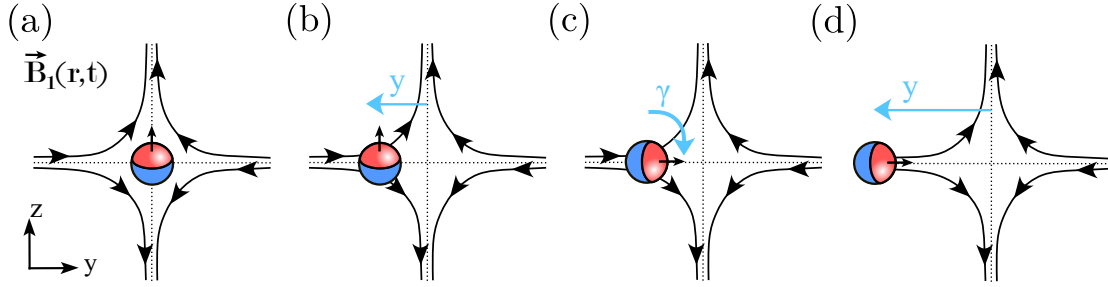


Figure 3.4: Four illustrations of a magnet levitating in a MPT in the presence of a magnetic field gradient that compensates for gravity. (a) The magnet is at the center of the trap. (b) The magnet is shifted to the left. (c) The magnet rotates to align its magnetic moment to the field. (d) The magnet is again shifted to the left.

The addition of a magnetic field gradient to compensate for gravity will however induce a coupling between the center of mass and the angular dynamics of the magnet. The physical origin of this coupling is explained in Fig. 3.4. We consider a magnet initially centered at the position  $(x, y, z) = 0$  as represented in in Fig. 3.4 (a). When the magnet moves along the  $y$  axis as shown in Fig. 3.4 (b), the magnet experiences a magnetic field perpendicular to its direction of magnetization resulting in a torque on the magnet as depicted in Fig. 3.4 (c). The alignment of the magnetic moment with the field will tend to move the particle further away from the trap as shown in Fig. 3.4 (d) because of the magnetic field gradient in the  $y$  direction. This coupling therefore creates an instability that can lead to the loss of the particle.

In the following, we establish a criterion for the magnet to maintain its stability in the presence of the magnetic field gradient. By keeping only second order terms in the position variables, the magnetic energy  $\tilde{E}_{\text{mag}}$  reads:

$$\tilde{E}_{\text{mag}} = \frac{1}{2}I \sum_{\nu=\beta,\gamma} \omega_{\nu}^2 \nu^2 + \frac{1}{2}m \sum_{u=x,y,z} \tilde{\omega}_u^2 u^2 + \sqrt{Im}\omega_c^2 \left( (c_{\alpha}\tilde{\beta} + s_{\alpha}\gamma)x + (s_{\alpha}\tilde{\beta} - c_{\alpha}\gamma)y \right), \quad (3.10)$$

with:

$$\omega_c = \sqrt{\sqrt{\frac{5}{2}} \frac{B_2' B_{\text{sat}}}{\mu_0 \rho_m a}}. \quad (3.11)$$

The necessary and sufficient condition for this system to be stable is calculated in the appendix C.2 and corresponds to the inequality:

$$\omega_{\gamma}\tilde{\omega}_x > \omega_c^2. \quad (3.12)$$

Using the same numerical values than before, the value of the coupling frequency is  $\omega_c/2\pi = 6.3 \times 10^2$  Hz. Considering the previous parameter values, we have the large inequality  $\omega_{\gamma}\tilde{\omega}_x > 10 \omega_c^2$  which is fulfilled. The validity of the stability condition could be

questioned since the confinement frequency of the center of mass results from a ponderomotive force. Numerical simulations have been performed and it shows that the coupled modes remain stable as expected.

In the following, we propose a magnetic Paul trap design that could allow the levitation of micrometer size hard magnet using an on-chip magnetic Paul trap.

### 3.2.2 Proposal for on-chip magnetic Paul trap

There are several difficulties in realizing the magnetic Paul trap mentioned above. On the one hand, the geometry of the magnetic field requires a specific configuration of the current carrying loops used as well as a carefully chosen size and current flowing inside. On the other hand, the possibility to reach strong curvatures of the magnetic field  $B_2'' = 10^5 \text{ T.m}^{-2}$  is challenging and crucial to allow the stable levitation of the center of mass. In the following, a design of an on-chip magnetic Paul trap that fulfills these conditions is proposed. The value of the induced currents in the trap chip as well as inside the levitated magnet is also calculated and we proved that it is negligible.

#### On-chip trap design

The homogeneous magnetic field and the magnetic field gradient used to compensate for gravity are not discussed since their production does not present any experimental difficulty for the required values. Figure 3.5 (a) shows the design of the proposed trap, which consists in two lithographically made current carrying loops on a silicon chip of radius  $r_1$  (resp.  $r_2$ ) and through which an alternating current  $i_1(t) = i_1 \cos(\Omega t)$  (resp.  $i_2(t) = i_2 \cos(\Omega t)$ ) flows. A single current carrying loop produces a magnetic field at its center with the desired magnetic field curvature. However, it also produces a homogeneous magnetic field at its center, which is not desired. To compensate for this homogeneous field without cancelling the curvature term, the two current carrying loops satisfy the condition  $i_1/i_2 = -r_1/r_2$ . This indeed removes the homogeneous field. Figure 3.5 (b) shows the magnetic field term  $B_z(\mathbf{r}, t)$  on the  $z$  axis with  $(x, y) = 0$  generated by each of the loops. The dashed blue curve is the magnetic field generated by the first loop of radius  $r_1$  taken to be equal to  $100 \mu\text{m}$  and the grey dashed line is the magnetic field generated by the second loop of radius  $r_2 = 200 \mu\text{m}$ . We have also represented by the red line, the sum of the two contributions that equals to zero at the position  $(x, y, z) = 0$  as expected.

The curvature of the generated magnetic field equals:

$$B_1'' = -\frac{9}{16} \frac{\mu_0 i_1}{r_1^3}. \quad (3.13)$$

This kind of microchip can reasonably carry current density of  $10^5 \text{ A.cm}^{-2}$  without experiencing too much heating (134; 135). By considering a  $50 \mu\text{m}$  large and  $2 \mu\text{m}$  thin gold layer, the current  $i_1$  equals 0.1 A. It leads to the desired value for the magnetic curvature  $B_1'' \approx 10^5 \text{ T.m}^{-2}$ .

The use of loops carrying alternating currents raises the question of the magnitude of the induced currents in each of the conducting elements of the device. It will be shown in the following that the eddy currents generated by one of the two loops on the other are negligible. We will also calculate the eddy currents induced in the levitated particle and we will show that it does not lead to a consequent heating of the magnet, even in ultra-high vacuum condition.

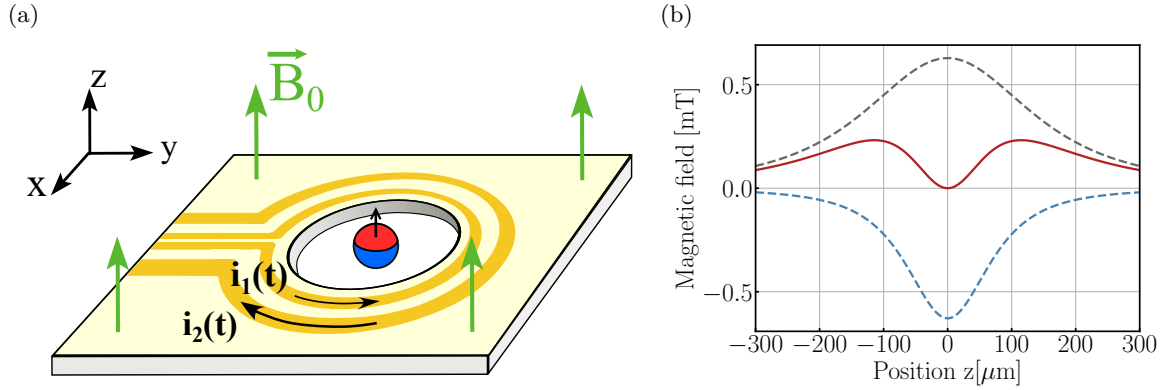


Figure 3.5: (a) Drawing of an on-chip magnetic Paul trap. (b) Magnetic field generated by the current carrying loop with radius  $r_1$  (dashed blue curve), with radius  $r_2$  (dashed grey curve) and by the sum of the two contributions (red curve).

### Eddy currents

The theoretical calculation of the currents induced from one current loop to another is presented in the appendix C.3 of this section. The formula for the ratio of the induced current to the initial current is:

$$\frac{i_{2 \rightarrow 1}(t)}{i_1} = -\frac{\mu_0 \sigma S \Omega}{4} \sin(\Omega t), \quad (3.14)$$

where  $\sigma = 4.4 \times 10^7 \text{ S.m}^{-1}$  is the electrical conductivity of gold and  $S = 100 \mu\text{m}^2$  is the area of a slice of the gold lithography. We obtain that this ratio is on the order of  $10^{-5}$  for  $\Omega/2\pi \approx \text{kHz}$  so we can safely neglect the eddy currents generated by a loop onto the other one.

The currents induced in the levitating magnet could lead to internal heating of the particle as well as damping of its motion. Since the magnet is levitated, its thermalization is only possible via collisions with the surrounding gas. In an ultra-high vacuum environment, collision processes are rare and the thermalization is slow. If the magnet heats up too much due to the Joule effect with the eddy current, it can reach a critical melting temperature and the levitating magnet is lost. It is therefore crucial to minimise these currents. A remarkable aspect of this trapping method is that although the curvature of the magnetic field is alternating, there is strictly speaking no oscillating magnetic field at the trap center. As the levitating magnet is not a purely point like object, it experiences an oscillating magnetic field that evolves in the square of the position on its edges and generates eddy currents within it. A quick calculation of the order of magnitude of the power dissipated by Joule effect presented in the appendix C.3 of this chapter gives:

$$P = \Omega^2 \sigma a^9 B_1''^2. \quad (3.15)$$

$P$  scales as the ninth power of the radius. For the considered size, we find that  $P$  is of the order of  $10^{-28} \text{ W}$ . This value is largely insufficient to heat the magnet even in ultra-high vacuum conditions.

### 3.2.3 Discussions and perspectives

This trapping technique has many advantages over current permanent magnet levitation techniques.

First, compared to electric traps, this technique does not depend on the surface charge density, which can vary greatly from one particle to another. The magnetic moment of permanent magnets is the same for magnets of the same size, so the resonance frequencies depend very little on the levitating particle. In addition, the levitating magnet can be electrically discharged, making it insensitive to electric fields and nearby charge fluctuations. This can be used to approach a diamond close to the levitating magnet to perform mechanical spin protocols (93; 123).

Second, compared to widely used superconducting trapping techniques, it is not necessary to work in a cryogenic environment, which greatly reduces the complexity of the experimental setup.

Third, the resonance frequencies of the modes can be easily and independently modified by adjusting the different trap parameters. These can be very high, in the megahertz range for the angular modes. The angular modes of levitating magnets could thus serve as an ideal mode to reach the ground state since the frequency of the mode is high and that the magnet is not heated at ultra-high vacuum environment (28; 136; 27).

Last, the trap can be made with simple currents carrying loops. These technologies have been largely developed during the last decades in the cold atom technology (135). One can imagine to switch from a magnetic Paul trap configuration to an Ioffe Pritchard trap configuration by changing the currents in the loops. This could allow to realize quantum spin stabilized levitation as proposed in (116; 105).

## 3.3. Experimental realization of a magnetic Paul trap

In this section, a macroscopic magnetic Paul trap is experimentally implemented to levitate millimeter-sized magnets. A magnetic saddle was constructed which allows the levitation of magnets when it is rotated at frequencies of the order of 100 Hz. As shown in the three pictures in Fig. 3.6, magnets with different shapes can levitate in this trap. This technique has already been used in (130) to stabilize the position of the magnet radially. However, the confinement in the  $z$  axis was ensured by a permanent field. In our case, we demonstrate that the anisotropy of the magnet combined with volumic effect allows its ponderomotive confinement along the  $z$  axis.

First, we recall the physical origin of the radial stabilization of a particle subjected to a rotating saddle potential. We then calculate the magnetic energy of a magnet subjected to a magnetic rotating saddle. We finally prove theoretically that the magnet can be stably levitated in this trap.

### 3.3.1 The rotating saddle potential

The rotating saddle potential problem is a specific problem of ponderomotive potential whose stability conditions can be simply calculated (137). In the remainder of this section, a rotating mechanical potential of the following form is considered:

$$U(X, Y) = \frac{1}{2}m\omega_r^2 (X^2 - Y^2), \quad (3.16)$$

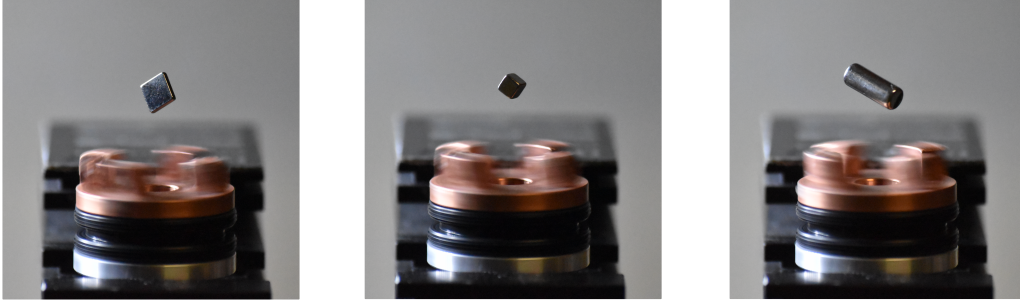


Figure 3.6: Serie of three pictures of different magnets levitating above a home-made magnetic Paul trap.

where  $\omega_r$  is a characteristic curvature.

#### Stability condition

A particle subjected to this rotating potential can be stabilized according to the saddle potential rotational speed  $\Omega$ . This phenomenon can be explained by reasoning in the rotating frame where the saddle potential is no more time-dependent. An explanatory drawing is shown in Fig. 3.7. In the rotating frame, the particle is subjected to the two inertial forces: the centrifugal force and the Coriolis force. In Fig. 3.7 (a), the centrifugal force as well as the negatively curved potential tend to move the particle away from the initial position  $(x, y, z) = 0$ . As it moves away from this position, the particle acquires a radial velocity as shown in Fig. 3.7 (b). The particle then feels the Coriolis force which depends on the radial velocity as well as on the rotational speed. The Coriolis force tends to deviate the trajectory of the particle towards confining potentials. Finally, the particle is brought back to its initial position  $(x, y, z) = 0$  as depicted in Fig. 3.7 (c).

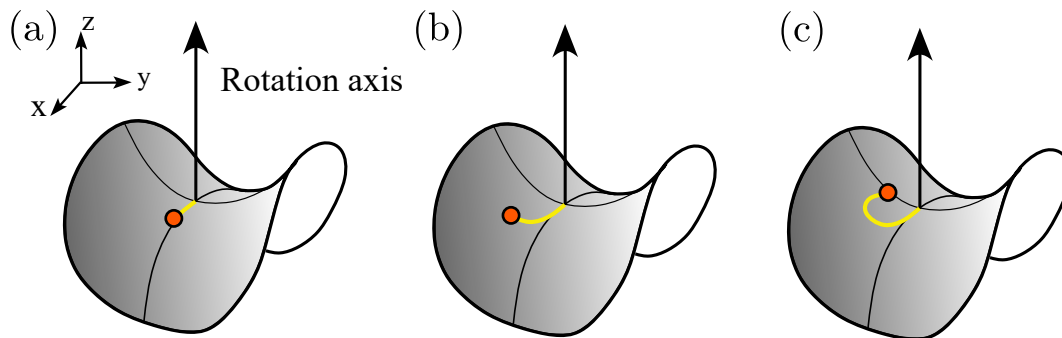


Figure 3.7: Motion of a particle subjected to a rotating saddle potential in the co-rotating frame at three different times ( $t_0 < t_1 < t_2$ ): (a)  $t_0$  (b)  $t_1$  (c)  $t_2$ .

We calculate this condition explicitly in the appendix C.4 of this chapter and obtain that the particle can be stabilized if and only if the rotation angular velocity is stronger

than the potential curvature:

$$\Omega > \omega_r. \quad (3.17)$$

Thus, a particle subjected to a rotating saddle potential can always be stabilized if the potential rotates at a sufficiently high speed.

### Resulting motion

Using the approach proposed in (138), one can calculate the resulting macromotion of the particle in the laboratory frame in the case where the rotational speed of the potential is very high compared to the angular frequency of the potential, i.e.  $\Omega \gg \omega_r$  (see appendix C.4). The radial motion of a particle taken from Kirillov et al. (138) is shown in Fig. 3.8. In Fig.3.8 (a), a numerical simulation of an example of motion of a trapped particle in a rotating saddle potential is shown. A micromotion at the rotating saddle frequency appears around a macromotion with a rosette shape. It can be proven that the macro motion has two components: a restoring force with a characteristic angular frequency  $\tilde{\omega} = \omega_r^2/2\Omega$  and a slow precessional motion given by the angular frequency  $\tilde{\omega}_{\text{prec}} = \omega_r^4/4\Omega^3$ . In Fig. 3.8 (b), the macromotion simulation is represented. We see in Fig. 3.8 (c) that the macromotion fits pretty well the real dynamics of the particle subjected to the rotating saddle potential. After the secular approximation, the equations of motion do not simply involve a confining secular potential but also involves a term depending on the velocity of the particle which leads to a precessional motion. This precessional motion is not present in oscillating ponderomotive trap such as the electric Paul trap or the magnetic Paul trap discussed above. Even if the physics behind ponderomotive traps is related, oscillating and rotating potentials do not lead to the exact same effects.

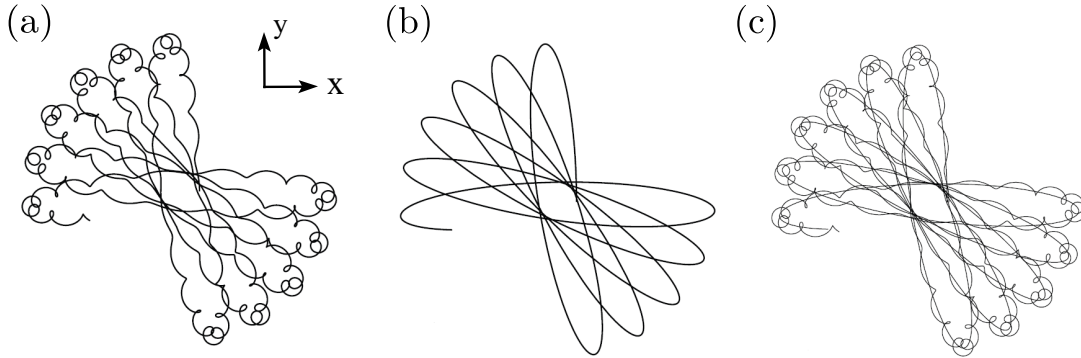


Figure 3.8: (a) Position of a particle in the  $xy$  plane subjected to a rotating saddle potential in the laboratory frame. (b) Calculated macromotion position evolution of the same particle in the same conditions. (c) Superposition of the (a) and (b) position evolution traces. Taken from (138).

In the following, we treat the problem of a rotating saddle magnetic potential that leads to radial confinement but also axial confinement due to magnet shape anisotropy as well as volumic effects.

### 3.3.2 The rotating magnetic saddle

In this part, we describe the home-made magnetic Paul trap set-up based on a rotating magnetic saddle. We theoretically and experimentally demonstrate the possibility to levitate a magnet inside this trap.

#### Experimental set-up

We use the experimental set-up shown in Fig. 3.9 (a). Four Neodymium magnets have been glued to a plate and attached to a motor from the HMS company. The magnets are glued so that the axis of rotation of the motor passes through the centre of the square formed by the positions of the four magnets. As shown in Fig. 3.9 (b), the North-South axis of the four magnets is alternated between two adjacent magnets in order to generate a saddle potential in the  $(x, y)$  plane. The motor rotation can reach a maximum speed of 100 Hz without any noticeable vibrations. For a sufficiently high rotation of the plate where the four magnets are glued (above 80 Hz in practice), a millimeter magnet can levitate above the trap as shown in Fig. 3.9 (c).

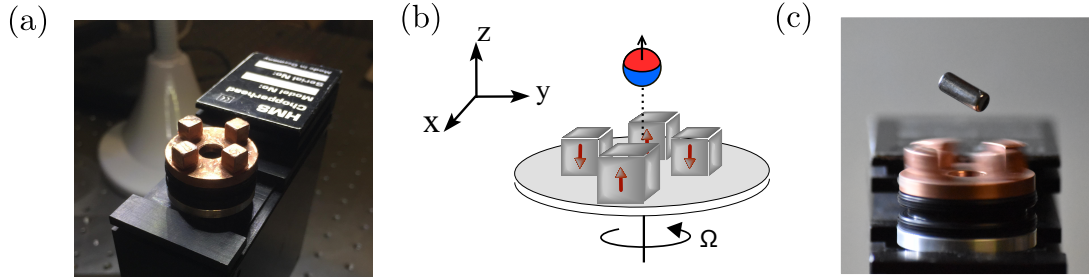


Figure 3.9: (a) Picture of the home-made magnetic Paul trap experimental set-up. (b) Drawing of a hard magnet levitating above the MPT. (c) Picture of a cylindrical magnet levitating above the MPT.

The magnet can levitate several hours above the trap without falling off, which means that its position is very stable. However, the injection of the levitating magnet in air is rather complicated because the parameter space for both angular and center of mass for which the magnet is stable is small. Therefore, the magnet is first injected into a liquid, which increases the friction with respect to the air and allows the equilibrium position to be reached without escaping. Once the magnet has reached its equilibrium position, the water can be removed from the container and the magnet can levitate stably in air.

#### Magnetic potential

COMSOL numerical simulations can be used to determine the shape of the magnetic field created by the four magnets. Figure 3.10 shows the  $z$  component of the magnetic field at a given height  $z_0$  above the four magnets as a function of the radial positions  $x$  and  $y$ . The simulations show that the magnetic field has a saddle shape around the position  $(x, y) = 0$ , as expected. The value of the curvature of the  $z$ -component of the field depends on the height  $z_0$ . The component of the field along  $z$  can therefore be written in the rotating frame of the motor as:

$$B_Z(\mathbf{R}) = \frac{B_Z''(Z)}{2} (X^2 - Y^2), \quad (3.18)$$

where  $B_z''$  is an even function of  $Z$ . In the laboratory frame, the magnetic field is time dependent and reads:

$$B_z(\mathbf{r}, t) = \frac{B_z''(z)}{2} \left( (x^2 - y^2) \cos(2\Omega t) - 2xy \sin(2\Omega t) \right). \quad (3.19)$$

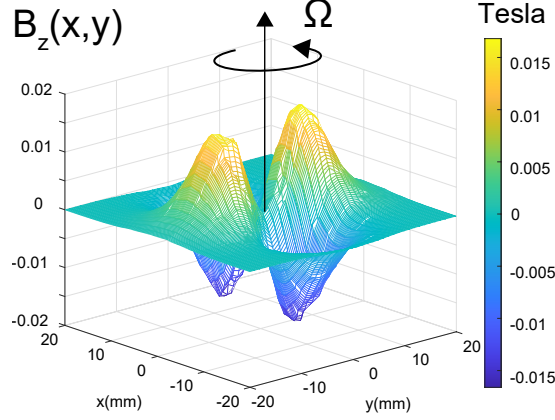


Figure 3.10: Two dimensional map of the magnetic field component along the  $z$  axis as a function of the  $x$  and  $y$  position at a given height  $z_0 = 1$  cm.

It is important to note that the magnetic energy depends on the direction of the magnetic dipole of the magnet. Experimentally, one adds a homogeneous field which fixes the direction of the magnetic dipole of the magnet along the  $z$  axis. This is done by adding a permanent magnet that orients the magnetic moment along the  $z$  axis. In the following, we will thus assume that the magnetic dipole of the magnet is well oriented along the  $z$  axis and that the magnet is angularly stable. This allows us to write the total magnetic energy of the magnet as:

$$E_{\text{mag}}(\mathbf{r}, t) = - \int_V M_z B_z(\mathbf{r}, t) dV, \quad (3.20)$$

with  $M_z$  the hard magnet magnetization component along  $z$ .

To simplify the calculations, we consider a parallelepiped magnet of length  $l$  and with the same height and width  $h$ . The magnetization of the magnet is considered to be perpendicular to its major axis. Under these conditions, the magnetic energy of the trapped magnet equals:

$$E_{\text{mag}}(\mathbf{r}, t) \approx \frac{1}{2} m \omega_r^2 \left( \cos(2\Omega t) (y^2 - x^2) + 2 \sin(2\Omega t) xy \right) + \frac{1}{2} m \omega_z^2 \cos(2\Omega t) z^2, \quad (3.21)$$

where we introduced the relevant frequencies:

$$\omega_r = \sqrt{\frac{2B_{\text{sat}} b_0''}{\mu_0 \rho_m}}, \quad (3.22)$$

$$\omega_z = \sqrt{\frac{B_{\text{sat}} b_2'' (l^2 - h^2)}{12 \mu_0 \rho_m}}. \quad (3.23)$$

with  $b_0''$  and  $b_2''$  defined with the formula:

$$\int_{-\frac{h}{2}+z}^{\frac{h}{2}+z} \frac{B_z''(z')}{2h} dz' = b_0'' + b_2'' \frac{z^2}{2} + o(z^3). \quad (3.24)$$

The magnetic potential is therefore the sum of two terms, one depending only on the radial positions  $x$  and  $y$  while the second term depends only on the position  $z$  and is zero if the particle is isotropic i.e.  $h = l$ .

#### Radial confinement

The first term in the magnetic potential allows the radial confinement of the magnet. It can be directly seen that the generated potential is identical to that of a rotating saddle potential. Thus, according to the criterion mentioned in the theoretical study of the rotating saddle potential, the stability condition is simply  $\Omega > \omega_r$ . The parameter  $b_0''$  is about  $b_0'' \approx 10^2 \text{ T.m}^{-2}$  in our experimental set-up. We obtain the numerical value:

$$\omega_r \approx (2\pi)10 - 100 \text{ Hz}. \quad (3.25)$$

This value coincides with the experimental observation that the magnet is stable when the magnetic saddle is rotated at frequencies above 80 Hz.

#### Axial confinement and size effect

A point permanent magnet, i.e. with a negligible size, could not levitate above this type of trap because the magnetic field is zero at the position  $(x, y) = 0$  at any time. Furthermore, a volumic magnet with a  $\pi/2$  rotational symmetry around the  $z$  axis does not experience any force along this axis because the sum of the fields of a magnetic saddle potential on a given volume of this magnet compensates each other. Thus, it is necessary to have a rather large and asymmetric particle to allow confinement in the  $z$  axis.

Indeed, the second term of the formula Eq. (3.21) cancels if  $l$  and  $h$  tend to zero or are equal. In the case of a volumetric and sufficiently asymmetric magnet, that is  $|l - h| \approx h, l$ , this term is responsible for the stabilization of the particle in the axial direction  $z$ . We can see from the formula Eq.(3.21) that this is an oscillating ponderomotive force and not a rotating ponderomotive force as it is radially. For this type of trap, the stability criterion can be formulated by calculating the  $q_z$  factor previously introduced for the electric Paul traps. The size of the magnets that are levitated is a few millimeters, which is on the order of the size of the trap. We can therefore deduce a relationship between the constants  $b_0''$  and  $b_2''$ :

$$b_2'' \approx \frac{b_0''}{l^2 - h^2}. \quad (3.26)$$

Thus, the axial characteristic frequency  $\omega_z/2\pi$  is of the order of magnitude of the radial characteristic frequency  $\omega_r/2\pi$ . The stability conditions in the radial and axial directions are thus similar which explains why the particle is also stable in the  $z$  direction. Several experimental elements testify that the axial confinement is indeed due to a ponderomotive force.

First, the resulting confinement frequency in a ponderomotive trap depends inversely on the oscillation frequency  $\Omega/2\pi$ . In Fig. 3.11 (a), we present the result of an experi-

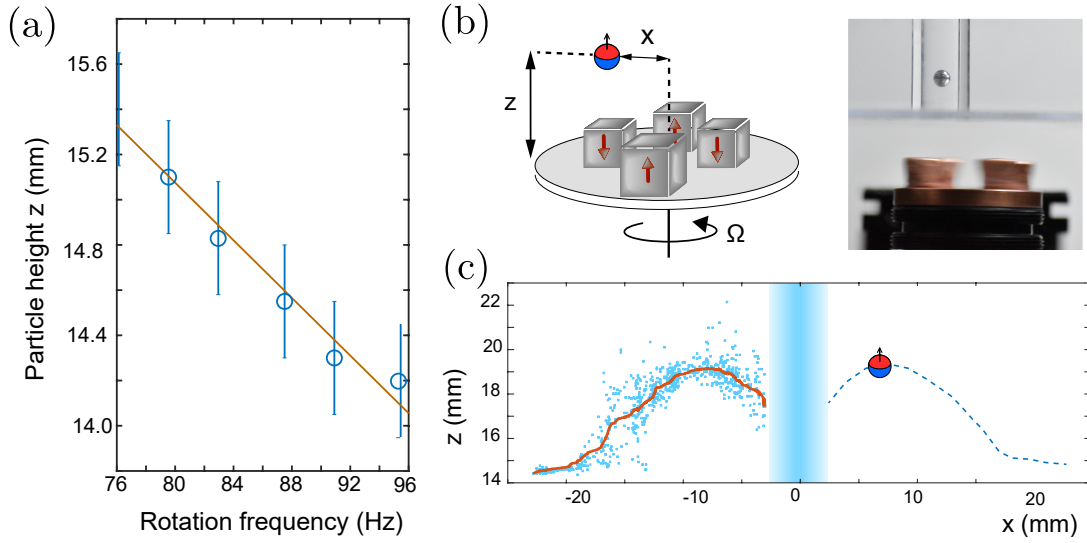


Figure 3.11: (a) Levitated magnet height as a function of the magnetic saddle rotation frequency. (b) Left: parametrization of the radial position  $x$  and the height  $z$ . Right: picture of a magnetic sphere in a test tube in water above the MPT. (c) Levitated magnet height as a function of the radial position. The blue zone designates an unstable area for the magnet.

ment where we continuously increase the rotation frequency of the magnetic saddle. It is observed that the height at which the magnet levitates above the trap decreases as the rotation frequency increases. This tells us that the axial confinement is weaker as the rotation speed of the magnetic saddle increases as expected from a ponderomotive confinement. When the rotation frequency is increased too much, the magnet is eventually lost, which is explained by the fact that the ponderomotive potential is no longer strong enough to counteract the effect of gravity.

Furthermore, another experimental proof that the axial confinement comes from a ponderomotive force and size effects is that one cannot levitate particles smaller than 2 mm. The frequency  $\omega_z$  depends linearly on the size as shown in Eq. (3.23). If the magnet is too small, the resulting secular frequency is too small to compensate for gravity and it is therefore impossible to levitate a particle below a certain diameter.

Finally, a last experiment presented in Fig. 3.11 (b) consists in radially stabilizing a spherical magnet with a test tube and moving this tube radially to measure the height of the particle at a different radial position than  $(x, y) = 0$ . The idea is to move the magnet away from the  $(x, y) = 0$  position where the magnetic fields give a zero resultant force due to the symmetries of the magnetic saddle and the magnet. Indeed, the magnetic energy at the magnet height  $z$  at an off centered radial position  $(x, y) = (x_0, 0)$  equals:

$$E_{\text{mag}}(z, t) \approx \frac{1}{2} m \omega_z^2(x_0) \cos(2\Omega t) z^2, \quad \text{with} \quad \omega_z = x_0 \sqrt{\frac{B_{\text{sat}} b_2''}{\mu_0 \rho_m}}, \quad (3.27)$$

The curvature of the potential  $\omega_z$  thus depends linearly on the radial position  $x_0$ . The resulting secular frequency  $\tilde{\omega}_z$  of the ponderomotive depends on the square of the angular frequency  $\omega_z$ .

In Fig. 3.11 (c), we have plotted the height  $z$  of the magnet as a function of the radial position shift  $x_0$  for the experiment presented Fig. 3.11 (b). We observe that the height of the magnet increases when we move away from the  $x_0 = 0$  position. This can be deduced from the fact that moving the magnet away from the center of the trap increases the confinement frequency along the  $z$  axis. Consequently, its height increases as gravity pushes the particle less far into the trap well. We also observe that the particle is not stable along  $z$  close to the trap center  $(x, y) = 0$  represented by the blue area which is well understood by the previously explained theory.

We thus show several experimental evidences that the magnet is stabilized along the  $z$  axis due to the ponderomotive confinement of the rotating magnets. This is consistent with theoretical predictions.

### 3.3.3 Discussion

Although the effects of ponderomotive confinement are generally well understood, there are still some grey areas about this magnetic trap.

First of all, it was assumed that the angle was well confined in order to be able to isolate the dynamics of the center of mass from the angular dynamics. However, it is not clear why the three angular degrees of freedom are well confined. Indeed, a magnetic dipole cannot be confined around its symmetric axis. Again, it is possible that volumic effects with asymmetric magnetic fields are involved to explain this stabilization.

Another noticeable point is that an external magnet can be used to control the direction of the levitating magnet. Surprisingly, the change in the direction of the levitating magnet does not seem to have much impact on the confinement of the center of mass.

Finally, although the confinement along the axial direction  $z$  is well understood, symmetric particles such as magnetic cubes or flat squares manage to levitate in this trap as shown in the figure of the introduction Fig. 3.6. It is therefore possible that another physical phenomenon intervenes so that the total magnetic field perceived by a symmetrical magnet at the position  $(x, y) = 0$  is not zero. This could be explained by the fact that the magnets are not perfectly symmetrical and therefore the axis of rotation does not coincide with the barycenter of the four magnets' positions. Another possibility is that under the centrifugal force of the rotating magnets, the motor axis performs a precessional movement around the axis  $(x, y) = 0$  that results into a magnetic force on the magnet.

## 3.4. Conclusion

In this chapter, we have presented different magnetic levitation techniques for permanent magnets. We then focused our attention on magnetic Paul traps, for which we proposed a new on-chip design that seems to be an ideal platform for the levitation of magnets. Finally, we realized a macroscopic Paul trap using rotating magnets. We demonstrated the levitation of millimeter sized magnets and observed that size effects play a crucial role.

As an outlook, let us stress once more the fact that, although magnetic Paul traps have been known for about 50 years, they have not been developed to any great extents. In the last ten years, a large research community has developed on the study of micro/nano particle levitation to access quantum regimes of mechanical modes (24). In this context, the advantages of the magnetic Paul trap levitation technique are many: there is no need

to work in a cryogenic environment, the parameters of the trap can be easily controlled on short time scales, the fluctuation of electric charges on the surface does not influence the levitation and the levitated particle should not heat up under ultra high vacuum. The on-chip design could even allow us to control in vivo magnetic particles, which could be excellent magnetometers. For all these reasons, we believe that this technology could play an important role in the coming years.

## Chapter 4: Fast electric rotation of trapped magnetic particles

---

Until now, we have admitted that the angles of the particles levitating in our electric Paul micro-traps were stabilized by a ponderomotive torque. We come back to this point in this chapter and explore in more detail the angular dynamics of particles levitating in electric Paul trap. We also show another stability regime where the particle performs a full rotation on itself. The rotation of magnetic micrometric particles has fundamental interests for studying gyromagnetic effects such as the Barnett effect (48), for observing the quantum geometric phases (46) and also for making ultra precise gyroscopes (139).

The widely developed technique to rotate levitating micro/nano particles relies on the absorption of photons from a circularly polarized laser that transfers angular momentum to the particle (140; 107; 141; 142; 143; 144; 145). This technique allows to reach record rotation speeds up to GHz at high vacuum, is very stable but requires the use of intense lasers under vacuum which can lead to heating and losing the particle as it is notably the case for diamond.

In this chapter, we present a new and purely electrical technique for rotating levitated particles. It uses no laser light, it is ultra stable and enables to rotate all types of charged particles. This technique is very well adapted to rotate magnetic particles.

This chapter is organized as follows. First, we establish the origin of the electric torque on an asymmetrically charged particle levitating in an asymmetric Paul trap. We then show that the dynamics of the three angles can be written in the form of a Mathieu equation as for the Kapitza pendulum leading to a possible stabilization of these three angles: this is the librating regime. Then, we show the existence of another stability regime where the particle can fully rotate at a multiple period of the Paul trap drive: this is the locking regime. Finally, we will prove both theoretically and experimentally that the particle is completely stable for the three angular degrees of freedom in the rotating frame of reference, which opens up bright perspectives for the study of rotating magnetic particles.

### 4.1. Angular stabilization in a Paul trap: the librating regime

The angular stabilization of levitating micro/nano particles is an essential condition for the realization of spin-mechanical protocols with NV centers (29) or magnetometers (45). Most experimental efforts directed towards the angular stabilization of levitated micro/nano particles uses the electric or the magnetic dipole to exert a restoring torque. In the case of dielectric particles, a linearly polarized laser can align the main axis of asymmetric particles with the laser polarization direction (145; 107; 146). For magnetic particles, one can directly use a homogeneous magnetic field as we have just discussed in the previous part (93). In this part, we recall that an asymmetrically charged particle levitating in an asymmetric Paul trap can be stabilized by a quadrupolar electric ponderomotive torque (29; 80).

### 4.1.1 The Kapitza pendulum

Let us briefly introduce a classical physics experiment featuring a ponderomotive angular stabilization that is very much related to the particle angular dynamics in Paul trap. The Kapitza pendulum (147) (or inverted pendulum) shown in Fig. 4.1 (a) is the best-known example of a ponderomotive torque giving rise to angular confinement. In this experiment, a weighted pendulum is attached to a point that can swing up and down. The equation of the dynamics for the angle  $\alpha$  is (148; 149):

$$\ddot{\alpha} + \left( \frac{g}{l} + \frac{Y\Omega^2}{l} \cos(\Omega t) \right) \sin(\alpha) = 0, \quad (4.1)$$

where  $\alpha$  is the angle represented Fig. 4.1 (a),  $\Omega/2\pi$  is the drive frequency of the point at the pendulum basis,  $g$  is the earth gravitationnal constant,  $l$  is the pendulum length and  $Y$  is the excitation amplitude. In the linear regime  $|\alpha| \ll 1$ , this equation is a Mathieu equation already mentioned in Chapter 2 and 3. We thus know that the angle can be stabilized despite the gravity for certain values of  $\Omega/2\pi$ . However, this equation differs from a classical Mathieu equation by its non-linearity given by  $\sin(\alpha)$ . This non-linearity gives rise to the existence of a second stability regime where the inverted pendulum rotates around its main axis. We will see in the second section of this chapter that this rotation regime also exists for a particle levitating in a Paul trap.

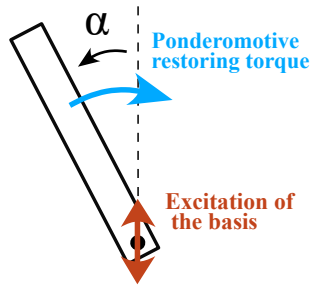


Figure 4.1: Schematics of a stable Kapitza pendulum.

The angular dynamics arising in a Paul trap is analogous to the angular dynamics of the Kapitza pendulum. Several references to the physics of the Kapitza pendulum will be made later and it is useful to keep this example in mind.

### 4.1.2 System description and parametrization

In this part, we introduce the key physical ingredients that allow a charged particle to be angularly stable in a Paul trap.

#### Asymmetric Paul trap

A particle cannot be totally stabilized angularly by an electric potential if it is invariant by rotation around an axis. This is for example the case of the Paul trap potential considered in Chapter 2 in Eq. (2.6) which is invariant by rotation around the  $z$  axis. The energy of a particle levitating in this trap does not depend on the angle around this axis and no torque about this axis can thus be exerted. It is therefore necessary to consider an

asymmetric Paul trap generating a potential of the form:

$$U(\mathbf{r}, t) = \frac{\eta U_{AC}}{z_0^2} (c_x x^2 + c_y y^2 + c_z z^2) \cos(\Omega t), \quad (4.2)$$

where  $c_i$  are geometrical unitless coefficients verifying  $c_x + c_y + c_z = 0$  to satisfy Poisson's law and also such that  $c_y > c_z > c_x$ .  $z_0$  is the characteristic size of the Paul trap and  $\eta$  is a correction factor with respect to the ideal hyperbolic shape. Note that we have considered that the spatial direction where the electric potential is curved the most is the  $y$  direction and not the  $z$  direction contrary to Eq. (2.6). This choice will be motivated later.

An asymmetric potential such as the one above can be generated by any electrodes configuration that has three mirror symmetries and no rotational invariance. We present two examples of electrodes configurations that can generate such a potential in Fig. 4.2 (a). The first trap geometry in Fig. 4.2 (a)-(i) is similar to the bottleneck region of our micro-trap and the second trap geometry in Fig. 4.2 (a)-(ii) is ellipsoidal.

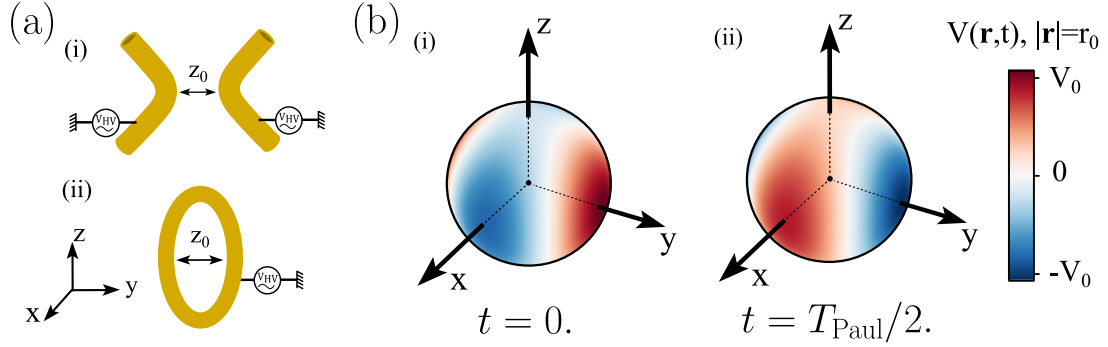


Figure 4.2: (a) (i) Bottleneck geometry of an asymmetric Paul trap. (ii) Elliptical geometry of an asymmetric Paul trap. (b) Potential of an asymmetric Paul trap on a sphere of radius  $r_0$  for the parameters  $c_y = 1, c_x = -0.8, c_z = -0.2$  at  $t = 0$  (i) and  $t = T_{\text{Paul}}/2$  (ii).  $V_0$  (resp.  $-V_0$ ) designates the maximal (resp. the minimal) value reached by  $V(\mathbf{r}, t)$ .

For the rest of this chapter, we use a spherical representation for the electric potential Eq. (4.2) where the potential value  $U(\mathbf{r}, t)$  is plotted for the positions  $\mathbf{r}$  verifying  $|\mathbf{r}| = r_0$  i.e. that are located on a sphere of radius  $r_0$ . This representation will be particularly relevant for understanding and visualizing the angular dynamics of a particle in a Paul trap, as we will see later. In Fig. 4.2 (b), we have represented the electrical potentials with  $c_y = 1, c_x = -0.8, c_z = -0.2$  at  $t = 0$  in (i) and  $t = T_{\text{Paul}}/2$  in (ii) where  $T_{\text{Paul}} = 2\pi/\Omega$  is the oscillation period of the Paul trap electric potential. The potential represented in Fig. 4.2 (b)-(ii) is the opposite value of the one of Fig. 4.2 (b)-(i). The electric potential in Fig. 4.2 (b)-(i) has two minima on the sphere of radius  $r_0$  that are given by the directions  $\mathbf{e}_x$  and  $-\mathbf{e}_x$ , two maximum in the directions  $\mathbf{e}_y$  and  $-\mathbf{e}_y$ . The directions  $\mathbf{e}_z$  and  $-\mathbf{e}_z$  give the position of a potential saddle.

Note that this representation has the advantage that the position of the minimum, maximum as well as the global evolution of the potential on the sphere is independent of the considered radius  $r_0$ .

### Asymmetrically charged particle

We are now interested in the types of particles levitating in an asymmetric Paul trap that can be angularly stabilized. To simplify the study, it is assumed that the center of mass of the particle is perfectly stationary at the position  $(x, y, z) = 0$  which is well-verified in practice. A particle which has a rotational symmetry around an axis cannot be angularly confined around this axis. Thus, we will consider a cylindrical particle with an elliptic basis, that we denote by "deformed cylinder", which does not have rotational symmetry around an axis. We also consider that the charges present on the surface of the cylinder are homogeneously distributed with a surface distribution  $\rho(\mathbf{r})$ . For simplicity, we chose the deformed cylinder to be positively charged. The physics is similar for a negatively charged particle.

In Fig. 4.3 (a), we represent a deformed cylinder in the  $zyz$  convention of Euler angles. For  $(\alpha, \beta, \gamma) = 0$ , the axis of the body frame  $(\mathbf{e}_1, \mathbf{e}_2, \mathbf{e}_3)$  coincides with the laboratory fix axis  $(\mathbf{e}_x, \mathbf{e}_y, \mathbf{e}_z)$ . We designate by  $I_1, I_2, I_3$  the inertia momenta axes along the  $(\mathbf{e}_1, \mathbf{e}_2, \mathbf{e}_3)$  directions. In addition, the cylinder shape is chosen such that the inequality  $I_1 > I_2 > I_3$  is verified.

In the following part, we give more physical insights about the origin of the electric torque in Paul trap.

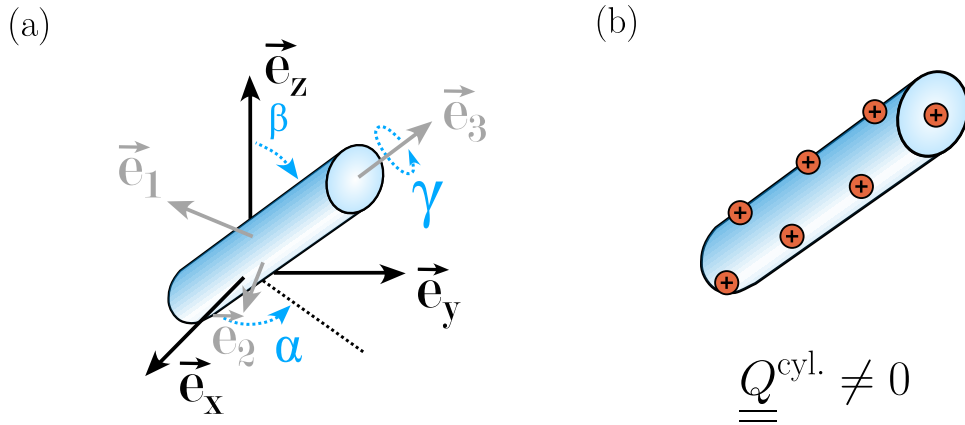


Figure 4.3: (a) Angular parametrization of a deformed cylinder in the  $zyz$  Euler angle convention. (b) Deformed cylinder particle uniformly charged on surface. The electric quadrupole tensor is not zero for this particle.

### Origin of the electric torque

The electric dipole of a particle is not sufficient to get full angular stabilization in an electric trap because of the rotational symmetry of the electric energy around the direction given by the dipole. It is therefore necessary to consider the next order terms in the multipole expansion i.e. the quadrupole moment to possibly obtain a full angular stabilization. For the following, the considered particles have no electric dipole moment but have an electric quadrupole moment. We have represented in Fig. 4.3 (b) an example of uniformly charged particle that has no electric dipole but have an electric quadrupole.

These considerations lead us to introduce the relevant notion of electric quadrupole moment tensor  $\underline{\underline{Q}}$  which quantifies the asymmetry in the charge distribution along the

different directions. The quadrupole tensor is defined as:

$$\underline{\underline{Q}} = \int_S \rho(\mathbf{r})(3\mathbf{r} \otimes \mathbf{r} - r^2\mathbf{1})dS. \quad (4.3)$$

For instance, the quadrupole moment of uniformly charged sphere  $\underline{\underline{Q}}^{\text{sph.}} = \mathbb{0}$  on the surface equals zero but is not zero for a uniformly charged ellipsoid or deformed cylinder as the one previously considered. In the case of the deformed cylinder, the quadrupole tensor is diagonal in the body basis  $(\mathbf{e}_1, \mathbf{e}_2, \mathbf{e}_3)$  and reads:

$$\underline{\underline{Q}}^{\text{cyl.}} = \begin{pmatrix} Q_1 & 0 & 0 \\ 0 & Q_2 & 0 \\ 0 & 0 & Q_3 \end{pmatrix}, \quad (4.4)$$

where  $Q_3 > Q_2 > Q_1$  and  $Q_1 + Q_2 + Q_3 = 0$ .

### Angular electric energy

Now that we have introduced the relevant concepts and the parameters of this problem, we can calculate the electric energy of a deformed cylinder subjected to the potential Eq. (4.2). It reads:

$$E_{\text{ele}}(\alpha, \beta, \gamma, t) = \frac{\eta U_{\text{AC}}}{z_0^2} \cos(\Omega t) \int_S (c_x x^2 + c_y y^2 + c_z z^2) \rho(\mathbf{r}) dS. \quad (4.5)$$

A dependency on the Euler angles and on the quadrupole electric tensor appears when performing the integration. Indeed, the charge distribution of the particle in the electric field depends on the particle shape characterized by the quadrupole tensor and on the particle angular position parametrized by the Euler angles. Unless we linearize this energy around angular positions of high symmetries, we cannot obtain a simple analytical expression.

For instance, the electric potential can be simply expressed to second order in the Euler angles around the angular position  $\alpha = 0, \beta = \pi/2, \gamma = 0$  as (see calculation in Appendix D.1):

$$E_{\text{ele}}(\alpha, \tilde{\beta}, \gamma, t) = \frac{1}{2} I_1 \omega_\alpha^2 \cos(\Omega t) \alpha^2 + \frac{1}{2} I_2 \omega_{\tilde{\beta}}^2 \cos(\Omega t) \tilde{\beta}^2 - \frac{1}{2} I_3 \omega_\gamma^2 \cos(\Omega t) \gamma^2, \quad (4.6)$$

where:

$$\omega_\alpha = \sqrt{\frac{2\eta U_{\text{AC}}}{3z_0^2} \frac{(c_y - c_z)(Q_3 - Q_2)}{I_1}}, \quad (4.7)$$

$$\omega_{\tilde{\beta}} = \sqrt{\frac{2\eta U_{\text{AC}}}{3z_0^2} \frac{(c_z - c_x)(Q_3 - Q_1)}{I_2}}, \quad (4.8)$$

$$\omega_\gamma = \sqrt{\frac{2\eta U_{\text{AC}}}{3z_0^2} \frac{(c_y - c_x)(Q_2 - Q_1)}{I_3}}, \quad (4.9)$$

where  $\beta = \pi/2 + \tilde{\beta}$ .

Considering an asymmetric Paul trap ensures that  $c_u - c_v \neq 0$  for  $u \neq v$  while considering an asymmetrically charged particle ensures that  $Q_i - Q_j \neq 0$  for  $i \neq j$ . We show

in Fig. 4.4 (a) both the deformed cylinder at the angular position  $\alpha = 0, \beta = \pi/2, \gamma = 0$  and at  $t = 0$  and the potential generated by the Paul trap in the spherical representation. Thanks to this representation, we can see that this angular position corresponds to a minimum of energy represented by the blue zone for  $\alpha$  and  $\beta$ . However, we can convince ourselves that the considered angular position is a maximum of energy for  $\gamma$ . This corresponds to the formula Eq. (4.6) where the only negative curvature of the energy is for the angle  $\gamma$  when  $t = 0$ . The angle  $\gamma$  reaches a minimum of energy at the position  $\gamma = \pm\pi/2$  as depicted in Fig. 4.4 (b). Technically, it is therefore not necessary to use an alternating voltage to confine the three angular degrees of freedom since the angular position  $\alpha = 0, \beta = \pi/2, \gamma = \pi/2$  corresponds to a minimum of energy for the three angles at  $t = 0$ . However, the use of a DC voltage leads to less stability for at least one center of mass mode which is constraining. Thus, we only consider AC potential. The curvatures for the different angles and thus the stability are inverted when  $t = T_{\text{Paul}}/2$  because  $\cos(\Omega t) = -1$  as we can see in Fig. 4.4 (c) for  $\alpha = 0, \beta = \pi/2, \gamma = 0$ . A ponderomotive torque is thus exerted on the three angular modes.

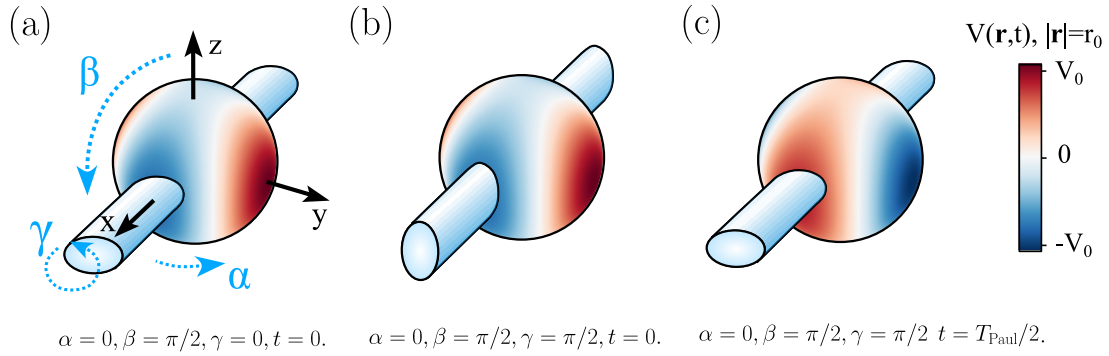


Figure 4.4: Schematic representation of a deformed cylinder in an asymmetric Paul trap potential for the three different set of parameters: (a)  $\alpha = 0, \beta = \pi/2, \gamma = 0, t = 0$ , (b)  $\alpha = 0, \beta = \pi/2, \gamma = \pi/2, t = 0$ , (c)  $\alpha = 0, \beta = \pi/2, \gamma = \pi/2, t = T_{\text{Paul}}/2$ . The spherical representation of the potential is shown in the middle of the deformed cylinder.

### 4.1.3 The librating regime

The regime for which a particle is angularly stable is called the librating regime. In order to attain stability with ponderomotive torque, one needs to estimate the  $q$  factor in the Mathieu equation.

#### Ponderomotive restoring torque

The potential of Eq. (4.6) gives rise to a restoring torque if the  $q$  factor of the Mathieu equation is below 0.9. In the same way as in Chapter 2 for the electric ponderomotive confinement of the center of mass and in Chapter 3 for the magnetic ponderomotive confinement of the magnet center of mass, we introduce the relevant  $q_\nu$  coefficient depending

Table 1: Experimental value of different physical parameters

Parameter	Approximate value	Unit
$U_{AC}$	$10^3$	V
$\eta$	0.1	-
$c_u$	1	-
$z_0$	30	$\mu\text{m}$
$I_i$	$10^{-22}$	$\text{kg}\cdot\text{m}^{-5}$
$Q_j$	$10^{-25}$	$\text{C}\cdot\text{m}^2$
$\omega_\alpha/2\pi$	$10^3$	Hz
$\gamma_\alpha/2\pi$	$10^3$	Hz
$\Omega/2\pi$	$10^3 - 10^4$	Hz

on the parameters of the problem for each angles  $\nu$ . We obtain:

$$q_\alpha = \frac{2\omega_\alpha^2}{\Omega^2} = \frac{4\eta U_{AC}}{z_0^2} \frac{(c_y - c_z)(Q_3 - Q_2)}{I_1 \Omega^2}, \quad (4.10)$$

$$q_{\tilde{\beta}} = \frac{2\omega_{\tilde{\beta}}^2}{\Omega^2} = \frac{4\eta U_{AC}}{z_0^2} \frac{(c_z - c_x)(Q_3 - Q_1)}{I_2 \Omega^2}, \quad (4.11)$$

$$q_\gamma = \frac{2\omega_\gamma^2}{\Omega^2} = \frac{4\eta U_{AC}}{z_0^2} \frac{(c_y - c_x)(Q_2 - Q_1)}{I_3 \Omega^2}. \quad (4.12)$$

Using the experimental values present in Table 1, we obtain a typical value for  $q_\nu$ :

$$q_\nu = \frac{10^7}{\Omega^2}. \quad (4.13)$$

For a Paul trap frequency drive  $\Omega/2\pi = 2.0$  kHz, we obtain that  $q_\nu \approx 0.1 < 0.9$  leading to angular ponderomotive confinement for all angles.

### Equilibrium positions

In the previous calculations, we performed a small angle approximation around the position  $\alpha = 0, \beta = \pi/2, \gamma = 0$  and we saw that the ponderomotive torque could result in a confining torque. This position is actually not the only accessible stable angular position. In Fig. 4.5, we have represented the 6 different positions allowing a ponderomotive angular stabilization. We have not counted the degenerated position given by a  $\pi$ -rotation around a symmetry axis of the particle which would multiply the number of angular positions by a factor 4 leading to a total of 24 stable positions. For each of the given positions  $i$ , the relevant  $q^{(i)} = \max(q_\alpha^{(i)}, q_\beta^{(i)}, q_\gamma^{(i)})$  coefficients can be estimated which leads to different stability criteria.

### Experimental observation

The librating regime has been reached experimentally in our micro Paul trap for different types of particles such as diamonds, silica rods and ferromagnets (80; 93). Experiments prove this angular stability. A robust proof is the observation of ODMR or MDMR spectra with 8 resonances corresponding to the 4  $\text{NV}^-$  classes of a levitating diamond in the presence of a magnetic field. If the diamond was not angularly stable, the resonances would be broadened due to the change of the anisotropy direction of the  $\text{NV}^-$  center

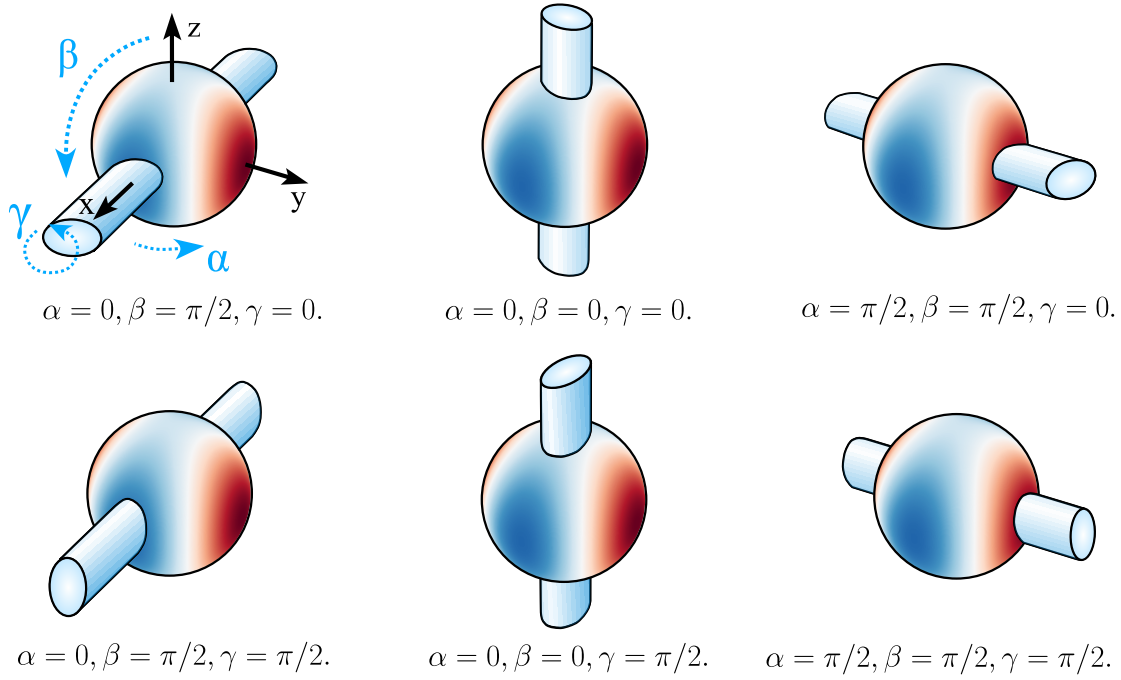


Figure 4.5: Schematic showing a deformed cylinder in an asymmetric Paul trap potential at  $t = 0$  for the six possible stable configurations of the librating regime.

in the laboratory frame. Moreover, this proves that the particle is sufficiently angularly confined not to see any enlargement of the ODMR linewidth due to the mean angular displacement caused by collisions with the surrounding gas particles. We have shown in Fig. 4.6 (a) an ODMR spectra of a stable levitating diamond. In addition, the stability of the speckle spot of particle like the one shown in Fig. 4.6 (b) is a practical proof of the angular stability of a levitated particle. Finally, a last proof is the possibility to observe the librating mechanical modes in vacuum, as presented in Fig. 4.6 (c).

#### Center of mass and angular stability

In our experiments, the six mechanical degrees of freedom, i.e. the three center of mass modes and the three angular modes, are confined by the ponderomotive potential generated by the Paul trap. Furthermore, the resulting frequencies of the six modes are generally in the 100's of Hz range. This means that the  $q_u$  factors of the center of mass modes and the  $q_\nu$  are of the same order of magnitude. We can estimate the ratio between these two coefficients to be:

$$\left| \frac{q_u}{q_\nu} \right| = \left| \frac{c_u}{\Delta c_\nu} \right| \left| \frac{Q_{\text{tot}}}{\Delta Q_\nu} \right| \frac{m}{I_\nu} \approx 1, \quad (4.14)$$

where  $c_u$  is the characteristic curvature along the  $u$  direction,  $\Delta c_\nu = c_\mu - c_\rho$  is the characteristic asymmetry of the Paul trap potential in the direction  $\nu$  perpendicular to the  $\mu$  and  $\rho$  directions,  $Q_{\text{tot}}$  is the total charge,  $\Delta Q_\nu$  is the total charge asymmetry between  $\nu$  and the two other angles,  $m$  is the mass and  $I_\nu$  is the moment of inertia. For an asymmetric Paul trap,  $|c_u/\Delta c_\nu| \approx 1$ . For an asymmetrically charged particle,  $\Delta Q_\nu = S Q_{\text{tot}}$  where  $S$  is the particle surface. We also have  $m/I_\nu \approx 1/S$ . Consequently, we can estimate that

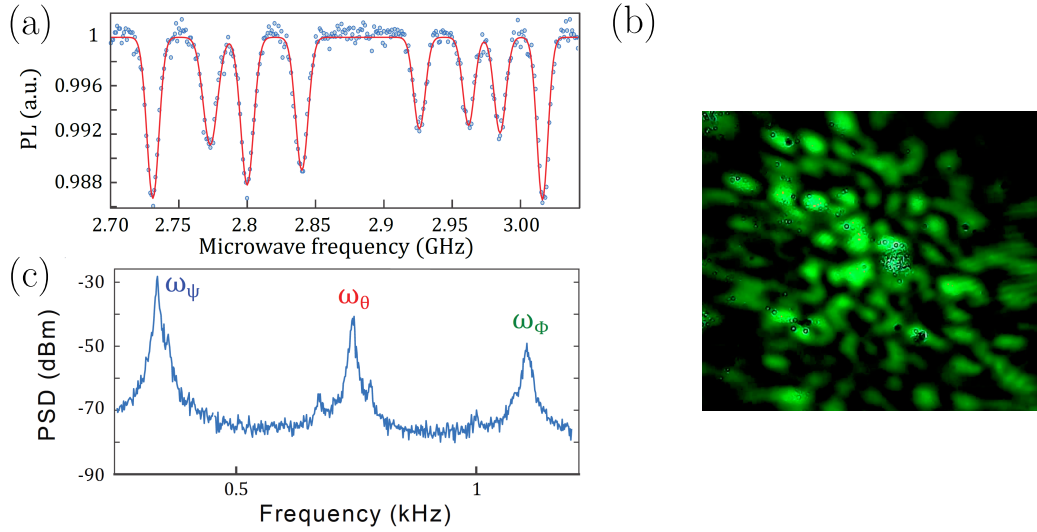


Figure 4.6: (a) ODMR spectra from an angularly stable levitating diamond. Taken from (80). (b) Characteristic speckle pattern of an angularly stable levitating diamond observed on a CCD camera in the image plane. The set-up used to obtain this pattern is described in Chapter 2. (c) PSD of the motion of an angularly stable diamond showing three libration modes. Taken from (90).

$q_u/q_v \approx 1$  meaning that the center of mass modes and the angular modes can be confined using the same Paul trap drive, as confirmed by the experiment.

The ponderomotive torque of the Paul trap on a levitating particle can thus lead to its angular confinement. In the following, we show the existence of a second angular stable regime where the particle fully rotates with a rotation period given by twice the Paul trap period.

## 4.2. Full rotation in a Paul trap: the locking regime

When one leaves the Paul trap stability domain for the center of mass, the particle is no longer confined and it escapes from the trap. Interestingly, leaving the stability domain for the angular ponderomotive confinement does not imply the particle loss but allows to explore a parameter space where the intrinsic nonlinearities of the angular dynamics are no longer negligible. We can then ask the following question: what is the resulting dynamics? We will see that, in this case, another stability regime can be reached where the particle rotates deterministically around itself at a specific rotating frequency given by half the Paul trap drive frequency  $\Omega/2$ : we named this regime the locking regime.

### 4.2.1 Origin of the locking regime

In this part, we explain the origin of the locking regime. First, we derive the equation of motion and we compare it to the Kapitza pendulum equation of dynamics. Then, we calculate the stability criterion for the locking regime.

#### Non linear equation of motion

Here, we no longer restrict the study of the dynamics of the angle  $\alpha$  around a specific angular position as we did in the previous chapter. We thus calculate the potential energy

of the deformed cylinder as a function of  $\alpha$  without making the small angle approximation. We also assume that the two angles  $\beta$  and  $\gamma$  remain fixed at positions  $\beta = \pi/2, \gamma = 0$ . We will verify *a posteriori* that the hypothesis  $\beta = \pi/2, \gamma = 0$  is well justified in the locking regime for high rotation speeds (see part 4.2.3). Under these conditions, the potential energy of the angle  $\alpha$  simply reads (see calculations in Appendix D.2):

$$E_{\text{ele}}(\alpha, t) = \frac{1}{2} I_1 \omega_\alpha^2 \cos(\Omega t) \sin^2 \alpha. \quad (4.15)$$

This potential features nonlinearity given by the  $\sin \alpha$  term. The equation of the dynamics for  $\alpha$  can be written:

$$\ddot{\alpha} + \omega_\alpha^2 \cos(\Omega t) \frac{\sin(2\alpha)}{2} = 0. \quad (4.16)$$

Apart from the DC term originating from the gravity that tends to reverse the pendulum in the Kapitza experiment, this equation is perfectly similar to the Kapitza pendulum dynamical equation mentioned in introduction Eq. (4.1). We have already discussed the fact that the Kapitza pendulum has two angular stable regimes. The first regime is when the angle is confined. We have seen that this stability regime also exists in the case of our levitating particles, this is the librating regime. The second stability regime of the Kapitza pendulum is the locking regime (148; 149) where the pendulum rotates in phase with the excitation frequency  $\Omega$  of the pendulum base. It is therefore expected that this stability regime also exists in the context of a particle levitating in a Paul trap.

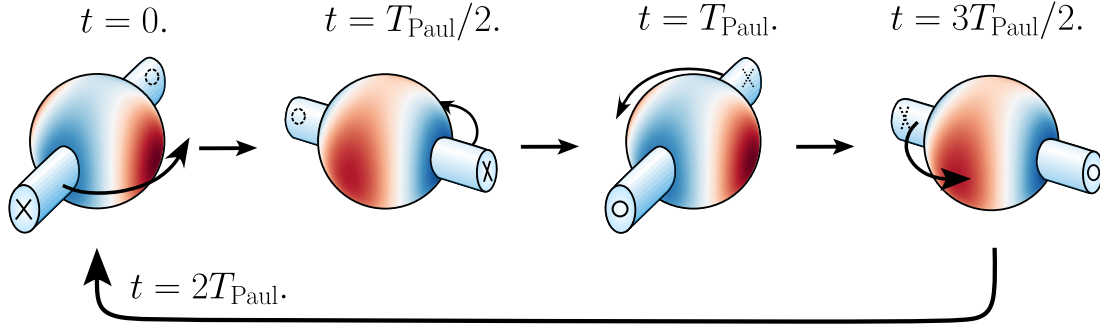


Figure 4.7: Schematic showing four steps in the rotation of a deformed cylinder in the locking regime. The rotation period equals  $2T_{\text{Paul}}$ .

#### Theoretical study of the locking regime

We can convince ourselves that the rotation of the particle around the  $z$  axis is stable for  $\alpha$  when the particle rotates at half the Paul trap frequency  $\Omega/2$ . In Fig. 4.7, we have represented the evolution of a deformed cylinder in the asymmetric Paul trap potential assuming an initial angular velocity  $\Omega/2$ . To distinguish the two degenerate positions  $\alpha = 0$  and  $\alpha = \pi$ , a cross has been drawn at one extremity of the cylinder and a circle at the other one. At  $t = 0$ , the particle is in a minimum of potential for  $\alpha = 0$ . At  $t = T_{\text{Paul}}/2$ , the trap potential is reversed and the particle is still in a minimum of potential at  $\alpha = \pi/2$ . At  $t = T_{\text{Paul}}$ , the Paul trap potential is the same than at  $t = 0$  and the position  $\alpha = \pi$  is at a minimum of potential. At  $t = 3T_{\text{Paul}}/2$ , the trap potential is reversed and the particle is

still in a minimum of potential at  $\alpha = 3\pi/2$ . Finally, at  $t = 2T_{\text{Paul}}$ , the cylinder recovers its initial angular position at  $\alpha = 0$ . The rotation period for the deformed cylinder is thus twice the Paul trap period, such that  $T_{\text{rot}} = 2T_{\text{Paul}}$ . We have considered a counterclockwise rotation but the particle could also rotate clockwise.

To evaluate the equation of motion governing the stability of  $\alpha$  in the anti-clockwise rotating frame, we consider the change of variable  $\tilde{\alpha} = \alpha - \Omega/2t$ . By injecting this expression into Eq. (4.16), we obtain the equation of motion for  $\tilde{\alpha}$ :

$$\ddot{\tilde{\alpha}} + \frac{\omega_\alpha^2}{2} \frac{\sin(2\tilde{\alpha})}{2} = -\frac{\omega_\alpha^2}{2} \frac{\sin(2\tilde{\alpha} + 2\Omega t)}{2}. \quad (4.17)$$

To study the stability of this equation, we can distinguish two cases: the fast rotation case corresponding to  $\Omega \gg \omega_\alpha$  and the slow rotation case  $\Omega \simeq \omega_\alpha$ .

**Fast rotation:**  $\Omega \gg \omega_\alpha$

In the case of a fast rotation i.e. where  $\Omega \gg \omega_\alpha$ , the right-hand side of Eq. (4.17) can be averaged out via the secular approximation and the equation of motion is simply the one of a classical pendulum:

$$\ddot{\tilde{\alpha}} + \frac{\omega_\alpha^2}{2} \frac{\sin(2\tilde{\alpha})}{2} = 0. \quad (4.18)$$

In this case, the angular potential energy for  $\tilde{\alpha}$  is simply:

$$E_{\text{ele}}(\tilde{\alpha}, t) = -\frac{1}{2} I_1 \frac{\omega_\alpha^2}{4} \cos(2\tilde{\alpha}). \quad (4.19)$$

This potential is confining around the equilibrium position  $\tilde{\alpha} = 0$ .

**Slow rotation:**  $\Omega \simeq \omega_\alpha$

In the case where  $\Omega$  and  $\omega_\alpha$  are of the same order of magnitude, we can perform the small angle approximation around the position  $\tilde{\alpha} = 0$  to estimate the stability of  $\tilde{\alpha}$ . This equation can be written as:

$$\ddot{\tilde{\alpha}} + \frac{\omega_\alpha^2}{2} (1 + \cos(2\Omega t)) \tilde{\alpha} \approx -\omega_\alpha^2 \sin(2\Omega t), \quad (4.20)$$

This equation is a Mathieu equation with a constant confinement term as well as a ponderomotive torque oscillating at  $2\Omega$ . The right-hand side of Eq. (4.20) is an excitation term at  $2\Omega$ . To simplify the study and get an intuition on the stability diagram of the locking regime, we assume that this term is negligible. Note that it is a strong approximation since it can contribute to move the particle away from the region where the small angle approximation is valid and therefore perturbs the stability. Under this approximation, we can calculate the Mathieu coefficients  $a_{\tilde{\alpha}}$  and  $q_{\tilde{\alpha}}$  and obtain:

$$a_{\tilde{\alpha}} = \frac{\omega_\alpha^2}{2\Omega^2} \quad \text{and} \quad q_{\tilde{\alpha}} = \frac{\omega_\alpha^2}{4\Omega^2}. \quad (4.21)$$

In Fig. 4.8, a stability diagram of the Mathieu equation as a function of the two parameters  $a_{\tilde{\alpha}}$  and  $q_{\tilde{\alpha}}$  has been plotted. We have drawn the line of equation  $a_{\tilde{\alpha}} = 2q_{\tilde{\alpha}}$ . We can see that in the case of sufficiently fast rotation, i.e. verifying  $\Omega \gg \omega_\alpha$  or equivalently

$0 < a_{\bar{\alpha}}, q_{\bar{\alpha}} \ll 1$ , the locking regime is always stable, as predicted in the previous subsection. In the opposite case i.e.  $\Omega \simeq \omega_{\bar{\alpha}}$ , there are regions of instability. Leaving the stability zone for the libration means that  $q_{\alpha} = 0.9$  (assuming that the linearized and non linear equations of motion for  $\alpha$  gives the same stability domain). However, the  $q_{\bar{\alpha}}$  factor calculated for the locking regime is four times smaller than the  $q_{\alpha}$  factor in the librating regime as shown by Eq. (4.12) and Eq. (4.21). It equals  $q_{\bar{\alpha}} = 0.225$  when  $q_{\alpha} = 0.9$ . Furthermore,  $a_{\bar{\alpha}} = 0.45$  in this case. The values of  $q_{\bar{\alpha}}$  and  $a_{\bar{\alpha}}$  are in the stability regime of the Mathieu equation so the locking regime is stable. We can therefore expect to reach the stable locking regime once the librating regime becomes unstable. Nevertheless, we must keep in mind that we neglected the right-hand side of Eq. (4.20), which can lead to instability. In the next part, we perform numerical simulations to confirm that we reach the locking regime when we leave the stability domain of the librating regime.

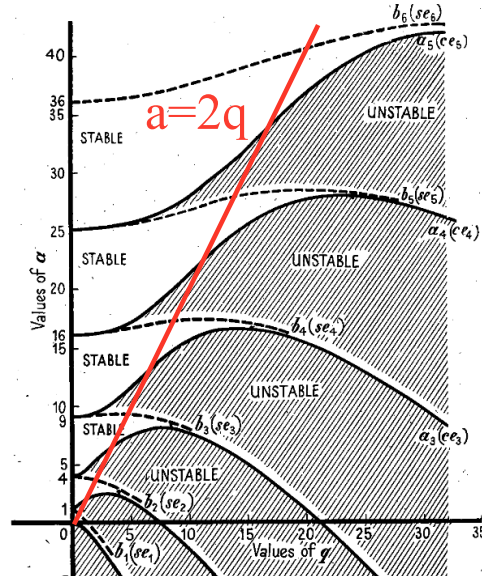


Figure 4.8: Stability diagram of Mathieu equation. Modified from (150).

#### Transition from the librating to the locking regime

One of the main questions of this section was: what happens to the angular dynamics when we leave the stability regime of libration? We have seen in the previous paragraphs that the locking regime has an *a priori* wider stability diagram. This regime is thus expected to be reached by progressively lowering the frequency of the Paul trap  $\Omega/2\pi$ , resulting in an increase in the  $q_{\alpha}$  factor leading to the instability of the librating regime. For this purpose, numerical simulations have been carried out by collaborators C.C. Rusconi and B. Stickler from Eq. (4.16) with realistic parameter values according to our experiment. Adding a damping term in the equation of motion in order to account for collisions of the levitated particle with the gas molecules. The equation of motion used to make the numerical simulations is:

$$\ddot{\alpha} + \gamma_{\alpha} \dot{\alpha} + \omega_{\alpha}^2 \cos(\Omega t) \frac{\sin(2\alpha)}{2} = 0, \quad (4.22)$$

where  $\gamma_\alpha$  can be estimated using (97). In our experiment,  $\gamma_\alpha/2\pi \approx 1.0$  kHz at atmospheric pressure (36). The addition of a friction term reduces the stability range of the locking regime because the friction adds a constant torque opposed to the rotational motion of a spinning particle. We study the role of the damping in more details in the following part.

The results of the numerical simulations are presented in Fig. 4.9. In Fig. 4.9 (a), a stability diagram of the equation Eq. (4.22) is presented as a function of the Paul trap frequency  $\Omega/2\pi$  and the voltage  $U_{AC}$ . The grey hatched area corresponds to the librating regime instability domain for Eq. (4.22) while the grey area corresponds to the librating regime instability domain for the linearized Eq. (4.22) by considering  $\sin(\alpha) = \alpha$  (which corresponds to the approximation we made to treat the librating regime). It can be seen that the stability zone is wider for the non-linear equation which means that the libration stability domain is actually slightly larger than the one estimated by linearizing the dynamical equation.

In Fig. 4.9 (b), we have represented the dynamics of  $\alpha$  inside the stability domain of Eq. (4.16) but outside of the stability domain of the corresponding linearized equation. It can be seen that the angle describes a parametric excited motion at twice the Paul trap period  $2T_{\text{Paul}}$ . For the remainder, this regime is called the transitional regime. For a lower Paul trap frequency, the angular dynamics shown in Fig. 4.9 (c) is a mix between the librating dynamics represented by the grey areas and the locking dynamics represented by the white area. Finally, we see in Fig. 4.9 (d) that we access to the locking regime for lower Paul trap frequency. These numerical simulations seem to confirm the theoretical expectations that the stability range of the locking regime is larger for low Paul trap frequencies.

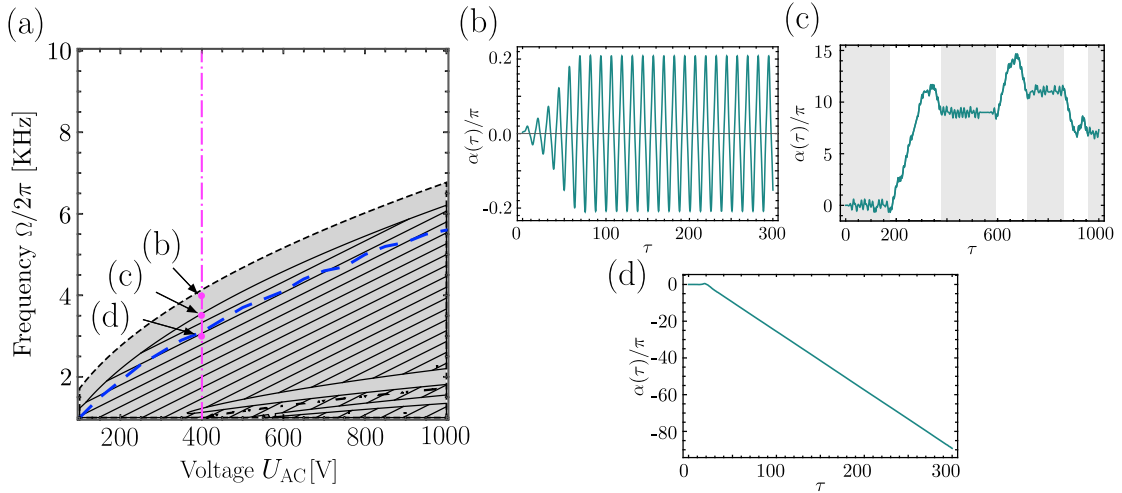


Figure 4.9: (a) Stability diagram for different angular regimes. The grey hatched area corresponds to the instability domain for the nonlinear Eq. (4.16). The uniform grey area corresponds to the instability domain of the linearized Eq. (4.16). (b), (c), (d) Temporal trace of the angular position  $\alpha$  for different values of the Paul trap frequency indicated on (a) where  $\tau = \Omega t$  is a rescaled quantity.

We will see in the following part that these results are also in full agreement with the experimental observations.

### 4.2.2 Experimental observations

The previous considerations give us a method for experimentally accessing the locking regime. In this part, we show stable locking for different types of particles.

#### Rotation at $\Omega/2$

The smoking gun of the locking regime is when the particle rotates at the angular velocity  $\Omega/2$ . We therefore expect to see a highly resolved peak at  $(\Omega/2)/2\pi$  on the spectrum analyzer when a particle enters this regime. In Fig. 4.10, we have represented two Power Spectral Densities (PSD) obtained with the transmission signal for the same  $15 \mu\text{m}$  diamond from Adamas company levitating in vacuum at  $7.0 \times 10^{-1}$  mbar. Figure 4.10 (a) represents a PSD in the librating regime at the trap frequency of  $\Omega/2\pi = 1510$  Hz. We see that there is a sharp peak at the Paul trap drive frequency  $\Omega/2\pi$  corresponding mostly to the center of mass micro motion. Moreover, we can see several mechanical modes that we will identify later. By lowering the frequency of the trap, we can see in Fig. 4.10 (b) that the particle changes regime and a peak appears at the frequency  $(\Omega/2)/2\pi$  in the PSD signal as well as a disappearance of some resonance peaks. The Paul trap frequency equals  $\Omega/2\pi = 1260$  Hz. This signal is a signature of the particle entering the locking regime where the particle rotates on itself.

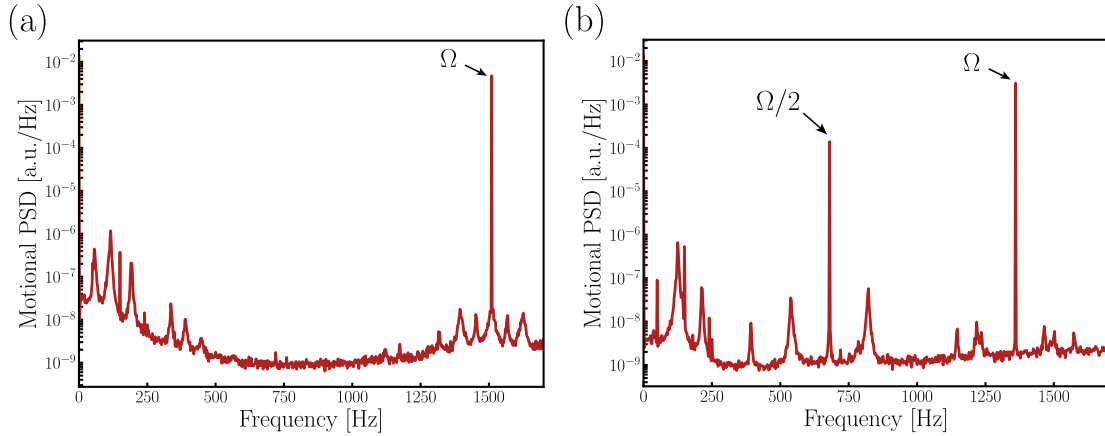


Figure 4.10: (a) PSD of the motion of a diamond in the librating regime at  $7.0 \times 10^{-1}$  mbar with a Paul trap frequency  $\Omega = 1510$  Hz. (b) PSD of the motion of a diamond in the locking regime at  $7.0 \times 10^{-1}$  mbar with a Paul trap frequency  $\Omega = 1260$  Hz.

The peak at  $(\Omega/2)/2\pi$  could however correspond to the transitional regime where the particle is parametrically excited at  $(\Omega/2)/2\pi$  as shown in Fig. 4.9 (b). An experimental method to convince oneself that the particle is indeed in the locking regime performing full rotation is to visualize the motion of the particle using a laser pulsed at a frequency close to  $(\Omega/2)/2\pi$ . To do this, we slightly defocus the laser from the particle and we use an AOM that turns on the laser for a short period of time  $\delta t_1$  every  $T_{\text{Paul}} + \delta t_2$  with  $\delta t_1, \delta t_2 \ll T_{\text{Paul}}$ . This technique allows us to visualize in slow motion the movement of the particle on a screen. In Fig. 4.11, we show the experimental set-up where the shadow of the particle is projected on a screen. In Fig. 4.11 (a)-(i) (resp. (b)-(i)), we schematically represent the cylinder at  $t = 0$  (resp.  $t = T_{\text{Paul}}/2$ ). We take a picture of the screen at these two particular moments that are shown Fig. 4.11 (a)-(ii) and (b)-(ii). We can then convince ourselves by looking at the shadow of the particle that the particle does

describe a total rotation motion and not a parametrically excited motion at the frequency  $(\Omega/2)/2\pi$ .

In the PSD shown in Fig. 4.10 (b), we make sure that the particle was indeed in the locking regime using this technique. In the next section, we will use  $NV^-$  centers inside the diamond to prove the full rotation of the particle.

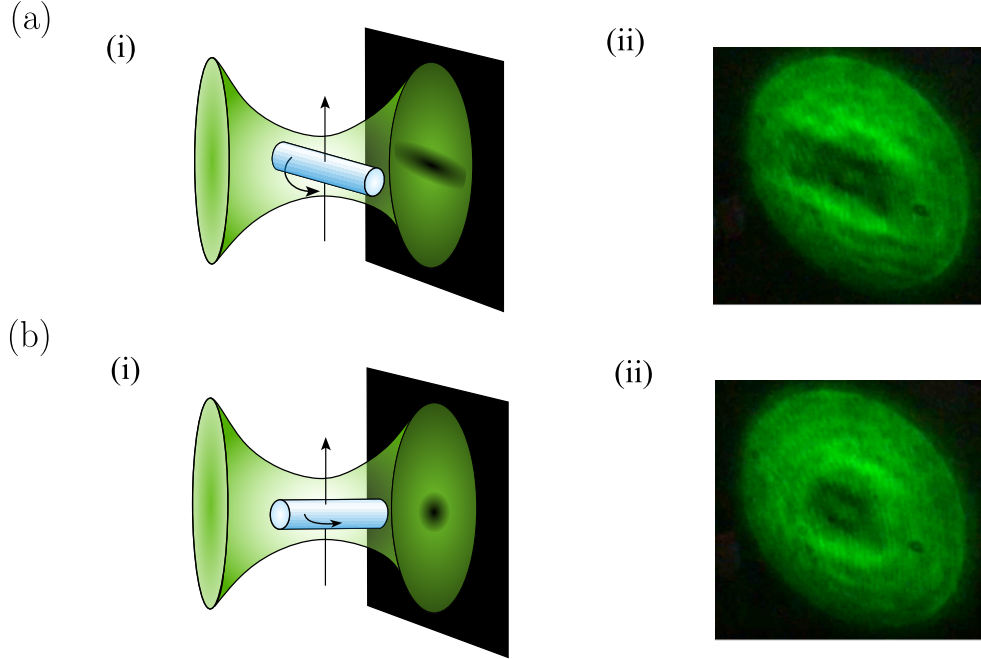


Figure 4.11: (a) (i) Schematic showing a rotating cylinder at  $t = 0$  illuminated by the transmitted light. The shadow of the cylinder can be seen on a distant screen. (ii) Photo of the screen at  $t = 0$ . (b) (i) Schematic picture of a rotating cylinder at  $t = T_{\text{Paul}}/2$  with a screen illuminated by the transmitted light. The shadow of the cylinder can be seen on a distant screen. (ii) Photo of the screen at  $t = T_{\text{Paul}}/2$ .

### Damping and hysteretic behavior

One of the interesting regime for magnetic particle rotation is when rotation frequency becomes comparable to the rate of change of the internal spin dynamics (in the kHz-MHz range for the  $NV^-$  center). Another benefit would be to have high frequency gyroscopic modes, which could be useful for spin-mechanical protocols away from noise and in the resolved sideband regime. One limitation that we have not touched upon is the influence of damping on the maximum reachable angular velocity in the locking regime. We will prove that damping strongly reduces the stability domain for the locking regime for high value of  $\Omega$ . We consider the equation of motion Eq. 4.22. The addition of friction increases the stability domain for Mathieu equations (151). The librating regime domain of stability is thus enlarged. However, a particle in rotation in the locking regime subjected to friction perceives a constant torque which tends to slow down the rotation and thus to move away the particle from its equilibrium position in the rotating frame. Damping thus reduces the stability domain of the locking regime. To simplify the calculation, we assume that

$\Omega \gg \omega_\alpha$ . The equation for the angle  $\tilde{\alpha}$  in the rotating frame reads:

$$\ddot{\tilde{\alpha}} + \gamma_\alpha \dot{\tilde{\alpha}} + \frac{\omega_\alpha^2 \sin(2\tilde{\alpha})}{2} = -\frac{\gamma_\alpha \Omega}{2}, \quad (4.23)$$

where  $-\frac{\gamma_\alpha \Omega}{2}$  is the constant damping torque in the rotating frame. We can write the potential energy as the sum of the Paul trap and damping torques giving:

$$E_{\text{ele}}(\tilde{\alpha}) = I_1 \frac{\gamma_\alpha \Omega}{2} \tilde{\alpha} - \frac{1}{2} I_1 \frac{\omega_\alpha^2}{4} \cos(2\tilde{\alpha}). \quad (4.24)$$

This potential energy has a minimum if and only if  $\Omega \ll \Omega_{\text{max}}^{(\text{lock.})}$  where:

$$\Omega_{\text{max}}^{(\text{lock.})} = \frac{\omega_\alpha^2}{\gamma_\alpha} \propto U_{\text{AC}}. \quad (4.25)$$

Using the experimental values at atmospheric pressure  $\omega_\alpha/2\pi \approx 1.0$  kHz and  $\gamma_\alpha/2\pi \approx 1.0$  kHz, we obtain that  $\Omega_{\text{max}}^{(\text{lock.})}/2\pi \approx 1.0$  kHz. The angular speed could reasonably reach the MHz range at 1 mbar where the damping coefficient  $\gamma_\alpha/2\pi$  is about 1 Hz.

Remembering that we have made the assumption  $\Omega \gg \omega_\alpha$  to calculate  $\Omega_{\text{max}}^{(\text{lock.})}$ , we can use numerical simulations to estimate the value of  $\Omega_{\text{max}}^{(\text{lock.})}$  in the general case. To do so, we numerically calculate the order parameter  $f_{\text{rot}} = \langle \dot{\alpha} \rangle$ , averaged on a time scale larger than  $1/\gamma_\alpha$ . When  $f_{\text{rot}} = \pm\Omega/2$ , the particle is in the locking regime while, when  $f_{\text{rot}} = 0$ , it is in the librating regime. In Fig. 4.12, we show two plots of  $f_{\text{rot}}$  as a function of the Paul trap frequency  $\Omega/2\pi$  using the experimental values presented in Table 1. We treated the case of a particle initially in the librating regime in Fig. 4.12 (a)-Top i.e. with the initial conditions  $2\alpha(0) = 0.01$  and  $\dot{\alpha}(0)/(\Omega/2) = 0.01$ . In Fig. 4.12 (a)-Bottom, we have treated the case of a particle initially in the locking regime, i.e. with the initial conditions  $2\alpha(0) = 0.01$  and  $\dot{\alpha}(0)/(\Omega/2) = 1.01$ . We can see that the libration is always stable for a trap frequency stronger than a threshold frequency while the locking regime is not. This is due to friction that prevents the particle from rotating beyond a certain value of angular velocity  $\Omega_{\text{max}}^{(\text{lock.})}$ , as expected by the previously exposed theoretical model. We observe a hysteretic behavior between the locking regime and the librating regime. Indeed, the transition frequency from one regime to another depends on the regime in which we are initially. This hysteretic behavior is characteristic of non-linear dynamics and attests of two stable regimes that can be accessed by changing the initial conditions  $\alpha(0), \dot{\alpha}(0)$ .

In order to access the angular regime of interest, it is important to estimate the stability limits of the librating and locking regimes as a function of experimental parameters such as the AC voltage  $U_{\text{AC}}$  and the Paul trap frequency  $\Omega/2\pi$ . We have already numerically estimated in Fig. 4.9 the stability limit of the librating regime. Using Eq. 4.12, an approximated value of the minimal Paul trap frequency  $\Omega_{\text{min}}^{(\text{lib.})}$  is found to be:

$$\Omega_{\text{min}}^{(\text{lib.})} = \sqrt{\frac{2}{0.9}} \omega_\alpha \propto \sqrt{U_{\text{AC}}}. \quad (4.26)$$

In Fig. 4.12 (b), we plotted in blue the stability threshold from the librating regime to the locking regime as well as in red the stability threshold from the locking regime to the librating regime as a function of the voltage  $U_{\text{AC}}$ . The dotted lines are the values obtained from numerical simulations while the dashed lines correspond to the expected values using

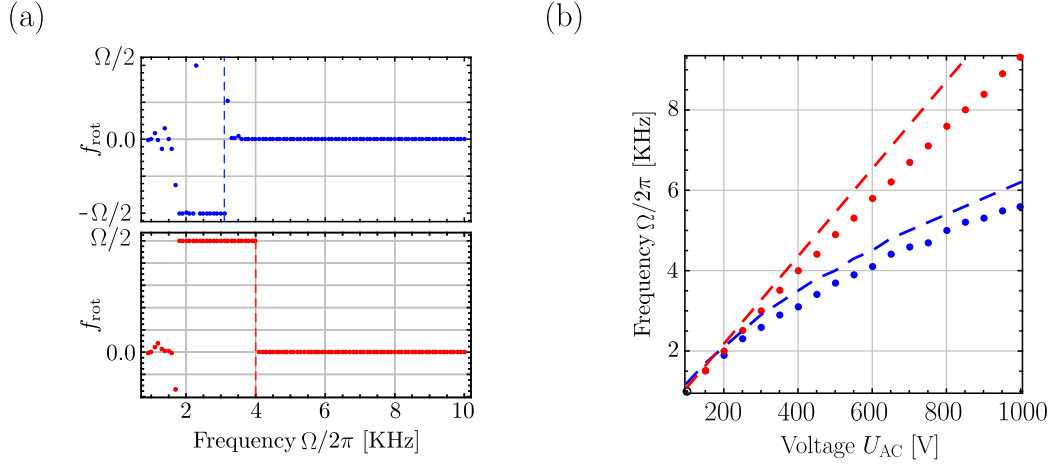


Figure 4.12: (a) Angular velocity as a function of the Paul trap frequency obtained by numerical simulations with the initial conditions  $2\alpha(0) = 0.01$  and  $\dot{\alpha}(0)/(\Omega/2) = 0.01$  (Top) and  $2\alpha(0) = 0.01$  and  $\dot{\alpha}(0)/(\Omega/2) = 1.01$  (Bottom). (b) Red dashed line: approximated value of  $\Omega_{\max}^{(\text{lock.})}$  using Eq. (4.25). Red dotted line: numerical value of  $\Omega_{\max}^{(\text{lock.})}$ . Blue dashed line: approximated value of  $\Omega_{\min}^{(\text{lib.})}$  using Eq. (4.26). Blue dotted line: numerical value of  $\Omega_{\min}^{(\text{lib.})}$ .

the approximated formulas given by Eq. (4.26) for  $\Omega_{\min}^{(\text{lib.})}$  (the blue dashed line) and by Eq. (4.25) for  $\Omega_{\max}^{(\text{lock.})}$  (the red dashed line). It can be seen that the approximate values and those obtained by numerical simulations are close to each other and follow the same trend.

### Experimental measurement of the stability domains

These threshold values could be measured experimentally with a levitated cylindrical silica rod from Nippon Electric Glass Company of radius  $r = 2 \mu\text{m}$  and length  $l = 15 \mu\text{m}$  at atmospheric pressure such as the one shown in Fig. 4.13 (a). To obtain an experimental graph like the one in Fig. 4.12 (b), a silica rod is injected at a given value of voltage  $V_{\text{AC}}$  and frequency  $\Omega/2\pi$  by being initially in the librating regime. We then decrease the Paul trap frequency until we reach the threshold value  $\Omega_{\min}^{(\text{lib.})}/2\pi$  where we enter the locking regime. Passed this value, we increase the frequency of the trap until we reach the upper limit of the locking regime given by the frequency  $\Omega_{\max}^{(\text{lock.})}/2\pi$ . We repeat this protocol with the same particle for different values of the voltage  $V_{\text{AC}}$  and record  $(\Omega, V_{\text{AC}})$  each time. We use the previously described stroboscopic technique using the AOM to verify in which angular regime the particle is. The measurement is not trivial because the center of mass stability also depends on the trap frequency and the trap voltage. This experiment thus required testing several silica particles before having one that has a large enough center of mass stability domain.

Figure 4.13 (b) shows a graph of the evolution of the two experimental threshold values  $\Omega_{\min}^{(\text{lib.})}/2\pi$  and  $\Omega_{\max}^{(\text{lock.})}/2\pi$ . We notice that the trend of the two curves is not the same, as expected. The red curve showing  $\Omega_{\max}^{(\text{lock.})}/2\pi$  is linear in  $V_{\text{AC}}$  to a good approximation. This is predicted by our proposed model and by the numerical simulations in Fig. 4.9 (b). Furthermore, the frequency dependence of the threshold value for the blue curve showing

the experimental value of  $\Omega_{\max}^{(\text{lock.})}/2\pi$  is not linear in the voltage  $V_{\text{AC}}$  and instead shows a square root dependency. Again, this is well predicted by the model and the numerical simulations presented in Fig. 4.12 (b).

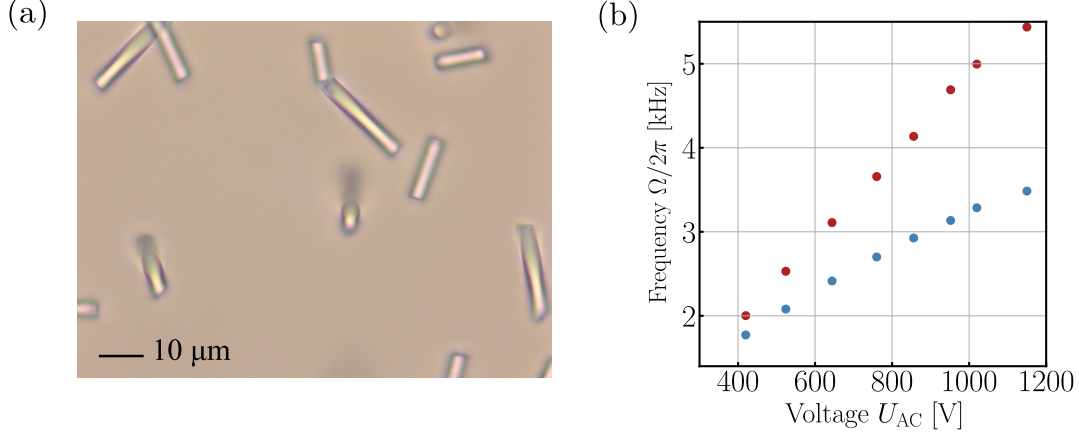


Figure 4.13: (a) Microscope image of the silica rods of radius  $r = 2 \mu\text{m}$  and length  $l = 15 \mu\text{m}$ . (b) Red dotted line: experimental value of  $\Omega_{\max}^{(\text{lock.})}$  obtained with a silica rod of radius  $r = 2 \mu\text{m}$  and length  $l = 15 \mu\text{m}$ . Blue dotted line: experimental value of  $\Omega_{\min}^{(\text{lib.})}$  obtained with the same silica rod.

#### Rotation under vacuum

A key requirement to observe the geometric quantum phase (46) or the Barnett effect (48) is to reach high rotation speeds, ideally in the MHz range. To do so, one needs to rotate magnetic particles under vacuum in order to reduce damping and thus increases  $\Omega_{\max}^{(\text{lock.})}$ . At  $10^{-1}$  mbar, it is expected that  $\Omega_{\max}^{(\text{lock.})}/2\pi \approx 1$  MHz.

In this part, we prove that we can rotate  $15 \mu\text{m}$  Adamas diamonds under vacuum at  $7.0 \times 10^{-1}$  mbar. In Fig. 4.14 (a), we show the PSD of the motion of an angularly stable  $15 \mu\text{m}$  Adamas diamond under vacuum for different values of the Paul trap frequency  $\Omega/2\pi$ . For every PSDs, we observe a sharp peak at  $\Omega/2\pi$  characteristic of the micro-motion. In addition, we observe at least five different resonant modes. These modes correspond to the 3 resonance modes of the center of mass as well as the 3 libration modes. Using the hysteretic behavior between the librating and locking regimes, we decrease the Paul trap frequency  $\Omega/2\pi$  until we reach the locking regime. Figure 4.14 (b) shows the PSD of the motion of the diamond being in the locking regime for different values of  $\Omega/2\pi$ . We observe a peak at  $(\Omega/2)/2\pi$  characteristic of the particle rotation in the locking regime and the micro-motion peak at  $\Omega/2\pi$ . Three distinct resonance peaks clearly detach from the noise. These three peaks correspond to the three frequencies of the center of mass modes. In Fig. 4.14 (a), we can thus determine which peak corresponds to a given center of mass mode because their resonant frequencies are not affected by the angular motion of the particle.

So far, we explained the physical origin of the locking regime in a Paul trap allowing a particle to rotate at a frequency corresponding to half the frequency of the Paul trap. We have also shown how this regime can be reached by playing on the frequency of the trap. We have given several experimental evidences that the locking regime can be reached for

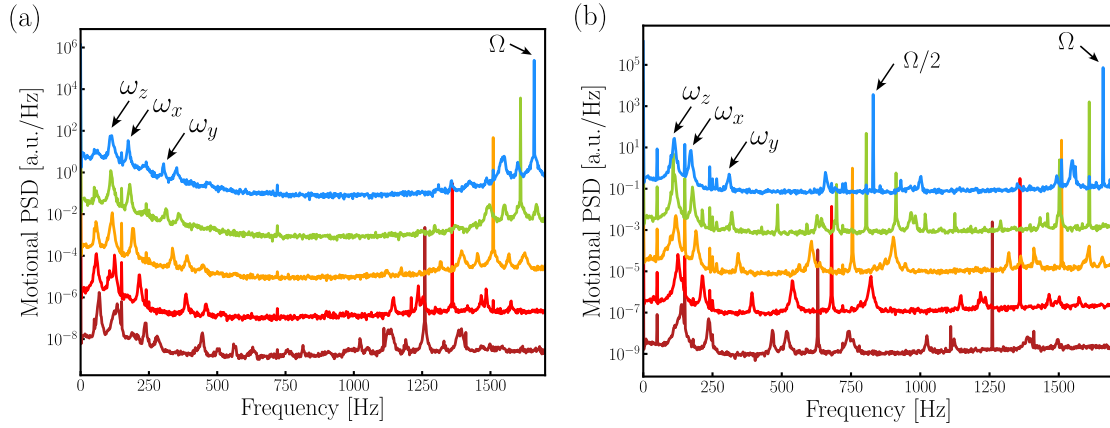


Figure 4.14: (a) PSD of the motion of a 15 micron Adamas diamond in the librating regime for different values of  $\Omega/2\pi$ . (b) PSD of the same 15 micron Adamas diamond in the locking regime for different values of  $\Omega/2\pi$ . The color code for the curves for different values of  $\Omega/2\pi$  is: brown: 1260 Hz, red: 1360 Hz, yellow: 1510 Hz, green: 1610 Hz and blue: 1660 Hz.

different particles such as diamonds or silica rods. Finally, we have proven that particles can even rotate under vacuum which is a key step towards reaching rotation speed in the MHz range.

We now return to the hypothesis formulated in section 4.2.1 where we reduced the angular dynamics of the levitated particles to the one-dimensional dynamics of the angle  $\alpha$ . We have thus assumed that the angles  $\beta, \gamma$  were fixed which is a strong assumption. In the following part, we prove the validity of this assumption.

### 4.2.3 Full angular stability in the rotating frame

In the previous section, the locking regime was studied by considering the angles  $\beta$  and  $\gamma$  at the angular positions  $\beta = \pi/2, \gamma = 0$ . This approximation is well justified because the  $\beta$  and  $\gamma$  angles are effectively confined in the rotating frame for high rotation speeds. Two physical phenomena in fact compete for the confinement of these two angles: an electric torque due to the Paul trap and gyroscopic torques due to the rotation of the particle at the angular velocity  $\Omega/2$ . We note that the confinement in the rotating frame due to the Paul trap potential for  $\beta$  and  $\gamma$  comes from DC and AC torques (see Eq. (4.20)) in the same manner than for the angle  $\tilde{\alpha}$ . In the regime where  $\Omega \gg \omega_\gamma, \omega_\beta, \omega_\gamma$ , the confinement frequency of these modes in the laboratory frame can be written as the quadratic sum of the gyroscopic and Paul trap contributions (see calculation in Appendix D.3):

$$\omega_{\text{tot}, \tilde{\alpha}} = \tilde{\omega}_{\tilde{\alpha}}, \quad (4.27)$$

$$\omega_{\text{tot}, \tilde{\beta}} = \sqrt{\omega_{(\text{gyr.}), \tilde{\beta}}^2 + \tilde{\omega}_{\tilde{\beta}}^2}, \quad (4.28)$$

$$\omega_{\text{tot}, \gamma} = \sqrt{\omega_{(\text{gyr.}), \gamma}^2 - \tilde{\omega}_{\gamma}^2}. \quad (4.29)$$

with:

$$\tilde{\omega}_{\tilde{\alpha}} = \sqrt{\frac{\eta U_{AC} (c_y - c_x)(Q_3 - Q_2)}{3z_0^2 I_1}}, \quad (4.30)$$

$$\tilde{\omega}_{\tilde{\beta}} = \sqrt{\frac{\eta U_{AC} (c_y - c_x)(Q_3 - Q_1)}{6z_0^2 I_2}}, \quad (4.31)$$

$$\tilde{\omega}_{\tilde{\gamma}} = \sqrt{\frac{\eta U_{AC} (c_y - c_x)(Q_2 - Q_1)}{6z_0^2 I_2}}, \quad (4.32)$$

$$\omega_{(\text{gyr.}),\tilde{\beta}}(\Omega) = \sqrt{\frac{I_1}{I_2} \frac{\Omega}{2}}, \quad (4.33)$$

$$\omega_{(\text{gyr.}),\gamma}(\Omega) = \sqrt{\frac{I_1}{I_3} \left( \frac{I_1}{I_2} - 1 \right) \frac{\Omega}{2}}. \quad (4.34)$$

The electric torque lowers the stability for the angle  $\gamma$  but the assumption  $\Omega \gg \omega_{\alpha}, \omega_{\beta}, \omega_{\gamma}$  ensures that the difference  $\omega_{(\text{gyr.}),\gamma}^2 - \tilde{\omega}_{\tilde{\gamma}}^2$  is still positive. For small values of  $\Omega$ , the electric torque can dominate the gyroscopic confinement. The stable position for the  $\gamma$  angle becomes the position  $\gamma = \pi/2$ . In this case, the gyroscopic effect lowers the stability for the angle  $\gamma$ . This is related to the tennis racket effect (152) which stipulates that rotation around the second principal axis of a solid is unstable. For sufficiently high values of the angular velocity  $\Omega/2$ , this gyroscopic instability can even perfectly compensate the confinement due to the Paul trap. In this case, the stability position for  $\gamma$  becomes the position  $\gamma = 0$  and the confinement of this angle is dominated by the gyroscopic effect. This transition can occur while increasing the Paul trap frequency  $\Omega$  for instance.

We do not go into the details of this physics for the following. We will retain that, in the locking regime, the three Euler angles are stable in the rotating frame of the particle. This is essential for observing the geometric quantum phase for example where the rotation has to be extremely stable.

### 4.3. Magnetic particle rotation in the locking regime

In this section, we study the rotation of particles with magnetic properties such as diamond embedded with  $NV^-$  centers or Yttrium Iron Garnet (YIG) ferromagnetic particles. The rotation of levitating micro/nanometric magnetic particles is of interest to observe gyromagnetic effects such as the Barnett effect (48), the geometric quantum phase of a spin (46; 139) or to perform spin-mechanics with gyroscopic angular modes. The locking regime rotation mechanism seems to be ideal to allow this kind of experiments because of its low invasiveness (purely electrical effect), the possibility to rotate particles at high speeds under vacuum and because of its stability over time.

In this section, we first focus on the rotation of a highly doped diamond in  $NV^-$  centers and we use the  $NV^-$  centers to precisely read-out the angular motion of the diamond. Then, we show how we can enter the locking regime with magnetic YIG particles using an external magnetic field. Finally, we conclude this section by discussing the advantages and prospects of spinning magnetic particles, especially using the locking regime.

### 4.3.1 Angular motion read-out using $NV^-$ centers in a rotating diamond

In this part, we reconstruct the angular trajectory of a rotating diamond in the locking regime by measuring the angle of the diamond crystalline axis with respect to a fixed external magnetic field using  $NV^-$  centers. This will allow us to confirm that the particle is fully stabilized in the rotating frame and to set the scene towards other studies involving geometric quantum phase of  $NV^-$  centers for instance.

#### ODMR signature of a rotating diamond

The use of ODMR measurements with a levitating diamond has been a powerful tool to prove the diamond angular stability in a Paul trap (80). Due to the sensitivity of this measurement technique to the angular position of the diamond, we could expect to obtain quantitative information on the angle of a rotating diamond by performing ODMR measurements.

To do so, we employ a levitating Adamas diamond that is highly doped in  $NV^-$  centers (3.5 ppm) and rotated in the Paul trap at atmospheric pressure. We schematically represent such a rotating diamond in a presence of an external magnetic field  $\mathbf{B}$  in Fig. 4.15 (a). The magnetic field is randomly chosen such that it has no reason to be aligned with the rotation axis. The four classes of  $NV^-$  centers describe circular angular trajectories around the rotation axis, as indicated by the dashed circles in Fig. 4.15 (a). Figure 4.15 (b) shows an example of evolution of the eight  $NV^-$  center transitions during a period of rotation of the diamond for a magnetic field  $|\mathbf{B}| = 0.01$  T. Except for the moment when the level anti-crossing between the  $|m_s = -1\rangle$  and  $|m_s = +1\rangle$  states takes place, each  $NV^-$  resonant frequencies approximately evolve as a time-dependent sinusoid.

We can perform continuous ODMR spectra (the green laser is always on while scanning the microwave frequency). We show in Fig. 4.15 (c)-(i) and (ii) two distinct  $NV^-$  center photoluminescence spectra obtained by using a continuous ODMR measurement on a rotating diamond for two different magnetic field directions with intensity close to 0.01 T. Contrary to a classical ODMR spectrum of a static diamond for which there are only eight resonance peaks, the resonance spectra proposed here are blurred. It is not surprising because the different  $NV^-$  centers resonant frequencies are time-dependent leading to a sinus distribution of the resonant frequencies. Looking at these ODMR spectra, it seems difficult to extract quantitative informations on the angular trajectory of the diamond using only continuous measurements.

One could think of doing real-time ODMR measurements while having a rotating diamond to obtain time-dependant ODMR spectra, like the one simulated in Fig. 4.15 (b). The difficulty with real-time ODMR measurement is that the rotation period  $T_{\text{rot}}$  is on the order of 0.1 – 1 ms. It would therefore be necessary to obtain ODMR spectra in few micro seconds which is too short compared to the relevant quantities such as the optical pumping rate in the  $|m_s = 0\rangle$  ( $\approx 10 \mu\text{s}$  in our experiment). We propose in the next part a stroboscopic sequence that overpass this issue.

#### Reconstruction of the angular trajectory using stroboscopic ODMR

As explained in the previous part, real-time ODMR spectra are not a realistic option to reconstruct the angular trajectory of a rotating diamond. To circumvent this problem, we use the stroboscopic ODMR measurements presented in Fig. 4.16. The idea relies on the fact that the  $NV^-$  center anisotropy axis is in principle at the exact same angular position

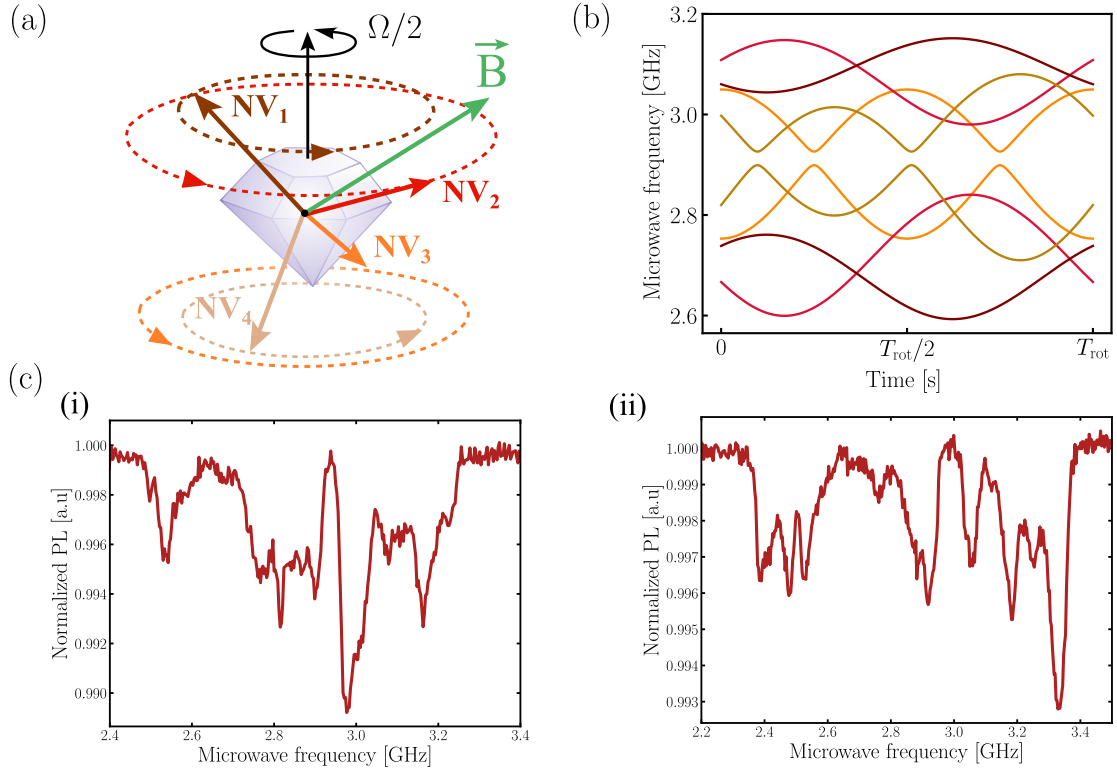


Figure 4.15: (a) Schematic picture of a diamond embedded with NV<sup>-</sup> centers rotating at the angular velocity  $\Omega/2$ . (b) NV<sup>-</sup> centers resonant frequencies of the four classes during a period of rotation of the diamond for a magnetic field  $|\mathbf{B}| = 0.01$  T. (c)-(i) Continuous ODMR spectra of a rotating diamond with a given magnetic field  $\mathbf{B}_1$ . (ii) Continuous ODMR spectra of a rotating diamond with a different magnetic field  $\mathbf{B}_2$ .

after a complete rotation of period  $T_{\text{rot}}$ . The frequencies of the transitions  $|m_s = 0\rangle \rightarrow |m_s = \pm 1\rangle$  are thus normally unchanged. We can thus turn on the microwave at a fixed microwave frequency for a short period of time  $\delta t$  after each rotation of the diamond while constantly illuminating the diamond with a green laser to polarize the NV<sup>-</sup> center in  $|m_s = 0\rangle$  state. We define the stroboscopic delay  $\Delta t$  as the delay between the moment the microwave is switched on and a phase reference signal oscillating at frequency  $1/T_{\text{rot}}$ . This protocol is presented in the first graph of Fig. 4.16 (a). If none of the NV<sup>-</sup> centers are resonant with the microwave during  $\delta t$ , there is no excitation to the  $|m_s = \pm 1\rangle$  state and the photoluminescence remains the same. In the opposite case, i.e. when an NV<sup>-</sup> center is on resonance with the microwave drive, one of the  $|m_s = \pm 1\rangle$  state is polarized, resulting in a decrease of the average photoluminescence. This is sketched in Fig. 4.16 (a). This protocol requires the microwave Rabi period given by  $2\pi/\Omega_r$  to be smaller than or on the order of  $\delta t$  in order to efficiently drive the excited state  $|m_s = \pm 1\rangle$ . This is experimentally verified because  $2\pi/\Omega_r \approx 1 \mu\text{s}$  and we have chosen  $\delta t = 4 \mu\text{s}$ .

In Fig. 4.16 (b), we show the electronical circuit used in the stroboscopic ODMR measurement. The first column is related to the Paul trap drive signal generation. A function generator delivers an AC voltage signal at a frequency between 1 – 10 kHz that is amplified by a high voltage amplifier. A second function generator is phase locked to the function generator of the Paul trap drive. This generator generates a TTL signal at

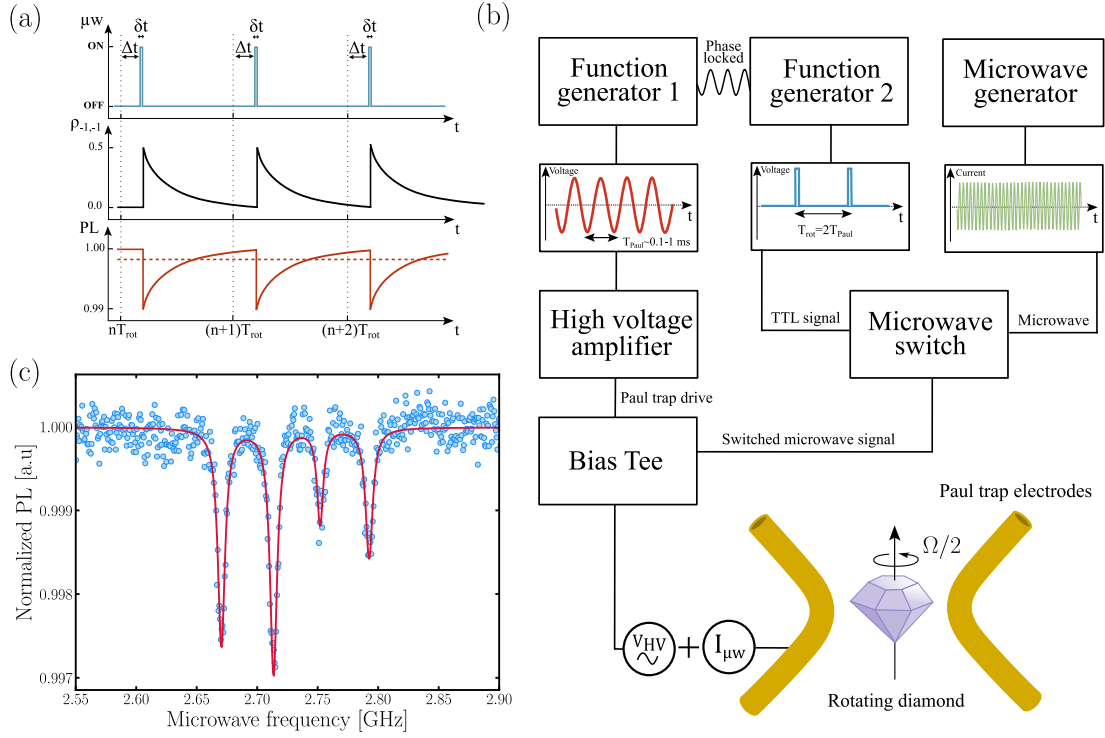


Figure 4.16: (a) Measurement protocol allowing the realization of stroboscopic ODMR. (b) Electronic diagram to perform stroboscopic ODMR. (c) Stroboscopic ODMR for a given value of the stroboscopic delay  $\Delta t$  showing the  $|m_s = 0\rangle \rightarrow |m_s = -1\rangle$  transitions.

every rotation period  $T_{\text{rot}} = 2T_{\text{Paul}}$ . The duty cycle time  $\delta t$  approximately equals  $4 \mu\text{s}$ , as already explained. This TTL signal is connected to a microwave switch in order to switch the microwave signal delivered by the microwave generator shown in the third column. After that, the high voltage Paul trap drive and the microwave signal are added using a bias tee and are finally connected to the Paul trap electrodes.

Figure 4.16 (c) shows the result of this experiment while scanning the microwave frequency. The characteristic time to obtain this spectra is a few minutes. We observe a stroboscopic ODMR spectra with four peaks corresponding to the four  $|m_s = 0\rangle \rightarrow |m_s = -1\rangle$  resonances of the  $\text{NV}^-$  classes. The linewidth of the four magnetic resonances are the same than for a non rotating diamond. This means that the  $\text{NV}^-$  centers spin properties are not affected by the rotation but also that there is no additional broadening due to the rotation. We can therefore conclude that the rotation is extremely stable on time scale on the order of the acquisition duration i.e. few minutes. The fact that the  $\text{NV}^-$  center spin coherence time is not affected by the diamond rotational motion is a key result for the study of the geometric quantum phase, as was done in (46) using diamonds rotated on a platform.

The use of a single magnetic field  $\mathbf{B}_1$  is not sufficient to fully characterize the angular position of the diamond. Indeed, the energy levels of the  $\text{NV}^-$  center eigenstates are unchanged by any rotation around the magnetic field axis. It is therefore necessary to use a second magnetic field  $\mathbf{B}_2$  that is not aligned with the first one  $\mathbf{B}_1$  to fully determine the angular position of the diamond in the laboratory frame. Note that this technique has

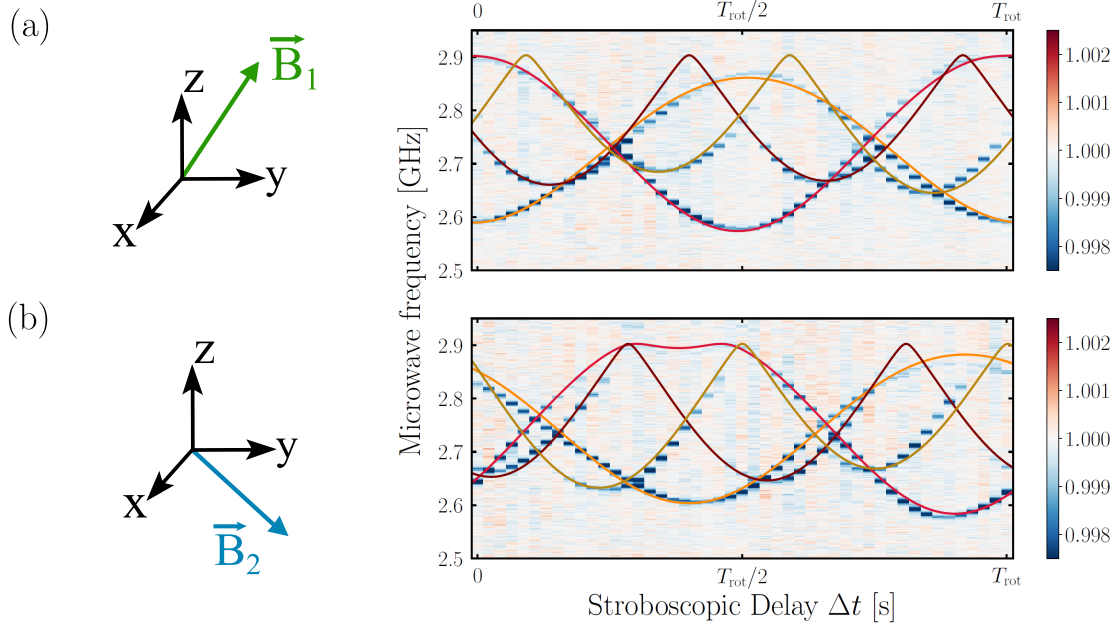


Figure 4.17: (a) Two-dimensional array of the  $\text{NV}^-$  center photoluminescence as a function of the microwave frequency and the stroboscopic delay  $\Delta t$  for a magnetic field  $\mathbf{B}_1$  such that  $|\mathbf{B}_1| \approx 0.01$  T. The colored lines represent fits of the ODMR spectra for an ideal rotation. (b) Same measurement with a magnetic field  $\mathbf{B}_2$  perpendicular to  $\mathbf{B}_1$  with approximately the same amplitude.

been used for example to track the angular and center of mass motion of a diamond in a cell (153).

Finally, the stroboscopic delay  $\Delta t$  can be varied to obtain ODMR spectra at different moments of the rotation. We perform this experiment for two different magnetic fields  $\mathbf{B}_1$  and  $\mathbf{B}_2$  that are perpendicular to each other and of the same amplitude  $\approx 0.01$  T. In Fig. 4.17, we have plotted a two-dimensional array of the  $\text{NV}^-$  center photoluminescence as a function of the microwave frequency and the stroboscopic delay. Figure 4.17 (a) corresponds to the magnetic field  $\mathbf{B}_1$  and Fig. 4.17 (b) corresponds to  $\mathbf{B}_2$ . Each acquisition requires about 5 hours of averaging. The colored lines are a fit to the  $\text{NV}^-$  transitions assuming ideal stable rotation. There is very good agreement with the data, proving that the three rotational modes of the diamond are fully confined in the rotating frame. Only a few milliradians shift has been observed from the beginning to the end of the experiment meaning that a rotation is extremely stable over time.

In this part, we used the  $\text{NV}^-$  centers to measure the angular position of a rotating diamond. We could thus verify that the spin state of the  $\text{NV}^-$  centers can be controlled without seeing any influence of the rotation on its coherence properties. It has also permitted us to verify that the diamond rotates around one single axis and is perfectly angularly stable in the rotating frame over few hours. These results prove the extreme stability of the locking mechanism to rotate levitated magnetic particles. This mechanism could thus allow to perform experiments that require a stable rotation such that the accumulation of a geometric quantum phase for a rotating  $\text{NV}^-$  center spin (46).

### 4.3.2 Rotation of ferromagnetic particles

Rotation of ferromagnetic micro/nanoparticles has not been widely explored experimentally despite the exacerbation of gyromagnetism at these scales. Magnetization induced by rotation, namely the Barnett effect (48), and the possibility to achieve a Levitron at the nanoscale are major motivations to rotate ferromagnets. In this part, we prove that 10  $\mu\text{m}$  Yttrium Iron Garnet particles (YIG) can rotate using the locking mechanism of the Paul trap. The YIG particles are made in the laboratory by grinding a single millimeter crystal manufactured at Lab-STICC by J. Ben Youssef.

We performed the experiment drawn in Fig. 4.18. We continuously approach a magnetic field close to a levitating YIG particle angularly stable i.e. in the librating regime. Figure 4.18 (b) shows the PSD of the motion of a YIG particle that is initially angularly stable without external magnetic field. After the magnetic field is applied, it can be seen in Fig. 4.18 (c) that the particle starts to rotate or is in an intermediate regime of parametric excitation at the frequency  $(\Omega/2)/2\pi$  between the librating and locking regime. This is due to the fact that the homogeneous field plays the role of an additional constant torque in the Mathieu equation governing the angular dynamics which can lead to visiting a domain of instability of the librating regime. The particle can therefore move to the locking regime or to the transition regime where the particle is parametrically excited at the frequency  $(\Omega/2)/2\pi$ . We also checked that one can remove the magnetic field letting the particle in the locking regime.

This gives an additional method to access to the locking regime that does not affect the dynamics of the center of mass unlike the method decreasing the trapping frequency  $\Omega/2\pi$ . This experiment has also been performed with other types of ferromagnetic materials like iron or cobalt.

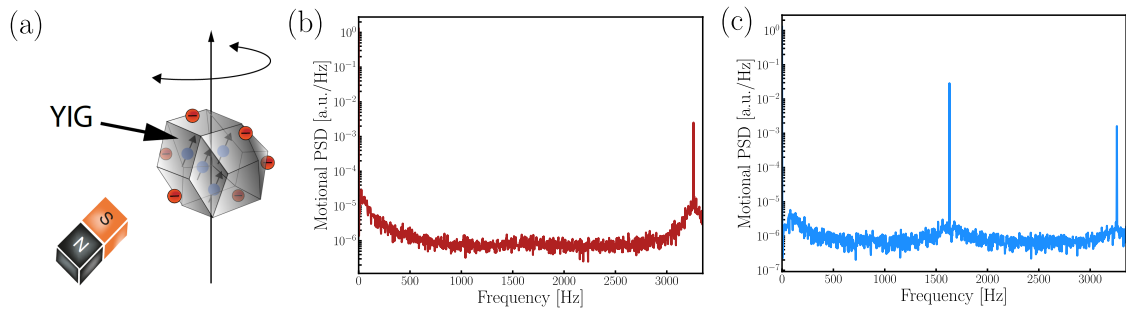


Figure 4.18: (a) Schematics of a levitating YIG microparticle subjected to an external magnetic field. (b) PSD of the motion of a YIG particle in the librating regime without magnetic field. (c) PSD of the motion of the same YIG particle in the locking regime in the presence of an external magnetic field.

The rotation of particles using the locking mechanism of the Paul trap has the advantage that it only depends on the surface charge state of the levitated particles. The access to this regime does not depend on the internal properties of the material and we can therefore rotate particles of any types, including magnetic particles. We can now discuss the interest of this rotation technique compared to the techniques used in this field as well as the possible perspectives, in particular with the rotation of magnetic particles.

### 4.3.3 Discussion and perspectives

In this part, we compare our rotation technique induced by the locking regime of the Paul trap with the usual rotation method in optical tweezers using circularly polarised light. Finally, we give some perspectives for research on the rotation of magnetic particles using this technique.

#### Comparison between the Paul trap rotation and optically polarised laser rotation techniques

The studies on the rotation of micro/nanometric particles have experienced a boom in the last five years (154). In the following, we introduce the several techniques of micro particle rotation. The most common technique of trapped particle rotation uses a circularly polarized laser that transfers angular momentum to birefringent particles (140; 107; 141; 142; 143; 144; 145). This transfer of angular momentum from the light to the particle causes the particle to rotate. The maximum reachable velocity depends on the competition between the rate of angular momentum transfer versus the friction with the surrounding gas. The types of particles that are being rotated using this technique are typically amorphous and take the form of silica nanorods and nanodumbbells. The maximum rotation frequency can reach GHz rotation frequencies at high vacuum (the rotation speed is ultimately limited by the material stress) (109; 108; 155).

Let us propose to compare this rotation technique to the locking mechanism in a Paul trap. First of all, the locking mechanism in Paul trap does not require a strongly focused laser as it is the case in optical tweezer. This generally heats up the levitated particle. For particles made out of silica, this heating is weak even under ultra vacuum and does not imply losing the particle. However, this technique does not allow to rotate crystals which heat up quickly under vacuum due to crystal impurities and are then ejected from the trap. This strongly limits the type of particles that can be rotated using the laser rotation technique. We have previously seen that in the case of rotation using the Paul trap locking mechanism, all types of particles can rotate as long as the particle is asymmetrically charged on the surface. In addition, no heating on the particle due to the Paul trap has yet been observed. Moreover, the torque allowing the rotation of particles with circularly polarized light is non-conservative because it originates from an angular momentum transfer to the particle. The precession angle  $\alpha$  is therefore not confined by a restoring torque in the rotating frame. In the case of the Paul trap rotation mechanism, the torque is conservative and the angular velocity is fixed and given by half the Paul trap frequency drive  $\Omega/2$ . The particle is angularly confined for the three Euler angles in the rotating frame. The maximum rotation speed reached using a circularly polarized laser is in the GHz range at  $10^{-5}$  mbar (109; 108; 155) while the maximum rotation speed reached in our experiment is in the kHz range at atmospheric pressure. Nevertheless, there is no theoretical limitation on the maximum speed of rotation that can be reached at high vacuum using the locking mechanism in Paul trap. Using the formula for  $\Omega_{\max}^{(\text{lock.})}$ , we estimate that we can reach a rotation frequency in the MHz range at  $10^{-1}$  mbar. This is the same order of magnitude than for silica nanorods at this same pressure using optical tweezers (108).

A crucial point to solve for faster rotation of particles using Paul trap is to keep the stability of the center of mass which is drastically decreased by using a very high trapping frequency. To solve this problem, we can imagine using two frequencies for the Paul trap, one at low frequency to stabilize the center of mass motion while the second

at higher frequency permits to rotate the particle. One can also imagine levitating the particle with another technique of optical or magnetic trap and controlling its rotation with the Paul trap. Finally, the size of the rotating particles in the circularly polarized optical tweezers is on the order of 100 nm while the size of the rotated particles in our experiment is 10  $\mu\text{m}$ . A rotation in the MHz range of 10  $\mu\text{m}$  size vaterite particles has been reported in (156). A priori nothing prohibits however to rotate particles of larger sizes with circularly polarized light nor to rotate particles of smaller sizes with the Paul trap locking mechanism.

We have summarized this information in Table 2 distinguishing between experimental realizations and theoretical possibilities in the future.

Table 2: Comparison table between particle rotation in Paul trap using the locking mechanism and rotation in optical tweezer using circularly polarized light.

Parameters	Rotation in optical trap	Rotation in Paul trap
Particle size	100 nm – 10 $\mu\text{m}$	10 $\mu\text{m}$
Type of particle	Birefringent particles: silica nanorods and nanodumbbells, vaterite	Asymmetrically charged particles: silica, diamond, ferromagnetic particles
Origine of the rotating torque	Non-conservative torque given by the absorption of circularly polarized photons	Conservative torque given by a restoring torque in the rotating frame
Maximum speed of rotation	GHz limited by the material stress	kHz but there is no theoretical limitations to reach higher rotation speed

Let us also quote other methods of levitation which are less developed currently: the rotation of a particle having a dipolar electric moment using a fast rotating electric field (110; 111; 112) or very recently using a transfer of transverse orbital angular momentum (113).

#### Magnetic particle rotation perspective

The strength of particle rotation using the Paul trap locking mechanism relies on the possibility to rotate magnetic particles in an ultra-stable and non-invasive way at potentially very high rotation speeds (in the MHz range at  $10^{-1}$  mbar). In this section, we list some experiments requiring the rotation of magnetic particles that seem to be accessible using the locking regime of the Paul trap.

First of all, researchers have recently observed the geometric quantum phase of an  $\text{NV}^-$  center in a diamond rotating at 3.3 kHz (46). This type of experiment requires a high stability of the rotation and is quickly limited by the speed of rotation of the motors not exceeding 10 kHz. By using the ultra stable rotation of the Paul trap locking regime, we can already reasonably see this effect. Moreover, we could think of realizing this experiment at even higher speeds of the MHz that will lead to a larger quantum phase.

Another notable effect is the appearance of a pseudo magnetic field for rotating magnetic particles: this is the Barnett effect, described in Chapter 2. Again, this effect has been recently observed by the same team of researchers with  $\text{NV}^-$  centers in a rotating diamond (115). The generated pseudo magnetic field evolves linearly with the rotation

speed which motivates to rotate the diamond at higher rotation speeds. This effect seems to be directly observable for rotation speeds of the order of the coherence time of  $NV^-$  centers, which corresponds to the MHz for the samples used in our experiment. By using better quality samples, we can reasonably imagine observing this effect at lower rotation frequencies close to the kHz.

Finally, the resonant frequency of the gyroscopic modes depends directly on the rotation speed and is therefore of the order of MHz if the particle rotates at these speeds. One of the current limitations of mechanical spin using angular resonance modes is that the frequency of these modes is too low to allow sideband cooling (43). Using the gyroscopic modes could thus solve this issue.

One of the challenges of spinning using the locking regime is therefore to be able to increase the frequency of the Paul trap by several orders of magnitude that will drastically increase the speed of rotation. This would allow us to explore the dynamics of spins in solids at rotational speeds never reached before.

#### 4.4. Conclusion

In this chapter, the angular dynamics of an asymmetrically charged particle in an asymmetric Paul trap was studied. This allowed us to highlight the existence of an already known and observed librating regime where the particle is angularly stable (29; 80; 36) as well as a new angular stability regime where the particle describes a full rotation at half the Paul trap drive frequency. The existence of these two stability regimes comes from non linearities in the angular dynamical equation of the particle that is similar to the motion equation of the parametrically excited pendulum, the Kapitza pendulum, known for these two stability regimes (149). The limits of the stability domains for these two angular stability regimes have been established and experimentally confirmed by reducing the equations to a one dimensional angular dynamics. Finally, we have demonstrated the flexibility of this rotation technique which allows to rotate any kind of particles including magnetic particles such as diamond doped with  $NV^-$  centers, YIG particles as well as other ferromagnetic particles. The use of  $NV^-$  centers in diamond has allowed us to completely reconstruct the angular trajectory of the rotation, thus confirming the extreme stability of this regime over time. It was also possible to verify that the coherence time of the spins was not affected by the rotation motion which is important for future experiment involving spin state control in the rotating frame.

Finally, the fast, stable and low invasive rotation of magnetic particles using a Paul trap seems to be an ideal technique to explore rich physics such as for instance gyromagnetic effects (48; 115), spin-mechanical coupling in rotating frame, magnetometry (45) and geometric quantum phase (46; 139).

## Chapter 5: Mechanical detection of the $NV^-$ centers diamagnetism

---

In chapters 3 and 4, we focused on the dynamics of magnetic particles levitated in ponderomotive traps. We have shown that the principle of the Paul trap, which allows for the levitation of electrically charged particles, can also be applied to levitate magnetic particles. This technique may facilitate the observation of gyromagnetic (47; 48) and spin-mechanical effects (93; 123). Furthermore, we have proven that magnetic particles levitating in a Paul trap can be rapidly rotated in an extremely stable manner. This new method of rotation for micro/nano particles could be useful for observing the Barnett effect (48; 115) and the geometric quantum phase of  $NV^-$  center spins (46).

In this chapter, we demonstrate a new form of magnetism for highly doped diamonds with NV centers: the Van Vleck spin-diamagnetism. Using torque magnetometry techniques discussed in Chapter 2, we mechanically probe the spin-diamagnetism of a levitated micro diamond. The spin-diamagnetism of the  $NV^-$  centers allows us to fully align the crystalline anisotropy axis of the diamond with the direction of the magnetic field, without the need for microwaves. Controlling the angle of an untethered micro diamond is a challenging task, but is a key requirement for hyperpolarization protocols (157; 158; 159) with diamonds in liquid as well as for spin-mechanics protocols with levitated diamonds (29; 30). We have published the results of this chapter in (50).

This chapter is structured as follows: First, we review the  $NV^-$  centers magnetic response theory developed in Chapter 1 and extend these results to the case of strong magnetic fields. We find that the magnetic response of  $NV^-$  centers transitions from a weak Van Vleck paramagnetic response to a strong Van Vleck diamagnetic response. We prove that the spin-diamagnetism of the  $NV^-$  centers can align the crystalline axis of a levitated diamond with the external magnetic field. Finally, we define a librational potential energy related to the spin-diamagnetism-induced torque.

### 5.1. $NV^-$ center magnetic response to a strong magnetic field

In Chapter 1, we studied the magnetic response of  $NV^-$  centers when the ground state is populated by the green laser optical pumping for weak magnetic field. In that case, we found that  $NV^-$  centers exhibit Van Vleck paramagnetism. In this section, we extend that result to the case of a strong magnetic field that is almost aligned with the  $NV^-$  center anisotropy axis. We show that the diamond's Van Vleck magnetism transitions from a paramagnetic to a diamagnetic regime.

#### 5.1.1 System description and parametrization

We consider a single class of  $NV^-$  centers in a diamond with a crystalline anisotropy axis given by the direction  $\mathbf{e}_3$ . We apply an external magnetic field  $\mathbf{B}$ , which we assume to be almost aligned with the  $NV^-$  center anisotropy axis, as shown in Fig. 5.1 (a). The magnetic field  $\mathbf{B}$  can thus be decomposed as the sum of a longitudinal component

$\mathbf{B}_0 = B_0 \mathbf{e}_3$ , which is aligned with the NV<sup>-</sup> center anisotropy axis, and a weak transverse component  $\delta \mathbf{B}$ , which verifies  $|\delta \mathbf{B}| \ll |\mathbf{B}_0|$ .

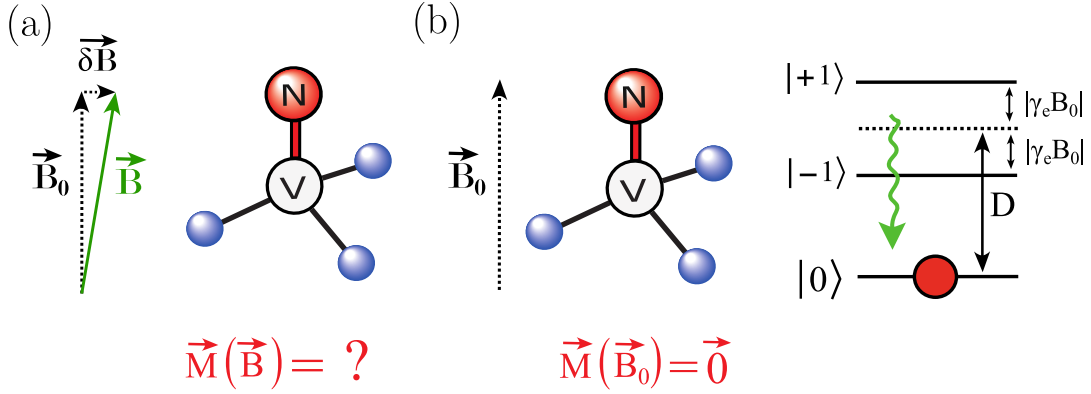


Figure 5.1: (a) Sketch showing an NV<sup>-</sup> center in the presence of a magnetic field  $\mathbf{B}$  almost aligned with the anisotropy axis of the NV<sup>-</sup> center. (b) NV<sup>-</sup> center in a presence of a magnetic field  $\mathbf{B}_0$  fully aligned with the anisotropy axis of the NV<sup>-</sup> center. The energy levels of the three eigenstates ( $|m_s = 0\rangle$ ,  $|m_s = -1\rangle$ ,  $|m_s = +1\rangle$ ) are shown on the right in the presence of a green laser optical pumping that populates the  $|m_s = 0\rangle$  state. The resulting magnetization  $\mathbf{M}(\mathbf{B}_0)$  of the NV<sup>-</sup> center is equal to 0.

The objective of this section is to calculate the magnetization  $\mathbf{M}(\mathbf{B})$  of the NV<sup>-</sup> center as a function of the magnetic field  $\mathbf{B}$  while optically pumping in the  $|m_s = 0\rangle$  state. The magnetization can be calculated using Eq. (1.44):

$$\mathbf{M} = d\hbar\gamma_e \text{Tr}(\hat{\rho}\hat{\mathbf{S}}), \quad (5.1)$$

and the density matrix coefficients calculated in Eq. (1.47):

$$M_1 = d\hbar\gamma_e \frac{\rho_{0-1} + \rho_{0-1}^* + \rho_{10} + \rho_{10}^*}{\sqrt{2}}, \quad (5.2)$$

$$M_2 = d\hbar\gamma_e \frac{i(\rho_{0-1} - \rho_{0-1}^* + \rho_{10} - \rho_{10}^*)}{\sqrt{2}}, \quad (5.3)$$

$$M_3 = d\hbar\gamma_e (\rho_{11} - \rho_{-1-1}). \quad (5.4)$$

The Hamiltonian of the system can be written as:

$$\hat{\mathcal{H}} = \hat{\mathcal{H}}_0 + \hat{V}, \quad (5.5)$$

with:

$$\hat{\mathcal{H}}_0 = \hbar D \hat{S}_3^2 - \hbar\gamma_e B_0 \hat{S}_3, \quad (5.6)$$

and:

$$\hat{V} = -\hbar\gamma_e \delta \mathbf{B} \cdot \hat{\mathbf{S}}. \quad (5.7)$$

In the case of a purely longitudinal magnetic field  $\mathbf{B} = \mathbf{B}_0$ , i.e.  $\delta \mathbf{B} = 0$ , the magnetization

$\mathbf{M}(\mathbf{B}_0)$  is equal to zero. This is because the states  $|m_s = -1\rangle$  and  $|m_s = +1\rangle$  are equally populated due to green laser pumping, resulting in  $M_3 = 0$  (see Fig. 5.1 (b)). Additionally, there is no state mixing, and the coherence terms  $\rho_{0-1}$ ,  $\rho_{10}$  equal zero, implying  $M_1$ ,  $M_2 = 0$ .

In the following, we calculate the magnetic response  $\mathbf{M}(\mathbf{B}_0 + \delta\mathbf{B})$  in the case where  $\delta\mathbf{B} \neq 0$ . As we have previously seen, the NV<sup>-</sup> center magnetization  $\mathbf{M}(\mathbf{B}_0) = 0$  for  $\mathbf{B}_0$  longitudinal to the anisotropy axis of the NV<sup>-</sup> center. We thus have the equality  $\mathbf{M}(\mathbf{B}_0 + \delta\mathbf{B}) = \mathbf{M}(\mathbf{B}_0) + \delta\mathbf{M} = \delta\mathbf{M}$ . Specifically, we calculate the magnetic susceptibility tensor  $\underline{\underline{\chi}}^{\text{NV}}$ , which is related to the magnetization according to Eq. (1.13), via the equality:

$$\delta\mathbf{M} = \underline{\underline{\chi}}^{\text{NV}} \cdot \frac{\delta\mathbf{B}}{\mu_0} + o(\delta\mathbf{B}) \quad \text{with} \quad \underline{\underline{\chi}}^{\text{NV}} = \mu_0 \frac{\partial\mathbf{M}}{\partial\mathbf{B}}(\mathbf{B}_0). \quad (5.8)$$

To do so, we will use a density matrix perturbative treatment by considering  $\hat{V} \ll \hat{\mathcal{H}}_0$ .

### 5.1.2 Van Vleck para/diamagnetism of the NV<sup>-</sup> center

Here, we study the magnetic response of the NV<sup>-</sup> center by considering the Hamiltonian  $\hat{V}$  as a perturbation of the Hamiltonian  $\hat{\mathcal{H}}_0$ . We demonstrate that there is a transition from a Van Vleck paramagnetic to a diamagnetic response as the strength of the applied magnetic field  $B_0$  increases.

#### Origin of the paramagnetism to diamagnetism transition at a Ground-State Level Anticrossing (GSLAC)

In this part, we provide physical insights into the magnetic response transition from a paramagnetic to a diamagnetic behavior of the NV<sup>-</sup> center. Notably, we show that this transition occurs at the Ground-State Level AntiCrossing (GSLAC) of the NV<sup>-</sup> center.

In Fig. 5.2, we show the evolution of the three magnetic eigenstates energies of the NV<sup>-</sup> center as a function of  $|\mathbf{B}_0|$ . We consider the two different cases  $\delta\mathbf{B} = 0$  and  $\delta\mathbf{B} \neq 0$ .

In the first case, the magnetic perturbation  $\delta\mathbf{B}$  is equal to 0, such that the total magnetic field  $\mathbf{B}$  is simply equal to  $\mathbf{B}_0$  which is aligned with the anisotropy direction  $\mathbf{e}_3$ . We have plotted in black the evolution of the energies of the three NV<sup>-</sup> center eigenstates, which are the states ( $|m_s = 0\rangle, |m_s = -1\rangle, |m_s = +1\rangle$ ). We have indicated with a red dot the population distribution due to the green laser optical pumping. The pumping process mainly populates the  $|m_s = 0\rangle$  state. When  $|\gamma_e|B_0 = D$  corresponding to  $B_0 = 102$  mT, the two states  $|m_s = 0\rangle$  and  $|m_s = -1\rangle$  are resonant, this is referred to as the NV<sup>-</sup> center GSLAC. After this crossing, the energy of the  $|m_s = -1\rangle$  state is lower than the energy of the  $|m_s = 0\rangle$  state. Thus, the occupied state due to the green laser pumping is no longer the NV<sup>-</sup> ground state after the GSLAC but it is the first excited state.

In the second case, we consider a small magnetic perturbation  $\delta\mathbf{B}$  that is transverse to the magnetic field  $\mathbf{B}_0$ <sup>1</sup>. We have plotted in green the evolution of the energies of the three NV<sup>-</sup> center eigenstates of the Hamiltonian  $\hat{\mathcal{H}}_0 + \hat{V}$  as a function of  $|\mathbf{B}_0|$ . The states ( $|m_s = 0\rangle, |m_s = -1\rangle, |m_s = +1\rangle$ ) are almost the eigenstates of  $\hat{\mathcal{H}}_0 + \hat{V}$  since  $|\delta\mathbf{B}| \ll |\mathbf{B}_0|$ . For simplicity, we use the notation ( $|m_s = 0'\rangle, |m_s = -1'\rangle, |m_s = +1'\rangle$ ) to designate these states.

<sup>1</sup>We have chosen  $\delta B = 20$  mT. This magnetic perturbation  $\delta B$  does not verify the large inequality  $\delta B \gg B_0$ . This value has been chosen for a pedagogical reason in order to visualize the eigenstates energies of the perturbed Hamiltonian  $\hat{\mathcal{H}}_0 + \hat{V}$  compared to the unperturbed one  $\hat{\mathcal{H}}_0$ .

Let us now consider the two zoomed boxes where we focus on the energy evolution of the state  $|m_s = 0'\rangle$  populated by the green laser for the two cases: before and after the GSLAC. Before the GSLAC, we observe (left box) that the energy of  $|m_s = 0'\rangle$  (green curve) is lower than the energy of  $|m_s = 0\rangle$  (black curve). After the GSLAC, we observe (right box) that the energy of  $|m_s = 0'\rangle$  is larger than the energy of  $|m_s = 0\rangle$ . Therefore, the evolution of the energy of  $|m_s = 0'\rangle$  as a function of the transverse magnetic field  $\delta\mathbf{B}$  is opposite when  $|\gamma_e|B_0 < D$  and  $|\gamma_e|B_0 > D$ . The energy of the only populated state  $|m_s = 0'\rangle$  decreases for a perturbation  $\delta\mathbf{B}$  when  $|\gamma_e|B_0 < D$ , resulting in a Van Vleck paramagnetic behaviour of the NV<sup>-</sup> center before the GSLAC. On the other hand, this energy increases while  $|\gamma_e|B_0 > D$ . This is responsible for a Van Vleck diamagnetic behaviour after the GSLAC.

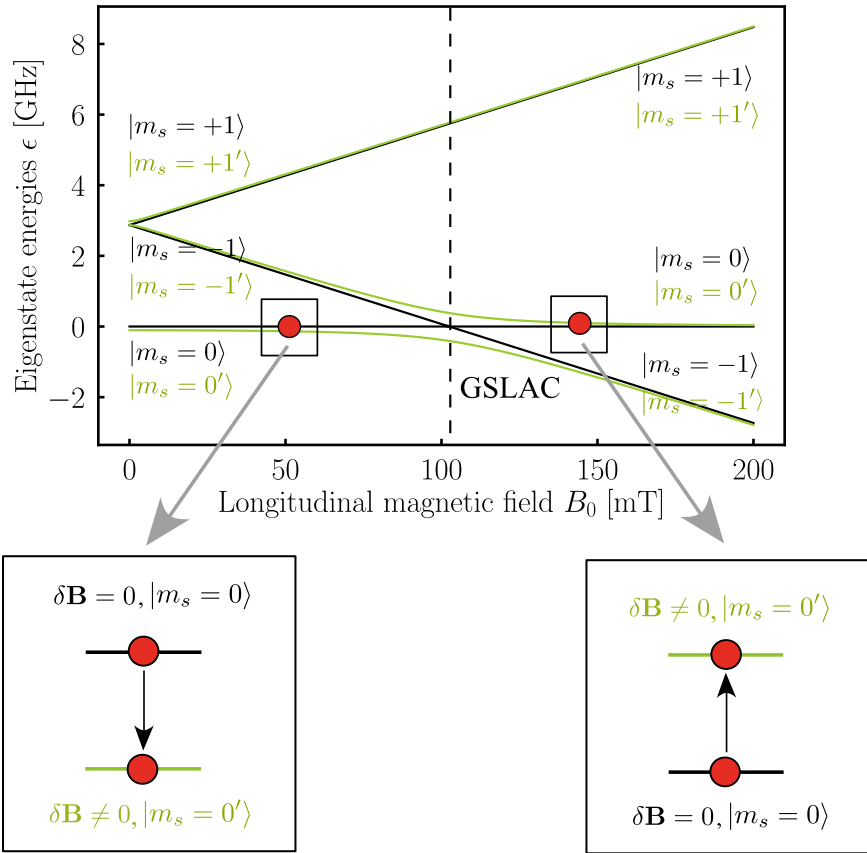


Figure 5.2: Eigenstate energies of an NV<sup>-</sup> center as a function of the longitudinal magnetic field  $B_0$ . The black lines correspond to the case where there is no additional transverse magnetic field while the green lines correspond to the case where a transverse magnetic field  $\delta B = 30$  mT is added. The bottom left box (resp. bottom right) corresponds to the energy evolution of the  $|m_s = 0'\rangle$  eigenstate before the GSLAC (resp. after the GSLAC) when  $\delta B$  is increased.

The strength of the magnetic response directly depends on the energy evolution of the state  $|m_s = 0'\rangle$  as a function of  $\delta\mathbf{B}$ . The stronger the energy evolution  $|m_s = 0'\rangle$  with respect to  $\delta\mathbf{B}$ , the stronger the magnetic response  $\delta\mathbf{M}$ . The evolution of the energy of  $|m_s = 0'\rangle$  is stronger as the states  $|m_s = 0\rangle$  and  $|m_s = -1\rangle$  are initially close in energy. We thus expect to have a very strong magnetic response close to the GSLAC where the

two states  $|m_s = 0\rangle$  and  $|m_s = -1\rangle$  are close to being resonant. This corresponds to the case where  $|\gamma_e|B_0 \simeq D$ .

In the following part, we calculate the magnetic susceptibility tensor as a function of the magnetic field  $B_0$  and show that the results correspond to the previously given physical insights.

### Magnetic susceptibility calculation

In this part, we calculate the value of the magnetic susceptibility tensor  $\underline{\underline{\chi}}^{\text{NV}}$  of the NV<sup>-</sup> center as a function of the constant longitudinal magnetic field  $\mathbf{B}_0$ . First of all, due to the rotational invariance of the Hamiltonian  $\hat{\mathcal{H}}_0$ , we can prove that the magnetic susceptibility tensor  $\underline{\underline{\chi}}^{\text{NV}}$  commutes with the elements of the group of continuous rotations around the symmetry axis of the NV<sup>-</sup> center  $\mathbf{e}_3$  (see calculation in Appendix E.1). We can thus simply write:

$$\underline{\underline{\chi}}^{\text{NV}} = \begin{pmatrix} \chi_{\perp} & -\chi_d & 0 \\ \chi_d & \chi_{\perp} & 0 \\ 0 & 0 & \chi_{\parallel} \end{pmatrix}, \quad (5.9)$$

in the basis  $(\mathbf{e}_1, \mathbf{e}_2, \mathbf{e}_3)$ , with coefficients  $\chi_{\perp}, \chi_d, \chi_{\parallel}$  where the parallel direction designates the anisotropy direction  $\mathbf{e}_3$ . The magnetization equals zero when the external magnetic field is parallel to the NV<sup>-</sup> center's anisotropy axis, and therefore the magnetic susceptibility in this direction is also zero, i.e.  $\chi_{\parallel} = 0$ .

To calculate the remaining coefficients  $\chi_{\perp}$  and  $\chi_d$ , we use density matrix perturbation theory by considering the Hamiltonian  $\hat{\mathcal{H}} = \hat{\mathcal{H}}_0 + \hat{V}$ , which was introduced in the previous section. To do this, we write the Taylor expansion of the density matrix  $\hat{\rho} = \hat{\rho}^{(0)} + \hat{\rho}^{(1)} + \dots$  as a function of  $\delta\mathbf{B}$  and we calculate the first-order term  $\hat{\rho}^{(1)}$ . It satisfies the equality:

$$0 = \frac{\partial \hat{\rho}^{(1)}}{\partial t} = -\frac{i}{\hbar} [\hat{\mathcal{H}}_0, \hat{\rho}^{(1)}] - \frac{i}{\hbar} [\hat{V}, \hat{\rho}^{(0)}] + \mathcal{L}(\hat{\rho}^{(1)}). \quad (5.10)$$

By introducing the energy differences  $\Delta_{kl}$  between the different eigenstates  $|k\rangle$  and  $|l\rangle$ , we obtain:

$$\rho_{kk}^{(1)} = 0, \quad (5.11)$$

$$\text{For } k \neq l: \quad \rho_{kl}^{(1)} = \frac{-i}{\hbar(\Gamma_2^* + i\Delta_{kl})} \langle k | \hat{V} | l \rangle (\rho_{kk}^{(0)} - \rho_{ll}^{(0)}), \quad (5.12)$$

Using the relation Eq. (1.47), we can deduce the value of the magnetic susceptibility tensor:

$$\chi_{\perp} = d\hbar\mu_0\gamma_e^2 \frac{\gamma_{\text{las}}}{3\Gamma_1 + \gamma_{\text{las}}} \left( \frac{\Delta_{-10}}{\Delta_{-10}^2 + (\Gamma_2^*)^2} + \frac{\Delta_{10}}{\Delta_{10}^2 + (\Gamma_2^*)^2} \right), \quad (5.13)$$

$$\chi_d = d\hbar\mu_0\gamma_e^2 \frac{\gamma_{\text{las}}}{3\Gamma_1 + \gamma_{\text{las}}} \left( \frac{\Gamma_2^*}{\Delta_{-10}^2 + (\Gamma_2^*)^2} - \frac{\Gamma_2^*}{\Delta_{10}^2 + (\Gamma_2^*)^2} \right). \quad (5.14)$$

where  $\Delta_{-10} = D - |\gamma_e|B_0$  is the energy difference between the unperturbed  $|m_s = -1\rangle$  and  $|m_s = 0\rangle$  states and  $\Delta_{10} = D + |\gamma_e|B_0$  is the energy difference between the unperturbed  $|m_s = +1\rangle$  and  $|m_s = 0\rangle$  states.

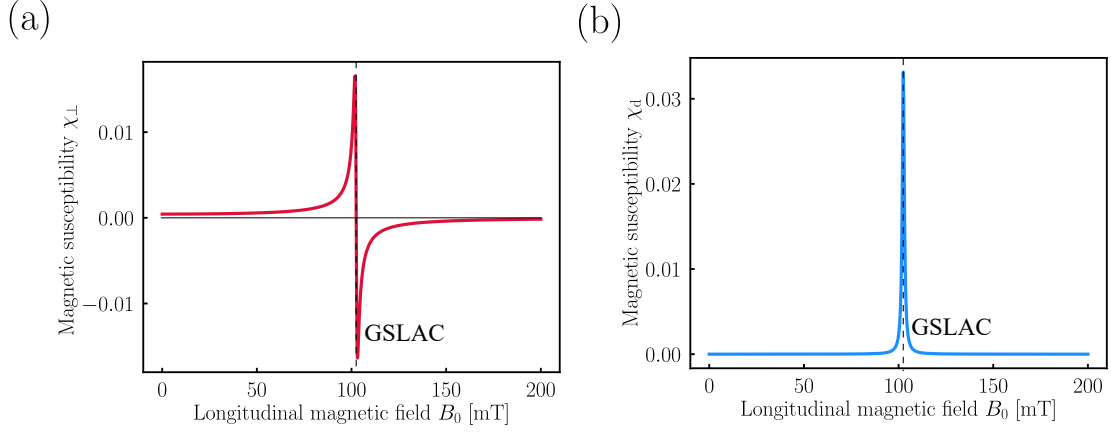


Figure 5.3: (a) Magnetic susceptibility tensor component  $\chi_{\perp}$  as a function of the strength of the longitudinal magnetic field  $\mathbf{B}_0$ . (b) Magnetic susceptibility tensor component  $\chi_d$  as a function of the strength of the longitudinal magnetic field  $\mathbf{B}_0$ .

In Fig. 5.3, we have plotted the two components  $\chi_{\perp}$  and  $\chi_d$  of the magnetic susceptibility tensor as a function of the magnetic field  $B_0$ . We have chosen parameters in agreement with the experimental parameters. Thus, we have chosen:  $d = 3.5$  ppm,  $\gamma_{\text{las}}/2\pi = 100$  kHz,  $\gamma_1/2\pi = 1$  kHz and  $\gamma_2/2\pi = 3.0$  MHz. We observe in Fig. 5.3 (a) that the component  $\chi_{\perp}$  is always positive when  $|\gamma_e|B_0 < D$  and negative when  $|\gamma_e|B_0 > D$ . This result means that the magnetic response transitions from a paramagnetic to a diamagnetic response when  $|\gamma_e|B_0 = D$ . This result is in accordance with the explanation of the previous part. Furthermore, the value of  $\chi_d$  is always much smaller than  $\chi_{\perp}$  except when  $|\gamma_e|B_0 \simeq D$ .

In the following, we study in more detail the magnetic susceptibility components  $\chi_{\perp}$  and  $\chi_d$  in the three relevant parameter regions: the paramagnetic phase corresponding to the low magnetic field regime where  $|\gamma_e|B_0 \ll D$ , the transition regime between the paramagnetic and diamagnetic phase where  $|\gamma_e|B_0 \simeq D$  and the diamagnetic phase corresponding to the high magnetic field regime where  $|\gamma_e|B_0 \gg D$ . For the rest of the manuscript, we assume that the optical pumping process is always stronger than the dissipation process, which means that  $\gamma_{\text{las}} \gg \Gamma_1$ . Thus, we consider that the ratio  $\gamma_{\text{las}}/(3\Gamma_1 + \gamma_{\text{las}}) \simeq 1$  and that  $\rho_{00}^{(0)} \simeq 1, \rho_{-1-1}^{(0)}, \rho_{11}^{(0)} \simeq 0$ .

#### Low magnetic field regime: the paramagnetic phase

We designate the region where  $|\gamma_e|B_0 \ll D$  as the low magnetic field regime (L.F.) which corresponds to  $B_0 \ll 102$  mT. We have already studied this case in the paragraph 1.3.3 of the Chapter 1. Applying Eq. (5.13) and keeping only the first order term in  $|\gamma_e|B_0/D$ , we obtain:

$$\chi_{\perp}^{\text{L.F.}} = 2d\hbar\mu_0 \frac{\gamma_e^2}{D}, \quad (5.15)$$

$$\chi_d^{\text{L.F.}} \ll \chi_{\perp}^{\text{L.F.}}, \quad (5.16)$$

which gives  $\chi_{\perp}^{\text{L.F.}} = 7.2 \times 10^{-5}$ . This value of the magnetic susceptibility tensor is a little bit larger than the value of the diamond orbital diamagnetic susceptibility which equals

$-2.2 \times 10^{-5}$ .

In Fig. 5.4, we have plotted the energy of the NV<sup>-</sup> center eigenstates under the assumption  $|\gamma_e|B_0 \ll D$ . Figure 5.4 (a) corresponds to the case of a purely longitudinal magnetic field without any transverse magnetic field perturbation. The resulting magnetization is equal to zero. Figure 5.4 (b) corresponds to the same case but we have added a small transverse magnetic perturbation  $\delta\mathbf{B}$ . In this case, the state  $|m_s = 0\rangle$  mixes a little bit with the two upper states  $|m_s = \pm 1\rangle$  giving rise to the eigenstate  $|m_s = 0'\rangle$ . The energy of  $|m_s = 0'\rangle$  is lower than the energy of  $|m_s = 0\rangle$  state. The total energy of the system thus decreases with the transverse perturbation field. This leads to a paramagnetic response of the system and  $\chi_{\perp}^{\text{L.F.}} < 0$ . The magnetization  $\delta\mathbf{M}$  is aligned in the same direction as the transverse perturbation field  $\delta\mathbf{B}$ .

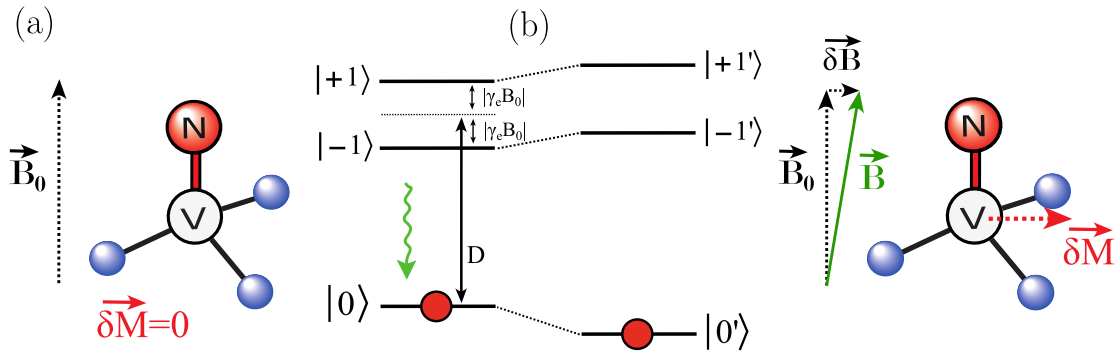


Figure 5.4: (a) Magnetic response of an NV<sup>-</sup> center in the regime of small magnetic field  $B_0$ . (b) Magnetic response of an NV<sup>-</sup> center in the regime of small magnetic field  $B_0$  with a transverse magnetic field  $\delta B$ .

### Transition regime from the paramagnetic to the diamagnetic phase

The transition from the paramagnetic to the diamagnetic phase corresponds to a range of parameter values where  $|\gamma_e|B_0 \simeq D$ . As previously explained, the magnetic response is expected to be strongest near the GSLAC due to the strong mixing of the states  $|m_s = -1\rangle$  and  $|m_s = 0\rangle$  when a transverse magnetic perturbation  $\delta\mathbf{B}$  is applied. This corresponds to a magnetic field value  $B_0$  close to 102 mT. By examining the expression of the magnetic susceptibility Eq. (5.13), the second term of the sum can be ignored in comparison to the first one since  $\Delta_{10} \simeq 2D$  and  $\Delta_{-10} \ll 2D$ . We thus obtain:

$$\chi_{\perp}^{\text{GSLAC}} = d\hbar\mu_0\gamma_e^2 \frac{\Delta_{-10}}{\Delta_{-10}^2 + (\Gamma_2^*)^2}, \quad (5.17)$$

$$\chi_{\text{d}}^{\text{GSLAC}} = d\hbar\mu_0\gamma_e^2 \frac{\Gamma_2^*}{\Delta_{-10}^2 + (\Gamma_2^*)^2}. \quad (5.18)$$

In Fig. 5.5 (a), the two magnetic susceptibility components  $\chi_{\perp}^{\text{GSLAC}}$  (in (i)) and  $\chi_{\text{d}}^{\text{GSLAC}}$  (in (ii)) are plotted as a function of the magnetic field  $B_0$ . As seen in Fig. 5.5 (a)-(i),  $\chi_{\perp}^{\text{GSLAC}}$  is negative for  $|\gamma_e|B_0 < D$ , which represents the paramagnetic regime, while it is positive for  $|\gamma_e|B_0 > D$ , which represents the diamagnetic regime. The susceptibility component  $\chi_{\perp}^{\text{GSLAC}}$  reaches values as strong as  $10^{-2}$  in absolute value in both regimes. To date, these are the strongest paramagnetic and diamagnetic susceptibility values reported

at 300 K for a material composed of uncorrelated electronic spins (this therefore excludes ferromagnetism and superconductors). This is for example three orders of magnitude stronger than the magnetic susceptibility at 300 K of graphite, which is known to be one of the best diamagnetic material, with  $\chi_{\perp}^{\text{Graphite}} = -1.4 \times 10^{-5}$  (160). The value of  $\chi_{\perp}^{\text{GSLAC}}$  is limited by the dephasing rate  $\Gamma_2^*$  as well as the NV<sup>-</sup> centers density. Therefore, it could be possible to reach stronger magnetic response with CVD grown diamonds with better dephasing rate  $\Gamma_2^*$  for example. In Fig. 5.5 (a)-(ii), it can be seen that  $\chi_{\text{d}}^{\text{GSLAC}}$  is of the same order as  $\chi_{\perp}^{\text{GSLAC}}$ . The impact of this term will not be discussed in this study as it would require to do further detailed analysis of the physical origin of the dephasing and also because it is challenging to experimentally reach this parameter regime.

In Fig. 5.5 (b) (resp.(c)), the energy of the NV<sup>-</sup> center eigenstates  $|m_s = 0'\rangle$  and  $|m_s = -1'\rangle$  are plotted in the paramagnetic phase (resp. diamagnetic phase). The two cases, where  $\delta\mathbf{B} = 0$  and  $\delta\mathbf{B} \neq 0$ , are distinguished in each plots. In the paramagnetic phase ( $|\gamma_e|B_0 < D$ ), the state  $|m_s = 0'\rangle$ , which is populated by the green laser pumping, is the ground state of the reduced two-level system ( $|m_s = 0'\rangle, |m_s = -1'\rangle$ ) whereas it is the excited state in the diamagnetic phase ( $|\gamma_e|B_0 < D$ ). The induced magnetization  $\delta\mathbf{M}$  is thus aligned or opposite to the direction of the perturbation  $\delta\mathbf{B}$  depending on the sign of  $|\gamma_e|B_0 - D$ .

It is noteworthy that the type of diamagnetism previously described originates from the electron spin of the NV<sup>-</sup> center, while diamagnetism typically arises from the orbital momenta of electrons. This is a result of the population inversion at the GSLAC of the spin system, which results in Van Vleck diamagnetism. Van Vleck magnetism is often referred to as Van Vleck paramagnetism, as a thermal occupation of the eigenstates always leads to a positive magnetic susceptibility as shown in Appendix A.3. The parameter region close the GSLAC is thus particularly interesting because of the transition from a paramagnetic to a diamagnetic regime, but also because the absolute values of the magnetic susceptibilities are extremely high compared to usual paramagnetic and diamagnetic susceptibilities at 300 K.

#### High magnetic field regime: the diamagnetic phase

We designate the region where  $|\gamma_e|B_0 \gg D$  as the high magnetic field regime ( $B_0 \gg 102\text{mT}$ ). Under this condition, the formula Eq. (5.13) can be applied in the limit of small  $D/|\gamma_e|B_0$  and we obtain:

$$\chi_{\perp}^{\text{H.F.}} = -2d\hbar\mu_0 \frac{D}{B_0^2}, \quad (5.19)$$

$$\chi_{\text{d}}^{\text{H.F.}} \ll \chi_{\perp}^{\text{H.F.}}. \quad (5.20)$$

This susceptibility is negative and tends to 0 for large  $B_0$  due to the scaling in  $1/B_0^2$ . It is due to the fact that the  $|m_s = 0\rangle$  states mixes quasi equally with the  $|m_s = -1\rangle$  and  $|m_s = +1\rangle$  states in the presence of a small transverse field for a large magnetic field  $B_0$  as shown in Fig. 5.6. However, even though the magnetic susceptibility tends to 0 for large  $B_0$ , the magnetic torque applied on a levitated diamond due to the diamond diamagnetism tends to a non-zero value as explained in the following section.

In this section, it has been shown that the NV<sup>-</sup> center exhibits a transition from paramagnetism to diamagnetism at a magnetic field value of  $B_0 = 102\text{ mT}$ . Around this specific magnetic field value, the magnetic susceptibility of diamonds highly doped with

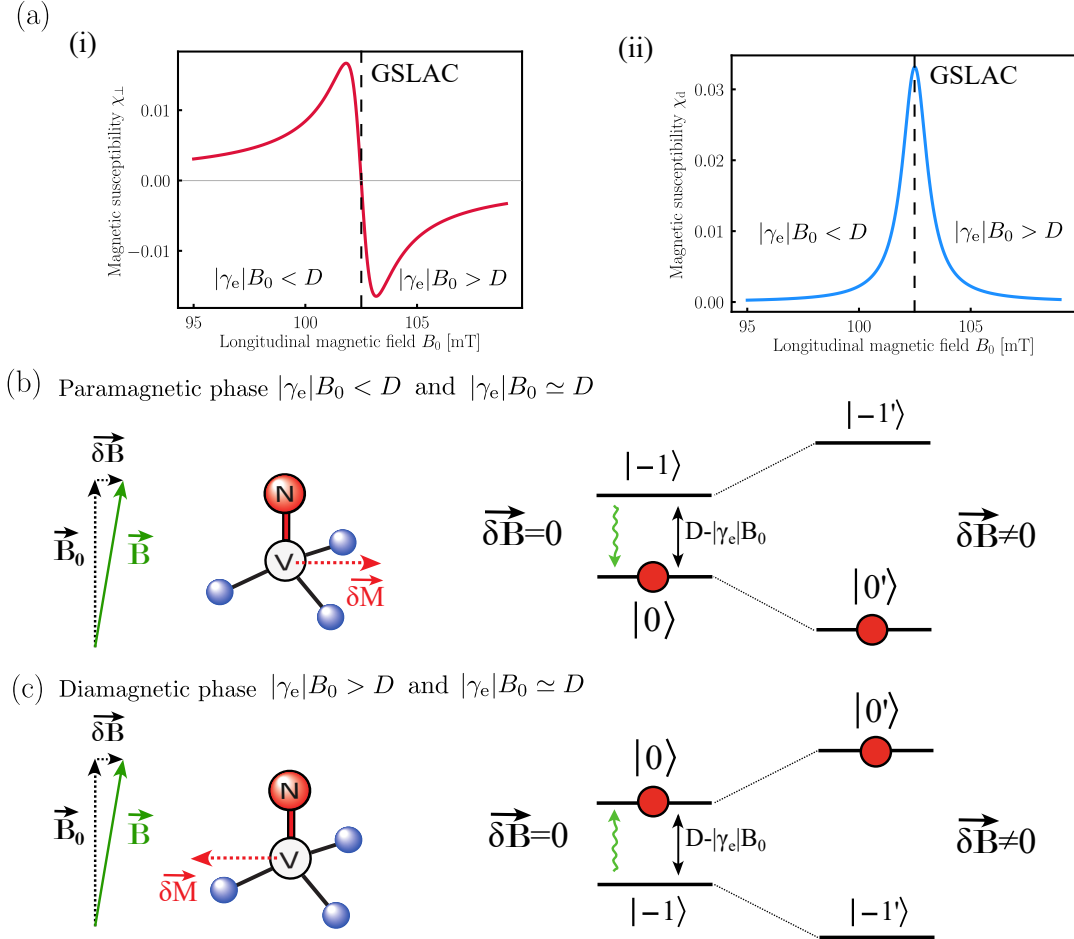


Figure 5.5: (a)(i) Magnetic susceptibility tensor component  $\chi_{\perp}$  as a function of the longitudinal magnetic field  $B_0$  close to the GSLAC. (ii) Magnetic susceptibility tensor component  $\chi_a$  as a function of the longitudinal magnetic field  $B_0$  close to the GSLAC. (b) Left: paramagnetic response of the  $\text{NV}^-$  center before the GSLAC. Right: evolution of the energies and populations of the  $\text{NV}^-$  eigenstates as a function of the transverse magnetic field  $\delta B$  before the GSLAC. (c) Left: diamagnetic response of the  $\text{NV}^-$  center after the GSLAC. Right: evolution of the energies and populations of the  $\text{NV}^-$  eigenstates as a function of the transverse magnetic field  $\delta B$  after the GSLAC.

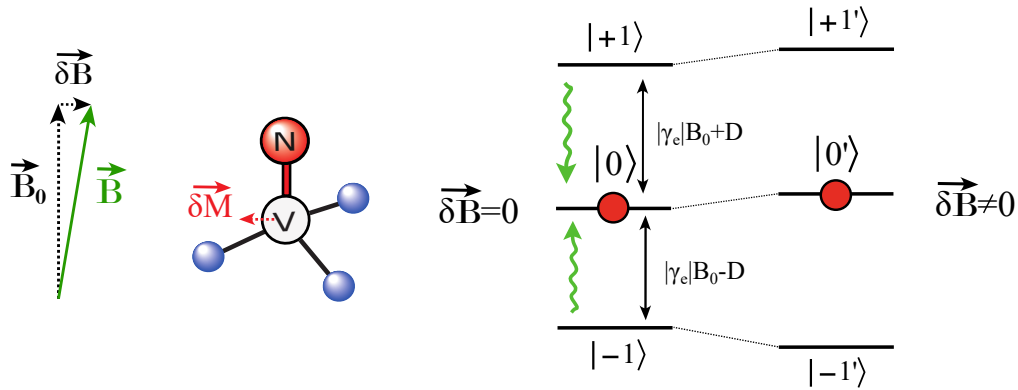


Figure 5.6: Magnetization of the  $NV^-$  center in the high magnetic field limit. The evolution of the eigenstates energies and populations as a function of the transverse magnetic field is depicted on the right.

$NV^-$  centers is of the order of  $10^{-2}$ , which is three order of magnitude higher than the best paramagnetic and diamagnetic materials at 300 K.

In the following section, the diamond magnetic transition is measured using torque magnetometry with a levitated micro diamond from the Adamas company. In the diamagnetic regime, it is proven that the diamond's anisotropy axis aligns with the direction of the external magnetic field, offering bright prospects for controlling the angular degree of freedom of untethered diamonds.

## 5.2. Angle locking of a levitating diamond using $NV^-$ centers diamagnetism

In this section, we experimentally prove the existence of the Van Vleck paramagnetic and diamagnetic phase described in the previous section by measuring the torque induced by the magnetic response of  $NV^-$ -doped diamond. To do this, we use a 15 micrometers levitating diamond with a high concentration of  $NV^-$  centers (3.5 ppm) from the Adamas company. In the diamagnetic phase, the  $NV^-$  centers exert a torque that is strong enough to counter the torque from the Paul trap discussed in the previous chapter and locks the anisotropy axis of the  $NV^-$  center in the direction of the external magnetic field. By varying parameters such as the magnetic field strength and direction or the intensity of the green laser, we demonstrate the robustness of this effect.

This section is structured as follows. First, we calculate the Van Vleck para/diamagnetic torque applied on a levitating diamond. Second, we prove that we can fully control the orientation of the levitating diamond using  $NV^-$  centers Van Vleck diamagnetism. Finally, we study the librational frequency dependence on the experimental parameters of the Van Vleck confining diamagnetic torque.

### 5.2.1 Calculation of the $NV^-$ centers diamagnetic torque

In the previous section, we calculated the magnetization  $\mathbf{M}(\mathbf{B})$  of an  $NV^-$  center doped diamond in response to an external magnetic field  $\mathbf{B}$  that is almost aligned with the  $NV^-$  anisotropy axis. Using the results obtained in the previous section, we calculate the magnetic torque applied on a levitated diamond due to the Van Vleck para/diamagnetism

of the  $NV^-$  centers as a function of the magnetic susceptibility tensor components.

### Magnetic torque as a function of the magnetic perturbation $\delta\mathbf{B}$

As explained in Chapter 2, torque magnetometry is a powerful method for probing the internal magnetism of magnetic particles. Here, we use torque magnetometry to probe the Van Vleck para/diamagnetism of diamonds which is not accessible by ODMR with fixed diamonds. The magnetic torque reads:

$$\boldsymbol{\tau}_{\text{mag}} = \boldsymbol{\mu} \times \mathbf{B}. \quad (5.21)$$

where  $\boldsymbol{\mu} = V\mathbf{M}$  is the total magnetic moment of the diamond. Using this formula, the torque induced by the magnetization of the diamond due to the Van Vleck para/diamagnetism is equal to:

$$\boldsymbol{\tau}_{\text{mag}} = V\mathbf{M}(\mathbf{B}) \times \mathbf{B}. \quad (5.22)$$

Using Eq. (5.8), we have:

$$\boldsymbol{\tau}_{\text{mag}} = \frac{V}{\mu_0} (\underline{\chi}^{NV} \cdot \delta\mathbf{B}) \times \mathbf{B}_0 + o(\delta\mathbf{B}). \quad (5.23)$$

Finally, we obtain (neglecting the contribution of  $\chi_d$ ):

$$\boldsymbol{\tau}_{\text{mag}} = \frac{V}{\mu_0} \chi_{\perp} \delta B_{\perp} B_0 (\mathbf{e}_{\perp} \times \mathbf{e}_3) + o(\delta B_{\perp}). \quad (5.24)$$

where  $\delta\mathbf{B} = \delta B_{\perp} \mathbf{e}_{\perp}$  with  $\mathbf{e}_{\perp}$  a direction perpendicular to the anisotropy axis given by  $\mathbf{e}_3$ . The value of the magnetic torque linearly depends on the magnetic susceptibility coefficient  $\chi_{\perp}$ . We therefore expect to have opposite torques in the Van Vleck paramagnetic phase ( $\chi_{\perp} > 0$ ) and in the Van Vleck diamagnetic phase ( $\chi_{\perp} < 0$ ).

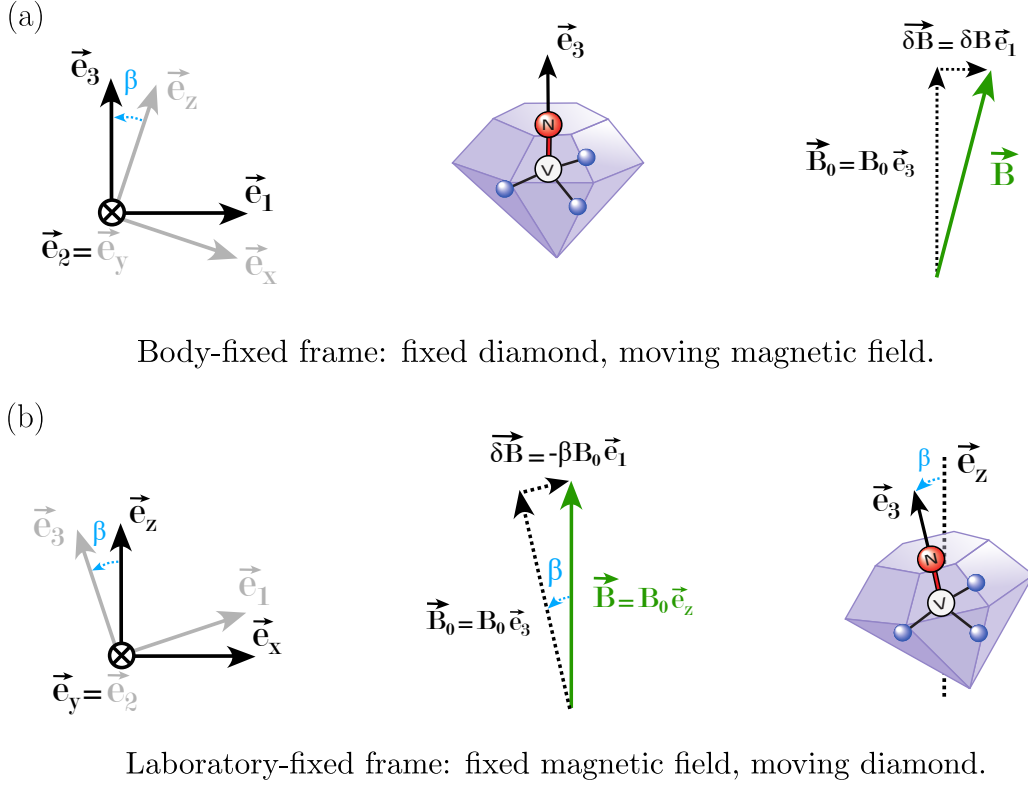
### Magnetic torque as a function of the levitating diamond angular position

As in Eq. (5.24), the magnetic torque is expressed as a function of the parameter  $\delta B_{\perp}$ . In order to study the angular dynamics of a diamond subjected to the magnetic torque, it is more convenient to reexpress the magnetic torque as a function of the diamond angular position given by the Euler angles  $(\alpha, \beta, \gamma)$ .

To do this, we no longer express the magnetic torque  $\boldsymbol{\tau}_{\text{mag}}$  in the body-fixed basis  $(\mathbf{e}_1, \mathbf{e}_2, \mathbf{e}_3)$  where the diamond is fixed and the magnetic field can be tuned considering the free parameter  $\delta B_{\perp}$  as shown in Fig. 5.7 (a). Instead, we express the magnetic torque in the laboratory-fixed basis  $(\mathbf{e}_x, \mathbf{e}_y, \mathbf{e}_z)$  where the diamond angular motion is parametrized by the Euler angles. In this laboratory-fixed frame, we consider that the magnetic field  $\mathbf{B}$  is fixed and along  $\mathbf{e}_z$  as shown in Fig. 5.7 (b). For simplicity, we only consider one angular degree of freedom of the diamond given by the nutation angle  $\beta$ . We further assume that the magnetic field  $\mathbf{B}$  is still almost aligned to the  $NV^-$  center anisotropy axis  $\mathbf{e}_3$ . Thus, we make the small angle approximation  $\beta \ll 1$ .

According to Fig. 5.7 (b),  $\mathbf{B}$  can be written in the body-fixed basis  $(\mathbf{e}_1, \mathbf{e}_2, \mathbf{e}_3)$  as a function of  $\beta$  (under the small angle approximation):

$$\mathbf{B} = B_0 \mathbf{e}_3 - \beta B_0 \mathbf{e}_1 + o(\beta). \quad (5.25)$$



Body-fixed frame: fixed diamond, moving magnetic field.

Laboratory-fixed frame: fixed magnetic field, moving diamond.

Figure 5.7: (a) Body-fixed frame: the position of the diamond is fixed and the magnetic field is changed via the free parameter  $\delta B$ . (b) Laboratory-fixed frame: the magnetic field is constant and the diamond is free to rotate, parametrized by the nutation angle  $\beta$ .

In the small angle approximation,  $\beta B_0 \ll B_0$  and we can then use the expression of the magnetic torque previously calculated in Eq. (5.24) using  $\delta B_{\perp} \mathbf{e}_{\perp} = -\beta B_0 \mathbf{e}_1$ . We obtain:

$$\tau_{\text{mag}} = \frac{V}{\mu_0} \chi_{\perp} B_0^2 \beta \mathbf{e}_y + o(\beta). \quad (5.26)$$

Thus, the magnetic torque is a restoring torque if and only if  $\chi_{\perp} < 0$  corresponding to the diamagnetic regime ( $B_0 \geq 102$  mT). We can thus estimate the characteristic confining frequency of the diamagnetic torque:

$$f_{\text{mag}} = \frac{1}{2\pi} \sqrt{\frac{V |\chi_{\perp}| B_0^2}{\mu_0 I}}. \quad (5.27)$$

In Fig. 5.8, the libration frequency has been plotted as a function of the magnetic field  $B_0$  for a  $15 \mu\text{m}$  diamond with a concentration of  $NV^-$  centers equals to 3.5 ppm. For magnetic fields below 102 mT, the  $NV^-$  centers are in the paramagnetic regime and the magnetic torque is not confining. For values of  $B_0$  stronger than 102 mT, the magnetic torque is a restoring torque and the magnetic libration frequency is well-defined.

Around  $B_0 = 102$  mT, the magnetic libration frequency can reach values of a few kHz. The reason is that the magnetic response is enhanced close to the GSLAC due to the proximity of the energy of the two eigenstates  $|m_s = 0\rangle$  and  $|m_s = -1\rangle$ . In the

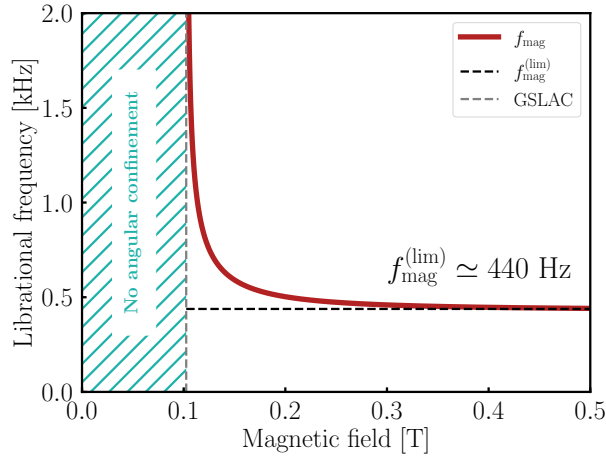


Figure 5.8: Magnetic librational frequency as a function of the longitudinal magnetic field. For magnetic fields smaller than 102 mT, the magnetic torque is anti-confining. For magnetic fields larger than 102 mT, the magnetic librational frequency is well-defined.

high magnetic field regime i.e.  $|\gamma_e|B_0 \gg D$ , it has been demonstrated in part 5.1.2 that the magnetic susceptibility coefficient  $\chi_{\perp}^{\text{H.F.}}$  is proportional to  $1/B_0^2$ . Thus, the libration frequency tends to a limit value  $f_{\text{mag}}^{(\text{lim})} \neq 0$  which is typically of the order of few hundreds of Hz. This frequency does not depend on the magnetic field strength but on the  $NV^-$  center anisotropy constant  $D$ :

$$f_{\text{mag}}^{(\text{lim})} = \frac{1}{2\pi} \sqrt{\frac{2dV\mu_0 D}{I}}. \quad (5.28)$$

In this part, it has been shown that the levitating diamond is subjected to a restoring torque in the diamagnetic regime i.e. when  $|\gamma_e|B_0 > D$ . For magnetic field values between 0.1 – 0.12 T, the diamagnetic torque confining frequency is on the order of 1 kHz, which is one order of magnitude above the typical Paul trap restoring torque. In the following, we experimentally prove that the diamagnetic torque dominates the Paul trap restoring torque in the regime of strong magnetic field ( $|\gamma_e|B_0 > D$ ) leading to the confinement of the anisotropy axis of the diamond along the direction of the magnetic field.

### 5.2.2 Orientation control of the diamond using $NV^-$ centers diamagnetism

In this part, we experimentally demonstrate the locking of the levitating diamond's orientation to the external magnetic field direction in the  $NV^-$  center diamagnetic regime ( $|\gamma_e|B_0 > D$ ). To do this, we propose two different experiments that confirm the locking of the diamond's orientation in the magnetic field direction. We use the MDMR measurement technique developed in Chapter 2 to precisely measure the angular direction of the diamond relative to the magnetic field direction.

#### Increase of the magnetic field strength

Before proceeding further, it is important to note that the theoretical analysis presented previously was performed for a single class of  $NV^-$  centers. However, diamonds containing large amounts of  $NV^-$  center impurities, such as the one used in our experiments, have an equal distribution of  $NV^-$  center among the four classes. The para/diamagnetic torque

applied on the diamond is therefore the sum of the contributions from the four  $NV^-$  center classes. As previously explained, the origin of the strong para/diamagnetic response of the  $NV^-$  centers is due to a large asymmetry in the population distribution between the three eigenstates ( $|m_s = 0\rangle, |m_s = -1\rangle, |m_s = +1\rangle$ ). This asymmetric population distribution is created by the green laser optical pumping to the  $|m_s = 0\rangle$  state, which is only efficient for small magnetic fields or for strong magnetic fields that are almost aligned with the  $NV^-$  center anisotropy axis. In the case of a strong magnetic field that is misaligned with an  $NV^-$  center class anisotropy axis, the three eigenstates of the  $NV^-$  center are not the states ( $|m_s = 0\rangle, |m_s = -1\rangle, |m_s = +1\rangle$ ) and the green laser optical pumping process does not populate a specific eigentate. In this case, the magnetic response of the  $NV^-$  center is expected to be similar to the magnetic response in the case of a thermal distribution of states. In the high magnetic field case, corresponding to the diamagnetic regime, it is therefore relevant to neglect the contribution of the  $NV^-$  center classes that are not aligned with the magnetic field direction in the diamond's magnetic response.

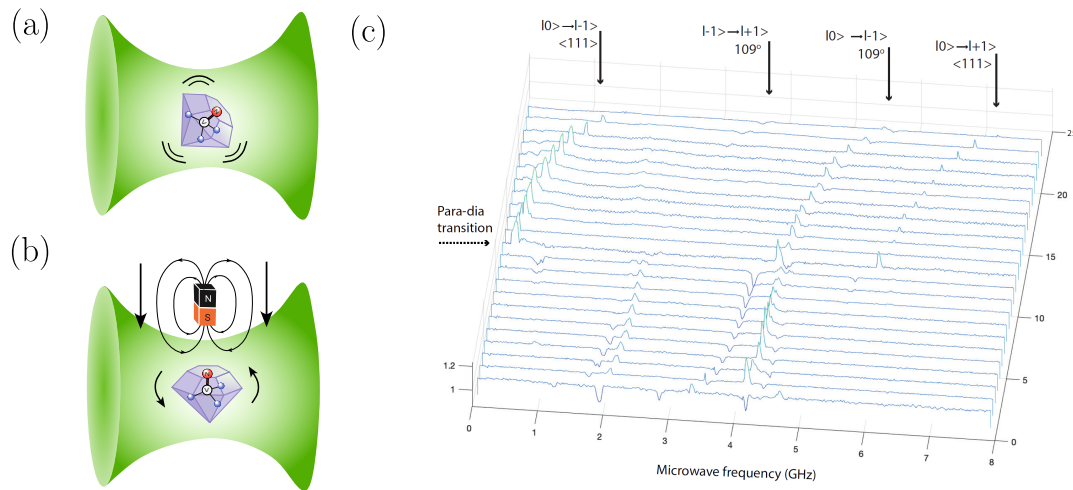


Figure 5.9: (a) Schematic of an angularly stable levitating diamond under green laser radiation. (b) Schematic of a levitating diamond under green laser radiation where a magnet is continuously brought close to the diamond. (c) Cascade diagram of the MDMR measurements performed while approaching the magnet close to the levitating diamond.

In order to observe the  $NV^-$  center restoring torque in the diamagnetic regime ( $|\gamma_e|B_0 > D$ ), the following experiment is proposed in Fig. 5.9 (a) and (b). A  $15 \mu\text{m}$  is initially levitated in our Paul trap without an external magnetic field as shown in Fig. 5.9 (a). The confinement of the diamond is ensured by the restoring torque of the Paul trap in the libration regime. We illuminate the diamond with a green laser in order to polarize the  $NV^-$  centers in the  $|m_s = 0\rangle$  state. We then progressively increase the magnetic field strength using an external magnet that we bring close to the levitating diamond, as shown in Fig. 5.9 (b). We ensure that the magnetic field direction at the diamond position remains the same during this process. MDMR measurements are continuously performed while bringing the magnet close to the levitating diamond. Here, the microwave drive is only used to read the angular position. In Fig.5.9 (c), we present a 2D graph of the different MDMRs obtained. Even though the number of magnetic resonance peaks observed on the MDMR plots is not 8 (four  $NV^-$  center classes with the two transitions

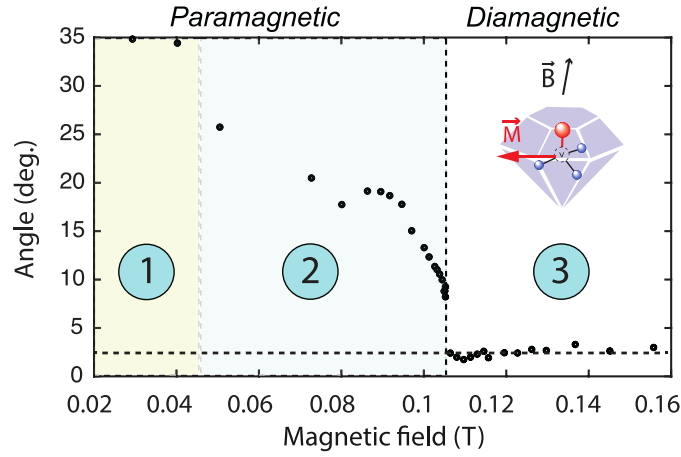


Figure 5.10: Angle between one of the  $NV^-$  center class and the magnetic field direction as a function of the external magnetic field strength. Phase 1 (yellow region) corresponds to the Paul trap dominating torque regime. Phase 2 (blue region) corresponds to the regime where the Paul trap torque and the magnetic torque are of the same order of magnitude. Phase 3 (white region) corresponds to the magnetic torque dominating regime.

$|m_s = 0\rangle \rightarrow |m_s = \pm 1\rangle$ ), we can still estimate the angular position of the diamond in the laboratory frame using the MDMR. In Fig. 5.10, the angle  $\beta$  between an  $NV^-$  center class and the external magnetic field direction is plotted as a function of the magnetic field strength  $B_0$ . First, we observe that  $\beta$  is constant for a magnetic field strength below 0.04 T. This phase is referred to as phase 1 on Fig. 5.10. Second,  $\beta$  continuously decreases for a magnetic field strength between 0.04 – 0.105 T. This phase is referred to as phase 2 on Fig. 5.10. Finally,  $\beta$  takes a constant value close to  $0^\circ$  for a magnetic field larger than 0.105 T. This phase is referred to as the phase 3 on Fig. 5.10. The results of this experiment can be explained as follows: during phase 1, the magnetic torque due to the paramagnetic behavior of the  $NV^-$  center is too small compared to the restoring torque of the Paul trap, and the angular position of the diamond remains the same. During phase 3, one of the  $NV^-$  center classes is fully aligned with the external magnetic field. The magnetic field strength being stronger than 102 mT, the magnetic response of the  $NV^-$  center is diamagnetic, leading to a restoring torque that is stronger than the Paul trap restoring torque, as proved in the previous part. The threshold magnetic field value at which the diamond aligns with the magnetic field direction equals 105 mT, which is very close to the theoretical value of the phase transition into the diamagnetic regime, which is 102 mT. Phase 2 is thus an intermediate phase between phase 1 and phase 3 where both electric torque from the Paul trap and magnetic torque from the diamond compete.

The  $NV^-$  center magnetic torque is strong enough to counter the restoring torque of the Paul trap in the diamagnetic regime i.e. for magnetic fields stronger than 102 mT. This type of experiment has been performed on a large number of diamonds and is highly reproducible. In the next part, we present a second experiment where we change the magnetic field orientation while keeping the magnetic field strength constant.

### Magnetic field rotation

In order to demonstrate the robustness of the diamond's angular alignment with the direction of the magnetic field  $\mathbf{B}_0$  in the high magnetic field regime ( $B_0 > 102$  T), we

conducted the experiment shown in Fig. 5.11 (a), where we change the direction of the magnetic field using a goniometer. In the small frame of Fig. 5.11 (b), we defined the angle  $\beta_B$  as the angle between a fixed direction in the laboratory frame and the magnetic field orientation, as well as the angle  $\beta_{NV}$  which is the angle between the  $NV^-$  center anisotropy direction and the magnetic field orientation. The value of  $\beta_B$  is directly given by the goniometer, while  $\beta_{NV}$  was experimentally measured using the same MDMR technique described previously. In Fig. 5.11 (b), we plotted  $\beta_{NV}$  as a function of  $\beta_B$ . We observed that the value of  $\beta_{NV}$  remains almost constant between  $5^\circ$  and  $7^\circ$  as  $\beta_B$  was changed by  $22^\circ$ . This clearly indicates that the diamond orientation follows the motion of the external magnetic field direction. The deviation of  $5 - 7^\circ$  from the equilibrium position given by the diamagnetic torque, which is supposed to be  $\beta_{NV} = 0^\circ$ , is due to the fact that the Paul trap torque is not entirely negligible, and it induces a small shift in the angular equilibrium position.

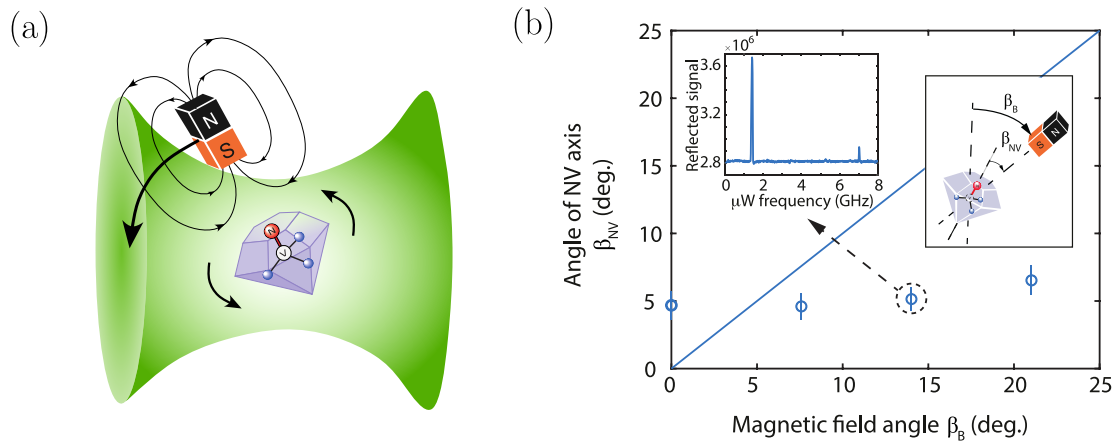


Figure 5.11: (a) Schematics of an angularly stabilized levitating diamond under a green laser radiation while rotating a magnet around that generates a magnetic field. (b) Angle  $\beta_{NV}$  between one of the  $NV^-$  center class and the magnetic field direction as a function of the angle  $\beta_B$  of the external magnetic field in the laboratory frame (blue dots). The blue line corresponds to an example of values that  $\beta_{NV}$  could take if there were no diamagnetism from the  $NV^-$  centers.

Thus, it is clear that the diamagnetic response of the  $NV^-$  centers is responsible for aligning the diamond with the direction of the external magnetic field after the GSLAC ( $B_0 = 102$  mT). In the following, we obtain quantitative experimental measurements of the libration frequency due to the diamagnetic torque by performing experiments in vacuum with a levitating diamond. We show that the results are in good agreement with the theory.

### 5.2.3 Librational frequency in the diamagnetic regime

In this part, we investigate the dependence of the libration frequency of the diamond in the diamagnetic phase on various parameters, such as the population difference between the eigenstates or the magnetic field strength. To accomplish this, we perform experiments in vacuum in order to resolve the libration modes.

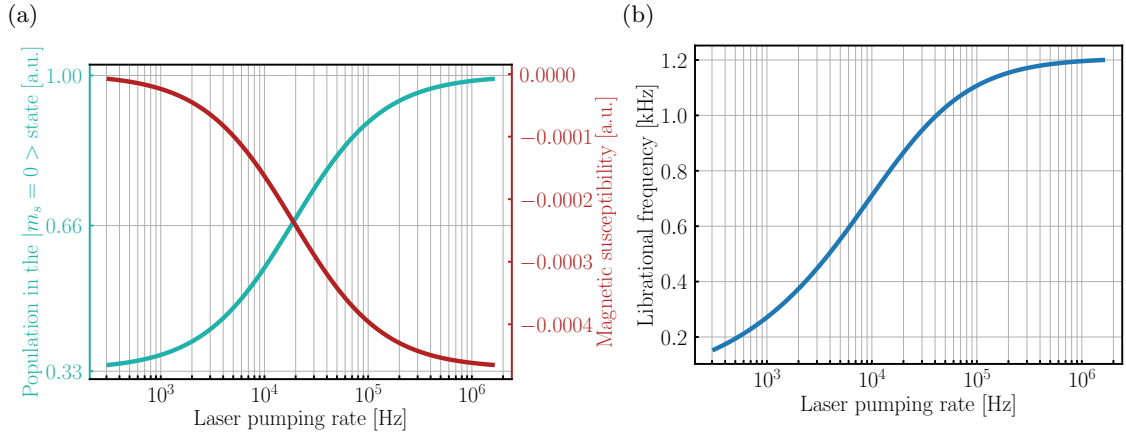


Figure 5.12: (a) Population in the  $|m_s = 0\rangle$  state and magnetic susceptibility  $\chi_{\perp}$  as a function of the green laser pumping rate  $\gamma_{\text{las}}$ . (b) Librational frequency as a function of the green laser pumping rate  $\gamma_{\text{las}}$

#### Dependence on the population distribution

The Van Vleck diamagnetic behavior of the  $NV^-$  center is caused by the significant population difference between the  $|m_s = 0\rangle$  and the  $|m_s = -1\rangle$  states, which are close in energy when  $|\gamma_e|B_0 \approx D$ . The population distribution among the three eigenstates can be adjusted by the power of the optical pumping laser. According to Eq. 5.13, the magnetic susceptibility of the  $NV^-$  centers close near the GSLAC depends on the green optical pumping rate  $\gamma_{\text{las}}$  as:

$$\chi_{\perp}^{\text{GSLAC}}(\gamma_{\text{las}}) = d\hbar\mu_0\gamma_e^2 \frac{\gamma_{\text{las}}}{3\Gamma_1 + \gamma_{\text{las}}} \frac{\Delta_{-10}}{\Delta_{-10}^2 + (\Gamma_2^*)^2}, \quad (5.29)$$

In Fig. 5.12 (a), we calculate the evolution of the magnetic susceptibility component  $\chi_{\perp}^{\text{GSLAC}}(\gamma_{\text{las}})$  and the population in the  $|m_s = 0\rangle$  state  $\rho_{00}^{(0)}$  as a function of the green laser pumping rate  $\gamma_{\text{las}}$  for a magnetic field value  $B_0 = 0.11$  T. As the optical pumping rate increases, the magnetic susceptibility value becomes stronger, which implies that the resulting librational frequency also increases, as shown in Fig. 5.12 (b).

Experimentally, the population distribution in the different eigenstates can be adjusted by varying the power of the green laser, which linearly depends on the rate  $\gamma_{\text{las}}$ . This rate is in competition with the decay rate  $\Gamma_1 = 2\pi/T_1$  as shown in Fig. 5.13 (a).

In Fig. 5.13 (b), we plot the angle  $\beta$  between the diamond anisotropy axis and the magnetic field direction as a function of the green laser power, which is measured using a power meter, for a magnetic field value stronger than 102 mT. As the laser power increases, the angle  $\beta$  decreases. This is because the increase of the green laser power leads to an increase in the magnetic torque compared to the residual Paul trap torque. As a result, the diamond tends to align its anisotropy axis to the external magnetic field  $\mathbf{B}_0$  for stronger values of the laser power.

One can also measure the value of the librational frequency as a function of the green laser power for a levitating diamond in vacuum. In Fig. 5.13 (c) and (d), we present the results of measuring the librational frequency as a function of the green laser power for different values of the laser power. The pressure at which the experiments were performed

is  $10^{-1}$  mbar. In Fig. 5.13 (c), we show two PSD of two librational modes of the diamond. Plot (i) shows two librational modes without green laser and plot (ii) shows the same two librational modes in the presence of a green laser. We observe that the librational frequencies are stronger when the green laser is switched on. This can be explained by the fact that switching on the green laser activates the diamagnetism of the  $NV^-$  centers, therefore increasing the libration frequency. In Fig. 5.13 (d), we plotted the librational frequency of one of the two librational modes of the diamond as a function of the laser power. The librational frequency increases as the laser power increases, which is in agreement with the previous explanations.

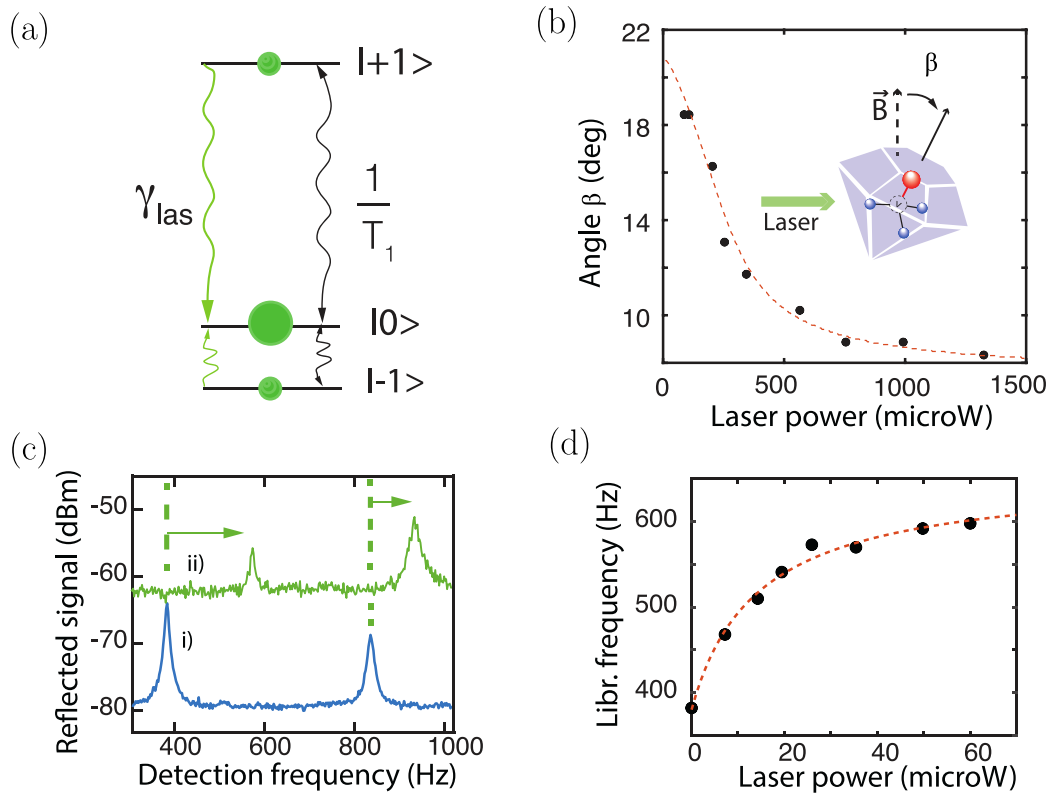


Figure 5.13: (a)  $NV^-$  center population distribution between the different eigenstates. Green arrows depict the optical pumping to the  $|m_s = 0\rangle$  state due to the green laser. Black arrows depict the decaying mechanisms at rates  $\Gamma_1 = 2\pi/T_1$ . (b) Angle  $\beta$  of one of the  $NV^-$  center anisotropy axis with respect to the external magnetic field direction as a function of the green laser power. (c) Trace i) and trace ii) are PSD of the librational modes without and with the green laser respectively. (d) Librational frequency of the first librational mode as a function of laser power.

We have demonstrated that the librational frequency induced by the diamagnetism of the  $NV^-$  centers is strongly dependent on the population distribution, as expected from theoretical predictions. In the following part, we demonstrate that the librational frequency also depends on the strength of the magnetic field.

#### Dependence on the strength of the magnetic field

In Eq. (5.27) and in the corresponding plot Fig. 5.8, we have demonstrated that the librational frequency induced by the diamagnetic torque is a decreasing function of

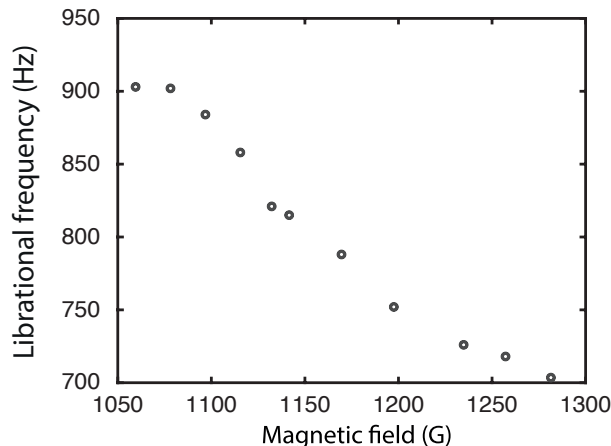


Figure 5.14: Librational frequency of the levitating diamond as a function of the external magnetic field strength.

the magnetic field strength after the GSLAC. The reason for this is that the  $|m_s = -1\rangle$  and the  $|m_s = 0\rangle$  are less resonant in the high magnetic field regime ( $|\gamma_e|B_0 \ll 102$  mT), leading to a smaller Van Vleck diamagnetic response.

We performed an experiment where we measured the librational frequency of a levitating diamond as a function of the magnetic field strength, at a pressure of  $10^{-1}$  mbar. In Fig. 5.14, we show the results of this experiment. We see that the librational frequency decreases with the magnetic field strength. This result is in agreement with the theoretical results shown in Fig. 5.8.

In this section, we have experimentally demonstrated how the diamagnetism of the  $NV^-$  centers can be used to lock the orientation of levitating diamonds with the magnetic field direction. We have provided numerous experimental proofs of this effect by varying experimental parameters such as the laser power, the magnetic field strength, and the magnetic field directions. This technique is extremely useful for controlling the angle of an untethered diamond, as it only requires a magnetic field stronger than 102 mT and a green laser focused on the diamond, without the need for microwave control of the  $NV^-$  center spin states. In the following section, we will use numerical simulations to explore the magnetic torque applied on the diamond in the general case of magnetic fields that are not almost aligned with the anisotropy direction of the  $NV^-$  center.

### 5.3. Librational magnetic energy

In previous sections, we have shown how a levitating diamond can align with the external magnetic field when  $B_0 > 102$  mT. The theoretical model, which is based on the magnetic susceptibility calculation, is valid in a regime where the angle  $\beta$  between the  $NV^-$  centers anisotropy axis and the magnetic field direction remains small. Thus, this theory does not allow us to fully understand the magnetism of  $NV^-$  centers for a random orientation of the magnetic field.

In this section, we use analytical calculations and numerical simulations to understand the magnetism of  $NV^-$  centers for a wide range of magnetic field orientations. Specifically, we calculate the librational magnetic energy as a function of the diamond angular position relative to the magnetic field direction. We will perform these calculations for a single

NV<sup>-</sup> class as well as for all four NV<sup>-</sup> classes. The goal of these calculations is to estimate the strength of the magnetic potential well created by the NV<sup>-</sup> center diamagnetism, which will confirm that the well is significantly deeper than thermal energy  $k_B T$ .

### 5.3.1 Theoretical calculation of the librational magnetic energy

In this part, the objective is to calculate the theoretical expression of the angular magnetic energy due to the NV<sup>-</sup> center magnetism. To achieve this, we use the Euler angle coordinate system introduced in Chapter 2 to parametrize the angular motion of the diamond. We assume that the magnetic torque induced by the NV<sup>-</sup> center derives from a potential energy  $E_{\text{mag}}(\alpha, \beta, \gamma)$  that depends on the angular position of the NV<sup>-</sup> centers and the magnetic field  $\mathbf{B}_0$ . We consider a fixed magnetic field  $\mathbf{B}_0 = B_0 \mathbf{e}_z$  in the laboratory frame, along the  $\mathbf{e}_z$  axis. Due to the rotational symmetry around the  $z$  axis, the magnetic potential energy does not depend on the precession angle  $\alpha$ , so that we can simplify the calculation by assuming  $\alpha = 0$ . We can write  $E_{\text{mag}}(\beta, \gamma)$  as:

$$E_{\text{mag}}(\beta, \gamma) - E_{\text{mag}}(0, 0) = E_{\text{mag}}(\beta, \gamma) - E_{\text{mag}}(\beta, 0) + E_{\text{mag}}(\beta, 0) - E_{\text{mag}}(0, 0), \quad (5.30)$$

which can be expressed using the magnetic torque  $\boldsymbol{\tau}_{\text{mag}}(\alpha, \beta, \gamma)$  (we define  $E_{\text{mag}}(0, 0)$  as the zero of the potential):

$$E_{\text{mag}}(\beta, \gamma) = \int_0^\beta \boldsymbol{\tau}_{\text{mag}}(0, \beta', 0) \cdot d\boldsymbol{\beta}' + \int_0^\gamma \boldsymbol{\tau}_{\text{mag}}(0, \beta, \gamma') \cdot d\boldsymbol{\gamma}', \quad (5.31)$$

where  $d\boldsymbol{\beta}' = d\beta' \mathbf{e}_y$  and  $d\boldsymbol{\gamma}' = d\gamma' \mathbf{e}_3$ . We use this formula to numerically calculate the librational magnetic energy.

### 5.3.2 Numerical simulation of the librational magnetic energy

Using the QuTiP library in Python (161; 162), the magnetic torque can be calculated for each angular configuration by solving the stationary master equation of the density matrix, and the magnetic energy  $E_{\text{mag}}(\beta, \gamma)$  can be obtained by integrating the torque. The energy depends on several parameters such as the strength of the magnetic field  $B_0$ , the optical pumping rate  $\gamma_{\text{las}}$ , the decay rate  $\Gamma_1$  and the dephasing rate given by  $\Gamma_2^*$ . We conduct numerical simulations for a typical diamond from Adamas Nanotechnology company of 15  $\mu\text{m}$  of diameter and a concentration of NV<sup>-</sup> centers of 3.5 ppm. We consider typical value of  $\Gamma_1, \Gamma_2^*$ , and an experimentally accessible value of  $\gamma_{\text{las}} = 50$  kHz.

In Fig. 5.15 (a), we show the magnetic energy of a diamond containing a single class of NV<sup>-</sup> center as a function of the angle  $\beta$  and the magnetic field strength  $B_0$ . The diamagnetic phase is clearly visible for  $B_0 > 102$  mT, where the position  $\beta = 0$  is a minimum of librational magnetic energy. The depth of the well is three orders of magnitude larger than the thermal energy at 300 K, which confirms that the diamagnetism of the NV<sup>-</sup> exerts a restoring torque strong enough to overpass the temperature. The depth of the well is also comparable to the typical angular energy due to the Paul trap.

In Fig. 5.15 (b), we plot the librational magnetic energy including the four NV<sup>-</sup> center classes for  $\gamma = 0^\circ$ . We observe that the angular position ( $\beta = 71^\circ, \gamma = 0^\circ$ ) is stable for the diamond, as it corresponds to the angle where another NV<sup>-</sup> class is aligned with the external magnetic field.

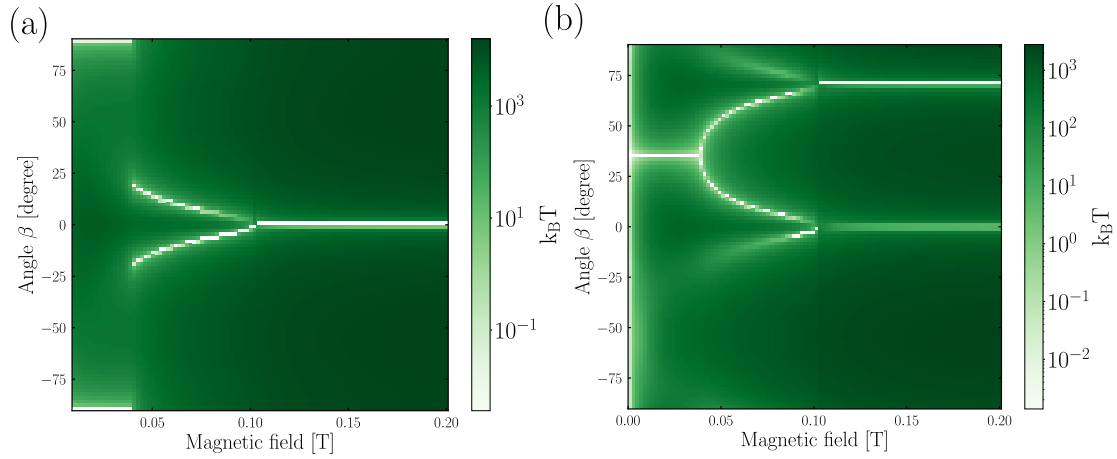


Figure 5.15: (a) Magnetic energy of the levitating diamond as a function of the external magnetic field strength and the diamond angle considering one NV center class. (b) Magnetic energy of the levitating diamond as a function of the external magnetic field strength and the diamond angle considering the four NV center classes.

We also observe that in the paramagnetic phase (i.e. for  $B_0 < 102$  mT) the position  $\beta = 0^\circ$  is a maximum of energy, as predicted by the theory. We see that the position of the energy minimum  $\beta_{\min}(B_0)$ , almost continuously tends to the equilibrium position  $\beta_{\min}(B_0 > 102 \text{ mT}) = 0$  for increasing value of  $B_0$ . This supports the experimental observation of a continuous transition in Fig. 5.10 from a regime where the Paul trap determines the equilibrium position to a regime where the diamond is angularly confined by spin-diamagnetism at  $\beta = 0$ .

## 5.4. Conclusion

In this chapter, we have demonstrated how the strong diamagnetic response of  $\text{NV}^-$  centers, when exposed to green laser light, can enable complete orientational control of a levitating diamond in the presence of a strong external magnetic field. To do so, we have shown that the magnetic response of the diamond transitions from a paramagnetic to a diamagnetic response after the Ground State Level-AntiCrossing of the  $\text{NV}^-$  center.

This work has potential applications in various fields that require angular control of unthetered diamonds. For instance,  $\text{NV}^-$  centers can be used to hyperpolarize  $\text{C}^{13}$  atoms of molecules in liquid environment (159; 158; 157). One of the challenge is to achieve large  $\text{NV}^-$  polarization in strong homogeneous magnetic field. Aligning the anisotropy axis of the  $\text{NV}^-$  centers with the magnetic field is crucial for maintaining high polarization efficiency in the  $|m_s = 0\rangle$  state driven by green laser pumping. Another possible application is controlling the angle of a levitating nano diamond in optical tweezers.



## Conclusion

Since the advent of quantum mechanics one century ago, engineering macroscopic quantum states has been a major objective (14). Despite the extreme sensitivity of quantum states to the environment, recent technological breakthroughs have made it possible to create and control increasingly large quantum systems: from single atoms decades ago (10; 11; 12) to micrometric mechanical oscillators today (13; 21). The generation of quantum states at unprecedented sizes paves the way for testing postulates of quantum physics such as the wave function collapse model (163; 23) and quantum gravity (22).

The mechanical modes of levitating nanoparticles are also good candidates for realizing macroscopic quantum systems because of their extreme isolation from the environment under ultra-high vacuum conditions (24). Notably, the rotational degree of freedom gives rise to unique classical dynamics (gyroscopic stabilization, precession, the tennis racket effect) as well as quantum dynamics (orientational quantum revival (164), the quantum tennis racket effect (165)) that have no equivalent for the center of mass (154). Recently, unprecedented level of control have been attained on the angle of levitating nano-objects: measurements of the angle of particles at the milliradian level (107; 141; 142), spinning particles at GHz rates (109; 108; 155), and cooling of the angular modes using crystal impurities (36; 43).

Additionally, the rotational degrees of freedom of magnetic particles are naturally coupled to their internal magnetization due to the equivalence between magnetic moment and angular momentum: these are the gyromagnetic effects (47; 48). These effects are accentuated at nanometric scales, giving rise to unique quantum effects such as the precession of nanometric magnets that constitute highly sensitive magnetometers (45) and the quantum levitation of a nanomagnet using the spin-rotational coupling (105).

In this thesis, we studied the angular dynamics of levitating crystals with embedded spins.

Towards the aforementioned goals, it is natural to consider using magnetic levitation for observing gyromagnetic effects with magnetic particles. Superconductive magnetic levitation is currently the state-of-the-art method for controlling the rotation of magnetic particles (120; 121; 122; 123; 124). In this thesis, we first presented another promising yet seldom studied technique: the magnetic Paul trap (128; 129; 131; 132; 133). We proposed a novel on-chip magnetic Paul trap design that could levitate micro and nano magnets in the near future using current technologies (49). We also designed a macroscopic version of this trap that demonstrates levitation of millimeter-size magnets. Notably, we decipher the role of size effects in the levitation. Compared to other well-known levitation methods, this approach is advantageous in several respects: first, there is no need to work in a cryogenic environment; second, surface charge fluctuations do not impact the trapping

method; third, the particle will not heat up significantly under vacuum; and last, the trapping parameters can, in principle, be controlled on short time scales. These assets are promising for a precise control of magnetic particle angles and for observing gyromagnetic effects.

It is also advantageous to trap and control the angle of particles without external magnetic fields. In particular, fast rotation of levitating magnetic particles using purely electric fields could be a key ingredient for observing the magnetization by rotation, also known as the Barnett effect (48). In this thesis, we found a new electrical rotation method using charged particles levitating in Paul traps originating from a non-linearity in the angular equation of motion. We theoretically investigate the limits of this technique, and compare it to experiments performed with particles of different size and nature. Notably, we used magnetometry techniques using NV centers inside a rotating diamond to fully reconstruct the angular motion, proving the extreme stability of this rotation method over hours and opening up the possibility to perform coherent spin manipulation in a levitating rotating diamond. Besides the Barnett effect (48), one can now envision observing geometric quantum phases (46) as well as strongly coupled spins and mechanics in the rotating frame (43).

Strong coupling between spins and rotational degrees of freedom was also investigated on an angularly stable levitating diamond particles. In this experimental setting, we discovered a new form of magnetism generated by the optically polarized electronic spin of the NV centers, which we coined Van Vleck diamagnetism (166; 50). This diamagnetism was found to yield a magnetic susceptibility large enough to align the diamond crystalline direction with the external magnetic field. We observed this spin-diamagnetism using mechanical detection of magnetic resonances and found good agreement with the theoretical predictions. To the best of our knowledge, this is the first observation of diamagnetism originating from the spin of the electron rather than their orbital angular momentum. This result could serve for controlling the angle of untethered diamond in optical tweezers or in liquids for hyperpolarization protocols (157; 158; 159).

Levitated magnetic crystals allow for exploration of multiple aspects of the interaction between magnetism and rotation. We believe that the technologies and theoretical analysis developed in this thesis will enhance this already interdisciplinary research field, paving the way for spin-controlled mechanical oscillators in the quantum regime and studies of gyromagnetism at previously unparalleled scales.

## Appendix

---

In this appendix, we calculate some of the results obtained in Chapter 1.

### 1.1. Magnetism in statistical and quantum physics

In this section, we calculate the formula of the magnetization of a system of uncorrelated ions subjected to a thermal bath given in Eq.(1.12). We recall the definition of the magnetization:

$$\mathbf{M} = d\langle \hat{\mathbf{m}} \rangle, \quad \text{with} \quad d = \frac{N_{\text{at}}}{V}. \quad (\text{A.1})$$

First, the population  $p_k$  in the different states of energy  $\epsilon_k$  is given by the Boltzmann distribution such that  $p_k = \exp(-\beta\epsilon_k) / \sum_{k'=1}^N \exp(-\beta\epsilon_{k'})$  with  $\beta = 1/k_{\text{B}}T$  and  $N$  the number of eigenstates.

We introduce the unitary transform  $\hat{U}$  that diagonalizes the Hamiltonian of the system such that  $\hat{\mathcal{H}}_{\text{Diag}} = \hat{U}\hat{\mathcal{H}}\hat{U}^\dagger$ . By writing the new density matrix in this basis  $\hat{\rho}_{\text{Diag}} = \hat{U}\hat{\rho}\hat{U}^\dagger$ , we obtain using Eq.(1.10):

$$\mathbf{M} = -d \text{Tr} \left( \hat{\rho} \frac{\partial \hat{U}^\dagger}{\partial \mathbf{B}} \hat{\mathcal{H}}_{\text{Diag}} \hat{U} \right) - d \text{Tr} \left( \hat{\rho}_{\text{Diag}} \frac{\partial \hat{\mathcal{H}}_{\text{Diag}}}{\partial \mathbf{B}} \right) - d \text{Tr} \left( \hat{\rho} \hat{U}^\dagger \hat{\mathcal{H}}_{\text{Diag}} \frac{\partial \hat{U}}{\partial \mathbf{B}} \right). \quad (\text{A.2})$$

The coherences between the different eigenstates are equal to zero since the system is in contact with a thermal bath that destroys coherences between the states. Thus, we have  $\rho_{\text{Diag},kk'} = 0$  for  $k \neq k'$ . Furthermore, the population in each state is given by the diagonal term of the density matrix  $\rho_{\text{Diag},kk} = p_k$ . Both  $\hat{\rho}_{\text{Diag}}$  and  $\hat{\mathcal{H}}_{\text{Diag}}$  are diagonal. The second term in the right handside of (A.2) is thus equal to  $-d \sum_{k=1}^N \frac{\partial \epsilon_k}{\partial \mathbf{B}} p_k$ . Using the relation  $\hat{U}^\dagger \frac{\partial \hat{U}}{\partial \mathbf{B}} + \frac{\partial \hat{U}^\dagger}{\partial \mathbf{B}} \hat{U} = 0$ , the two other contributions can be merged into a unique term:

$$\mathbf{M} = -d \sum_{k=1}^N \frac{\partial \epsilon_k}{\partial \mathbf{B}} p_k - d \text{Tr} \left( \hat{U} \frac{\partial \hat{U}^\dagger}{\partial \mathbf{B}} [\hat{\mathcal{H}}_{\text{Diag}}, \hat{\rho}_{\text{Diag}}] \right) \quad (\text{A.3})$$

The matrixes  $\hat{\rho}_{\text{Diag}}$  and  $\hat{\mathcal{H}}_{\text{Diag}}$  are both diagonal so we have  $[\hat{\mathcal{H}}_{\text{Diag}}, \hat{\rho}_{\text{Diag}}] = 0$ . Finally, we obtain the equality in (1.12).

### 1.2. Langevin paramagnetism

In this section, we calculate the Langevin magnetic susceptibility tensor under a thermal distribution of states and we demonstrate that the magnetization is always positive.

We use the formula of Eq.(1.21):

$$\chi_{\text{Lan},ii} = -d\mu_0 \sum_{k=1}^N \frac{\partial \Delta \epsilon_k^{(\text{Lan})}}{\partial B_i} \frac{\partial p_k}{\partial B_i}. \quad (\text{A.4})$$

The population  $p_k$  equals  $p_k = \exp(-\beta \epsilon_k) / \sum_{k'=1}^N \exp(-\beta \epsilon_{k'})$ . Injecting this formula into the previous equation, we obtain:

$$\chi_{\text{Lan},ii} = d\mu_0 \beta \frac{\sum_{k,k'=1, k \neq k'}^N \left( \frac{\partial \Delta \epsilon_k^{(\text{Lan})}}{\partial B_i} - \frac{\partial \Delta \epsilon_{k'}^{(\text{Lan})}}{\partial B_i} \right)^2 \exp(-\beta(\epsilon_k - \epsilon_{k'}))}{\left( \sum_{k=1}^N \exp(-\beta \epsilon_k) \right)^2} > 0 \quad (\text{A.5})$$

This term is positive, the Langevin contribution is thus always paramagnetic.

### 1.3. Van Vleck paramagnetism

In this section, we calculate the Van Vleck magnetic susceptibility tensor under a thermal distribution of states and we demonstrate that the magnetization is always positive. We use the formula of Eq.(1.23):

$$\chi_{\text{V.V.},ii} = -d\mu_0 \sum_{k=1}^N \frac{\partial^2 \Delta \epsilon_k^{(\text{V.V.})}}{\partial B_i^2} p_k. \quad (\text{A.6})$$

We can explicitly write this formula using:

$$\Delta \epsilon_k^{(\text{V.V.})} = \sum_{k' \neq k} \frac{\left| \langle k | \frac{\mu_B}{h} (\hat{\mathbf{L}} + g_s \hbar \hat{\mathbf{S}}) \cdot \mathbf{B} | k' \rangle \right|^2}{\epsilon_k - \epsilon_{k'}} \quad (\text{A.7})$$

We get the formula:

$$\chi_{\text{V.V.},ii} = -d\mu_0 \gamma_e^2 \sum_{k=1}^N \left( \sum_{k'=1, k' \neq k}^N \frac{|\langle k | \hat{J}_{\text{tot},i} | k' \rangle|^2}{\epsilon_k - \epsilon_{k'}} \right) p_k. \quad (\text{A.8})$$

Rearranging the terms in the previous equation, we obtain that:

$$\chi_{\text{V.V.},jj} = -d\mu_0 \gamma_e^2 \sum_{k=1}^{N''} \sum_{k' > k}^{N''} \frac{|\langle k | \hat{J}_{\text{tot},j} | k' \rangle|^2}{\epsilon_k^{(0)} - \epsilon_{k'}^{(0)}} (p_k - p_{k'}) > 0. \quad (\text{A.9})$$

because  $(p_k - p_{k'}) / (\epsilon_k^{(0)} - \epsilon_{k'}^{(0)}) < 0$  due to the thermal distribution of states. The Van Vleck magnetic susceptibility is thus positive leading to a paramagnetic behavior.

### 1.4. Magnetization of $\text{NV}^-$ center under microwave excitation

In this section, we estimate the value of the magnetization of a diamond embedded with  $\text{NV}^-$  centers under a microwave excitation. The Hamiltonian of the system in the

microwave rotating frame reads:

$$\hat{\mathcal{H}}_1 = \hbar\omega_{+1,0} | +1 \rangle \langle +1 | + \hbar\omega_{-1,0} | -1 \rangle \langle -1 | \quad (\text{A.10})$$

$$+ \hbar \frac{\Omega_r}{2\sqrt{2}} (| +1 \rangle \langle 0 | + | 0 \rangle \langle +1 | + | 0 \rangle \langle -1 | + | -1 \rangle \langle 0 |). \quad (\text{A.11})$$

We consider the Lindbladian operator  $\mathcal{L}$  that takes into account the longitudinal decay rate  $\Gamma_1$ , the optical pumping rate  $\gamma_{\text{las}}$  in the  $|m_s = 0\rangle$  state and the spin dephasing rate  $\Gamma_2^*$  of the  $NV^-$  center as described in part 1.3.1. We have the equation in the stationary states:

$$0 = \frac{\partial \hat{\rho}}{\partial t} = -\frac{i}{\hbar} [\hat{\mathcal{H}}_1, \hat{\rho}] + \mathcal{L}(\hat{\rho}) \quad \text{with} \quad \hat{\rho} = \begin{pmatrix} \rho_{11} & \rho_{10} & \rho_{1-1} \\ \rho_{10}^* & \rho_{00} & \rho_{0-1} \\ \rho_{1-1}^* & \rho_{0-1}^* & \rho_{-1-1} \end{pmatrix}. \quad (\text{A.12})$$

We obtain the set of equations:

$$0 = -i \frac{\Omega_r}{2\sqrt{2}} (\rho_{10}^* - \rho_{10}) - \Gamma_1 (\rho_{11} - \rho_{00}) - \gamma_{\text{las}} \rho_{11} \quad (\text{A.13})$$

$$0 = -i \frac{\Omega_r}{2\sqrt{2}} (\rho_{0-1} - \rho_{0-1}^*) - \Gamma_1 (\rho_{-1-1} - \rho_{00}) - \gamma_{\text{las}} \rho_{-1-1} \quad (\text{A.14})$$

$$0 = -i \left( \frac{\Omega_r}{2\sqrt{2}} (\rho_{-1-1} - \rho_{00}) - \omega_{-1,0} \rho_{0-1} + \frac{\Omega_r}{2\sqrt{2}} \rho_{1-1} \right) - \Gamma_2^* \rho_{0-1} \quad (\text{A.15})$$

$$0 = -i \left( \frac{\Omega_r}{2\sqrt{2}} (\rho_{00} - \rho_{11}) + \omega_{+1,0} \rho_{10} - \frac{\Omega_r}{2\sqrt{2}} \rho_{1-1} \right) - \Gamma_2^* \rho_{10} \quad (\text{A.16})$$

$$0 = -i \left( (\omega_{+1,0} - \omega_{-1,0}) \rho_{1-1} + \frac{\Omega_r}{2\sqrt{2}} (\rho_{0-1} - \rho_{10}) \right) - \Gamma_2^* \rho_{1-1} \quad (\text{A.17})$$

$$1 = \rho_{11} + \rho_{00} + \rho_{-1-1}. \quad (\text{A.18})$$

In the limit  $\gamma_{\text{las}} \gg \Gamma_1$  that can be experimentally achieved, we obtain the expression for the population:

$$\rho_{-1-1} = \frac{4\Gamma_1(\Gamma_2^{*2} + \omega_{-1,0}^2) + \Omega_r^2 \Gamma_2^*}{4\gamma_{\text{las}}(\Gamma_2^{*2} + \omega_{-1,0}^2) + 2\Omega_r^2 \Gamma_2^*}, \quad (\text{A.19})$$

$$\rho_{+1+1} = \frac{4\Gamma_1(\Gamma_2^{*2} + \omega_{+1,0}^2) + \Omega_r^2 \Gamma_2^*}{4\gamma_{\text{las}}(\Gamma_2^{*2} + \omega_{+1,0}^2) + 2\Omega_r^2 \Gamma_2^*}. \quad (\text{A.20})$$

Finally, we have the formula for the magnetization in the anisotropy direction of the  $NV^-$  center  $\mathbf{e}_3$ :

$$M_3 = -d\hbar\gamma_0 \left( \frac{4\Gamma_1(\Gamma_2^{*2} + \omega_{+1,0}^2) + \Omega_r^2 \Gamma_2^*}{4\gamma_{\text{las}}(\Gamma_2^{*2} + \omega_{+1,0}^2) + 2\Omega_r^2 \Gamma_2^*} - \frac{4\Gamma_1(\Gamma_2^{*2} + \omega_{-1,0}^2) + \Omega_r^2 \Gamma_2^*}{4\gamma_{\text{las}}(\Gamma_2^{*2} + \omega_{-1,0}^2) + 2\Omega_r^2 \Gamma_2^*} \right). \quad (\text{A.21})$$



## Appendix

---

In this appendix, we calculate some of the results obtained in Chapter 2.

### 2.1. Spin-mechanical dynamics equations

In this section, we calculate the two commutators  $[\hat{\mathbf{L}}, \hat{\mathcal{H}}_{\text{s.m.}}]$  and  $[\hat{\mathbf{S}}, \hat{\mathcal{H}}_{\text{s.m.}}]$  in order to calculate the equation of dynamics given in Eq. (2.18):

$$\frac{d\mathbf{L}}{dt} = \frac{1}{i\hbar} \langle [\hat{\mathbf{L}}, \hat{\mathcal{H}}_{\text{s.m.}}] \rangle, \quad (\text{B.1})$$

$$\forall i \in [1, N], \quad \frac{d\mathbf{S}^{(i)}}{dt} = \frac{1}{i\hbar} \langle [\hat{\mathbf{S}}^{(i)}, \hat{\mathcal{H}}_{\text{s.m.}}] \rangle. \quad (\text{B.2})$$

We recall that:

$$\hat{\mathcal{H}}_{\text{s.m.}} = \frac{\hat{\mathbf{L}}^2}{2I} + \hbar D \sum_{i=1}^N (\hat{S}_3^{(i)})^2 - \hbar \gamma_e \mathbf{B} \cdot \left( \sum_{i=1}^N \hat{\mathbf{S}}^{(i)} \right) + U_{\text{trap}}(\hat{\alpha}, \hat{\beta}, \hat{\gamma}). \quad (\text{B.3})$$

#### B.1.1 Calculation of $[\hat{\mathbf{L}}, \hat{\mathcal{H}}_{\text{s.m.}}]$

In this part, we calculate the commutator  $[\hat{\mathbf{L}}, \hat{\mathcal{H}}_{\text{s.m.}}]$ . We can estimate term-by-term the commutators and we have:

$$\left\langle \left[ \hat{\mathbf{L}}, \frac{\hat{\mathbf{L}}^2}{2I} \right] \right\rangle = 0, \quad (\text{B.4})$$

$$\left\langle \left[ \hat{\mathbf{L}}, -\hbar \gamma_e \mathbf{B} \cdot \left( \sum_{i=1}^N \hat{\mathbf{S}}^{(i)} \right) \right] \right\rangle = 0, \quad (\text{B.5})$$

because  $\hat{L}_\mu$  and  $\hat{S}_\nu^{(i)}$  commute with  $\mu, \nu = x, y, z$ .

$$\left\langle [\hat{\mathbf{L}}, U_{\text{trap}}(\hat{\alpha}, \hat{\beta}, \hat{\gamma})] \right\rangle = i\hbar \boldsymbol{\tau}_{\text{trap}}, \quad (\text{B.6})$$

and

$$\left\langle \left[ \hat{\mathbf{L}}, \hbar D \sum_{i=1}^N (\hat{S}_3^{(i)})^2 \right] \right\rangle = i\hbar \boldsymbol{\tau}_{\text{anis.}}. \quad (\text{B.7})$$

In the following, we explicitly calculate the commutator:

$$\left[ \hat{\mathbf{L}}, \hbar D \sum_{i=1}^N \left( \hat{S}_3^{(i)} \right)^2 \right] = \sum_{i=1}^N \hbar D \left[ \hat{\mathbf{L}}, \left( \hat{S}_3^{(i)} \right)^2 \right]. \quad (\text{B.8})$$

We introduce the rotation matrix defined as:

$$R(\hat{\boldsymbol{\Omega}}) = R_z(\hat{\alpha})R_y(\hat{\beta})R_z(\hat{\gamma}) = \begin{pmatrix} c_{\hat{\alpha}} & -s_{\hat{\alpha}} & 0 \\ s_{\hat{\alpha}} & c_{\hat{\alpha}} & 0 \\ 0 & 0 & 1 \end{pmatrix} \begin{pmatrix} c_{\hat{\beta}} & 0 & s_{\hat{\beta}} \\ 0 & 1 & 0 \\ -s_{\hat{\beta}} & 0 & c_{\hat{\beta}} \end{pmatrix} \begin{pmatrix} c_{\hat{\gamma}} & -s_{\hat{\gamma}} & 0 \\ s_{\hat{\gamma}} & c_{\hat{\gamma}} & 0 \\ 0 & 0 & 1 \end{pmatrix}, \quad (\text{B.9})$$

that we can write as:

$$R(\hat{\boldsymbol{\Omega}}) = \begin{pmatrix} \hat{R}_{1,x} & \hat{R}_{2,x} & \hat{R}_{3,x} \\ \hat{R}_{1,y} & \hat{R}_{2,y} & \hat{R}_{3,y} \\ \hat{R}_{1,z} & \hat{R}_{2,z} & \hat{R}_{3,z} \end{pmatrix}. \quad (\text{B.10})$$

We have the relations:

$$\hat{S}_x^{(i)} = \hat{R}_{1,x} \hat{S}_1^{(i)} + \hat{R}_{2,x} \hat{S}_2^{(i)} + \hat{R}_{3,x} \hat{S}_3^{(i)}, \quad (\text{B.11})$$

$$\hat{S}_y^{(i)} = \hat{R}_{1,y} \hat{S}_1^{(i)} + \hat{R}_{2,y} \hat{S}_2^{(i)} + \hat{R}_{3,y} \hat{S}_3^{(i)}, \quad (\text{B.12})$$

$$\hat{S}_z^{(i)} = \hat{R}_{1,z} \hat{S}_1^{(i)} + \hat{R}_{2,z} \hat{S}_2^{(i)} + \hat{R}_{3,z} \hat{S}_3^{(i)}. \quad (\text{B.13})$$

We also have for  $\mu = x, y, z$ :

$$\left[ \hat{L}_\mu, \left( \hat{S}_3^{(i)} \right)^2 \right] = \left\{ \left[ \hat{L}_\mu, \hat{S}_3^{(i)} \right], \hat{S}_3^{(i)} \right\}. \quad (\text{B.14})$$

From (95), we get the commutation rules:

$$\left[ \hat{L}_x, \hat{S}_3^{(i)} \right] = i\hbar \left( \hat{R}_{1,x} \hat{S}_2^{(i)} - \hat{R}_{2,x} \hat{S}_1^{(i)} \right), \quad (\text{B.15})$$

$$\left[ \hat{L}_y, \hat{S}_3^{(i)} \right] = i\hbar \left( \hat{R}_{1,y} \hat{S}_2^{(i)} - \hat{R}_{2,y} \hat{S}_1^{(i)} \right), \quad (\text{B.16})$$

$$\left[ \hat{L}_z, \hat{S}_3^{(i)} \right] = i\hbar \left( \hat{R}_{1,z} \hat{S}_2^{(i)} - \hat{R}_{2,z} \hat{S}_1^{(i)} \right). \quad (\text{B.17})$$

Finally, we get for  $\mu = x, y, z$ :

$$\left[ \hat{L}_\mu, \left( \hat{S}_3^{(i)} \right)^2 \right] = i\hbar \left( \hat{R}_{1,\mu} \left\{ \hat{S}_2^{(i)}, \hat{S}_3^{(i)} \right\} - \hat{R}_{2,\mu} \left\{ \hat{S}_1^{(i)}, \hat{S}_3^{(i)} \right\} \right). \quad (\text{B.18})$$

Under the semiclassical approximation, we have  $\left\langle \hat{R}_{1,\mu} \left\{ \hat{S}_2^{(i)}, \hat{S}_3^{(i)} \right\} \right\rangle = R_{1,\mu} \left\langle \left\{ \hat{S}_2^{(i)}, \hat{S}_3^{(i)} \right\} \right\rangle$ .

By defining  $\tau_{\text{anis.},\mu}^{(i)} = \hbar D \left( R_{1,\mu} \left\langle \left\{ \hat{S}_2^{(i)}, \hat{S}_3^{(i)} \right\} \right\rangle - R_{2,\mu} \left\langle \left\{ \hat{S}_1^{(i)}, \hat{S}_3^{(i)} \right\} \right\rangle \right)$ , we finally get using the Ehrenfest theorem:

$$\frac{d\mathbf{L}}{dt} = \sum_{i=1}^N \boldsymbol{\tau}_{\text{anis.}}^{(i)} + \boldsymbol{\tau}_{\text{trap}} = \boldsymbol{\tau}_{\text{anis.}} + \boldsymbol{\tau}_{\text{trap}}. \quad (\text{B.19})$$

### B.1.2 Calculation of $[\hat{\mathbf{S}}, \hat{\mathcal{H}}_{\text{s.m.}}]$

In this part, we calculate the commutator  $[\hat{\mathbf{S}}^{(i)}, \hat{\mathcal{H}}_{\text{s.m.}}]$ . We can estimate term-by-term the commutators and we have:

$$\left\langle \left[ \hat{\mathbf{S}}^{(i)}, \frac{\hat{\mathbf{L}}^2}{2I} \right] \right\rangle = 0, \quad (\text{B.20})$$

and:

$$\left\langle \left[ \hat{\mathbf{S}}^{(i)}, U_{\text{trap}}(\hat{\alpha}, \hat{\beta}, \hat{\gamma}) \right] \right\rangle = 0 \quad (\text{B.21})$$

$$, \quad (\text{B.22})$$

Furthermore, we have:

$$\left\langle \left[ \hat{\mathbf{S}}^{(i)}, -\hbar\gamma_e \mathbf{B} \cdot \left( \sum_{i=1}^N \hat{\mathbf{S}}^{(i)} \right) \right] \right\rangle = i\boldsymbol{\tau}_{\text{mag}}^{(i)}, \quad (\text{B.23})$$

with:

$$\boldsymbol{\tau}_{\text{mag}}^{(i)} = \hbar\gamma_e \mathbf{S}^{(i)} \times \mathbf{B}. \quad (\text{B.24})$$

Indeed, we have:

$$\left[ \hat{\mathbf{S}}^{(i)}, -\hbar\gamma_e \mathbf{B} \cdot \left( \sum_{i=1}^N \hat{\mathbf{S}}^{(i)} \right) \right] = -\hbar\gamma_e \left[ \hat{\mathbf{S}}^{(i)}, \mathbf{B} \cdot \hat{\mathbf{S}}^{(i)} \right] = i\hbar\gamma_e \hat{\mathbf{S}}^{(i)} \times \mathbf{B}. \quad (\text{B.25})$$

Furthermore:

$$\left\langle \left[ \hat{\mathbf{S}}^{(i)}, \hbar D \sum_{i=1}^N \left( \hat{S}_3^{(i)} \right)^2 \right] \right\rangle = -i\boldsymbol{\tau}_{\text{anis.}}^{(i)}. \quad (\text{B.26})$$

$$. \quad (\text{B.27})$$

Indeed, we have:

$$\left[ \hat{S}_\mu^{(i)}, \hat{S}_3^2 \right] = \left\{ \left[ \hat{S}_\mu, \hat{S}_3 \right], \hat{S}_3 \right\} \quad (\text{B.28})$$

and:

$$\left[ \hat{S}_\mu^{(i)}, \hat{S}_3 \right] = \left[ \hat{R}_{1,\mu} \hat{S}_1 + \hat{R}_{2,\mu} \hat{S}_2 + \hat{R}_{3,\mu} \hat{S}_3, \hat{S}_3 \right]. \quad (\text{B.29})$$

We obtain:

$$\left[ \hat{S}_\mu^{(i)}, \left( \hat{S}_3^{(i)} \right)^2 \right] = i \left( \hat{R}_{2,\mu} \left\{ \hat{S}_1^{(i)}, \hat{S}_3^{(i)} \right\} - \hat{R}_{1,\mu} \left\{ \hat{S}_2^{(i)}, \hat{S}_3^{(i)} \right\} \right) \quad (\text{B.30})$$

We finally obtain:

$$\hbar \frac{d\mathbf{S}^{(i)}}{dt} = -\boldsymbol{\tau}_{\text{anis.}}^{(i)} + \boldsymbol{\tau}_{\text{mag}}^{(i)}. \quad (\text{B.31})$$

## 2.2. Precessing magnet

In this section, we consider the experiment proposed in part 2.4.2 of a spherical freely floating hard magnet in a presence of a magnetic field. We determine the dynamical angular equations of motion of the magnet. We use the  $zyz$  convention of the Euler angles presented Fig. B.1 to perform the calculation and suppose that  $\mathbf{B} = B\mathbf{e}_x$  (for simplicity, we consider that  $\boldsymbol{\mu}$  and  $\mathbf{B}$  are both along  $x$  and not  $z$  as consider in 2.4.2).

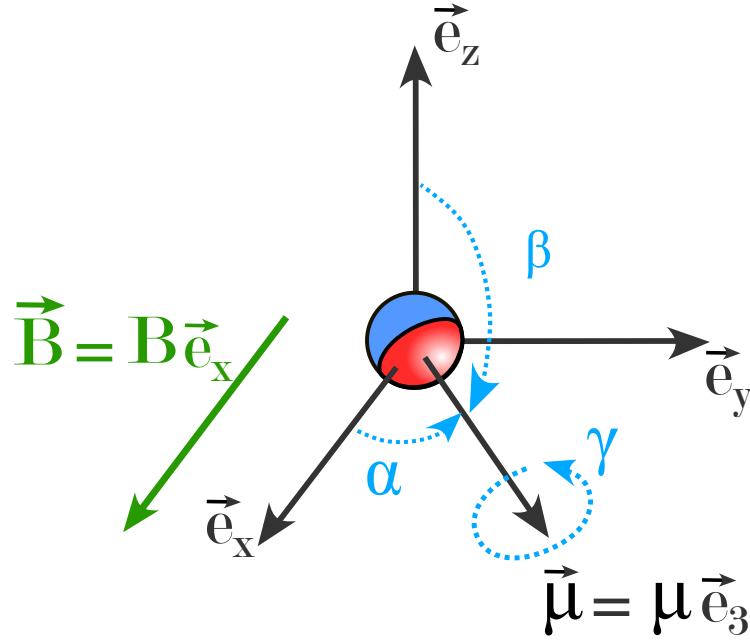


Figure B.1: Schematic of a freely floating.

We want to calculate the dynamics of a hard magnet given by the magnetic momenta  $\boldsymbol{\mu} = \mu\mathbf{e}_3 = -\hbar N\gamma_e\mathbf{e}_3$  where  $N$  is the number of spin. We use the Lagrangian formalism to obtain the dynamical equation of motions. The Lagrangian of the system reads:

$$\mathcal{L} = T_{\text{rot}} + T_{\text{gm}} - U_{\text{mag}}, \quad (\text{B.32})$$

with  $T_{\text{rot}}$  the angular kinetic energy,  $T_{\text{gm}}$  the gyromagnetic energy of the spin and  $U_{\text{mag}}$  the magnetic energy of the spin that depends on the Euler angles as (95; 105; 106):

$$T_{\text{rot}} = \frac{I}{2}(\dot{\alpha}^2 + \dot{\beta}^2 + \dot{\gamma}^2 + 2\dot{\alpha}\dot{\gamma}\cos\beta), \quad (\text{B.33})$$

$$T_{\text{gm}} = -\hbar N\dot{\alpha}\cos\beta, \quad (\text{B.34})$$

$$U_{\text{mag}} = \hbar N\gamma_e B \cos\alpha \sin\beta. \quad (\text{B.35})$$

The angular momentum is conserved about the  $\mathbf{e}_3$  axis such that  $\dot{\gamma} + \dot{\alpha}\cos\beta = I\omega_S$  where  $\omega_S$  is the initial rotation about the  $\mathbf{e}_3$  axis. We assume that the particle has no initial angular speed such that  $\omega_S = 0$ . Using the Euler-Lagrange equation, we obtain the

following equations of motion:

$$\ddot{\alpha} = -2\dot{\alpha}\dot{\beta} \cot \beta - \frac{\omega_I}{\sin \beta} \dot{\beta} - \omega_L \omega_I \frac{\sin \alpha}{\sin \beta}, \quad (\text{B.36})$$

$$\ddot{\beta} = \dot{\alpha}^2 \sin \beta \cos \beta + \omega_I \dot{\alpha} \sin \beta + \omega_L \omega_I \cos \alpha \cos \beta. \quad (\text{B.37})$$

with  $\omega_I = \hbar N/I$ ,  $\omega_L = -\gamma_e B$ .

We move to the equatorial plane by doing the transformation  $\tilde{\beta} = \beta - \pi/2$  and we consider the small oscillation limit for  $\alpha, \tilde{\beta}, \dot{\alpha}, \dot{\tilde{\beta}} \ll 1$ . Linearizing the previous equation gives:

$$\ddot{\alpha} = -\omega_L \omega_I \alpha - \omega_I \dot{\tilde{\beta}}, \quad (\text{B.38})$$

$$\ddot{\tilde{\beta}} = -\omega_L \omega_I \tilde{\beta} + \omega_I \dot{\alpha}. \quad (\text{B.39})$$

In these equations, we have two contributions: the precession motion due to the angular momentum nature of the spin and the magnetic torque.

The stability of the linear system of coupled equation depends on the eigenvalues of the following matrix:

$$A_{\parallel} = \begin{pmatrix} 0 & 0 & 1 & 0 \\ 0 & 0 & 0 & 1 \\ -\omega_L \omega_I & 0 & 0 & -\omega_I \\ 0 & -\omega_L \omega_I & \omega_I & 0 \end{pmatrix} \quad (\text{B.40})$$

The associated characteristic polynomial equals:

$$P(X) = X^4 + (\omega_I^2 + 2\omega_L \omega_I)X^2 + (\omega_L \omega_I)^2. \quad (\text{B.41})$$

If  $\lambda$  is a solution of  $P(X) = 0$  then  $-\lambda, \bar{\lambda}, -\bar{\lambda}$  are solutions. Thus, if  $\lambda$  has a non negative real part, then one of the solution has a positive real part and the system is not stable. Thus, a necessary and sufficient condition for this linear system to be stable is that the roots are imaginary. A calculation of the roots of  $P(X)$  gives the condition:

$$\omega_L > -\frac{1}{4}\omega_I. \quad (\text{B.42})$$

We can analyze this result in term of two stable regimes with different physical origin. When  $\omega_L > 0$ , the magnetic field is aligned with the dipole momenta and the configuration is stable due to the magnetic restoring torque. When  $\omega_L < 0$ , the magnetic field tends to misalign the magnet from the equilibrium position but the gyromagnetic confinement is strong enough to ensure gyromagnetic confinement in the regime  $\omega_I > 4|\omega_L|$  in full analogy with a rotating top that did not fall in the gravitational field.





## Appendix

---

In this appendix, we calculate some of the results obtained in Chapter 3.

### 3.1. Magnetic energy of a magnet in a magnetic Paul trap

In this section, we calculate the magnetic energy  $E_{\text{mag}}(\tilde{\beta}, \gamma, t)$  given in Eq. (3.4). We designate by  $O\mathbf{e}_1\mathbf{e}_2\mathbf{e}_3$  the body-fixed reference frame of the magnet and by  $O\mathbf{e}_x\mathbf{e}_y\mathbf{e}_z$  the laboratory frame. We use the Euler angle  $\mathbf{\Omega} = {}^t(\alpha, \beta, \gamma)$  in the  $\mathbf{zyz}$  convention to parametrize the angular motion of the magnet such that  ${}^t(\mathbf{e}_1, \mathbf{e}_2, \mathbf{e}_3) = {}^tR(\mathbf{\Omega}){}^t(\mathbf{e}_x, \mathbf{e}_y, \mathbf{e}_z)$  with:

$$R(\mathbf{\Omega}) = R_z(\alpha)R_y(\beta)R_z(\gamma) = \begin{pmatrix} c_\alpha & -s_\alpha & 0 \\ s_\alpha & c_\alpha & 0 \\ 0 & 0 & 1 \end{pmatrix} \begin{pmatrix} c_\beta & 0 & s_\beta \\ 0 & 1 & 0 \\ -s_\beta & 0 & c_\beta \end{pmatrix} \begin{pmatrix} c_\gamma & -s_\gamma & 0 \\ s_\gamma & c_\gamma & 0 \\ 0 & 0 & 1 \end{pmatrix}. \quad (\text{C.1})$$

where  $c_\nu = \cos(\nu)$  and  $s_\nu = \sin(\nu)$ . Deriving the product, we get:

$$R(\mathbf{\Omega}) = \begin{pmatrix} c_\alpha c_\beta c_\gamma - s_\alpha s_\gamma & -s_\alpha c_\gamma - c_\alpha c_\beta s_\gamma & c_\alpha s_\beta \\ c_\alpha s_\gamma + s_\alpha c_\beta c_\gamma & c_\alpha c_\gamma - s_\alpha c_\beta s_\gamma & s_\alpha s_\beta \\ -s_\beta c_\gamma & s_\beta s_\gamma & c_\beta \end{pmatrix}. \quad (\text{C.2})$$

The magnetic moment of the ferromagnet is supposed to be fixed in the body frame (strong anisotropy condition). We consider that the magnetic moment is oriented along the  $-\mathbf{e}_1$  axis such that  $\boldsymbol{\mu} = -\mu\mathbf{e}_1$  with  $\mu > 0$ . In the laboratory-fixed coordinate system, we have:

$$\boldsymbol{\mu} = -\mu((c_\alpha c_\beta c_\gamma - s_\alpha s_\gamma)\mathbf{e}_x + (c_\alpha s_\gamma + s_\alpha c_\beta c_\gamma)\mathbf{e}_y - s_\beta c_\gamma\mathbf{e}_z). \quad (\text{C.3})$$

We perform the angular change of variable  $\beta = \tilde{\beta} + \pi/2$  and obtain:

$$\boldsymbol{\mu} = -\mu((-c_\alpha s_{\tilde{\beta}} c_\gamma - s_\alpha s_\gamma)\mathbf{e}_x + (c_\alpha s_\gamma - s_\alpha s_{\tilde{\beta}} c_\gamma)\mathbf{e}_y - c_{\tilde{\beta}} c_\gamma\mathbf{e}_z). \quad (\text{C.4})$$

To second order in the variables  $\tilde{\beta}, \gamma$ , we obtain:

$$\mathbf{B}_0 = \mu \begin{pmatrix} c_\alpha \tilde{\beta} + s_\alpha \gamma \\ -c_\alpha \gamma + s_\alpha \tilde{\beta} \\ 1 - \frac{\tilde{\beta}^2 + \gamma^2}{2} \end{pmatrix} \quad (\text{C.5})$$

The total magnetic field  $\mathbf{B}_{\text{tot}}(\mathbf{r}, t)$  reads:

$$\mathbf{B}_{\text{tot}}(\mathbf{r}, t) = \mathbf{B}_0 + \mathbf{B}_1(\mathbf{r}, t), \quad (\text{C.6})$$

with:

$$\mathbf{B}_0 = B_0 \begin{pmatrix} 0 \\ 0 \\ 1 \end{pmatrix} \quad \text{and} \quad \mathbf{B}_1(\mathbf{r}, t) = \frac{B_1''}{2} \cos(\Omega t) \begin{pmatrix} -xz \\ -yz \\ z^2 - \frac{1}{2}x^2 - \frac{1}{2}y^2 \end{pmatrix}. \quad (\text{C.7})$$

To second order in the variables, only the component along the  $\mathbf{e}_z$  contributes to the magnetic energy  $E_{\text{mag}} = -\boldsymbol{\mu} \cdot \mathbf{B}_{\text{tot}}(\mathbf{r}, t)$ . We thus get the formula Eq. (3.4):

$$E_{\text{mag}} = \mu B_0 \left( \frac{\gamma^2}{2} + \frac{\tilde{\beta}^2}{2} \right) - \frac{\mu B_1''}{2} \left( z^2 - \frac{1}{2}(x^2 + y^2) \right) \cos(\Omega t). \quad (\text{C.8})$$

### 3.2. Stability condition taking into account gravity and a compensating magnetic field gradient

In this section, we estimate the stability criterion of 3.12. The total magnetic field reads:

$$\mathbf{B}_{\text{tot}}(\mathbf{r}, t) = \mathbf{B}_0 + \mathbf{B}_1(\mathbf{r}, t) + \mathbf{B}_2(\mathbf{r}), \quad (\text{C.9})$$

with:

$$\mathbf{B}_0 = B_0 \begin{pmatrix} 0 \\ 0 \\ 1 \end{pmatrix}, \quad \mathbf{B}_1(\mathbf{r}, t) = \frac{B_1''}{2} \cos(\Omega t) \begin{pmatrix} -xz \\ -yz \\ z^2 - \frac{1}{2}x^2 - \frac{1}{2}y^2 \end{pmatrix} \quad \text{and} \quad \mathbf{B}_2(\mathbf{r}) = B_2' \begin{pmatrix} -x/2 \\ -y/2 \\ z \end{pmatrix}. \quad (\text{C.10})$$

Making the secular approximation on the dynamics of the center of mass, we obtain that the magnetic energy equals to second order in the variables (we do not keep the first order term that fully compensates the gravity):

$$\tilde{E}_{\text{mag}} = \frac{1}{2}I \sum_{\nu=\tilde{\beta},\gamma} \omega_\nu^2 \nu^2 + \frac{1}{2}m \sum_{u=x,y,z} \tilde{\omega}_u^2 u^2 + \sqrt{Im}\omega_c^2 \left( (c_\alpha \tilde{\beta} + s_\alpha \gamma)x + (s_\alpha \tilde{\beta} - c_\alpha \gamma)y \right), \quad (\text{C.11})$$

with:

$$\omega_c = \sqrt{\sqrt{\frac{5}{2}} \frac{B_2' B_{\text{sat}}}{\mu_0 \rho_m a}}. \quad (\text{C.12})$$

The coupling coefficient between the angles and the center of mass motion can lead to instability. The total Hamiltonian reads:

$$\mathcal{H}_{\text{tot}} = \frac{\mathbf{p}^2}{2m} + \frac{\mathbf{L}^2}{2I} + \tilde{E}_{\text{mag}}, \quad (\text{C.13})$$

where  $\mathbf{p} = p_x \mathbf{e}_x + p_y \mathbf{e}_y + p_z \mathbf{e}_z$  is the center of mass moment,  $\mathbf{L} = L_x \mathbf{e}_x + L_y \mathbf{e}_y + L_z \mathbf{e}_z$  is the angular moment. We have

$$\frac{\mathbf{L}^2}{2I} = \frac{(p_\alpha + p_\gamma \sin \tilde{\beta})^2}{2I \cos \tilde{\beta}^2} + \frac{p_\beta^2}{2I} + \frac{p_\gamma^2}{2I}. \quad (\text{C.14})$$

The angular moment  $p_\alpha, p_\beta$  and  $p_\gamma$  are linked to the angles by the relations:

$$p_\beta = I \dot{\tilde{\beta}}, \quad (\text{C.15})$$

$$p_\alpha = I(\dot{\alpha} - \dot{\gamma} \sin \tilde{\beta}), \quad (\text{C.16})$$

$$p_\gamma = I(\dot{\gamma} - \dot{\alpha} \sin \tilde{\beta}). \quad (\text{C.17})$$

In the small angle approximation  $\tilde{\beta} \ll 1$ , we simply have:

$$\frac{\mathbf{L}^2}{2I} = \frac{p_\alpha^2}{2I} + \frac{p_\beta^2}{2I} + \frac{p_\gamma^2}{2I}. \quad (\text{C.18})$$

and:

$$p_\beta = I \dot{\tilde{\beta}}, \quad (\text{C.19})$$

$$p_\alpha = I \dot{\alpha}, \quad (\text{C.20})$$

$$p_\gamma = I \dot{\gamma}. \quad (\text{C.21})$$

We finally get the equations of motion:

$$\frac{dp_x}{dt} = -\frac{\partial \tilde{E}_{\text{mag}}}{\partial x}, \quad (\text{C.22})$$

$$\frac{dp_y}{dt} = -\frac{\partial \tilde{E}_{\text{mag}}}{\partial y}, \quad (\text{C.23})$$

$$\frac{dp_z}{dt} = -\frac{\partial \tilde{E}_{\text{mag}}}{\partial z}, \quad (\text{C.24})$$

$$\frac{dp_\alpha}{dt} = 0, \quad (\text{C.25})$$

$$\frac{dp_\beta}{dt} = -\frac{\partial \tilde{E}_{\text{mag}}}{\partial \tilde{\beta}}, \quad (\text{C.26})$$

$$\frac{dp_\gamma}{dt} = -\frac{\partial \tilde{E}_{\text{mag}}}{\partial \gamma}. \quad (\text{C.27})$$

We get:

$$m\ddot{x} = -m\tilde{\omega}_x^2 x - \sqrt{Im}\omega_c^2 (c_\alpha \tilde{\beta} + s_\alpha \gamma), \quad (\text{C.28})$$

$$m\ddot{y} = -m\tilde{\omega}_y^2 y - \sqrt{Im}\omega_c^2 (s_\alpha \tilde{\beta} - c_\alpha \gamma), \quad (\text{C.29})$$

$$m\ddot{z} = -m\tilde{\omega}_z^2 z, \quad (\text{C.30})$$

$$I\ddot{\tilde{\beta}} = -I\omega_\beta^2 \tilde{\beta} - \sqrt{Im}\omega_c^2 (c_\alpha x + s_\alpha y), \quad (\text{C.31})$$

$$I\ddot{\gamma} = -I\omega_\gamma^2 \gamma - \sqrt{Im}\omega_c^2 (s_\alpha x - c_\alpha y). \quad (\text{C.32})$$

The motion along the  $z$  direction is stable and independent from the other degrees of freedom. By introducing the vector  $\mathbf{R} = {}^t(x, y, \tilde{\beta}, \gamma, \dot{x}, \dot{y}, \dot{\tilde{\beta}}, \dot{\gamma})$ , we have the equation:

$$\dot{\mathbf{R}} = \mathbf{Q}\mathbf{R} \quad (\text{C.33})$$

where:

$$\mathbf{Q} = \begin{pmatrix} 0 & \text{Id} \\ A & 0 \end{pmatrix} \quad \text{with} \quad A = \begin{pmatrix} -\tilde{\omega}_x^2 & 0 & -\sqrt{\frac{I}{m}}\omega_c^2 c_\alpha & -\sqrt{\frac{I}{m}}\omega_c^2 s_\alpha \\ 0 & -\tilde{\omega}_y^2 & -\sqrt{\frac{I}{m}}\omega_c^2 s_\alpha & \sqrt{\frac{I}{m}}\omega_c^2 c_\alpha \\ -\sqrt{\frac{m}{I}}\omega_c^2 c_\alpha & -\sqrt{\frac{m}{I}}\omega_c^2 s_\alpha & -\omega_\beta^2 & 0 \\ -\sqrt{\frac{m}{I}}\omega_c^2 s_\alpha & \sqrt{\frac{m}{I}}\omega_c^2 c_\alpha & 0 & -\omega_\gamma^2 \end{pmatrix} \quad (\text{C.34})$$

To study the stability of this linear differential equation, we calculate the characteristic polynomial of the system  $\chi(X) = \det(\mathbf{Q} - X\text{Id}) = \det(X^2\text{Id} - A)$ :

$$\chi(X) = \det \begin{pmatrix} X^2 + \tilde{\omega}_x^2 & 0 & \sqrt{\frac{I}{m}}\omega_c^2 c_\alpha & \sqrt{\frac{I}{m}}\omega_c^2 s_\alpha \\ 0 & X^2 + \tilde{\omega}_y^2 & \sqrt{\frac{I}{m}}\omega_c^2 s_\alpha & -\sqrt{\frac{I}{m}}\omega_c^2 c_\alpha \\ \sqrt{\frac{m}{I}}\omega_c^2 c_\alpha & \sqrt{\frac{m}{I}}\omega_c^2 s_\alpha & X^2 + \omega_\beta^2 & 0 \\ \sqrt{\frac{m}{I}}\omega_c^2 s_\alpha & -\sqrt{\frac{m}{I}}\omega_c^2 c_\alpha & 0 & X^2 + \omega_\gamma^2 \end{pmatrix}. \quad (\text{C.35})$$

Since  $\tilde{\omega}_x = \tilde{\omega}_y$ , we have:

$$\chi(X) = \det \begin{pmatrix} (X^2 + \tilde{\omega}_x^2)(X^2 + \omega_\beta^2) - \omega_c^4 & 0 \\ 0 & (X^2 + \tilde{\omega}_y^2)(X^2 + \omega_\gamma^2) - \omega_c^4 \end{pmatrix}. \quad (\text{C.36})$$

We finally obtain:

$$\chi(X) = (X^4 + (\tilde{\omega}_x^2 + \omega_\beta^2)X^2 + \tilde{\omega}_x^2\omega_\beta^2 - \omega_c^4) (X^4 + (\tilde{\omega}_y^2 + \omega_\gamma^2)X^2 + \tilde{\omega}_y^2\omega_\gamma^2 - \omega_c^4). \quad (\text{C.37})$$

The dynamical equations Eq. (C.32) are stable if and only if all the roots of  $\chi(X)$  have a negative real part. However, if  $\lambda$  is a root of  $\chi$ , then  $-\lambda$  is also a root of  $\chi$ . Thus, there is one of the two roots in the set  $\{\lambda, -\lambda\}$  that has a negative real part if  $\text{Re}(\lambda) \neq 0$ . Consequently, the system is stable if and only if the roots of  $\chi$  are purely imaginary numbers. This condition reads:

$$-(\tilde{\omega}_x^2 + \omega_\beta^2) + \sqrt{(\tilde{\omega}_x^2 - \omega_\beta^2)^2 + 4\omega_c^4} < 0 \quad (\text{C.38})$$

We finally obtain the condition Eq. (3.12):

$$\omega_\beta \tilde{\omega}_x > \omega_c^2. \quad (\text{C.39})$$

### 3.3. Eddy currents

In this section, we calculate the influence of the oscillating magnetic field on both the trapping mechanism and on the levitating ferromagnet given in Eq. (3.14) and Eq. (3.15).

### C.3.1 Eddy currents in the loops

In this part, we calculate the eddy current generated by one current carrying loop into the other one. The magnetic flux inside the loop 1 equals:

$$\Phi_{B,1} = \pi r_1^2 B_2(t) = \pi r_1^2 \frac{\mu_0 i_2}{2r_2} \cos(\Omega t). \quad (\text{C.40})$$

The circulation of the electric field reads:

$$\oint \mathbf{E}_1 \cdot d\mathbf{l} = 2\pi r_1 E_1 \quad (\text{C.41})$$

The Faraday's law gives:

$$E_1 = \frac{\mu_0 i_2 \Omega r_1}{4 r_2} \sin(\Omega t) \quad (\text{C.42})$$

Finally, we obtain the eddy current value normalized by the initial current in the loop:

$$i_{2 \rightarrow 1}(t) = \frac{\mu_0 \sigma S \Omega r_1}{4 r_2} i_2 \sin(\Omega t), \quad (\text{C.43})$$

where  $\sigma$  is the electrical conductivity of gold and  $S = 100 \mu\text{m}^2$  is the area of a slice of the gold lithography. Using  $i_1/i_2 = -r_1/r_2$ , we get the formula Eq. (3.14):

$$\frac{i_{2 \rightarrow 1}(t)}{i_1} = -\frac{\mu_0 \sigma S \Omega}{4} \sin(\Omega t). \quad (\text{C.44})$$

Using the numerical values  $\Omega = (2\pi)2.0 \times 10^3$  Hz,  $\sigma = 4.4 \times 10^7$  S.m<sup>-1</sup>, we obtain that this ratio is of the order of  $10^{-5}$ . Thus, we can safely neglect the eddy current generated by a loop onto the other one.

### C.3.2 Induction current in the levitated magnet

In this part, we calculate the induction current that could lead to particles heating. The levitated sphere does not feel any oscillating magnetic field at the equilibrium position (0,0,0). However, one has to take into account the volume effects and the magnetic field value inside the levitated sphere is of the order of  $B_{\text{ind}} \simeq B_1'' a^2$ . The Faraday's law gives the relation:

$$a E_{\text{ind}} \simeq a^2 B_{\text{ind}} \Omega. \quad (\text{C.45})$$

Using  $B_{\text{ind}} \simeq B_1'' a^2$  and  $j = \sigma E$ , we obtain:

$$j \simeq \Omega \sigma a^3 B_1''. \quad (\text{C.46})$$

The power dissipated by the Joule effect that is in the order of  $P \simeq l S \sigma j^2$  equals:

$$P \simeq \Omega^2 \sigma a^9 B_1''^2. \quad (\text{C.47})$$

The dependance at the power of nine in the magnet size makes the induction current heating of the order of  $10^{-28}$  W. This is not sufficient to heat the internal temperature of

the magnet even at ultra high vacuum.

### 3.4. Rotating saddle

In this section, we calculate the stability criterion for a particle subjected to a rotating saddle potential. We also calculate the resulting macromotion.

#### C.4.1 Stability criterion

The rotating saddle potential is:

$$U(X, Y) = \frac{1}{2}m\omega_r^2 (X^2 - Y^2). \quad (\text{C.48})$$

Writing the motion equation of the particle in the rotating frame, one has to add the centrifugal force  $\mathbf{F}_{\text{cen}} = m\Omega^2(X\mathbf{e}_X + Y\mathbf{e}_Y)$  and the Coriolis force  $\mathbf{F}_{\text{Cor}} = -2m(\Omega\mathbf{e}_Z) \times (\dot{X}\mathbf{e}_X + \dot{Y}\mathbf{e}_Y)$ . The fundamental principle of dynamics gives the set of equations:

$$\ddot{X} - 2\Omega\dot{Y} + (\omega_r^2 - \Omega^2)X = 0, \quad (\text{C.49})$$

$$\ddot{Y} + 2\Omega\dot{X} - (\omega_r^2 + \Omega^2)Y = 0. \quad (\text{C.50})$$

This set of equations can be written as  $\ddot{\mathbf{U}} = \mathbf{A}\mathbf{U}$  with  $\mathbf{U} = {}^t(X, Y, \dot{X}, \dot{Y})$  and

$$\mathbf{A} = \begin{pmatrix} 0 & 0 & 1 & 0 \\ 0 & 0 & 0 & 1 \\ \Omega^2 - \omega_r^2 & 0 & 0 & 2\Omega \\ 0 & \omega_r^2 + \Omega^2 & -2\Omega & 0 \end{pmatrix}. \quad (\text{C.51})$$

The particle is stable if and only if the eigenvalues of the matrix  $\mathbf{A}$  have a negative real part. The eigenvalues verify the equality:

$$\lambda^4 + 2\Omega^2\lambda^2 + \Omega^4 - \omega_r^4 = 0, \quad (\text{C.52})$$

and therefore:

$$\lambda^2 = \pm\omega_r^2 - \Omega^2. \quad (\text{C.53})$$

The eigenvalues have no positive real part if and only if  $\Omega - \omega_r > 0$ . Thus, we obtain the stability condition:

$$\Omega > \omega_r. \quad (\text{C.54})$$

#### C.4.2 Resulting motion

In this part, we calculate the resulting motion of a particle subjected to a quickly rotating saddle potential. The motional equation of the particle in the laboratory-fixed frame reads:

$$\ddot{\mathbf{V}} + \omega_r^2\mathbf{S}(\Omega t)\mathbf{V} = 0, \quad (\text{C.55})$$

with:

$$\mathbf{V} = {}^t(x, y), \quad (\text{C.56})$$

$$\mathbf{S}(\Omega t) = \begin{pmatrix} \cos(2\Omega t) & \sin(2\Omega t) \\ \sin(2\Omega t) & -\cos(2\Omega t) \end{pmatrix}. \quad (\text{C.57})$$

We consider the transformation of the guiding-center proposed in (138):

$$\mathbf{W} = \mathbf{V} - \frac{1}{4} \left( \frac{\omega_r}{\Omega} \right)^2 \mathbf{S}(\Omega t) \left( \mathbf{V} - \frac{1}{\Omega} \mathbf{J} \dot{\mathbf{V}} \right), \mathbf{J} = \begin{pmatrix} 0 & -1 \\ 1 & 0 \end{pmatrix}. \quad (\text{C.58})$$

We obtain a differential equation for  $\mathbf{W}$ :

$$\ddot{\mathbf{W}} - \frac{1}{4} \omega_r \left( \frac{\omega_r}{\Omega} \right)^3 \mathbf{J} \dot{\mathbf{W}} + \frac{1}{4} \omega_r^2 \left( \frac{\omega_r}{\Omega} \right)^2 \mathbf{W} = \left( \frac{\omega_r}{\Omega} \right)^4 f \left( \omega_r^2 \mathbf{W}, \omega_r \dot{\mathbf{W}}, \frac{\omega_r}{\Omega} \right), \quad (\text{C.59})$$

where  $f$  a linear function in  $\omega_r^2 \mathbf{W}$ ,  $\omega_r \dot{\mathbf{W}}$  and analytic in  $\omega_r/\Omega$  in a fixed neighborhood of  $\omega_r/\Omega = 0$  (138). In the limit  $\omega_r/\Omega \rightarrow 0$ , this equation results in a radial motion given by the characteristic confining secular frequency  $\tilde{\omega} = \frac{1}{2} \frac{\omega_r^2}{\Omega}$  and by a precessional motion of characteristic secular frequency  $\tilde{\omega}_{\text{prec}} = \frac{1}{4} \frac{\omega_r^4}{\Omega^3}$ .





## Appendix

---

In this appendix, we calculate some of the results obtained in Chapter 4.

### 4.1. Angular electric energy in the small angle limit

In this section, we calculate the electric energy  $E_{\text{ele}}(\alpha, \beta, \gamma, t)$  of Eq. (4.6) to second order in the Euler angles  $\alpha, \beta, \gamma$  around the position  $\alpha = 0, \beta = \pi/2, \gamma = 0$ . We define the shifted nutation angle  $\tilde{\beta}$  such as  $\beta = \pi/2 + \tilde{\beta}$ . We have:

$$E_{\text{ele}}(\alpha, \beta, \gamma, t) = \frac{\eta U_{\text{AC}}}{z_0^2} \cos(\Omega t) \int_S (c_x x^2 + c_y y^2 + c_z z^2) \rho(\mathbf{r}) dS. \quad (\text{D.1})$$

We perform the integration in the body frame. We define by  $\mathbf{r} = (x, y, z)$  the spatial coordinates in the laboratory frame and by  $\mathbf{R} = (X, Y, Z)$  the spatial coordinates in the body frame. We have the following equality:

$${}^t \mathbf{r} = R(\boldsymbol{\Omega}) {}^t \mathbf{R}, \quad (\text{D.2})$$

with:

$$R(\boldsymbol{\Omega}) = R_z(\alpha) R_y(\beta) R_z(\gamma) = \begin{pmatrix} c_\alpha & -s_\alpha & 0 \\ s_\alpha & c_\alpha & 0 \\ 0 & 0 & 1 \end{pmatrix} \begin{pmatrix} c_\beta & 0 & s_\beta \\ 0 & 1 & 0 \\ -s_\beta & 0 & c_\beta \end{pmatrix} \begin{pmatrix} c_\gamma & -s_\gamma & 0 \\ s_\gamma & c_\gamma & 0 \\ 0 & 0 & 1 \end{pmatrix}. \quad (\text{D.3})$$

where  $(X, Y, Z)$  are the spatial coordinates in the body frame. Up to second order in the angular variables, we get:

$$R(\boldsymbol{\Omega}) = \begin{pmatrix} -\tilde{\beta} - \alpha\gamma & -\alpha + \tilde{\beta}\gamma & 1 - \frac{\alpha^2 + \tilde{\beta}^2}{2} \\ \gamma - \tilde{\beta}\alpha & 1 - \frac{\alpha^2 + \gamma^2}{2} & \alpha \\ \frac{\tilde{\beta}^2 + \gamma^2}{2} - 1 & \gamma & -\tilde{\beta} \end{pmatrix}. \quad (\text{D.4})$$

We inject Eq.(D.2) into Eq.(D.1) using the formula for  $R(\boldsymbol{\Omega})$  calculated in Eq.(D.4). The integration over the particle surface of the cross terms in  $XY$ ,  $XZ$  and  $YZ$  cancels out because of the mirror symmetry of the particle charge distribution. We thus obtain:

$$\begin{aligned} E_{\text{ele}}(\alpha, \tilde{\beta}, \gamma, t) &= \frac{\eta U_{\text{AC}}}{z_0^2} \cos(\Omega t) \left( \int_S c_x (\tilde{\beta}^2 X^2 + \alpha^2 Y^2 - (\alpha^2 + \tilde{\beta}^2) Z^2) \rho(\mathbf{R}) dS \right. \\ &\quad + \int_S c_y (\gamma^2 X^2 - (\alpha^2 + \gamma^2) Y^2 + \alpha^2 Z^2) \rho(\mathbf{R}) dS \\ &\quad \left. + \int_S c_z (-(\gamma^2 + \tilde{\beta}^2) X^2 + \gamma^2 Y^2 + \tilde{\beta}^2 Z^2) \rho(\mathbf{R}) dS \right). \end{aligned} \quad (\text{D.5})$$

By reordering the terms of the previous equation, we get:

$$\begin{aligned}
E_{\text{ele}}(\alpha, \tilde{\beta}, \gamma, t) = & \frac{\eta U_{\text{AC}}}{z_0^2} \cos(\Omega t) ((c_y - c_x) \alpha^2 \int_S (Z^2 - Y^2) \rho(\mathbf{R}) dS \\
& + (c_x - c_z) \tilde{\beta}^2 \int_S (X^2 - Z^2) \rho(\mathbf{R}) dS \\
& + (c_z - c_y) \gamma^2 \int_S (Y^2 - X^2) \rho(\mathbf{R}) dS).
\end{aligned} \tag{D.6}$$

The terms of integration can be simply calculated using the electric quadrupole tensor and we obtain:

$$\begin{aligned}
E_{\text{ele}}(\alpha, \tilde{\beta}, \gamma, t) = & \frac{\eta U_{\text{AC}}}{3z_0^2} \cos(\Omega t) ((c_y - c_x)(Q_3 - Q_2) \alpha^2 + (c_x - c_z)(Q_1 - Q_3) \tilde{\beta}^2 \\
& - (c_y - c_z)(Q_2 - Q_1) \gamma^2).
\end{aligned} \tag{D.7}$$

We finally obtain the formula Eq. (4.6):

$$E_{\text{ele}}(\alpha, \tilde{\beta}, \gamma, t) = \frac{1}{2} I_1 \omega_\alpha^2 \cos(\Omega t) \alpha^2 + \frac{1}{2} I_2 \omega_{\tilde{\beta}}^2 \cos(\Omega t) \tilde{\beta}^2 - \frac{1}{2} I_3 \omega_\gamma^2 \cos(\Omega t) \gamma^2, \tag{D.8}$$

where:

$$\omega_\alpha = \sqrt{\frac{2\eta U_{\text{AC}} (c_y - c_x)(Q_3 - Q_2)}{3z_0^2 I_1}}, \tag{D.9}$$

$$\omega_{\tilde{\beta}} = \sqrt{\frac{2\eta U_{\text{AC}} (c_z - c_x)(Q_3 - Q_1)}{3z_0^2 I_2}}, \tag{D.10}$$

$$\omega_\gamma = \sqrt{\frac{2\eta U_{\text{AC}} (c_y - c_z)(Q_2 - Q_1)}{3z_0^2 I_3}}. \tag{D.11}$$

## 4.2. Non linear angular electric energy

In this section, we calculate the electric potential energy given in Eq. (4.15) for  $\beta = \pi/2, \gamma = 0$ . The rotation matrix thus reads:

$$R(\boldsymbol{\Omega}) = \begin{pmatrix} 0 & -s_\alpha & c_\alpha \\ 0 & c_\alpha & s_\alpha \\ -1 & 0 & 0 \end{pmatrix}. \tag{D.12}$$

Using Eq.(D.2) and Eq.(D.1), we obtain (the cross terms  $XY$ ,  $XZ$  and  $YZ$  cancel out as previously explained):

$$\begin{aligned}
E_{\text{ele}}(\alpha, t) = & \frac{\eta U_{\text{AC}}}{z_0^2} \cos(\Omega t) \left( \int_S c_x (s_\alpha^2 Y^2 + c_\alpha^2 Z^2) \rho(\mathbf{R}) dS \right. \\
& + \int_S c_y (c_\alpha^2 Y^2 + s_\alpha^2 Z^2) \rho(\mathbf{R}) dS \\
& \left. + \int_S c_z X^2 \rho(\mathbf{R}) dS \right).
\end{aligned} \tag{D.13}$$

Using  $c_\alpha^2 = 1 - s_\alpha^2$  and suppressing the terms that have no contributions in  $\alpha$ , we obtain:

$$E_{\text{ele}}(\alpha, t) = \frac{\eta U_{\text{AC}}}{3z_0^2} (c_y - c_x)(Q_3 - Q_2) \cos(\Omega t) \sin^2 \alpha. \quad (\text{D.14})$$

Finally, we get Eq. (4.15):

$$E_{\text{ele}}(\alpha, t) = \frac{1}{2} I_1 \omega_\alpha^2 \cos(\Omega t) \sin^2(\alpha). \quad (\text{D.15})$$

### 4.3. Angular potential in the rotating frame

In this section, we calculate the angular potential in the rotating frame coming both from the Paul trap potential and the gyroscopic effects.

#### D.3.1 Angular electric energy

In this part, we calculate the electric energy  $E_{\text{ele}}(\alpha, \tilde{\beta}, \gamma, t)$  to second order in the Euler angles  $\tilde{\beta}, \gamma$  without approximation on  $\alpha$ . We have:

$$R(\mathbf{\Omega}) = \begin{pmatrix} -c_\alpha \tilde{\beta} - s_\alpha \gamma & -s_\alpha \left(1 - \frac{\gamma^2}{2}\right) + c_\alpha \tilde{\beta} \gamma & c_\alpha \left(1 - \frac{\tilde{\beta}^2}{2}\right) \\ c_\alpha \gamma - s_\alpha \tilde{\beta} & -s_\alpha \gamma \tilde{\beta} + c_\alpha \left(1 - \frac{\gamma^2}{2}\right) & s_\alpha \left(1 - \frac{\tilde{\beta}^2}{2}\right) \\ \frac{\tilde{\beta}^2 + \gamma^2}{2} - 1 & \gamma & -\tilde{\beta} \end{pmatrix}. \quad (\text{D.16})$$

We obtain a non simplified expression for  $E_{\text{ele}}(\alpha, \tilde{\beta}, \gamma, t)$ :

$$E_{\text{ele}}(\alpha, \tilde{\beta}, \gamma, t) = \frac{\eta U_{\text{AC}}}{z_0^2} \cos(\Omega t) (A_1 + A_2 + A_3). \quad (\text{D.17})$$

with:

$$A_1 = \int_S c_x \left( (c_\alpha \tilde{\beta} + s_\alpha \gamma)^2 X^2 + \left( -s_\alpha \left(1 - \frac{\gamma^2}{2}\right) + c_\alpha \tilde{\beta} \gamma \right)^2 Y^2 + c_\alpha^2 \left(1 - \frac{\tilde{\beta}^2}{2}\right)^2 Z^2 \right) \rho(\mathbf{R}) dS, \quad (\text{D.18})$$

$$A_2 = \int_S c_y \left( (c_\alpha \gamma - s_\alpha \tilde{\beta})^2 X^2 + \left( c_\alpha \left(1 - \frac{\gamma^2}{2}\right) - s_\alpha \tilde{\beta} \gamma \right)^2 Y^2 + s_\alpha^2 \left(1 - \frac{\tilde{\beta}^2}{2}\right)^2 Z^2 \right) \rho(\mathbf{R}) dS, \quad (\text{D.19})$$

$$A_3 = \int_S c_z \left( -(\gamma^2 + \tilde{\beta}^2) X^2 + \gamma^2 Y^2 + \tilde{\beta}^2 Z^2 \right) \rho(\mathbf{R}) dS. \quad (\text{D.20})$$

We consider the change of variable  $\alpha = \Omega/2t + \tilde{\alpha}$ . We make use of the following trigonometric formula:

$$\cos(\Omega t) \cos^2(\alpha) = \frac{1}{2} \left( \cos(\Omega t) + \frac{1}{2} \cos(2\Omega t + 2\tilde{\alpha}) + \frac{1}{2} \cos(2\tilde{\alpha}) \right), \quad (\text{D.21})$$

$$\cos(\Omega t) \sin^2(\alpha) = \frac{1}{2} \left( \cos(\Omega t) - \frac{1}{2} \cos(2\Omega t + 2\tilde{\alpha}) - \frac{1}{2} \cos(2\tilde{\alpha}) \right), \quad (\text{D.22})$$

$$\cos(\Omega t) \sin(\alpha) \cos(\alpha) = \frac{1}{4} (\sin(2\tilde{\alpha}) + \sin(2\Omega t + 2\tilde{\alpha})). \quad (\text{D.23})$$

We consider the high rotation speed case such that  $\Omega \gg \omega_\alpha, \omega_\beta, \omega_\gamma$  as well as the small angle approximation for  $\tilde{\alpha}, \tilde{\beta}, \gamma$ . We can thus neglect the time-dependent torques compared to the constant torques. We obtain:

$$\cos(\Omega t)A_1 = \frac{1}{4} \int_S c_x \left( (-\gamma^2 + \tilde{\beta}^2)X^2 + (\gamma^2 + 2\tilde{\alpha}^2)Y^2 - (\tilde{\beta}^2 + 2\tilde{\alpha}^2)Z^2 \right) \rho(\mathbf{R})dS, \quad (\text{D.24})$$

$$\cos(\Omega t)A_2 = \frac{1}{4} \int_S c_y \left( (\gamma^2 - \tilde{\beta}^2)X^2 - (\gamma^2 + 2\tilde{\alpha}^2)Y^2 + (\tilde{\beta}^2 + 2\tilde{\alpha}^2)Z^2 \right) \rho(\mathbf{R})dS, \quad (\text{D.25})$$

$$\cos(\Omega t)A_3 = 0. \quad (\text{D.26})$$

The last term cancels out because we neglect the time-dependent second order terms. Summing the three expressions, we obtain:

$$\begin{aligned} \cos(\Omega t)(A_1 + A_2 + A_3) &= \frac{1}{6}(c_y - c_x)(Q_3 - Q_2)\tilde{\alpha}^2 + \frac{1}{12}(c_y - c_x)(Q_3 - Q_1)\tilde{\beta}^2 \\ &\quad + \frac{1}{12}(c_y - c_x)(Q_1 - Q_2)\gamma^2. \end{aligned} \quad (\text{D.27})$$

Using this expression, we can simply write the angular electric potential in the rotating frame as:

$$E_{\text{ele}}(\tilde{\alpha}, \tilde{\beta}, \gamma, t) = \frac{1}{2}I_1\tilde{\omega}_{\tilde{\alpha}}^2\tilde{\alpha}^2 + \frac{1}{2}I_2\tilde{\omega}_{\tilde{\beta}}^2\tilde{\beta}^2 - \frac{1}{2}I_3\tilde{\omega}_\gamma^2\gamma^2. \quad (\text{D.28})$$

with:

$$\tilde{\omega}_{\tilde{\alpha}} = \sqrt{\frac{\eta U_{\text{AC}}}{3z_0^2} \frac{(c_y - c_x)(Q_3 - Q_2)}{I_1}}, \quad (\text{D.29})$$

$$\tilde{\omega}_{\tilde{\beta}} = \sqrt{\frac{\eta U_{\text{AC}}}{6z_0^2} \frac{(c_y - c_x)(Q_3 - Q_1)}{I_2}}, \quad (\text{D.30})$$

$$\tilde{\omega}_\gamma = \sqrt{\frac{\eta U_{\text{AC}}}{6z_0^2} \frac{(c_y - c_x)(Q_2 - Q_1)}{I_2}}. \quad (\text{D.31})$$

### D.3.2 Gyroscopic potential

In this part, we calculate the gyroscopic terms arising in the potential of the rotating particle. The rotational Hamiltonian of the system reads:

$$\begin{aligned} \mathcal{H}_{\text{rot}} &= \frac{p_\gamma^2}{2I_3} + \frac{(p_\beta \sin(\beta) \sin(\gamma) - (p_\alpha - p_\gamma \cos(\beta)) \cos(\gamma))^2}{2I_1 \sin^2(\beta)} \\ &\quad + \frac{(p_\beta \sin(\beta) \cos(\gamma) + (p_\alpha - p_\gamma \cos(\beta)) \sin(\gamma))^2}{2I_2 \sin^2(\beta)}. \end{aligned} \quad (\text{D.32})$$

We can develop this Hamiltonian:

$$\begin{aligned}\mathcal{H}_{\text{rot}} &= \frac{p_\gamma^2}{2I_3} + p_\beta^2 \left( \frac{\sin^2(\gamma)}{2I_1} + \frac{\cos^2(\gamma)}{2I_2} \right) \\ &\quad + (p_\alpha - p_\gamma \cos(\beta))^2 \left( \frac{\cos^2(\gamma)}{2I_1 \sin^2(\beta)} + \frac{\sin^2(\gamma)}{2I_2 \sin^2(\beta)} \right) \\ &\quad + p_\beta (p_\alpha - p_\gamma \cos(\beta)) \frac{\sin(\gamma) \cos(\gamma)}{\sin(\beta)} \left( \frac{1}{I_2} - \frac{1}{I_1} \right).\end{aligned}\quad (\text{D.33})$$

We move to the rotating frame  $\alpha = \Omega/2t + \tilde{\alpha}$  and we make the small angle approximation  $\tilde{\alpha}, \tilde{\beta}, \gamma \ll 1$  where  $\beta = \pi/2 + \tilde{\beta}$ . We obtain to second order:

$$\begin{aligned}\mathcal{H}_{\text{rot}} &= \frac{p_\gamma^2}{2I_3} + \frac{p_{\tilde{\beta}}^2}{2I_2} + \left( p_{\tilde{\alpha}} + I_1 \frac{\Omega}{2} + p_\gamma \tilde{\beta} \right)^2 \left( \frac{1 - \gamma^2 + \tilde{\beta}^2}{2I_1} + \frac{\gamma^2}{2I_2} \right) \\ &\quad + \gamma p_{\tilde{\beta}} \left( p_{\tilde{\alpha}} + I_1 \frac{\Omega}{2} + p_\gamma \tilde{\beta} \right) \left( \frac{1}{I_2} - \frac{1}{I_1} \right).\end{aligned}\quad (\text{D.34})$$

We obtain:

$$\begin{aligned}\mathcal{H}_{\text{rot}} &= \frac{p_\gamma^2}{2I_3} + \frac{p_{\tilde{\beta}}^2}{2I_2} + \frac{\left( p_{\tilde{\alpha}} + I_1 \frac{\Omega}{2} \right)^2}{2I_1} + \left( \frac{I_1}{I_2} - 1 \right) \frac{\Omega}{2} \gamma p_{\tilde{\beta}} + \frac{\Omega}{2} \tilde{\beta} p_\gamma \\ &\quad + \frac{I_2 I_1}{2} \left( \frac{\Omega}{2} \right)^2 \tilde{\beta}^2 + \frac{I_3}{2} \left( \frac{\Omega}{2} \right)^2 \left( \frac{I_1^2}{I_2 I_3} - \frac{I_1}{I_3} \right) \gamma^2.\end{aligned}\quad (\text{D.35})$$

The two last terms define a confining potential for the angles  $\tilde{\beta}$  and  $\gamma$ . We can define the gyroscopic frequencies  $\omega_{(\text{gyr.}),\tilde{\beta}}/2\pi$  and  $\omega_{(\text{gyr.}),\gamma}/2\pi$  such that:

$$\omega_{(\text{gyr.}),\tilde{\beta}} = \sqrt{\frac{I_1}{I_2}} \frac{\Omega}{2}, \quad (\text{D.36})$$

$$\omega_{(\text{gyr.}),\gamma} = \sqrt{\frac{I_1}{I_3} \left( \frac{I_1}{I_2} - 1 \right)} \frac{\Omega}{2}. \quad (\text{D.37})$$

### D.3.3 Total angular potential

Summing both contributions from the Paul trap and the gyroscopic effects, we get the total angular potential:

$$E_{\text{tot}}(\tilde{\alpha}, \tilde{\beta}, \gamma, t) = \frac{1}{2} I_1 \omega_{\text{tot},\tilde{\alpha}}^2 \tilde{\alpha}^2 + \frac{1}{2} I_2 \omega_{\text{tot},\tilde{\beta}}^2 \tilde{\beta}^2 + \frac{1}{2} I_3 \omega_{\text{tot},\gamma}^2 \gamma^2. \quad (\text{D.38})$$

where:

$$\omega_{\text{tot},\tilde{\alpha}} = \tilde{\omega}_{\tilde{\alpha}}, \quad (\text{D.39})$$

$$\omega_{\text{tot},\tilde{\beta}} = \sqrt{\omega_{(\text{gyr.}),\tilde{\beta}}^2 + \tilde{\omega}_{\tilde{\beta}}^2}, \quad (\text{D.40})$$

$$\omega_{\text{tot},\gamma} = \sqrt{\omega_{(\text{gyr.}),\gamma}^2 - \tilde{\omega}_\gamma^2}. \quad (\text{D.41})$$

The assumption  $\Omega \gg \omega_\alpha, \omega_\beta, \omega_\gamma$  ensures that the difference  $\omega_{(\text{gyr.}),\gamma}^2 - \tilde{\omega}_\gamma^2$  is positive.



## Appendix

---

In this appendix, we calculate some of the results obtained in Chapter 5.

### 5.1. Rotational invariance of the magnetic susceptibility tensor around the NV<sup>-</sup> center axis

In this section, we prove that the magnetic susceptibility tensor  $\underline{\chi}^{\text{NV}}$  of the NV<sup>-</sup> center commutes with the elements of the group of continuous rotations around the symmetry axis of the NV<sup>-</sup> center  $\mathbf{e}_3$ .

We consider the basis adapted to the NV<sup>-</sup> center  $B = (\mathbf{e}_1, \mathbf{e}_2, \mathbf{e}_3)$  and another basis  $B' = (\mathbf{e}_{1'}, \mathbf{e}_{2'}, \mathbf{e}_3)$  rotated by an angle  $\phi$  around the  $\mathbf{e}_3$  axis. We thus have  $\mathbf{e}_{1'} = \cos(\phi)\mathbf{e}_1 + \sin(\phi)\mathbf{e}_2$ ,  $\mathbf{e}_{2'} = -\sin(\phi)\mathbf{e}_1 + \cos(\phi)\mathbf{e}_2$ .

We consider a magnetic field  $\mathbf{B}$  with coordinates  ${}^t(B_1, B_2, B_3)$  in the basis  $B$  and coordinates  ${}^t(B'_1, B'_2, B'_3)$  in the basis  $B'$ . We have the relation  ${}^t(B'_1, B'_2, B'_3) = R_{3,-\phi} {}^t(B_1, B_2, B_3)$  where  $R_{3,-\phi}$  is the rotational matrix of angle  $-\phi$  around the  $\mathbf{e}_3$  axis.

We also consider the function  $\mathbf{f}$  that relates the magnetic field written in the basis  $B$  to the magnetization written in the basis  $B$  such that  ${}^t(M_1, M_2, M_3) = \mathbf{f}({}^t(B_1, B_2, B_3))$ .

The Hamiltonian of the system reads:

$$\hat{\mathcal{H}} = \hbar D \hat{S}_3^2 - \hbar \gamma_e (B_1 \hat{S}_1 + B_2 \hat{S}_2 + B_3 \hat{S}_3) \quad (\text{E.1})$$

and also:

$$\hat{\mathcal{H}} = \hbar D \hat{S}_3^2 - \hbar \gamma_e (B'_1 \hat{S}'_1 + B'_2 \hat{S}'_2 + B'_3 \hat{S}'_3) \quad (\text{E.2})$$

We apply the unitary transformation  $\hat{U} = e^{-i\phi \hat{S}_3}$  to the Hamiltonian  $\hat{\mathcal{H}}$  and we obtain using the formula  $\hat{\mathcal{H}}' = \hat{U}^\dagger \hat{\mathcal{H}} \hat{U}$ :

$$\hat{\mathcal{H}}' = \hbar D \hat{S}_3^2 - \hbar \gamma_e (B'_1 \hat{S}_1 + B'_2 \hat{S}_2 + B'_3 \hat{S}_3). \quad (\text{E.3})$$

Seen as a function of the component  ${}^t(B_1, B_2, B_3)$ , we have the equality  $\hat{\mathcal{H}}' = \hat{\mathcal{H}} \circ R_{3,-\phi}$ . The Lindbladian of the system  $\mathcal{L}(\hat{\rho})$  describes longitudinal relaxation of the spin population at a rate  $\Gamma_1$ , optical pumping from the  $|m_s = \pm 1\rangle$  to the  $|m_s = 0\rangle$  state at a rate  $\gamma_{\text{las}}$  as well as pure dephasing of all the states at a rate  $\Gamma_2^*$ . It is invariant under a rotation along the  $\mathbf{e}_3$  axis so that we have  $\mathcal{L}' = \mathcal{L}$ .

We can deduce from these considerations that the same goes for the density matrix  $\hat{\rho}'$  seen as a function of the coefficients  ${}^t(B_1, B_2, B_3)$ , so that  $\hat{\rho}' = \hat{\rho} \circ R_{3,-\phi}$ .

The magnetization vector  $\mathbf{M} = {}^t(M_1, M_2, M_3)$  written in the basis  $B$  is equal to  $-d \text{Tr}(\hat{\rho} \frac{\partial \hat{\mathcal{H}}}{\partial \mathbf{B}})$  which is a function of  $\mathbf{B}$  via the density matrix  $\hat{\rho}$ . In the basis  $B'$ , we have

the equality  ${}^t(M'_1, M'_2, M'_3) = R_{3,-\phi} {}^t(M_1, M_2, M_3)$ . Furthermore, we can write:

$${}^t(M'_1, M'_2, M'_3) = -d \operatorname{Tr} \left( \hat{\rho} \frac{\partial \hat{\mathcal{H}}}{\partial \mathbf{B}'} \right) = -d \operatorname{Tr} \left( \hat{U} (\hat{\rho} \circ R_{3,-\phi}) \hat{U}^\dagger \frac{\partial \hat{\mathcal{H}}}{\partial \mathbf{B}'} \right). \quad (\text{E.4})$$

and thus:

$${}^t(M'_1, M'_2, M'_3) = -d \operatorname{Tr} \left( \hat{\rho} \circ R_{3,-\phi} \frac{\partial \hat{\mathcal{H}}}{\partial \mathbf{B}} \right). \quad (\text{E.5})$$

We finally get  ${}^t(M'_1, M'_2, M'_3) = \mathbf{f}(R_{3,-\phi} {}^t(B_1, B_2, B_3))$ . Finally, we obtain:

$$\mathbf{f} = R_{3,\phi} \mathbf{f} \circ R_{3,-\phi} \quad (\text{E.6})$$

This relationship implies that the jacobian matrix of  $\mathbf{f}$  evaluated in  $\mathbf{0}$  verifies  $\mathbf{d}_0 \mathbf{f} = R_{3,\phi} \mathbf{d}_0 \mathbf{f} R_{3,-\phi}$ . But  $\underline{\underline{\chi}}_B^{\text{NV}} = \mathbf{d}_0 \mathbf{f}$  which means that the magnetic susceptibility tensor  $\underline{\underline{\chi}}_B^{\text{NV}}$  is invariant upon a rotation along the  $\mathbf{e}_3$  axis. Thus, the magnetic susceptibility tensor is independent of the orthonormal basis containing  $\mathbf{e}_3$  and the tensor can be simplified as the following antisymmetric matrix:

$$\underline{\underline{\chi}}^{\text{NV}} = \begin{pmatrix} \chi_\perp & -\chi_d & 0 \\ \chi_d & \chi_\perp & 0 \\ 0 & 0 & \chi_\parallel \end{pmatrix}. \quad (\text{E.7})$$

## Bibliography

- [1] Rabi II, Zacharias JR, Millman S, Kusch P (1938) A New Method of Measuring Nuclear Magnetic Moment. *Physical Review* 53:318–318.
- [2] Bloch F (1946) Nuclear Induction. *Physical Review* 70:460–474.
- [3] Bardeen J, Brattain WH (1948) The Transistor, A Semi-Conductor Triode. *Physical Review* 74:230–231.
- [4] Schawlow AL, Townes CH (1958) Infrared and Optical Masers. *Physical Review* 112:1940–1949.
- [5] Cohen-Tannoudji CN (1998) Nobel Lecture: Manipulating atoms with photons. *Reviews of Modern Physics* 70:707–719.
- [6] Raimond JM, Brune M, Haroche S (2001) Manipulating quantum entanglement with atoms and photons in a cavity. *Reviews of Modern Physics* 73:565.
- [7] MacFarlane AGJ, Dowling JP, Milburn GJ (2003) Quantum technology: the second quantum revolution. *Philosophical Transactions of the Royal Society of London. Series A: Mathematical, Physical and Engineering Sciences* 361:1655–1674.
- [8] De Leon NP, et al. (2021) Materials challenges and opportunities for quantum computing hardware. *Science* 372:eabb2823.
- [9] Degen C, Reinhard F, Cappellaro P (2017) Quantum sensing. *Reviews of Modern Physics* 89:035002.
- [10] Brune M, et al. (1996) Observing the Progressive Decoherence of the “Meter” in a Quantum Measurement. *Physical Review Letters* 77:4887–4890.
- [11] Leibfried D, Blatt R, Monroe C, Wineland D (2003) Quantum dynamics of single trapped ions. *Reviews of Modern Physics* 75:281–324.
- [12] Arndt M, et al. (1999) Wave–particle duality of C60 molecules. *Nature* 401:680–682.
- [13] Aspelmeyer M, Kippenberg TJ, Marquardt F (2014) Cavity optomechanics. *Reviews of Modern Physics* 86:1391–1452.
- [14] Schrödinger E (1935) Die gegenwärtige Situation in der Quantenmechanik. *Naturwissenschaften* 23:844–849.
- [15] Schliesser A, Rivière R, Anetsberger G, Arcizet O, Kippenberg TJ (2008) Resolved-sideband cooling of a micromechanical oscillator. *Nature Physics* 4:415–419.

- 
- [16] Chan J, et al. (2011) Laser cooling of a nanomechanical oscillator into its quantum ground state. *Nature* 478:89–92.
- [17] Cohadon PF, Heidmann A, Pinard M (1999) Cooling of a Mirror by Radiation Pressure. *Physical Review Letters* 83:3174–3177.
- [18] Wollman EE, et al. (2015) Quantum squeezing of motion in a mechanical resonator. *Science* 349:952–955.
- [19] Palomaki TA, Teufel JD, Simmonds RW, Lehnert KW (2013) Entangling Mechanical Motion with Microwave Fields. *Science* 342:710–713.
- [20] Kotler S, et al. (2021) Direct observation of deterministic macroscopic entanglement. *Science* 372:622–625.
- [21] Barzanjeh S, et al. (2022) Optomechanics for quantum technologies. *Nature Physics* 18:15–24.
- [22] Rovelli C (2004) *Quantum Gravity* (Cambridge University Press).
- [23] Schlosshauer M (2005) Decoherence, the measurement problem, and interpretations of quantum mechanics. *Reviews of Modern Physics* 76:1267–1305.
- [24] Gonzalez-Ballester C, Aspelmeyer M, Novotny L, Quidant R, Romero-Isart O (2021) Levitodynamics: Levitation and control of microscopic objects in vacuum. *Science* 374:eabg3027.
- [25] Gieseler J, Novotny L, Quidant R (2013) Thermal nonlinearities in a nanomechanical oscillator. *Nature Physics* 9:806–810.
- [26] Delić U, et al. (2020) Cooling of a levitated nanoparticle to the motional quantum ground state. *Science* 367:892–895.
- [27] Tebbenjohanns F, Mattana ML, Rossi M, Frimmer M, Novotny L (2021) Quantum control of a nanoparticle optically levitated in cryogenic free space. *Nature* 595:378–382.
- [28] Magrini L, et al. (2021) Real-time optimal quantum control of mechanical motion at room temperature. *Nature* 595:373–377.
- [29] Delord T, Nicolas L, Chassagneux Y, Hétet G (2017) Strong coupling between a single nitrogen-vacancy spin and the rotational mode of diamonds levitating in an ion trap. *Physical Review A* 96:063810.
- [30] Rusconi CC, Perdriat M, Hétet G, Romero-Isart O, Stickler BA (2022) Spin-Controlled Quantum Interference of Levitated Nanorotors. *Physical Review Letters* 129:093605.
- [31] Jelezko F, Gaebel T, Popa I, Gruber A, Wrachtrup J (2004) Observation of Coherent Oscillations in a Single Electron Spin. *Physical Review Letters* 92:076401.

- [32] Kennedy TA, Colton JS, Butler JE, Linares RC, Doering PJ (2003) Long coherence times at 300 K for nitrogen-vacancy center spins in diamond grown by chemical vapor deposition. *Applied Physics Letters* 83:4190–4192.
- [33] Rugar D, Budakian R, Mamin HJ, Chui BW (2004) Single spin detection by magnetic resonance force microscopy. *Nature* 430:329–332.
- [34] Arcizet O, et al. (2011) A single nitrogen-vacancy defect coupled to a nanomechanical oscillator. *Nature Physics* 7:879–883.
- [35] Kolkowitz S, et al. (2012) Coherent Sensing of a Mechanical Resonator with a Single-Spin Qubit. *Science* 335:1603–1606.
- [36] Delord T, Huillery P, Nicolas L, Hétet G (2020) Spin-cooling of the motion of a trapped diamond. *Nature* 580:56–59.
- [37] Ma Y, Hoang TM, Gong M, Li T, Yin Zq (2017) Proposal for quantum many-body simulation and torsional matter-wave interferometry with a levitated nanodiamond. *Physical Review A* 96:023827.
- [38] Wei BB, Burk C, Wrachtrup J, Liu RB (2015) Magnetic ordering of nitrogen-vacancy centers in diamond via resonator-mediated coupling. *EPJ Quantum Technology* 2:1–7.
- [39] Rabl P, et al. (2010) A quantum spin transducer based on nanoelectromechanical resonator arrays. *Nature Physics* 6:602–608.
- [40] Feynman RP (1982) Simulating physics with computers. *International Journal of Theoretical Physics* 21:467–488.
- [41] Schneider C, Porras D, Schaetz T (2012) Experimental quantum simulations of many-body physics with trapped ions. *Reports on Progress in Physics* 75:024401.
- [42] Blatt R, Roos CF (2012) Quantum simulations with trapped ions. *Nature Physics* 8:277–284.
- [43] Perdriat M, Pellet-Mary C, Huillery P, Rondin L, Hétet G (2021) Spin-Mechanics with Nitrogen-Vacancy Centers and Trapped Particles. *Micromachines* 12:651.
- [44] Alzetta G, Arimondo E, Ascoli C, Gozzini A (1967) Paramagnetic resonance experiments at low fields with angular-momentum detection. *Il Nuovo Cimento B (1965-1970)* 52:392–402.
- [45] Jackson Kimball DF, Sushkov AO, Budker D (2016) Precessing Ferromagnetic Needle Magnetometer. *Physical Review Letters* 116:190801.
- [46] Wood A, Hollenberg L, Scholten R, Martin A (2020) Observation of a Quantum Phase from Classical Rotation of a Single Spin. *Physical Review Letters* 124:020401.
- [47] Einstein A, de Haas WJ (1915) Experimental proof of the existence of Ampère’s molecular currents. *Koninklijke Nederlandse Akademie van Wetenschappen Proceedings Series B Physical Sciences* 18:696–711.

- [48] Barnett SJ (1915) Magnetization by Rotation. *Physical Review* 6:239–270.
- [49] Perdriat M, Pellet-Mary C, Copie T, Hétet G (2022) Planar Magnetic Paul Traps for Ferromagnetic Particles.
- [50] Perdriat M, Huillery P, Pellet-Mary C, Hétet G (2022) Angle Locking of a Levitating Diamond Using Spin Diamagnetism. *Physical Review Letters* 128:117203.
- [51] Maxwell JC (1865) VIII. A dynamical theory of the electromagnetic field. *Philosophical Transactions of the Royal Society of London* 155:459–512.
- [52] (1905) *Annales de chimie et de physique*.
- [53] Bohr N (1911) *Studier over metallernes elektrontheori* (Thaning et Appel in Komm.).
- [54] Uhlenbeck GE, Goudsmit S (1925) Ersetzung der Hypothese vom unmechanischen Zwang durch eine Forderung bezüglich des inneren Verhaltens jedes einzelnen Elektrons. *Die Naturwissenschaften* 13:953–954.
- [55] Heisenberg W (1925) Über quantentheoretische Umdeutung kinematischer und mechanischer Beziehungen. *Zeitschrift für Physik* 33:879–893.
- [56] Van Vleck JH (1932) *The Theory of Electric and Magnetic Susceptibilities* (Clarendon Press).
- [57] Van Vleck JH (1978) Quantum Mechanics: The Key to Understanding Magnetism. *Science* 201:113–120.
- [58] Ashcroft NW, Mermin ND (2002) *Physique des solides* (EDP Sciences).
- [59] Born M, Oppenheimer R (1927) Zur Quantentheorie der Molekeln. *Annalen der Physik* 389:457–484.
- [60] Alloul H (2007) *Physique des électrons dans les solides: Structure de bandes, supraconductivité et magnétisme. I* (Editions Ecole Polytechnique).
- [61] Bethe H (1929) Term aufspaltung in Kristallen. *Annalen der Physik* 395:133–208.
- [62] Sewani VK, et al. (2020) Spin thermometry and spin relaxation of optically detected  $\text{Cr}_3^+$  ions in ruby  $\text{Al}_2\text{O}_3$ . *Physical Review B* 102:104114.
- [63] Ghamnia M, Jardin C, Bouslama M (2003) Luminescent centres F and F+ in  $\alpha$ -alumina detected by cathodoluminescence technique. *Journal of Electron Spectroscopy and Related Phenomena* 133:55–63.
- [64] Liu L, Bi Y, Xu JA (2013) Ruby fluorescence pressure scale: Revisited. *Chinese Physics B* 22:056201.
- [65] Esposti CD, Bizzocchi L (2007) Absorption and Emission Spectroscopy of a Lasing Material: Ruby. *Journal of Chemical Education* 84:1316.
- [66] Awschalom DD, Hanson R, Wrachtrup J, Zhou BB (2018) Quantum technologies with optically interfaced solid-state spins. *Nature Photonics* 12:516–527.

- [67] White RM (2007) *Quantum theory of magnetism: magnetic properties of materials*, Springer series in solid-state sciences (Springer, Berlin ; New York), 3rd, completely rev. edition.
- [68] Hill E, Van Vleck JH (1928) On the Quantum Mechanics of the Rotational Distortion of Multiplets in Molecular Spectra. *Physical Review* 32:250–272.
- [69] Bitter F (1929) Magnetic Susceptibility of Nitric Oxide at 296 degrees K. and 216 degrees K. *Proceedings of the National Academy of Sciences of the United States of America* 15:638–642.
- [70] Aharoni J, Scherrer P (1929) Die Suszeptibilität des NO-Gases bei verschiedenen Temperaturen. *Zeitschrift für Physik* 58:749–765.
- [71] Hudgens S, Kastner M, Fritzsche H (1974) Diamagnetic Susceptibility of Tetrahedral Semiconductors. *Physical Review Letters* 33:1552–1555.
- [72] Nikolaev A, Verberck B (2006) in *Carbon Based Magnetism* pp 245–278.
- [73] Chadi DJ, White RM, Harrison WA (1975) Theory of the Magnetic Susceptibility of Tetrahedral Semiconductors. *Physical Review Letters* 35:1372–1375.
- [74] Zaitsev AM (2001) *Optical Properties of Diamond: A Data Handbook* (Springer Science & Business Media).
- [75] Wehner S, Elkouss D, Hanson R (2018) Quantum internet: A vision for the road ahead. *Science* 362:eaam9288.
- [76] Dréau A (2013) These de doctorat (Cachan, Ecole normale supérieure).
- [77] Doherty M, et al. (2012) Theory of the ground-state spin of the nv- center in diamond. *Physical Review B* 85:205203.
- [78] Robledo L, Bernien H, Sar Tvd, Hanson R (2011) Spin dynamics in the optical cycle of single nitrogen-vacancy centres in diamond. *New Journal of Physics* 13:025013.
- [79] Tetienne JP, et al. (2012) Magnetic-field-dependent photodynamics of single NV defects in diamond: an application to qualitative all-optical magnetic imaging. *New Journal of Physics* 14:103033.
- [80] Delord T, et al. (2018) Ramsey Interferences and Spin Echoes from Electron Spins Inside a Levitating Macroscopic Particle. *Physical Review Letters* 121.
- [81] Jarmola A, Acosta VM, Jensen K, Chemerisov S, Budker D (2012) Temperature- and Magnetic-Field-Dependent Longitudinal Spin Relaxation in Nitrogen-Vacancy Ensembles in Diamond. *Physical Review Letters* 108:197601.
- [82] Pelka R (2011) Full Susceptibility Tensor for Localized Spin Models with  $S = 1, 3/2, 2, 5/2$  and with Rhombic Anisotropy. *Acta Physica Polonica A* 119:428–436.
- [83] Pellet-Mary C, Huillery P, Perdriat M, Hétet G (2021) Magnetic torque enhanced by tunable dipolar interactions. *Physical Review B* 104:L100411.

- 
- [84] Rugar D, Yannoni CS, Sidles JA (1992) Mechanical detection of magnetic resonance. *Nature* 360:563–566.
- [85] Arimondo E (1968) Angular momentum detection of non-linear phenomena in paramagnetic resonance. *Annales de Physique* 14:425–447.
- [86] Paul W, Steinwedel H (1953) Notizen: Ein neues Massenspektrometer ohne Magnetfeld. *Zeitschrift für Naturforschung A* 8:448–450.
- [87] Paul W (1990) Electromagnetic traps for charged and neutral particles. *Reviews of Modern Physics* 62:531–540.
- [88] Lovelace R, Mehanian C, Tommila T, Lee D (1985) Magnetic confinement of a neutral gas. *Nature* 318:30–36.
- [89] Mathieu (1868) Mémoire sur le mouvement vibratoire d’une membrane de forme elliptique. *Journal de Mathématiques Pures et Appliquées* 13:137–203.
- [90] Delord T (2019) These de doctorat (Université Paris sciences et lettres).
- [91] Achard J, Jacques V, Tallaire A (2020) Chemical vapour deposition diamond single crystals with nitrogen-vacancy centres: a review of material synthesis and technology for quantum sensing applications. *Journal of Physics D: Applied Physics* 53:313001.
- [92] Tallaire A, et al. (2017) Thick CVD diamond films grown on high-quality type IIa HPHT diamond substrates from New Diamond Technology. *Diamond and Related Materials* 77:146–152.
- [93] Huillery P, et al. (2020) Spin mechanics with levitating ferromagnetic particles. *Physical Review B* 101:134415.
- [94] Mori K, et al. (2020) Einstein–de Haas effect at radio frequencies in and near magnetic equilibrium. *Physical Review B* 102:054415.
- [95] Rusconi CC, Romero-Isart O (2016) Magnetic rigid rotor in the quantum regime: Theoretical toolbox. *Physical Review B* 93:054427.
- [96] Conangla GP (2019) Sensing with the harmonic oscillator.
- [97] Martinetz L, Hornberger K, Stickler BA (2018) Gas-induced friction and diffusion of rigid rotors. *Physical Review E* 97:052112.
- [98] Scott GG (1962) Review of Gyromagnetic Ratio Experiments. *Reviews of Modern Physics* 34:102–109.
- [99] Wasilewski W, et al. (2010) Quantum Noise Limited and Entanglement-Assisted Magnetometry. *Physical Review Letters* 104:133601.
- [100] Dang HB, Maloof AC, Romalis MV (2010) Ultrahigh sensitivity magnetic field and magnetization measurements with an atomic magnetometer. *Applied Physics Letters* 97:151110.

- [101] Sheng D, Li S, Dural N, Romalis MV (2013) Subfemtotesla Scalar Atomic Magnetometry Using Multipass Cells. *Physical Review Letters* 110:160802.
- [102] Allred JC, Lyman RN, Kornack TW, Romalis MV (2002) High-Sensitivity Atomic Magnetometer Unaffected by Spin-Exchange Relaxation. *Physical Review Letters* 89:130801.
- [103] Kominis IK, Kornack TW, Allred JC, Romalis MV (2003) A subfemtotesla multi-channel atomic magnetometer. *Nature* 422:596–599.
- [104] Savukov IM, Romalis MV (2005) Effects of spin-exchange collisions in a high-density alkali-metal vapor in low magnetic fields. *Physical Review A* 71:023405.
- [105] Rusconi C, Pöchhacker V, Kustura K, Cirac J, Romero-Isart O (2017) Quantum Spin Stabilized Magnetic Levitation. *Physical Review Letters* 119:167202.
- [106] Kustura K, Wachter V, Rubio López AE, Rusconi CC (2022) Stability of a magnetically levitated nanomagnet in vacuum: Effects of gas and magnetization damping. *Physical Review B* 105:174439.
- [107] Kuhn S, et al. (2017) Full rotational control of levitated silicon nanorods. *Optica* 4:356–360.
- [108] Reimann R, et al. (2018) GHz Rotation of an Optically Trapped Nanoparticle in Vacuum. *Physical Review Letters* 121:033602.
- [109] Ahn J, et al. (2018) Optically Levitated Nanodumbbell Torsion Balance and GHz Nanomechanical Rotor. *Physical Review Letters* 121:033603.
- [110] Kane BE (2010) Levitated spinning graphene flakes in an electric quadrupole ion trap. *Physical Review B* 82:115441.
- [111] Coppock JE, Nagornykh P, Murphy JPJ, Kane BE (2016) Phase locking of the rotation of a graphene nanoplatelet to an RF electric field in a quadrupole ion trap. 9922:99220E.
- [112] Nagornykh P, Coppock JE, Murphy JPJ, Kane BE (2017) Optical and magnetic measurements of gyroscopically stabilized graphene nanoplatelets levitated in an ion trap. *Physical Review B* 96:035402.
- [113] Hu Y, et al. (2022) Structured transverse orbital angular momentum probed by a levitated optomechanical sensor.
- [114] Chudo H, et al. (2014) Observation of Barnett fields in solids by nuclear magnetic resonance. *Applied Physics Express* 7:063004.
- [115] Wood AA, et al. (2017) Magnetic pseudo-fields in a rotating electron–nuclear spin system. *Nature Physics* 13:1070–1073.
- [116] Rusconi CC, Pöchhacker V, Cirac JI, Romero-Isart O (2017) Linear stability analysis of a levitated nanomagnet in a static magnetic field: Quantum spin stabilized magnetic levitation. *Physical Review B* 96:134419.

- 
- [117] Fadeev P, et al. (2021) Ferromagnetic gyroscopes for tests of fundamental physics. *Quantum Science and Technology* 6:024006.
- [118] Bassani R (2006) Earnshaw (1805–1888) and Passive Magnetic Levitation. *Meccanica* 41:375–389.
- [119] Gao Q, et al. (2021) Magnetic levitation using diamagnetism: Mechanism, applications and prospects. *Science China Technological Sciences* 64:44–58.
- [120] Nemoshkalenko VV, Brandt EH, Kordyuk AA, Nikitin BG (1990) Dynamics of a permanent magnet levitating above a high-Tc superconductor. *Physica C: Superconductivity* 170:481–485.
- [121] Hull JR, Cansiz A (1999) Vertical and lateral forces between a permanent magnet and a high-temperature superconductor. *Journal of Applied Physics* 86:6396–6404.
- [122] Vinante A, et al. (2021) Surpassing the Energy Resolution Limit with ferromagnetic torque sensors. *Physical Review Letters* 127:070801.
- [123] Gieseler J, et al. (2020) Single-Spin Magnetomechanics with Levitated Micromagnets. *Physical Review Letters* 124:163604.
- [124] Druge J, Jean C, Laurent O, Méasson MA, Favero I (2014) Damping and non-linearity of a levitating magnet in rotation above a superconductor. *New Journal of Physics* 16:075011.
- [125] Flanders P, Gov S, Shtrikman S, Thomas H (1999) On the spinning motion of the hovering magnetic top. *Physica D: Nonlinear Phenomena* 126:225–235.
- [126] Berry MV (1996) The Levitron™: an adiabatic trap for spins. *Proceedings of the Royal Society of London. Series A: Mathematical, Physical and Engineering Sciences* 452:1207–1220.
- [127] Dullin H, Easton R (1999) Stability of Levitrons. *ZAMM Journal of applied mathematics and mechanics: Zeitschrift für angewandte Mathematik und Mechanik* 79:S167–S170.
- [128] Sackett C, Cornell E, Monroe C, Wieman C (1993) A magnetic suspension system for atoms and bar magnets. *American journal of physics* 61:304–309.
- [129] Cornell EA, Monroe C, Wieman CE (1991) Multiply loaded, ac magnetic trap for neutral atoms. *Physical Review Letters* 67:2439–2442.
- [130] der Heide H. V (1974) Stabilization by oscillation.
- [131] BASSANI R (2005) Stability of Permanent Magnet Bearings under Parametric Excitations. *Tribology Transactions* 48:457–463.
- [132] Bassani R (2006) A Stability Space of a Magnetomechanical Bearing. *Journal of Dynamic Systems, Measurement, and Control* 129:178–181.
- [133] Bassani R (2007) Dynamic stability of passive magnetic bearings. *Nonlinear Dynamics* 50:161–168.

- [134] Folman R, et al. (2000) Controlling Cold Atoms using Nanofabricated Surfaces: Atom Chips. *Physical Review Letters* 84:4749–4752.
- [135] Feenstra L, Andersson LM, Schmiedmayer J (2004) Microtraps and Atom Chips: Toolboxes for Cold Atom Physics. *General Relativity and Gravitation* 36:2317–2329.
- [136] Delić U, et al. (2020) Cooling of a levitated nanoparticle to the motional quantum ground state. *Science* 367:892–895.
- [137] Guery-odelin D, Lahaye T (2010) *Classical Mechanics Illustrated By Modern Physics: 42 Problems With Solutions* (World Scientific Publishing Company).
- [138] Kirillov O, Levi M (2017) A Coriolis force in an inertial frame. *Nonlinearity* 30:1109–1119.
- [139] Wood AA, Goldblatt RM, Scholten RE, Martin AM (2021) Quantum control of nuclear-spin qubits in a rapidly rotating diamond. *Physical Review Research* 3:043174.
- [140] Kuhn S, et al. (2015) Cavity-Assisted Manipulation of Freely Rotating Silicon Nanorods in High Vacuum. *Nano Letters* 15:5604–5608.
- [141] Arita Y, Mazilu M, Dholakia K (2013) Laser-induced rotation and cooling of a trapped microgyroscope in vacuum. *Nature Communications* 4:2374.
- [142] Kuhn S, et al. (2017) Optically driven ultra-stable nanomechanical rotor. *Nature Communications* 8:1670.
- [143] Bellando L, Kleine M, Amarouchene Y, Perrin M, Louyer Y (2022) Giant diffusion of nanomechanical rotors in a tilted washboard potential. *Physical Review Letters* 129:023602.
- [144] Rashid M, Toroš M, Setter A, Ulbricht H (2018) Precession Motion in Levitated Optomechanics. *Physical Review Letters* 121:253601.
- [145] Hoang TM, et al. (2016) Torsional Optomechanics of a Levitated Nonspherical Nanoparticle. *Physical Review Letters* 117:123604.
- [146] van der Laan F, et al. (2020) Optically levitated rotor at its thermal limit of frequency stability. *Physical Review A* 102:013505.
- [147] Kapitza PL (1951) Dynamic stability of the pendulum with vibrating suspension point. *Soviet Physics–JETP* 21:588–597.
- [148] Xu X, Wiercigroch M, Cartmell MP (2005) Rotating orbits of a parametrically-excited pendulum. *Chaos, Solitons & Fractals* 23:1537–1548.
- [149] Litak G, Borowiec M, Wiercigroch M (2006) Phase lock and rotational motion of a parametric pendulum. *arXiv:nlin/0607046*.
- [150] Arscott FM (1968) Theory and Application of Mathieu Functions. By N. W. Mclachlan. Pp. xii, 401. (Dover, New York.). *The Mathematical Gazette* 52:94–95.

- 
- [151] Kovacic I, Rand R, Mohamed Sah S (2018) Mathieu's Equation and Its Generalizations: Overview of Stability Charts and Their Features. *Applied Mechanics Reviews* 70:020802.
- [152] Ashbaugh MS, Chicone CC, Cushman RH (1991) The twisting tennis racket. *Journal of Dynamics and Differential Equations* 3:67–85.
- [153] Feng X, et al. (2021) Association of Nanodiamond Rotation Dynamics with Cell Activities by Translation-Rotation Tracking. *Nano Letters* 21:3393–3400.
- [154] Stickler BA, Hornberger K, Kim MS (2021) Quantum rotations of nanoparticles. *Nature Reviews Physics* 3:589–597.
- [155] Ahn J, et al. (2020) Ultrasensitive torque detection with an optically levitated nanorotor. *Nature Nanotechnology* 15:89–93.
- [156] Monteiro F, Ghosh S, van Assendelft EC, Moore DC (2018) Optical rotation of levitated spheres in high vacuum. *Physical Review A* 97:051802.
- [157] Shagieva F, et al. (2018) Microwave-assisted cross-polarization of nuclear spin ensembles from optically pumped nitrogen-vacancy centers in diamond. *Nano letters* 18:3731–3737.
- [158] Broadway DA, et al. (2018) Quantum probe hyperpolarisation of molecular nuclear spins. *Nature Communications* 9:1246.
- [159] Fernández-Acebal P, et al. (2018) Toward Hyperpolarization of Oil Molecules via Single Nitrogen Vacancy Centers in Diamond. *Nano Letters* 18:1882–1887.
- [160] Ganguli N, Krishnan KS (1941) Magnetic and other properties of the free electrons in graphite. *Proceedings of the Royal Society of London. Series A. Mathematical and Physical Sciences* 177:168–182.
- [161] Johansson JR, Nation PD, Nori F (2012) QuTiP: An open-source Python framework for the dynamics of open quantum systems. *Computer Physics Communications* 183:1760–1772.
- [162] Johansson JR, Nation PD, Nori F (2013) QuTiP 2: A Python framework for the dynamics of open quantum systems. *Computer Physics Communications* 184:1234–1240.
- [163] Bassi A, Lochan K, Satin S, Singh TP, Ulbricht H (2013) Models of wave-function collapse, underlying theories, and experimental tests. *Reviews of Modern Physics* 85:471–527.
- [164] Stickler BA, et al. (2018) Probing macroscopic quantum superpositions with nanorotors. *New Journal of Physics* 20:122001.
- [165] Ma Y, Khosla KE, Stickler BA, Kim M (2020) Quantum Persistent Tennis Racket Dynamics of Nanorotors. *Physical Review Letters* 125:053604.
- [166] Van Vleck JH (1928) On Dielectric Constants and Magnetic Susceptibilities in the New Quantum Mechanics Part III—Application to Dia- and Paramagnetism. *Physical Review* 31:587–613.

